Measurement of the helicity dependence for single π^0 photoproduction on the deuteron

Dissertation

submitted to attain the academic degree
"Doctor of Natural Sciences"
at the Department of Physics, Mathematics and Computer Science of the Johannes Gutenberg-Universität Mainz

Federico Cividini
born in Bergamo (Italy)

Mainz, December 2019

Abstract

The subject of this thesis is the measurement of the helicity dependence of single π^0 photoproduction with deuteron target in the energy region from pion threshold up to 1500 MeV. This work is part of a systematic measurement of the excited states of the nucleon performed by the A2@MAMI collaboration. Because the electromagnetic excitations are isospin dependent, it is fundamental to study the excited states both of the proton and of the neutron. The experimental data were collected using the circularly photon beam and the large acceptance Crystal Ball/TAPS detector available in the taggerhall at MAMI, in combination with the Mainz-Dubna frozen spin target, that provides a highly longitudinal polarized deuteron target. The new results of the single π^0 inclusive polarized photoproduction cross section on the deuteron and of the E observable for single π^0 photoproduction on quasi-free protons and quasi free-neutrons provide addition information and input for the theoretical models, particularly important especially for the neutron channel.

Contents

List of Figures

List of Tables

Chapter 1

Introduction

During a photoproduction reaction, the nucleon is excited to an intermediate resonant state. Then the nucleon decays to the ground state emitting one (or more) pseudoscalar meson. A systematic measurement of the photoproduction reactions allows to increase our knowledge of the main properties (mass, lifetime, electromagnetic couplings and quantum numbers) of the baryon resonances. Furthermore, a precise measurement of the nucleon spectrum gives fundamental constraints on the theoretical models of nucleon structure. However, the accurate determination of this spectrum has remained elusive despite decades of study. The main reasons for this situation are the lack of measurements of the observables accessible using polarized photon beam and/or polarized nucleon targets and the lack of data in many channels, especially in those induced on the neutron.

The new precision measurements of double-polarization observables on the proton and on the neutron, carried on by the A2 collaboration at MAMI (Mainz Microtron in Mainz, Germany), extend the available statistics, especially in those involving the neutron.

From a theoretical point of view, the pion photoproduction reaction from the nucleon is described by four helicity amplitudes, from which it is possible to extract 16 real experimental observables. These observables are accessible by exploiting the polarization degrees of freedom of the incident photon, along with spin degrees of freedom in the target and recoiling nucleons.

This work, which makes use of a circularly polarized photon beam and longitudinally polarized proton and neutron (deuteron) targets, focuses on the measurement of the single π^0 inclusive polarized photoproduction cross section

on deuteron and of the E observable for single π^0 photoproduction on quasi-free proton and quasi free-neutron.

The final results are compared with the existing data, if available, and with different theoretical models. Fits using Legendre polynomials were performed to extract the Legendre coefficients and to study the waves dependencies of the resonances.

Outline of the thesis

The thesis is organized as follows: in Chapter 2 gives an overview of the theoretical motivation and the physics processes involved in the experiment. Focus is given on the quark model description used in Quantum Chromodynamics and on the pion-photoproduction from the nucleon.

In Chapter 3 there is the description of the Crystal Ball-TAPS setup at the Institut für Kernphysik in Mainz (KPH), where the data of this work were collected, and a presentation of the experimental setup, from the beam production to the data taking electronics.

Chapter 4 describes the software used for the data analysis, the calibration procedure of the experimental data and the random background subtraction. Chapter 5 includes the description of the event selection and physics analyses required for the extraction of the results as well as the analysis of the statistical and systematical errors..

In chapter 6 the results of this work are presented, including the fits to extract the partial waves based on the Legendre polynomials.

The conclusions are summarized in Chapter 7.

Chapter 2

Theoretical Background

In order to understand the structure of the world in which we live, it is crucial to study the constituents of the matter and the way they interact with each other. There are four fundamental interactions that cannot be further reduced. These are the gravitational, the electromagnetic, and the weak and the strong nuclear forces.

The gravitational and electromagnetic forces have an infinite range, and we directly experience them in our everyday life. Because their effects can be seen in the macroscopic world, they were the first to be described. Gravity was described by Isaac Newton in 1687 [1], and electromagnetism by Maxwell with the famous equations named after him in 1861 [2]. A later development of the description of the electromagnetic interaction with a relativistic quantum field approach resulted in quantum electrodynamics (QED). The other two forces are effective only at very short distances, in the subatomic range ($\lesssim 10^{-13}$ m), and are responsible for nuclear interactions. The weak force is described, together with electromagnetism, by the electroweak theory, and its mediators are the Z^0 and $W^{\pm}$ bosons. Quantum chromodynamics (QCD) describes the strong interaction, whose mediators are the gluons. The strong force is responsible for binding the quarks together inside the hadrons.

The description of the electromagnetic, weak, and strong interactions, of their respective mediator boson particles and of all elementary particles has been unified into the Standard Model theory, as shown in Fig. 2.1.

There are two groups of elementary particles: those with half-integer spin are called fermions (quarks, leptons and respective antiparticles), and those with integer spin are calles bosons.

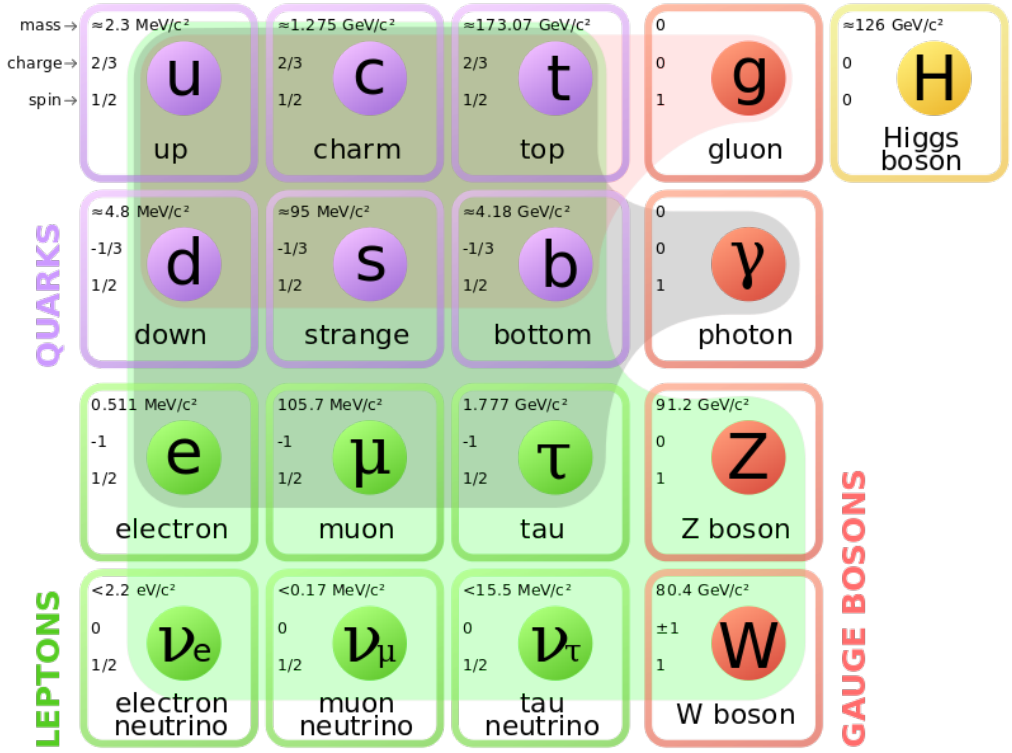

Figure 2.1: Chart of the elementary particles of the Standard Model. The colored background shadows represent the three interactions included in the Model and the particles involved in the interactions (red shadow for the strong force, gray for the electromagnetic and green for the weak). Picture from [3].

Quarks bind together to form hadrons via the strong force which is mediated by gluons. Hadrons are classified into mesons (e.g., pion, eta, kaon...) and baryons (e.g., nucleons, Λ ...). Mesons are bound states consisting of a quark-antiquark pair in a sea of gluons, while baryons (including nucleons) are bound states composed of three quarks in a sea of gluons and quark-antiquark pairs.

The description of the gravitational force as a quantum field has not been achieved yet, and it is currently an object of study.

2.1 The nucleon (within QCD)

Nucleons (that is, protons and neutrons) are the basic components of atomic nuclei, and they contribute to more than 98% of the visible mass in the Universe.

At the beginning of the 20$^{\text{th}}$ Century, Rutherford experimentally proved that a charged particle with a constant mass (later called 'proton') is present in all nuclei, including the hydrogen nucleus [4]. In the 1930s, Chadwick interpreted the results of several experiments as evidence for the existence of a neutral particle with a mass similar to that of the proton, thus leading to the identification of the neutron [5].

Theories developed early after these experimental evidences, described these two new large-mass particles as elementary particles lacking an internal structure. Around the same period of time the first measurements of the magnetic moment of both the proton and the neutron were also performed. The result was unexpected: if the proton and the neutron were point-like particles with spin 1/2, the predicted values would have been $\mu_{p/n} = e\hbar/(2m_{p/n}c)$. Instead, the results for the proton was larger than expected, while for the neutron it was non-zero, and with sign which was opposite to that of the proton value.

Murray Gell-Mann [6] and George Zweig [7] independently developed the quark model in 1964, in order to describe the internal composition of the hadrons and mesons. The proton can be described as being composed of one *down* (d) and two *up* (u) quarks, and the neutron by two d and one u quarks.

Although the quark model could successfully describe the new particles discovered in the early age of baryon spectroscopy, its limitations became quickly evident. The first problem was that the quark model could not explain why the free quark had not been observed. The second problem was the apparent violation of the Pauli exclusion principle, when the baryon Δ^{++} with spin 3/2 and quark composition of three u quarks was observed. With the advent of the QCD it became possible to provide a theoretical interpretation and an explanation for these ambiguities.

In 1964 Oscar Greenberg theorized the introduction of a new quantum number for each quark [8], called color, ('red', 'green', 'blue'), as well as an anti-color for the anti-quarks. Any composite particle made of a combination of quarks can be observed in nature only if it is colorless.

In QCD theory the strong interaction is described through the exchange of gluons, which are the carriers of the color charge. At the nuclear scale, the coupling constant of the strong interaction α_s behaves oppositely to the electromagnetic coupling constant α_{elm}. This α_s decreases when the momentum transfer Q increases (small distances), as shown in Figure 2.2. Therefore, at a

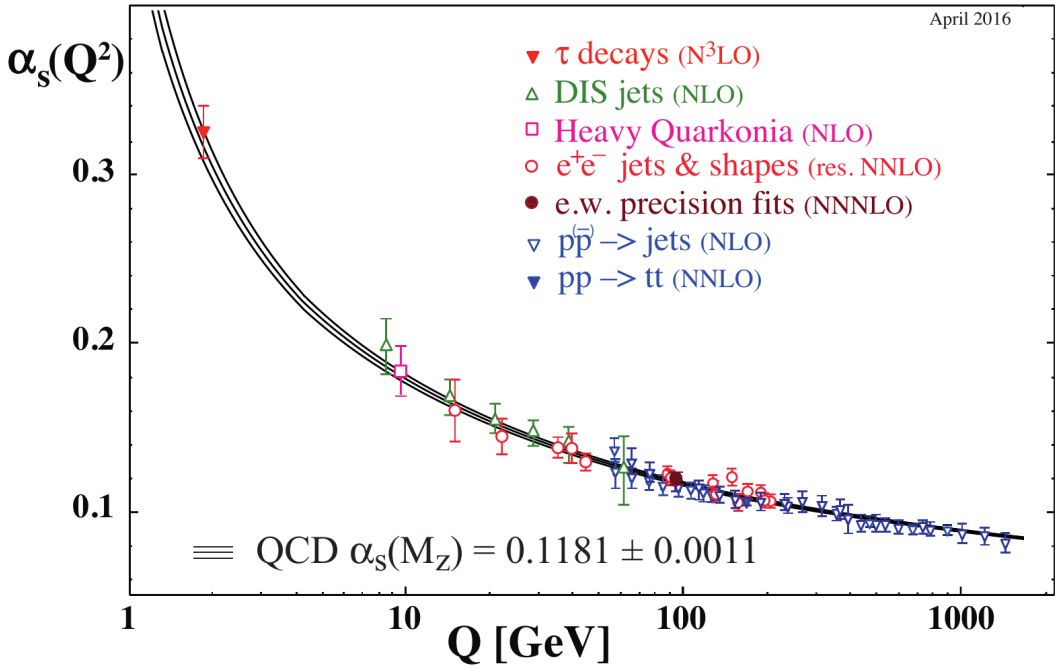

Figure 2.2: Summary of measurements of α_s as a function of the energy scale Q, picture from [9].

very short distance the coupling constant is very small and the quarks bound inside a meson or hadron behave like free particles. This characteristic of the quarks is called *asymptotic freedom*.

On the other hand, at small values of Q (large distances), α_s becomes larger and larger; this explains why quarks are always bound inside a structure, and it is not possible to find them isolated outside of nucleons. This effect is known as *quark confinement*. If the distance between quarks increases, the potential energy is large enough to produce another quark-antiquark pair.

Furthermore, the QCD description of the quark-gluon interaction explains the difference between the sum of masses of the constituent quarks and the mass of the nucleon, which is around 80-100 times larger (e.g. the mass of proton is $\sim$ 938 MeV/c^2 when the sum of its constituent quarks is $<$ 10 MeV/c^2). This discrepancy has been solved by introducing another type of quark mass, termed the constituent quark mass. This mass also takes into account the interaction inside the hadrons, and is significantly larger than the masses, being 350 MeV/c^2 for u and d quarks and around 500 MeV/c^2 for the s quark.

The asymptotic behavior of the parameter α_s, that was described above,

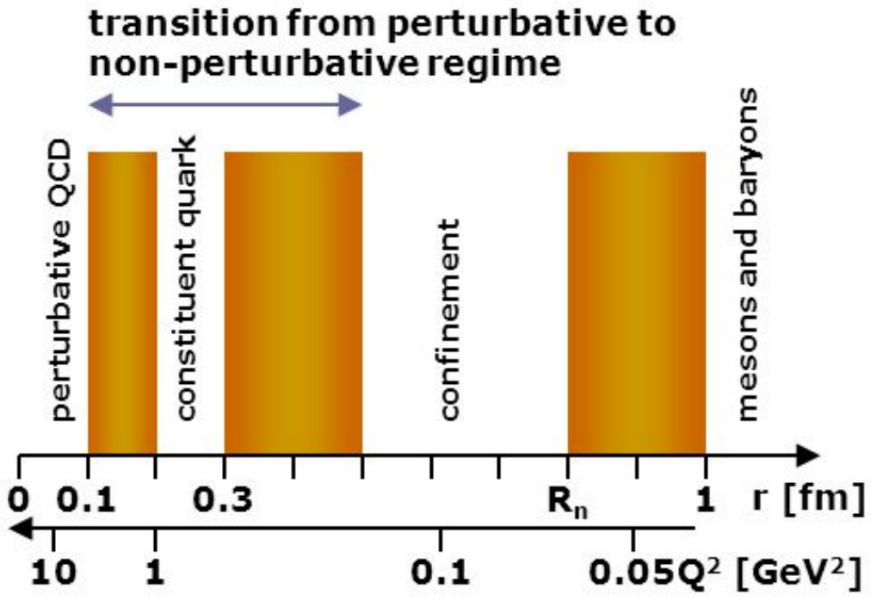

Figure 2.3: Transition from perturbative to non-perturbative regime as function of momentum transfer [10].

also affects the approach used to describe the different regimes. At very large values of momentum transfer Q (small distances), it is possible to describe the interactions among quarks and gluons by using perturbation theory. On the other hand, at low values of Q (large distances), it is not possible to use a perturbative approach. The number of integrals to solve for extracting an exact solution would be infinite, making this approach not feasible. To study the low-Q region, two different approaches have been developed, namely, the Lattice QCD and Chiral Perturbation Theory (ChPT).

LQCD was proposed by K. Wilson in 1974. This lattice gauge theory can be used to perform non-perturbative calculations with a discretized lattice of the space-time [11]. The lattice has a spacing a and volume V, quarks are located on sites in the lattice, and gluons propagate, thus connecting neighboring quarks. Furthermore, it is possible to perform these calculations using Monte Carlo techniques. At the limit $a \to 0$ the required computational power increases dramatically, making it impractical to obtain results. Hence, the predictions are extracted using different values (larger than 0) of the lattice spacing. LQCD gives results for ground and excited states of the nucleon, but it does not provide full explanations for the excitation spectra.

At low energies in QCD, the effective degrees of freedom are no longer quarks and gluons, but can be approximated as hadrons. ChPT is an effective field theory based on the hypothesis that the Lagrangian is symmetric for chiral rotations. This assumption requires the quarks to be massless. At low energies, the matrix elements of the Lagrangian and the scattering amplitudes can be expanded in a Taylor series. Under these conditions, a perturbation approach is feasible for solving the Lagrangian. It allows the extraction of the solutions for hadrons with light quarks, but it does not allow for an evaluation of nucleon resonances.

2.1.1 Isospin

Hadrons with similar masses are grouped into families. Particles belonging to each family have the same spin, baryon number, parity, strangeness, charm and beauty, but different electric charge. The focus of this work are the proton (uud) and the neutron (udd), shown in Fig 2.4.

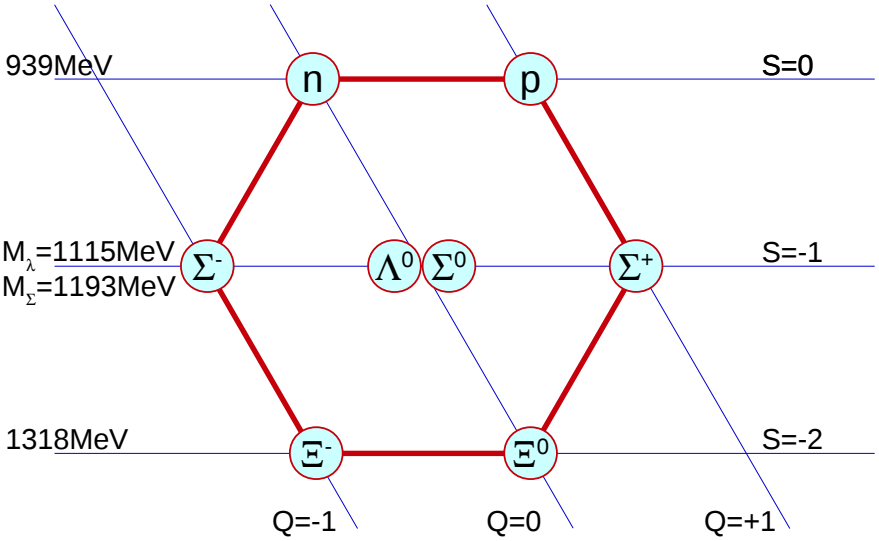

Figure 2.4: Baryon octet with spin 1/2.

The masses of the two nucleons are very similar, so it is assumed that quarks u and d are symmetric. Hence the proton and the neutron are treated

as if they were the same particle, but having two different values of isospin quantum number. Because of the difference in the masses of the quarks u and d, this symmetry is predicted to be broken by both electromagnetic and strong interactions [12].

To test these predictions, a deuteron target is particularly relevant, because it allows to study both isospin states.

2.1.2 Excited states of the nucleon

The nucleon resonances are excited states of a nucleon. The interaction between the nucleon and an energetic probe can excite the nucleon from its ground state to a resonance. These excited states, having a larger mass than the ground state, decay, and nucleons return to their ground state with the emission of a meson.

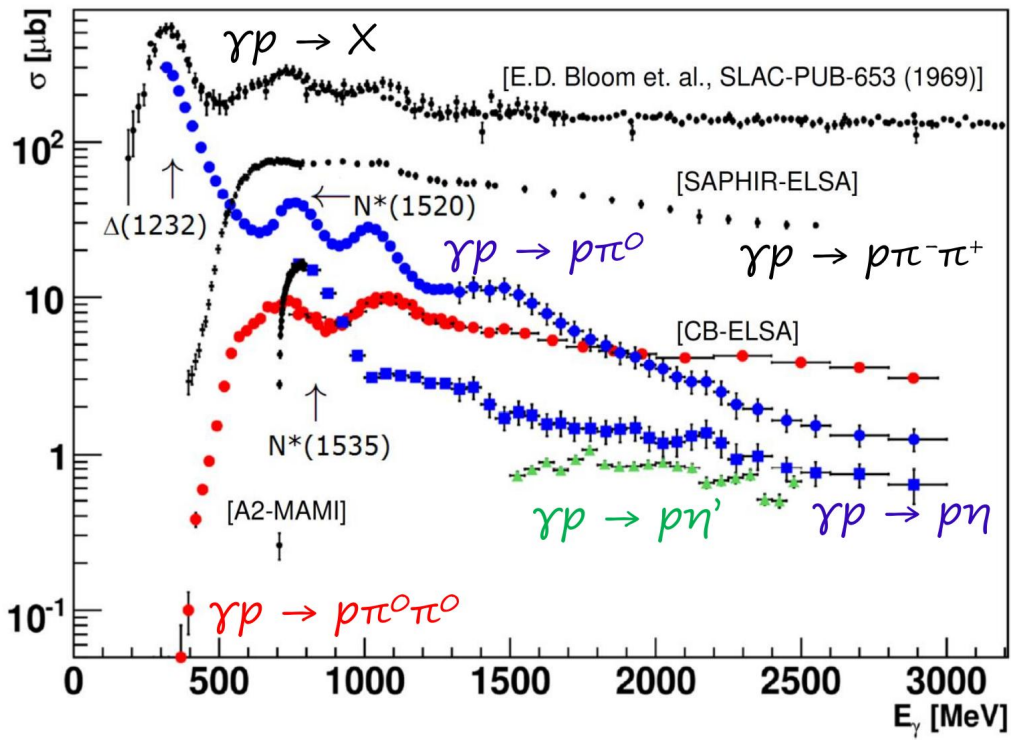

Figure 2.5: Total cross section for $\gamma + p$ with the different final state contributions from single- and double-meson production.

A problem with baryon spectroscopy arises because the excited states of the nucleon are very broad, with a usual width $\Gamma \sim 100\,\mathrm{MeV}$ and a very short

corresponding life $\tau \sim 10^{-24}$ s. Such a small lifetime is due to the fact that their decay is mediated by the strong interaction. An additional complication is that the energy spacing between different resonances is often much smaller than Γ. Hence, the resonances overlap each other and it is difficult to study and analyze each excited state individually.

Fig. 2.5 shows the total photo-absorption cross section for the proton where only few resonances are clearly visible. It is evident that the measurement of the total cross section for the reaction $\gamma + p$ cannot give detailed information about every overlapping excited state of the nucleon.

Different models, in particular those based on the quark models describing the baryon as a three-quark bound state, predict a profusion of excited states of the nucleon, but several of those excited states have not been experimentally observed yet [13].

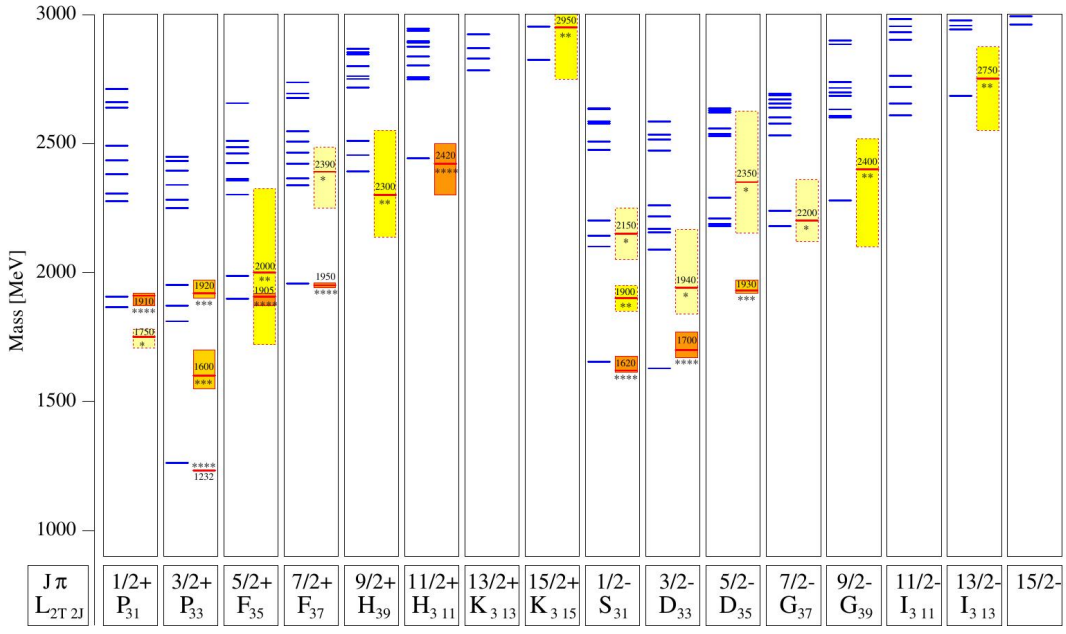

Figure 2.6: Delta-resonances spectrum in a quark model. For each column: the calculated resonances are represented on the left with a blue line, the experimental results are represented with a box on the right [13].

One of the possible reasons for the differences between predicted and observed states could be that most of the experiments have been performed using pion or kaon beams scattering on the nucleons. There is the possibility that the reactions induced by pion or kaon couple only weakly to the missing resonances.

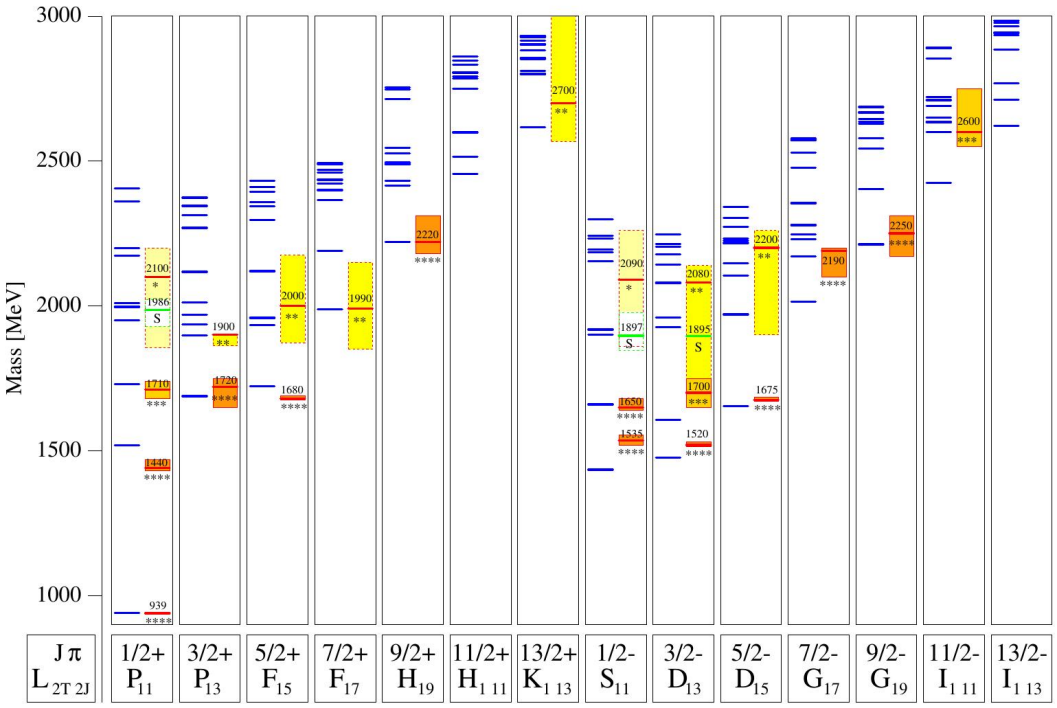

Figure 2.7: Nucleon-resonances spectrum in a quark model. For each column: the calculated resonances are represented on the left with a blue line, the experimental results are represented with a box on the right [13].

Conversely, the missing resonances could couple stronger to other interacting probes [14]. It is then important to access the nucleon resonance by using different production probes, for instance through electron- or photoproduction.

Meson photoproduction is a particularly good tool to investigate nucleon resonances and to study the electromagnetic transition amplitudes, because the photon probe is well understood and the initial state of the reaction is fully described.

For this reason, MAMI has significantly studied meson photoproduction. For example, the measurement of the meson unpolarized differential cross sections are in agreement with the descriptions of the theoretical models MAID, SAID, Bonn-Gatchina (see Sec. 2.5 for more details), which utilize partial wave analysis. These models are in good agreement with each other.

However, the three models give significantly different predictions for the different electromagnetic multipoles [15]. These discrepancies show that a more detailed experimental investigation of the polarization observables (further de-

scribed in Sec. 2.4) is needed in order to fully understand the properties of the nucleon resonances. New experimental results are necessary to better constrain the different partial wave analyses.

Moreover, most of the experiments performed up to now focused on the study of the proton, but, to achieve a full understanding of the internal structure of the nucleon, both its isospin states have to be investigated. To accomplish this, a deuterium target has been used in the experiment presented in this thesis, in order to access contributions both from the proton and the neutron.

2.2 Meson photoproduction

Meson photoproduction is a reaction that involves a photon (γ) and a nucleon (N) in the ground state. This reaction produces a baryon (N') and a meson (m) in the final state, as shown in Fig. 2.8, and can be written as:

$$\gamma(\vec{k}) + N(\vec{p_i}) = m(\vec{q}) + N'(\vec{p_f}), \tag{2.1}$$

where the four-vectors related to each particle involved in the reaction are explicitly indicated.

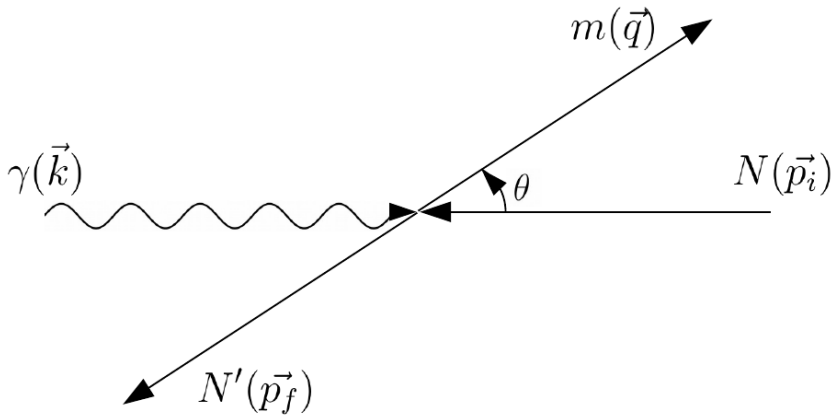

Figure 2.8: Kinematics of the meson photoproduction reaction.

The kinematics of a reaction with two initial and two final particles is fully described by the Lorentz-invariant Mandelstam variables, as follows:

$$\begin{aligned} s &= (k + p_i)^2 = (q + p_f)^2, \\ u &= (k - p_f)^2 = (q - p_i)^2, \\ t &= (q - k)^2 = (p_i - p_f)^2. \end{aligned} \tag{2.2}$$

The variables s and t are the square of the energy and the square of the momentum transfer of the reaction, respectively. The sum of the Mandelstam variables gives the sum of the masses squared for the particles involved:

$$s + t + u = 2m_N^2 + m_m^2, \tag{2.3}$$

with m_N being the rest mass of the nucleon and m_m the rest mass of the meson. The variable s is also the square of the center of mass of the reaction, W_{CM}. Eq. 2.2 can be described as:

$$\begin{aligned} s &= W^2 = (E_i + k_0)^2, \\ u &= M^2 + k^2 - 2k_0 E_f - 2|\vec{q}||\vec{k}|\cos\theta, \\ t &= m_m + k^2 - 2k_0 E_m + 2|\vec{q}||\vec{k}|\cos\theta, \end{aligned} \tag{2.4}$$

where k and q are the energy of the photon in Eq. 2.6 and the magnitude of the 3-momentum vector of the meson in the CM frame, respectively. The parameter θ is the scattering angle of the meson in the CM frame and it can be written as:

$$\cos(\theta) = \frac{\vec{q} \cdot \vec{k}}{|\vec{q}||\vec{k}|}. \tag{2.5}$$

The energy for each particle in the CM frame can be evaluated as:

$$E_\gamma = \frac{W^2 - m_N^2}{2W} = q, \tag{2.6}$$

$$E_i = \frac{W^2 + m_N^2}{2W}, \tag{2.7}$$

$$E_m = \frac{W^2 - m_m - m_N^2}{2W}, \tag{2.8}$$

$$E_f = \frac{W^2 - m_m + m_N^2}{2W}. \tag{2.9}$$

The differential cross section can be used to describe the angular distribution of the meson produced in photoproduction as follows:

$$\frac{d\sigma}{d\Omega} = |A(s, \cos\theta)|^2. \tag{2.10}$$

The scattering theory describes the transition from the initial photon-nucleon state $\langle i|$ to the final meson-baryon state $|f\rangle$, with use of the matrix S that represents the transition amplitude. This theory makes use of the Bjorken-Drell notation [16]. This matrix can be written as:

$$S_{fi} = \delta_{fi} - \frac{i}{(2\pi)^2}\delta^4(p_f + q - k - p_i)\sqrt{(\frac{m^2}{4E_\gamma E_i E_m E_f})} \cdot \mathcal{M}_{fi}, \tag{2.11}$$

where $\mathcal{M}$ is the transition matrix linking the initial and the final states. Consequently, the differential cross section can be expressed as:

$$\frac{d\sigma}{d\Omega} = \frac{q}{k}\sum \left|\frac{m}{4\pi W}\mathcal{M}_i\right|^2, \tag{2.12}$$

where the sum is over all the possible photon polarizations and all the possible magnetic quantum numbers for the nucleon states.

The matrix $\mathcal{M}$ can be written as:

$$\mathcal{M} = \epsilon_\mu J_\mu, \tag{2.13}$$

with ϵ_μ as the photon polarization vector and J_μ the electromagnetic current [17].

2.2.1 Multipole expansion

In the initial state, the photon has spin $\vec{s_\gamma}(s = 1)$, orbital angular momentum $\vec{l}$, and total angular momentum $\vec{L_\gamma} = \vec{l} + \vec{s_\gamma}$, while the nucleon has spin $\vec{J_N}(J = 1/2)$. Photon and nucleon couple electromagnetically producing a resonance with spin $\vec{J_{N^*}}$ and parity P_{N^*} according to the following selection rules [18]:

$$|L_\gamma - J_N| = |L_\gamma - 1/2| \leq J_{N^*} \leq |L_\gamma + 1/2| = |L_\gamma + J_N|,$$
$$P_{N^*} = P_N \cdot P_\gamma = P_\gamma. \tag{2.14}$$

The resonance decays to the nucleon ground state by emitting a meson with spin $\vec{s}_m(s = 0)$, parity $P_m = -1$ and relative orbital angular momentum L_m. The selection rules in Eq. 2.14 give [18]:

$$|L_m - J_N| = |L_m - 1/2| \leq J_{N^*} \leq |L_m + 1/2| = |L_m + J_N|,$$
$$P_{N^*} = P_N \cdot P_m \cdot (-1)^{L_m} = (-1)^{L_m+1}. \tag{2.15}$$

Therefore, the results of parity and orbital angular momentum are:

$$P_\gamma = P_{N^*} = (-1)^{L_m+1},$$
$$L \pm 1/2 = J_{N^*} = L_m \pm 1/2, \tag{2.16}$$

where the two signs '$\pm$' are independent from each other. To fulfill the parity and angular momentum conservation laws, the possible resulting electric and magnetic multipoles are:

$$EL: \ L = L_m \pm 1,$$
$$ML: \ L = L_m. \tag{2.17}$$

2.2.2 CGLN amplitudes

For meson photoproduction, the transition current $\boldsymbol{J}$ of Eq. 2.13 can be expressed using the Chew, Goldberg, Low and Nambu (CGLN) amplitudes F_i:

$$\boldsymbol{J} \ = \ \frac{4\pi W}{m}(i\widetilde{\boldsymbol{\sigma}})F_1 + (\boldsymbol{\sigma}\cdot\hat{\boldsymbol{k}})(\boldsymbol{\sigma}\times\hat{\boldsymbol{q}})F_2 + i\widetilde{\boldsymbol{k}}(\boldsymbol{\sigma}\cdot\hat{\boldsymbol{q}})F_3 + i\widetilde{\boldsymbol{k}}(\boldsymbol{\sigma}\cdot\hat{\boldsymbol{k}})F_4, \tag{2.18}$$

where σ are the Pauli matrices, $\widehat{\boldsymbol{k}}$ and $\widehat{\boldsymbol{q}}$ the photon and meson unit vectors, $\widetilde{\boldsymbol{\sigma}} = \boldsymbol{\sigma} - (\boldsymbol{\sigma}\cdot\hat{\boldsymbol{q}})\hat{\boldsymbol{q}}$ and $\widetilde{\boldsymbol{k}} = \boldsymbol{k} - (\boldsymbol{k}\cdot\hat{\boldsymbol{q}})\hat{\boldsymbol{q}}$.

Since the excited states of the nucleon are functions of spin and parity, the CGLN amplitudes can be written as functions of electric and magnetic multipoles using a partial wave expansion [19]:

$$\begin{aligned}
F_1(\theta) &= \sum_{l=0}^{\infty}\{[lM_{l+} + E_{l+}]P'_{l+1}(\cos\theta) + [(l+1)M_{l-} + E_{l-}]P'_{l-1}(\cos\theta)\}, \\
F_2(\theta) &= \sum_{l=0}^{\infty}[(l+1)M_{l+} + lM_{l-}]P'_l(\cos\theta), \\
F_3(\theta) &= \sum_{l=0}^{\infty}[(E_{l+} - M_{l+})P''_{l+1}(\cos\theta) + (E_{l-} + M_{l-})P''_{l-1}(\cos\theta)], \\
F_4(\theta) &= \sum_{l=0}^{\infty}(M_{l+} - E_{l+} - M_{l-} - E_{l-})P''_l(\cos\theta),
\end{aligned} \tag{2.19}$$

where P' and P'' are the derivatives of Legendre polynomials and θ is the angle of the meson in the c.m. frame. The subscript index l indicates the relative orbital angular momentum of the meson-nucleon system; the signs '+' and '−' indicate if the spin of the nucleon must be added or subtracted from l to get the total angular momentum of the excited state.

From Eq. 2.19 the electric and magnetic multipoles can be expressed as [19]:

$$\begin{aligned}
E_{l+} = \int_{-1}^{1} \frac{dx}{2(l+1)} &(P_l(\cos\theta)F_1 - P_{l+1}F_2 \\
&+ \frac{l}{2l+1}(P_{l-1}(\cos\theta) - P_{l+1}(\cos\theta))F_3 \\
&+ \frac{l+1}{2l+3}(P_l(\cos\theta) - P(\cos\theta)_{l+2})F_4), \\
E_{l-} = \int_{-1}^{1} \frac{dx}{2l} &(P_l(\cos\theta)F_1 - P_{l-1}(\cos\theta)F_2 \\
&- \frac{l+1}{2l+1}(P_{l-1}(\cos\theta) - P_{l+1}(\cos\theta))F_3 \\
&+ \frac{l}{2l+1}(P_l(\cos\theta) - P_{l-2}(\cos\theta))F_4),
\end{aligned} \tag{2.20}$$

$$
\begin{aligned}
M_{l+} = \int_{-1}^{1} \frac{dx}{2(l+1)} (P_l(\cos\theta)F_1 - P_{l+1}(\cos\theta)F_2 \\
- \frac{1}{2l+1}(P_{l-1}(\cos\theta) - P_{l+1}(\cos\theta))F_3), \\
M_{l-} = \int_{-1}^{1} \frac{dx}{2l} (-P_l(\cos\theta)F_1 + 1 - P_{l-1}(\cos\theta)F_2 \\
+ \frac{1}{2l+1}(P_{l-1}(\cos\theta) - P_{l+1}(\cos\theta))F_3).
\end{aligned}
\tag{2.21}
$$

In Tab. 2.1 the amplitudes of the lowest order multipoles are presented. Each resonance can be excited by a single electric and a single magnetic multipole. An exception is the case $J_{N^*} = 1/2$, which is excited only by a single multipole. If a resonance is dominant in the cross section, the angular distribution depends on the quantum number of the intermediate state.

Table 2.1: Lowest order multipoles amplitudes for pseudoscalar meson photoproduction ($x = \cos\theta$) [18].

Photon M-pole	Init. state (L_γ^P, J_N^P)	Interm. state J_N^P	Final state (J_N^P, L_m^P)	M-pole	$(k^*/q^*)d\sigma/d\Omega$
$E1$	$(1^-, \frac{1}{2}^+)$	$\frac{1}{2}^-$	$(\frac{1}{2}^+, 0^-)$	E_{0+}	$\lvert E_{0+}\rvert^2$
		$\frac{3}{2}^-$	$(\frac{1}{2}^+, 2^-)$	E_{2-}	$\frac{1}{2}\lvert E_{2-}\rvert^2(5-3x^2)$
$E2$	$(1^+, \frac{1}{2}^+)$	$\frac{1}{2}^+$	$(\frac{1}{2}^+, 1^+)$	M_{1-}	$\lvert M_{1-}\rvert^2$
		$\frac{3}{2}^+$	$(\frac{1}{2}^+, 1^+)$	M_{1+}	$\frac{1}{2}\lvert M_{1-}\rvert^2(5-3x^2)$
$M1$	$(2^+, \frac{1}{2}^+)$	$\frac{3}{2}^+$	$(\frac{1}{2}^+, 1^+)$	E_{1+}	$\frac{9}{2}\lvert E_{1+}\rvert^2(1+x^2)$
		$\frac{5}{2}^+$	$(\frac{1}{2}^+, 3^+)$	E_{3-}	$\frac{9}{2}\lvert E_{3-}\rvert^2(1+6x^2-5x^4)$
$M2$	$(2^-, \frac{1}{2}^+)$	$\frac{3}{2}^-$	$(\frac{1}{2}^+, 2^-)$	M_{2-}	$\frac{9}{2}\lvert M_{2-}\rvert^2(1+x^2)$
		$\frac{5}{2}^-$	$(\frac{1}{2}^+, 2^-)$	M_{2+}	$\frac{9}{2}\lvert M_{2+}\rvert^2(1+6x^2-5x^4)$

For the pion photoproduction, the multipole M_{1+} is responsible for the Δ-resonance, with an angular distribution of $(5 - 3cos^2\theta)$. In order to analyze the contributions of the different resonances to pion photoproduction, a parametrization of the cross section in terms of multipole amplitudes has been used. Despite this, the differential cross section is not sufficient to unequivocally extract the multipoles. The study of the polarization observables (see Sec. 2.4) is crucial to clearly understand the multipoles without ambiguity [18].

2.2.3 Helicity amplitudes

The helicity states can be used to describe meson photoproduction. The initial and final states of the nucleon have helicity $\nu_{i,f} = \pm 1/2$, the photon has $\lambda_\gamma = \pm 1$ and the meson has $\lambda = 0$. Therefore, there are eight possible matrix elements $H_{\nu_f,\mu} = \langle \nu_f | T | \lambda_\gamma \nu_i \rangle$. Finally, due to parity conservation, there are only four independent helicity amplitudes [18]:

$$\begin{aligned} H_1 &= H_{+1/2,+3/2} = +H_{-1/2,-3/2}, \\ H_2 &= H_{+1/2,+1/2} = +H_{-1/2,-1/2}, \\ H_3 &= H_{-1/2,+3/2} = +H_{+1/2,-3/2}, \\ H_4 &= H_{+1/2,-3/2} = +H_{-1/2,+1/2}. \end{aligned} \tag{2.22}$$

The helicity amplitudes as functions of CGLN amplitudes are as follows [18]:

$$\begin{aligned} H_1(\theta,\phi) &= \frac{-1}{\sqrt{2}} e^{i\phi} \sin(\theta) \cos(\frac{\theta}{2})(F_3 + F_4), \\ H_2(\theta,\phi) &= \sqrt{2} \cos(\frac{\theta}{2})[(F_2 - F_1) + \frac{1}{2}(1 - \cos(\theta))(F_3 - F_4)], \\ H_3(\theta,\phi) &= \frac{1}{\sqrt{2}} e^{i\phi} \sin(\theta) \sin(\frac{\theta}{2})(F_3 - F_4), \\ H_4(\theta,\phi) &= \sqrt{2} e^{i\phi} \sin(\frac{\theta}{2})[(F_1 + F_2) + \frac{1}{2}(1 + \cos(\theta))(F_3 + F_4)]. \end{aligned} \tag{2.23}$$

The combination of Eq. 2.23 into a bilinear product, results in sixteen polarization observables, which are described in Sec. 2.4.

The differential cross section can be expressed as [18]:

$$\frac{d\sigma}{d\Omega} = \frac{1}{2} \frac{q^*}{k^*} (H_1^2 + H_2^2 + H_3^2 + H_4^2), \tag{2.24}$$

where $q^*$and k^* are the c.m. momenta of the meson and the photon, respectively.

Another way to describe the double polarization observables is using the 'transversity' amplitudes, defined as [20]:

$$\begin{aligned} b_1 &= \frac{1}{2}[(H_1 + H_4) + i(H_2 - H_3)], \\ b_2 &= \frac{1}{2}[(H_1 + H_4) + i(H_2 - H_3)], \\ b_3 &= \frac{1}{2}[(H_1 - H_4) + i(H_2 + H_3)], \\ b_4 &= \frac{1}{2}[(H_1 - H) + i(H_2 + H_3)]. \end{aligned} \tag{2.25}$$

With use of those amplitudes, the differential cross section can be expressed as:

$$\frac{d\sigma}{d\Omega} = \frac{1}{2}\frac{q^*}{k^*}(b_1^2 + b_2^2 + b_3^2 + b_4^2). \tag{2.26}$$

2.3 Pion photoproduction

Pion photoproduction is a particular case of pseudoscalar meson photoproduction. In this case the absorption of a real photon by the nucleon produces a pion. The channels involving a photon and a nucleon are the following:

$$\gamma + p \rightarrow p + \pi^0, \tag{2.27}$$

$$\gamma + p \rightarrow n + \pi^+, \tag{2.28}$$

$$\gamma + n \rightarrow n + \pi^0, \tag{2.29}$$

$$\gamma + n \rightarrow p + \pi^-. \tag{2.30}$$

The goal of this work is to analyze single π^0 production on both isospin states of the nucleon, therefore the channels in Eq. 2.27 and 2.29 is where this thesis focuses.

2.3.1 Isospin amplitudes

An additional complication of pion photoproduction is the presence of isospin. It is therefore necessary to study the isospin of the initial and the final state of the reaction. In hadronic reactions isospin is conserved, while electromagnetic interactions violate isospin conservation. In meson photoproduction, illustrated in Fig. 2.9, isospin is conserved in the hadronic vertex on the right, but not in the electromagnetic vertex on the left. If we analyze the isospin of the initial state, there is the nucleon with isospin $I = \frac{1}{2}$, which interacts with the electromagnetic current, which itself contains isoscalar ($\Delta I = 0$) and isovector ($\Delta I = 0, \pm 1$) components [21].

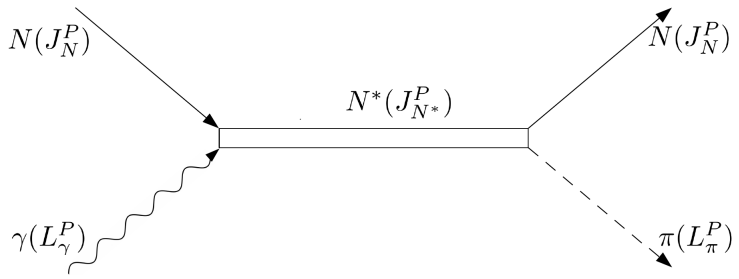

Figure 2.9: Feynman diagram for meson photoproduction.

Assuming the conservation of isospin in the hadronic system, the final state is described as an isospin interaction $\tau \cdot \phi$, where ϕ describes the pion, which is an isovector particle, and τ are the Pauli isospin matrices. They can be written in the overall matrix in a symmetrical form [21]:

$$A = \frac{1}{2} A^{(-)}[\tau_\alpha, \tau_0] + A^{(+)}\delta_{\alpha 0} + A^{(0)}\tau_\alpha, \tag{2.31}$$

where α is the isospin index for the pion ($\alpha = 0$ for π^0 and $\alpha = \pm 1$ for $\pi^\pm$). From the three isospin amplitudes, the four pion photoproduction channels can be written as:

$$\begin{aligned} A(\gamma p \to n\pi^+) &= \sqrt{2}(A^{(-)} + A^{(0)}), \\ A(\gamma n \to p\pi^-) &= -\sqrt{2}(A^{(-)} - A^{(0)}), \\ A(\gamma p \to p\pi^0) &= (A^{(+)} + A^{(0)}), \\ A(\gamma n \to n\pi^0) &= (A^{(+)} - A^{(0)}). \end{aligned} \tag{2.32}$$

The amplitudes $A^{(0)}$ have only a final state $I = \frac{1}{2}$, while $A^{(\pm)}$ could have

isospin final state $I = \frac{1}{2}$ or $I = \frac{3}{2}$. In order to analyze the πN system in terms of isospin, the three Eq. 2.31 are combined as:

$$\begin{aligned} A^{(0)} \qquad\qquad & (I = \tfrac{1}{2}), \\ A^{(1/2)} = A^{(+)} + 2A^{(-)} \quad & (I = \tfrac{1}{2}), \\ A^{(3/2)} = A^{(+)} - A^{(-)} \quad & (I = \tfrac{3}{2}). \end{aligned} \tag{2.33}$$

Plugging the amplitudes from Eq. 2.33 into Eq. 2.32 results in:

$$\begin{aligned} A(\gamma p \to n\pi^+) &= \sqrt{2}(\frac{1}{3}A^{(1/2)} - \frac{1}{3}A^{(3/2)} + A^{(0)}), \\ A(\gamma n \to p\pi^-) &= -\sqrt{2}(\frac{1}{3}A^{(1/2)} - \frac{1}{3}A^{(3/2)} - A^{(0)}), \\ A(\gamma p \to p\pi^0) &= \frac{1}{3}A^{(1/2)} + \frac{2}{3}A^{(3/2)} + A^{(0)}, \\ A(\gamma n \to n\pi^0) &= (1A^{(1/2)} + \frac{2}{3}A^{(3/2)} - A^{(0)}. \end{aligned} \tag{2.34}$$

Another way to express the isospin amplitudes is by splitting the transition operator into the isoscalar part $\hat{S}$ ($\Delta I = 0$) and the isovector part $\hat{V}$ ($\Delta I = 0, \pm 1$). For the pion photoproduction, three independent matrix elements are obtained. These are the isoscalar A^{IS}, the isovector A^{IV} and the isospin changing A^{V3} defined as [18]:

$$\begin{aligned} A^{IS} &= \left\langle \frac{1}{2}, \pm\frac{1}{2} | \hat{S} | \frac{1}{2}, \pm\frac{1}{2} \right\rangle, \\ A^{IV} &= \left\langle \frac{1}{2}, \pm\frac{1}{2} | V | \frac{1}{2}, \pm\frac{1}{2} \right\rangle, \\ A^{V3} &= \left\langle \frac{3}{2}, \pm\frac{1}{2} | \hat{V} | \frac{1}{2}, \pm\frac{1}{2} \right\rangle. \end{aligned} \tag{2.35}$$

The isospin amplitudes for pion photoproduction can be then written as:

$$
\begin{aligned}
A(\gamma p \to n\pi^+) &= -\sqrt{\frac{1}{3}}A^{V3} + \sqrt{\frac{2}{3}}(A^{VI} - A^{IS}),\\
A(\gamma n \to p\pi^-) &= +\sqrt{\frac{1}{3}}A^{V3} - \sqrt{\frac{2}{3}}(A^{VI} + A^{IS}),\\
A(\gamma p \to p\pi^0) &= +\sqrt{\frac{2}{3}}A^{V3} + \sqrt{\frac{1}{3}}(A^{VI} - A^{IS}),\\
A(\gamma n \to n\pi^0) &= +\sqrt{\frac{2}{3}}A^{V3} + \sqrt{\frac{1}{3}}(A^{VI} + A^{IS}).
\end{aligned}
\tag{2.36}
$$

The presence of isospin complicates the full understanding of the photoproduction amplitudes. For this reason the analysis of a neutron target is crucial, even if it adds the complication of nuclei effect (described in Sec. 2.6) since the neutron does not exist as a free target.

2.4 Polarization observables

In a pion photoproduction experiment, three different components can be polarized: the target nucleon, the photon beam, and the recoil nucleon. The nucleon target polarization P^T is traditionally described using the laboratory frame. In this frame, the z-axis is aligned in the direction of the incoming photon beam momentum $\hat{\vec{k}}$, while the y-axis is perpendicular to the reaction plane $\hat{\vec{y}} = \hat{\vec{k}} \times \hat{\vec{q}}/\sin\theta$ ($\hat{\vec{q}}$ is the momentum vector of the outgoing meson), and the x-axis is defined as $\hat{\vec{x}} = \hat{\vec{y}} \times \hat{\vec{z}}$. The recoil nucleon polarization P^R is usually described in the CM frame $\{x', y', z'\}$, where the z'-axis is coincident to $\hat{\vec{q}}$, the y-axis is $\hat{\vec{y}} = \hat{\vec{k}} \times \hat{\vec{q}}/sin\theta$ and the x-axis is $\hat{\vec{x}} = \hat{\vec{y}} \times \hat{\vec{z}}$. Lastly, there are two possible types of photon polarization: linear and circular. The linear polarization P_L^γ can have two different orientations: either 'PARA', when it is in direction of the reaction plane $(\hat{\vec{x}}, \hat{\vec{z}})$, $\varphi = 0$, or 'PERP', when the polarization angle is $\varphi = \pi/2$ and the direction is $\hat{\vec{y}}$. In the case of a circularly polarized photon beam, the polarization can be right or left handed, $P_\odot^\gamma = \pm 1$.

The combination of the polarization components, as shown in Tab. 2.2, offers the possibility to access 16 measurable observables: the unpolarized cross section, three single-polarized, and twelve double-polarized observables, the latter divided in three sets.

The general cross section, including all polarization observables, is fully reported in App. A. It can be divided in three sets involving a combination of

Table 2.2: Polarization observables which can be extracted in a meson photoproduction reaction. Shown in blue the unpolarized cross section and the single polarized observables. Each observable can also be measured through an experiment with an additional degree of polarization (e.g. triple-polarization experiment for the double-polarized observables and a double polarization experiment for the single ones). Some of these cases are shown within brackets.

Photon polarization		Target polarization			Recoil polarization			Target and recoil polarizations			
	-	-	-	-	x'	y'	x'	x'	x'	z'	z'
	-	x	y	z	-	-	-	x	z	x'	z
Unpolarized	σ	-	T	-	-	P	-	$T_{x'}$	$L_{x'}$	$T_{z'}$	$L_{z'}$
Linear	Σ	H	$(-P)$	G	$O_{x'}$	$(-T)$	$O_{z'}$	$(-L_{z'})$	$(T_{z'})$	$(L_{z'})$	$(-T_{z'})$
Circular	-	F	-	E	$C_{x'}$	-	$C_{z'}$	-	-	-	-

two polarization degrees [22]:

- polarized nucleon target and polarized photon beam $(\mathcal{S}, \mathcal{BT})$

$$\begin{aligned}\frac{d\sigma}{d\Omega} =&\sigma_0\{1 - P_L^\gamma \Sigma\cos(2\phi) + P_x^T[-P_L^\gamma H\sin(2\phi) + P_\odot^\gamma F] \\ &+ P_y^T(T - P_L^\gamma P\cos(2\phi)) + P_z^T[P_L^\gamma G\sin(2\phi) - P_\odot^\gamma E]\},\end{aligned} \tag{2.37}$$

- polarized nucleon target and recoil polarization $(\mathcal{S}, \mathcal{TR})$

$$\begin{aligned}\frac{d\sigma}{d\Omega} =&\sigma_0\{1 + P_y^T T + P_{y'}^R P + P_{x'}^R(P_x^T T_{x'} - P_z^T L_{x'}) \\ &+ P_{y'}^R P_y^T \Sigma + P_{x'}^R(P_x^T T_{z'} + P_z^T L_{z'})\},\end{aligned} \tag{2.38}$$

- polarized photon beam and recoil polarization $(\mathcal{S}, \mathcal{BR})$

$$\begin{aligned}\frac{d\sigma}{d\Omega} =&\sigma_0\{1 - P_L^\gamma \Sigma\cos(2\phi) + P_{x'}^R[-P_T^\gamma O_{x'}\sin(2\phi) + P_\odot^\gamma C_{x'}] \\ &+ P_{y'}^R(P - P_L^\gamma T\cos(2\phi)) + P_{z'}^R[P_L^\gamma O_{z'}\sin(2\phi) - P_\odot^\gamma C_{z'}]\}.\end{aligned} \tag{2.39}$$

2.4.1 The complete experiment

The general cross section expressed in Eq. A.1 depends on 16 observables. The measurement of all these observables is not necessary to determine the cross section. On the other hand, it is crucial to identify a set of observables, which allows the determination of amplitudes without ambiguities. Such a set is called a *complete experiment*. This topic has been a matter of study since the 1970s [23].

There have been several updates and studies for the determination of the amplitudes [22, 23, 24], all of them requiring at least the measurement of 7 or 8 observables. In addition, they all include the unpolarized cross section and a combination of polarized observables with different combinations of beam, target and recoil polarization.

A different approach to determine the *complete experiment* is the use of a truncated partial wave analysis (TPWA). A few years ago Wunderlich and coauthors showed that five properly chosen observables are sufficient to obtain a *complete experiment* using a TPWA with maximum angular momentum $l_{max} = 4$ [25].

Nevertheless, the measurement of any observable provides useful information to determine the resonance contributions, and to give more constrains to the theoretical models.

2.4.2 The double polarization observable E

In the A2 experimental hall at MAMI, experiments with polarized targets and polarized photon beams have been performed. In particular, for this work, the aim was the extraction of the double-polarization observable E. The target was longitudinally polarized, the photon beam had a circular polarization, and no measurements of the recoil polarization were performed. Under these conditions Eq. 2.37 can be reduced to:

$$\frac{\mathrm{d}\sigma}{\mathrm{d}\Omega} = \sigma_0\{1 \mp P_z^T P_\odot^\gamma E\}. \tag{2.40}$$

Furthermore, the E observable can be written as the asymmetry between the helicity dependent cross section $\sigma_{1/2}$, with anti-parallel spin configuration for target and beam, and $\sigma_{3/2}$, with parallel spin configuration:

$$E = \frac{\sigma_{1/2} - \sigma_{3/2}}{\sigma_{1/2} + \sigma_{3/2}}. \tag{2.41}$$

With E being an asymmetry, the factors included in the calculation of the cross section cancel out. Therefore Eq. 2.41 can be written as the ratio between the difference and the sum of the anti-parallel and parallel events $N_{1/2}$ and $N_{3/2}$ corrected for the target and beam polarization degree, as follows:

$$E = \frac{N_{1/2} - N_{3/2}}{N_{1/2} + N_{3/2}} \cdot \frac{1}{P_z^T} \cdot \frac{1}{P_\odot^\gamma}. \tag{2.42}$$

The E observable gives information about static properties of the nucleon and, in order to extract the contribution to the nucleon resonance, it can be expressed in terms of CGLN amplitudes [26]:

$$\hat{E} = E \cdot \frac{\mathrm{d}\sigma}{\mathrm{d}\Omega} = +Re\{F_1^* F_1 + F_1^* F_1 - 2\cos\theta F_1^* F_2 + sin^2\theta(F_2^* F_3 + F_1^* F_4)\}\rho_0, \tag{2.43}$$

where $\rho_0 = q/k$ indicates the phase-space factor.

The E observable can be written in terms of helicity amplitudes (Eq. 2.22) as [22]:

$$E = \frac{1}{2}\frac{q^*}{k^*}(-H_1^2 - H_2^2 + H_3^2 + H_4^2), \tag{2.44}$$

and as a function of the transversity amplitudes as [20]:

$$E = -2Re(b_1 b_3^* + b_2 b_4^*) \tag{2.45}$$

The other polarization observables are given as function of helicity and transversity amplitudes in App. A.

As described in Eq. 2.19, the polarization observables can be described as combination of multipoles and associated Legendre Polynomials in order to describe their energy and angular dependence. In particular, according to [27, 28], the quantity $\hat{E}$ can be fitted using the following truncated partial wave equation:

$$E(\hat{W,\theta}) = E(W,\theta) \cdot \frac{\mathrm{d}\sigma}{\mathrm{d}\Omega}(W,\theta) = \sum_{k=0}^{2l_{max}} A_k^E(W) P_k^0(\cos\theta), \tag{2.46}$$

where A_k^E are the Legendre coefficients for the polynomials functions truncated at l_{max} and $P_k^0(\cos\theta)$ are the associated Legendre polynomials of order zero.

The selected value of l_{max} determines the sensitivity to different waves and multipoles, as shown in Tab. 2.3.

Table 2.3: Sensitivity on multipoles for different values of l_{max}.

l_{max}	wave	M-poles
1	S-wave	E_{0+}
	P-wave	E_{1+}, M_{1+}, M_{1-}
2	D-wave	$E_{2+}, E_{2-}, M_{2+}, M_{2-}$
3	F-wave	$E_{3+}, E_{3-}, M_{3+}, M_{3-}$
4	G-wave	$E_{4+}, E_{4-}, M_{4+}, M_{4-}$
5	H-wave	$E_{5+}, E_{5-}, M_{5+}, M_{5-}$

2.5 Partial wave analysis models

The amplitudes extracted through experiments give crucial constraints and information to understand the nucleon resonances. Moreover, several models have been developed by different theory groups in order to parametrize the energy dependence as well as interpret the experimental results. The models differ on the techniques used to parametrize the background contributions and the nucleon resonances.

2.5.1 MAID (Unitary Isobar Model)

This model was developed at the physics faculty of the University of Mainz in the 1990s in order to analyze the experimental results on pion photo- and electro-production [29]. The initial model was MAID1998 and it was based on the unitarized description of the nucleon resonances by Breit-Wigner. To

evaluate the non-resonant background, the Born terms and the t-channel contribution were used.

The MAID model has had several upgrades with the latest version being MAID2007 [30]. The resonance shapes, since version MAID1998, have been based on the Breit-Wigner forms [29]:

$$t_{\gamma\pi}^{R,\alpha} = (W, Q^2) = \mathcal{A}_{\alpha}^{R}(W, Q^2) \frac{f_{\gamma N}(W) \Gamma_{tot} M_R f_{\pi N}(W)}{M_R^2 - W^2 - i M_R \Gamma_{tot}} e^{i\phi R}, \tag{2.47}$$

where $\Gamma_{tot}(W)$ is the total width of the resonance, and $f_{\pi N}(W)$ is the Breit-Wigner factor that is expressed as [29]:

$$f_{\pi N}(W) = C_{\pi N} \left[\frac{1}{(2j+1)\pi} \frac{k_W}{q} \frac{m}{M_R} \frac{\Gamma_{\pi N}}{\Gamma_{tot}^2} \right]^{1/2}, \tag{2.48}$$

where j is the spin of the resonance, $\Gamma_{\pi N}$ is the partial width of πN, and C depends on the isospin.

The background contribution is evaluated using complex functions with the K-matrix formalism [29]:

$$t_{\gamma\pi}^{B,\alpha}(W, Q^2) = v_{\gamma\pi}^{B,\alpha}(W, Q^2)[1 + i t_{\pi N}^{\alpha}(W)], \tag{2.49}$$

where $t_{\pi N}^{\alpha} = [\eta_\alpha \exp(2i\delta_\alpha) - 1]/2i$ indicate the pion-nucleon elastic scattering amplitudes and are described using the phase shifts δ_α and the inelasticity parameters η_α.

MAID describes all the four-star resonances below 2 GeV and the corresponding longitudinal and transverse helicity amplitudes of the nucleon resonance. This model is particularly effective for describing the $P_{33}(1232)$, $P_{11}(1440)$, $S_{11}(1535)$, $D_{13}(1520)$, and $F_{15}(1680)$ resonances, while for higher resonances more data from polarization observables are necessary in order to understand the background of the multipoles [30].

The theoretical predictions of the MAID model are used in Chap. 6 to compare the results of this work. The MAID results are accessible through the database [31].

2.5.2 SAID

The SAID (Scattering Analysis Interactive Dial-in) model was developed at the Virginia Polytechnic Institute and it is currently maintained and updated by the Department of Physics of the George Washington University [32] and is periodically updated.

This model exploits the Chew-Mandelstam formalism to parametrize the hadronic T-matrix [33], and the wave amplitudes are parametrized using polynomials. This parametrization was successful in describing the hadronic two-body sector, and SAID extended the Chew-Mandelstam to include also the electromagnetic contribution in order to describe meson photoproduction.

In order to fit the new polarized data and to improve the model independence, the phenomenological form, described in [34], and based on a Heitler K-matrix approach:

$$M = (\text{Born} + A)(1 + iT_{\pi N}) + BT_{\pi N}, \tag{2.50}$$

was upgraded adding the term:

$$(C + iD)(\text{Im}T_{\pi N} - |T_{\pi N}|^2) \tag{2.51}$$

where $T_{\pi N}$ is the partial wave amplitude for the elastic πN scattering related with the amplitude M for the pion photoproduction multipole. The new parametrization has fewer parameters and unifies the single-pion photoproduction data with the pion and eta hadron-production.

Information about this model can be found on the website [35].

2.5.3 Bonn-Gatchina (BnGa) Model

The Bonn-Gatchina (BnGa) model was developed within a collaboration of the University of Bonn, Germany, and the Petersburg Nuclear Physics Institute in Gatchina, Russia.

The K-matrix approach is used at low energies to describe the resonances, while at energies higher than 2.2 GeV, the relativistic multi-channel Breit-Wigner amplitudes are used. For photoproduction, the non resonant contribution is evaluated using t- and u-channel amplitudes in the Reggie form. The database with BnGa results is accessible from the web [36].

2.6 Pion photoproduction on the deuteron

Due to the lack of a free neutron target, in order to investigate this nucleon, it is necessary to use light nuclei. The two main options are ^{3}He and deuterium, because their theoretical description is well understood, and approximations are not needed, while they would be necessary for many-body systems. For the work presented in this thesis, a deuterium target was chosen.

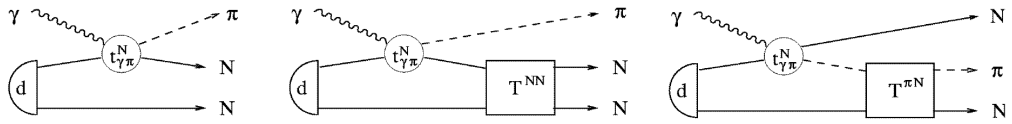

Figure 2.10: Feynman diagrams for pion photoproduction from deuteron: impulse approximation (a), $N\,N$ re-scattering (b), $\pi\,N$ re-scattering. Picture from [37].

Pion photoproduction from the deuteron is affected by nuclear effects. The main contributions are from Fermi motion and final state interaction (FSI) [38, 39, 40, 41].

The deuteron nucleus is at rest in the laboratory frame but, inside the nucleus, the two nucleons have momentum due to the Fermi motion. If this nuclear effect is taken into account and after the pion production there is no re-scattering, the approximation can be referred to as *impulse approximation* (IA), as shown in Fig. 2.10 [37, 38]. The mathematical evaluation of Fermi motion used during the work is described in App. B.

The second effect presents in pion photoproduction on the deuteron, is the re-scattering of the spectator nucleon with the pion or with the nucleon involved in the reaction. These effects are referred to as *final state interactions* (FSI). In Fig. 2.10, $N - N$ re-scattering and $\pi - N$ re-scattering are shown. In the first case, there is an interaction between the spectator nucleon and the nucleon involved in the pion production. In the second case the pion interacts with the spectator nucleon. This contribution is much smaller than the $N - N$ contribution [42]. The effect of the final state interaction is particularly relevant for π^0 production, while it is almost negligible for the π^- channel [40]. The effect for π^0 is also illustrated in Chapter 6.

2.6.1 Single π^0 polarized photoproduction cross section on the deuteron

The amplitude of the helicity dependent cross section of inclusive single π^0 photoproduction on the deuteron ($\overrightarrow{\sigma}$) is not equivalent to the sum of $\overrightarrow{\sigma}$ on the proton and the neutron, due to the nuclear effects described above.

Experiments with a deuteron target have been performed in the tagger hall of the Institut für Kernphysik using the MAMI beam since the 90s'. The main goal was the investigation of the GDH sum rule [43, 44]. At that time the available energy range of the beam was quite limited and the acceptance coverage smaller than the actual setup. An intermediate step of this work focused on the extraction of this cross section, in order to enlarge the statistics and the energy range of the data available from the GDH experiment. The helicity dependent cross section of inclusive single π^0 photoproduction on the deuteron is described as the difference between the helicity dependent cross section $\sigma_{\uparrow\uparrow}$ with parallel spin configuration for target and beam, and $\sigma_{\uparrow\downarrow}$ with anti-parallel spin configuration. This cross section is equivalent at the numerator of Eq. 2.41, and it can be written as follows:

$$\overrightarrow{\sigma} = \sigma_{\uparrow\uparrow} - \sigma_{\uparrow\downarrow} = \frac{N_{\uparrow\uparrow} - N_{\uparrow\downarrow}}{N_\gamma} \cdot \frac{1}{P_z^T} \cdot \frac{1}{P_\odot^\gamma}. \tag{2.52}$$

where N_γ indicates the photon flux reaching the target.

It is important to keep in mind for further discussion that in this observable all the non-polarized contributions cancel out and it is therefore not necessary to perform a background subtraction.

Chapter 3

Experimental Setup

This chapter describes the experimental equipment used to collect the data for this thesis. This setup is located in the A2 tagger hall of the Institut für Kernphysik at the Johannes Gutenberg-University of Mainz.

In the first section a description of the electron beam produced by the Mainz Mikrotron (MAMI) is provided. The following section 3.2 introduces the photon tagging facility. In section 3.3 the frozen spin target is described, while section 3.4 describes the detectors. The data-taking electronics and the experimental trigger are briefly outlined in sections 3.5 and 3.6, respectively. In the final section, the running conditions for the different data-taking beamtimes used to obtain the results presented in this thesis are given.

3.1 The Mainz Mikrotron (MAMI)

MAMI is an electron beam facility founded in 1979 at the campus of the Johannes Gutenberg-University in Mainz, Germany. After several upgrades during its history, it can now provide an electron beam with a maximum energy of about 1.6 GeV [45, 46].

After the electron gun and the injector linac, there is a cascade of three Race Track Microtrons (RTMs in Fig. 3.1). This part is the accelerator stage of MAMI-B, which can provide a maximum energy of 910 MeV. In 2006 the facility underwent an important upgrade, with the installation of the new Harmonic Double Sided Microtron that can accelerate the electrons up to 1.6 GeV. This new higher energy part is known as MAMI-C.

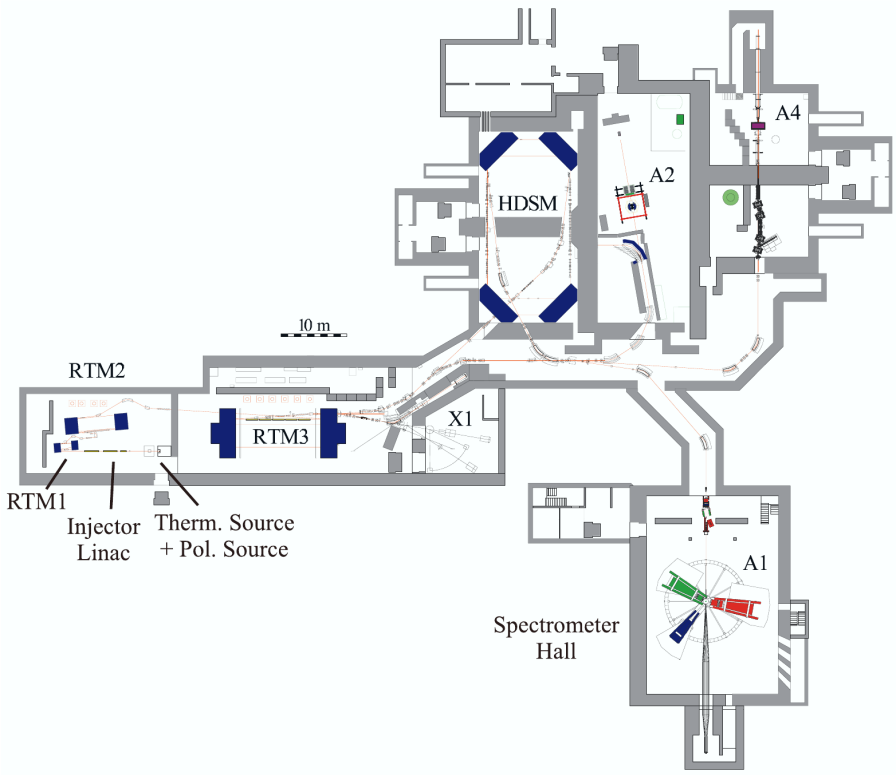

Figure 3.1: Floor plan of MAMI, with the experimental halls of A1, A2, X1 and A4. Picture from [47].

As it will be further described later, the electron beam produced by MAMI is continuous and it can be either unpolarized or longitudinally polarized. In Fig. 3.1 the floor plan of MAMI is shown, with the accelerator and the experimental halls: A1 (Electron scattering), A2 (Tagged photons, the one used for this work) or X1 (X-rays). The experimental hall A4 in the picture is not any more present, as construction is in progress for the new MESA (Mainz Energy-Recovering Superconducting Accelerator) facility.

For the experiment described in this work the energy of the MAMI beam was set at 1557 MeV and the electrons were polarized.

3.1.1 The electron gun and the injector linac

The unpolarized electron beam is generated using a simple thermionic electron gun. In the early years of MAMI operation, after being emitted, the electrons were pre-accelerated with a Van de Graaff accelerator. In the late '80s, this pre-accelerating device was replaced with a radio frequency linac. Thanks to this

upgrade it was possible to achieve better beam stability. It was also a necessary requirement for the implementation of a new polarized electron source, which started operating in 1992.

This polarized electron source is based on photo-electron emission from a strained GaAsP III-V semiconductor. The configuration at MAMI provides a longitudinally polarized beam with a maximum current of 20 μA and a maximum polarization of about 80%. The GaAsP cathode is irradiated with polarized light generated by a pulsed titanium-sapphire laser. The initially linearly polarized light becomes circularly polarized with use of a quarter-wave plate made of a birefringent material with a specific thickness [48]. Such a feature induces a +(-) 90° rotation of the light-phase transmitted along a given axis. To get circular polarization, the parallel and the perpendicular components of the transmitted light must be equal. It is possible to obtain this condition by setting the orientation of the plane of polarization of the incoming light at 45° with respect to the optical axis of this material.

The quarter-wave plate at MAMI is a Pockels cell, which flips the helicity of the transmitted laser light when the sign of the voltage applied to the cell is reversed. The spin flip is done with a frequency of approximately 1 Hz. This flip helps to reduce the systematic errors in the off-line data analysis [49].

The polarization degree of the electron beam is measured with a Mott polarimeter, Fig. 3.2, located near the source [50].

The measurement is based on Mott scattering, which exploits the elastic scattering asymmetry of spin polarized electrons from a nuclear Coulomb field. Two detectors located at the same polar scattering angle measure the asymmetry of the scattered electrons on a high Z material. This asymmetry is proportional to the spin polarization. To perform this measurement, the polarization direction must be perpendicular to the motion direction, but the MAMI electron beam is initially polarized in the direction of motion, so a spin rotation before the polarimeter is required. A Wien filter is used, that produces a magnetic field perpendicular to an electric field. Both those fields are perpendicular to the beam direction. With a correct field intensity, it is possible to rotate the spin without any effect on the beam direction [52].

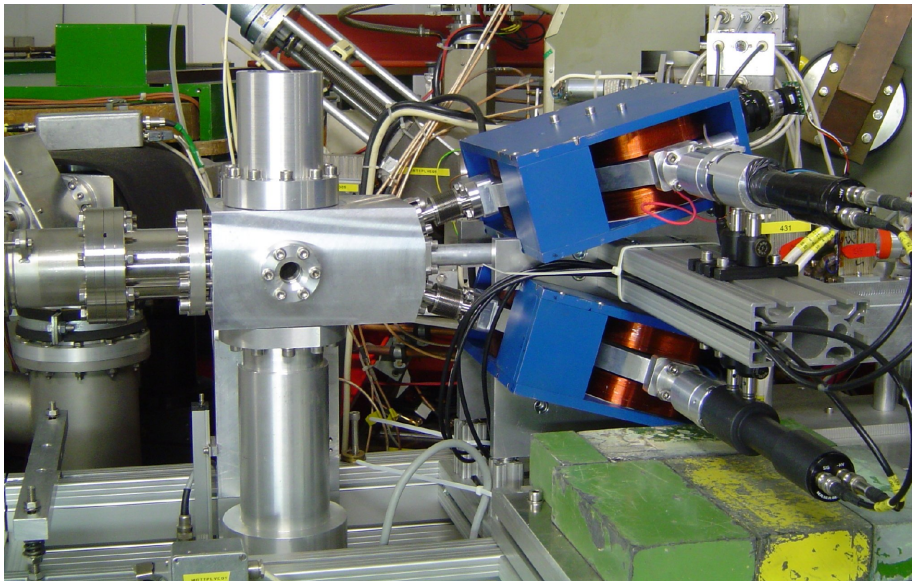

Figure 3.2: Mott polarimeter at MAMI. Electrons enter from the left. The blue boxes are the dipole magnets, which are responsible for bending the electrons into the detectors. Picture from [51].

3.1.2 The Race-Track Microtron

A microtron is an electron accelerator where the electrons pass several times in the same linac. A particular microtron type is the Race-Track Microtron (RTM), which has a single linac placed between two dipole magnets, as shown in Fig. 3.3.

The electrons are injected into the microtron and are recirculated into the linac several times, until the radius of the electrons path is too large to make further acceleration possible. The linac is composed of a series of wave cavities, in which the accelerating potential is alternated by using a radio-frequency klystron.

In each passage inside the linac the electrons gain a ΔE given by:

$$\Delta E = \frac{ec^2 B}{2\pi\nu_{rf}} \tag{3.1}$$

where e is the electron charge, c is the speed of light, B is the magnetic field, and ν_{rf} is the frequency of the klystrons given by $\nu_{rf} = c/\lambda_{rf} = 2.45$ GHz [53].

After each acceleration the electrons are bent by the dipole magnets. Their magnetic field is properly set up in order to deflect the electrons of any energy range (from initial injection to second to last energy) by 180°. After each recir-

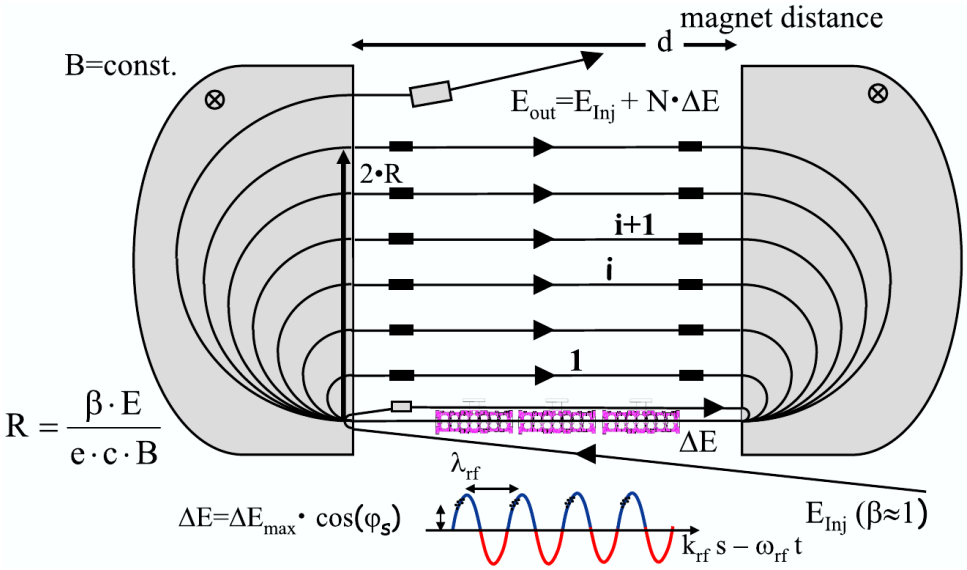

Figure 3.3: Race-Track Microtron. Picture from [53].

culation, the electrons path on the side opposite to the linac is more external, as shown in Fig. 3.3.

A problem with the microtron is that the magnetic field of the dipoles has a negative impact on the polarization, because induces precession on the electron spin. A countermeasure is taken with use of the Wien filter, to select an appropriate spin rotation angle in order to have the final spin direction parallel to the beam direction after all the microtrons stages.

The energy of the extracted electrons is given by:

$$E_{out} = E_o + N \cdot \Delta E \tag{3.2}$$

where E_o is the energy of the entering electrons, N the number of recirculations inside the microtron and ΔE is given by Eq. 3.1.

3.1.3 Harmonic Double-Sided Microtron (HDSM)

To further increase the electron energy, a fourth accelerator step was planned. An additional RTM was not a feasible solution because synchrotron radiation would have been too high and the magnets too large and heavy. Hence, the two bending magnets have been split into four lighter magnets forming a harmonic Double-Sided Microtron (HDSM) with two different linacs located on the longest sides of the circulation, as shown in Fig. 3.4. The two linacs are

not the same, since one works at 4.90 GHz, while the other at 2.45 GHz.

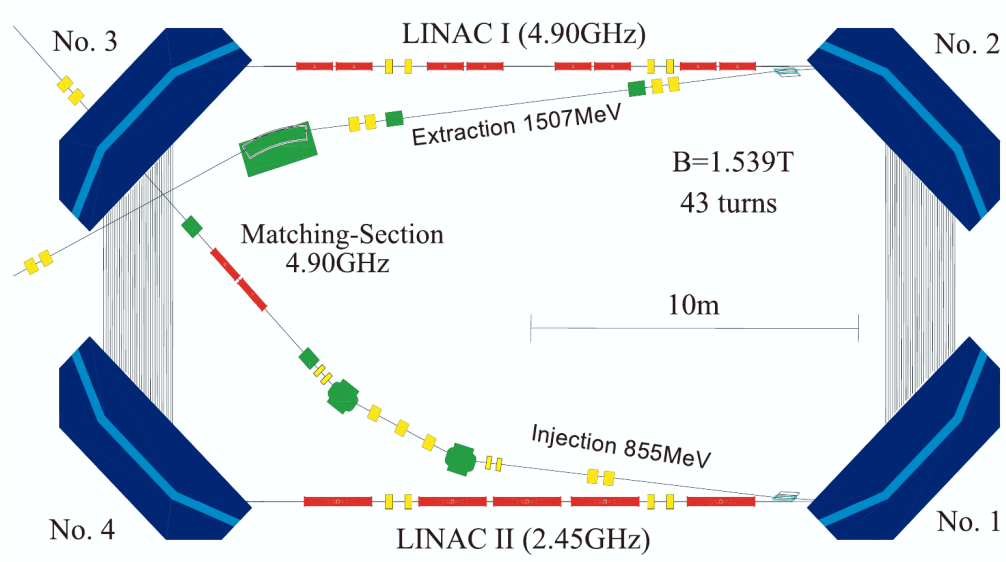

Figure 3.4: Double-Sided Microtron. Picture from [53].

Another characteristic of this Double-Sided Microtron is that electrons of any energy have the same path on the long sides, while on the short ones the path becomes larger as the energy increases.

The HDSM step was installed in 2006 to reach a nominal maximum electron energy of 1508 MeV. After additional upgrades and fine tuning of the magnetic field maps, it is now possible to reach 1604 MeV.

Tab. 3.1 presents the maximum performance achievable and the setup used for this work for the three RTMs and the HDSM at MAMI [47, 53].

3.2 Photon beam apparatus

The electron beam from MAMI enters the A2 hall, where experiments with real photons are performed.

Photons are produced exploiting the Bremsstrahlung effect with the electrons impinging on a thin and high-Z material radiator. This choice is to minimize the possibility of multiple interactions of the primary electrons and to maximize the photon emission probability ($\propto Z^2$).

The secondary photon beam has a continuous energy distribution and the Glasgow-Mainz photon tagger provides the information to evaluate the energy

Table 3.1: Energy performance of the microtrons at MAMI [47, 53].

		RTM1	RTM2	RTM3	HDSM
	Number of cycles	18	51	90	42
Max performance setup	Injection E (MeV)	4.22	15.81	191.46	909.54
	Extraction E (MeV)	15.81	191.46	909.54	1604
	Magnetic field (T)	0.109	0.59	1.366	1.471
	ΔE per cycle (MeV)	0.64	3.44	7.98	16.58
Setup for this work	Injection E (MeV)	4.10	15.35	185.9	883.11
	Extraction E (MeV)	15.35	185.9	883.11	1557.4
	Magnetic field (T)	0.106	0.573	1.326	1.428
	ΔE per cycle (MeV)	0.63	3.34	7.75	16.05

of each produced photon. Additional devices are: a lead glass detector, to measure the photon flux impacting on the target, a Møller polarimeter, to measure the polarization of the electron beam, and a pair spectrometer, to control the photon flux during the data taking runs. The overview of the photon beam production and tagging apparatus in the A2 experimental hall is illustrated in Fig. 3.5.

3.2.1 Photon beam

The production of electromagnetic radiation when a charged particle is decelerated by another charged particle is called Bremsstrahlung effect. In this case the former charged particles are the electrons of the MAMI beam, and the latter are the heavy atomic nuclei of a thin radiator. The probability of emission varies as the inverse square of the particle mass, therefore it is mainly effective only for light particles as electrons.

The Bremsstrahlung emission has the following energy and angular dependences:

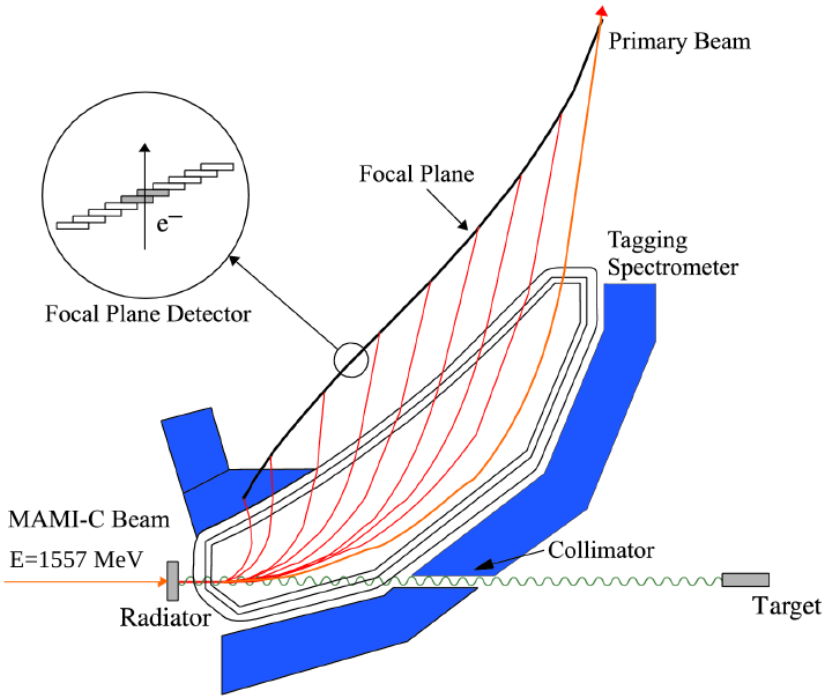

Figure 3.5: Overview of the photon beam production and tagging apparatus, with the radiator, the Glasgow-Mainz photon tagger spectrometer and the collimator. The red lines indicate the trajectories of the electron with different energies after interacting with the radiator [54].

$$\frac{d\sigma}{dE_\gamma} \propto \frac{1}{E_\gamma}, \tag{3.3}$$

$$\frac{d\sigma}{d\theta_\gamma} \propto \frac{\theta_\gamma}{(\theta_\gamma^2 + \theta_c^2)^2}, \tag{3.4}$$

where E_γ and θ_γ are the energy and angle, respectively, of the emitting photon and θ_c is the characteristic angle. The value of θ_c separates the two angular regions where 50% of the photons are emitted, and it is defined as [55]:

$$\theta_c = \sqrt{\langle\theta_\gamma\rangle^2} \propto \frac{m_{e^-}}{E_{e^-}}, \tag{3.5}$$

where m_{e^-} and E_{e^-} are the mass and the energy of the electron. Since the ratio between these two values is very small ($\sim 10^{-3}$), the photons are mainly emitted in the very forward polar region. In order to have a small photon profile at the

target center, which is located about 10 m downstream of the Bremsstrahlung radiator, a lead collimator with a 2 mm diameter opening is located between the radiator and the target. In Fig. 3.6 a picture of this collimator is shown.

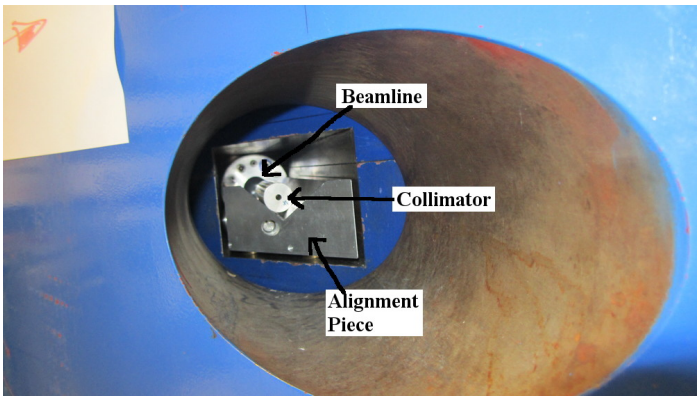

Figure 3.6: Collimator located in the beam-line, inside the dipole magnet of the tagger [54].

The mass of the electron is much smaller than the mass of a nucleus in the radiator, so the scattering is a purely elastic and only a negligible amount of energy is transferred to the recoil nucleons.

Therefore, the energy of the photon E_γ can be evaluated with the following relation:

$$E_\gamma = E_{beam} - E_{e^-} \tag{3.6}$$

where E_{beam} is the energy of the incoming beam from MAMI (1557 MeV for this experiment) and E_{e^-} is the energy of the electron after the photon emission measured by the photon tagger.

In the A2 setup it is possible to use different Bremsstrahlung radiators. The simplest radiator is a 10 µm thick copper foil, which is usually used for experiments with unpolarized beam.

Two different radiators have been used for the experiment described in this work: a Møller foil and a diamond. The first consists of a highly polarizable cobalt-iron alloy. Its peculiarity is that it provides information about the polarization degree of the electron beam via the polarized $e - e$ scattering. On the other hand the diamond has the feature to provide also a linearly polarization component to the photons via coherent Bremsstrahlung [56], resulting in an elliptically polarized photon beam. This setup allows the simultaneous

determination of the E and the G double polarization observables. The linearly polarized component does not affect the experiment with circularly polarized photons [57] and, thus it is not relevant for this work, will not be further described in this thesis.

In the case of a longitudinally polarized electron beam, the polarization degree of the electrons P_e is transfered to the photons according to the following relation:

$$P_\gamma = P_e \cdot \frac{4x - x^2}{4 - 4x + 3x^2} \tag{3.7}$$

where $x = E_\gamma / E_{beam}$ [58]. Fig. 3.7 shows the percentage of the polarization transfer from the electron beam, with an energy of 1557 MeV, to the photon beam.

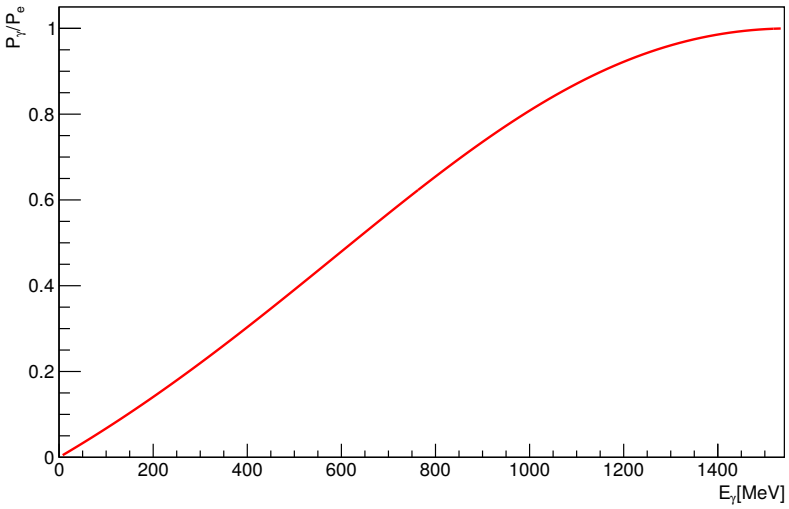

Figure 3.7: Ratio of polarization transfer as a function of the energy from the primary electron beam (set at 1557 MeV) to the photon beam.

3.2.2 Photon Tagger

In order to extract E_γ from Eq. 3.6, the measurement of E_{e^-} is required. The Glasgow-Mainz photon tagger, a magnetic spectrometer developed to measure the energy of the electrons [59, 60, 61], was built for this purpose. It consists (see Fig. 3.5) of two main parts: the dipole magnet and the focal plane detector (FPD).

The dipole magnet produces a magnetic field B, which deflects and separates the electrons from the emitted photons. The value of B is set in order to deflect into the beam dump the electrons that do not produce Bremsstrahlung radiation. With the electron beam energy of 1557 MeV the dipole magnet is set to provide a magnetic field of ~ 1.96 T. The electrons that emitted a photon, having a lower energy than the primary beam, are deflected into the detector located in the focal-plane with a bending radius R given by the Lorentz force:

$$R = \frac{E_{e^-}\beta}{ecB} \tag{3.8}$$

where e is the charge of the electron and B the intensity of the magnetic field dipole, and $\beta = \frac{v}{c}$.

The FPD is composed of 353 plastic scintillators. They are 80 mm long, 2 mm thick and their width varies from 9 to 32 mm. This different width is crucial to have an almost constant energy region coverage for each channel. Each scintillator is coupled to one Hamamatsu R1635 photomultiplier tube (PMT). The scintillators are arranged to overlap by more than half of their width with the adjacent elements. Such overlapping is necessary to have a precise identification of the electrons, using the coincidence between two adjacent scintillators. Because of this arrangement the final configuration has 352 overlapping channels.

The electron's energy after the Bremsstrahlung E_{e^-} can be calculated from Eq. 3.8:

$$E_{e^-} = \frac{RecB}{\beta}, \tag{3.9}$$

where the information about R is given by position of the FPD channels. Hence, the energy of the emitted photon E_γ can be extracted using Eq. 3.6.

With the electron beam energy of 1557 MeV, the 352 FPD channels have an energy width of ~ 4 MeV, an energy overlap of 0.4 MeV and cover the photon energy range between 110 and 1469 MeV.

3.2.3 Tagging efficiency detectors

It is important to emphasize that each post-Bremsstrahlung electron tagged in the focal plane detector corresponds to a photon produced, but not every pro-

duced photon reaches the target. This is due to the conical angular distribution that has the characteristic opening angle θ_c of Eq. 3.5, and to the presence of a collimator.

The ratio of the number of photons passing through the collimator and the number of electrons in the focal plane detector is called tagging efficiency ϵ_{tagg}, and it is defined as:

$$\epsilon_{tagg} = \frac{N_\gamma}{N_e}, \tag{3.10}$$

where N_γ is the number of photons reaching the target, and N_e the number of electrons in the FPD.

The measurement of ϵ_{tagg} is performed with a lead glass detector (Pb-glass). Once a day a dedicated set of runs specifically for tagging efficiency is collected. A set of tagging efficiency runs usually consists of one initial background measurement without beam, one or more runs with beam (depending by which radiators are used for the Bremsstrahlung production) and a final background measurement without beam. During these runs the lead glass is placed into the beamline downstream of all the detectors, just before the photon beam dump, and the beam current is set very low ($\sim 10^4$ photons/sec) to avoid the saturation of the detector signals. This apparatus is a Čerenkov detector and it is only sensitive to the radiation emitted by charged particles when their speed inside a material with a high refractive index is greater than the speed of light in that material (for more details about Čerenkov detector principles see Sec. 3.4.3). When a photon hits the detector, it produces an electromagnetic shower where the positrons and the electrons are very energetic and, due to the lead glass high refractive index (~ 1.8), they are faster than light in the lead glass. The positrons and electrons emit in turn low energetic photons, which are collected and transformed into an electronic signal by a PMT.

The efficiency of the lead glass detector is basically 100%, and this value has been used during the tagging efficiency data analysis, illustrated in Sec. 5.3.

During the normal data runs, the tagging efficiency is monitored with a low efficiency pair spectrometer located in the photon beamline just beyond the collimator. It consists of a thin tungsten foil ($\sim$20 μm) and 2 scintillators, each coupled to 2 silicon photomultipliers. A photon that passes through the thin foil is converted into an electron-positron with a probability of $\sim 10^{-3}$ (see

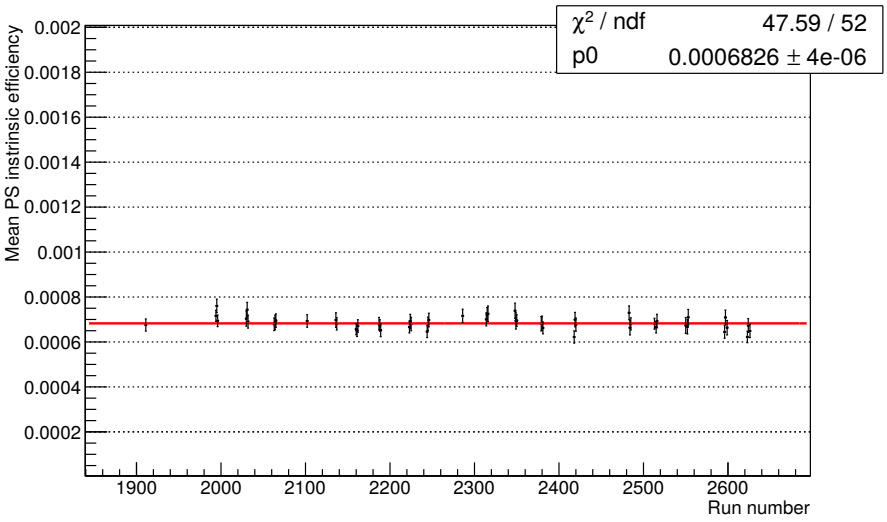

Figure 3.8: Averaged pair spectrometer intrinsic efficiency during D-butanol 2014 beamtime.

Fig. 3.8), and a permanent magnetic field deflects the two charged particles into the scintillators.

This measurement is particularly useful during the runs with the diamond to monitor the coherent peak position, a crucial parameter to determine both the linear polarization degree and the tagging efficiency.

3.3 Frozen Spin Target

The Frozen Spin Target (FST) of A2 was built by the Mainz-Dubna target group, with the goal of reaching high nucleus polarization degrees ($\sim$ 70% or higher) and long relaxation times (several hundreds hours). An overview of the target is shown in Fig. 3.9.

The target material, located in the internal cell, is initially cooled to a temperature lower than 1 K. A high magnetic field is then applied, which polarizes the free electrons of the target material. The polarization is then transferred from the electrons to the nuclei of the target, using the Dynamic Nuclear Polarization (DNP) effect. When this process is completed, the temperature is further reduced to $\sim$ 20/25 mK, the high magnetic field is removed and a smaller uniform holding magnetic field applied. At this point the target is ready for the measurement.

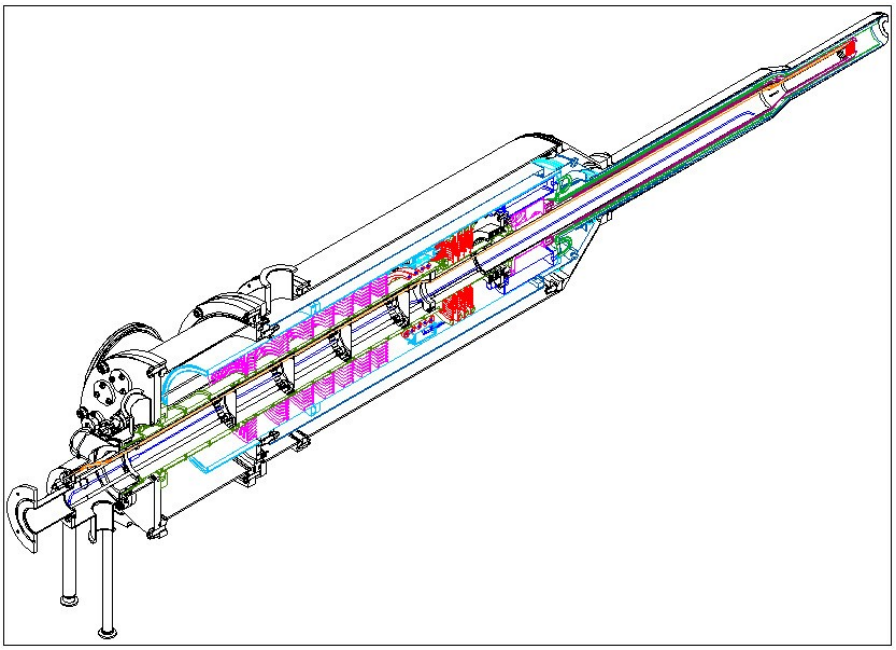

Figure 3.9: Drawing of the Mainz-Dubna frozen spin target. The beam enters from the left, the target cell is located near the edge on the right [62].

3.3.1 Polarization mechanism

A particle can be polarized when it is cooled to a low temperature and placed inside a high magnetic field. The external magnetic field B interacts with the magnetic moment μ splitting the level into $2I + 1$ sub-levels, where I indicates the particle spin (1/2 for protons and electrons, 1 for deuterons).

The Boltzmann law describes the population of these two levels at thermal equilibrium:

$$N_1 = N_2 \cdot exp(\frac{-\Delta E}{k_B T}), \tag{3.11}$$

where k_B is the Boltzmann constant, T the temperature of the system, N_1 and N_2 the population of the sub-levels and $\Delta E = E_2 - E_1 = -g_i \mu_i B$ is the energy difference between two sub-levels [63]. The parameter g_i and μ_i are the g-factor and the magnetic moment of the particle, respectively.

The polarization degree is generally described by the Brillouin function [64]:

$$P_S = \frac{2S+1}{2S}\coth(\frac{2S+1}{2S}\frac{\mu BS}{kT}) - \frac{1}{2S}\coth(\frac{1}{2S}\frac{\mu BS}{kT}), \tag{3.12}$$

For the half-integer spin electron and proton, it becomes:

$$P(1/2) = \frac{(N_{1/2} - N_{-1/2})}{(N_{1/2} + N_{-1/2})} = \tanh(\frac{g_i\mu_i B}{2k_B T}), \tag{3.13}$$

and for the integer spin deuteron, it results in:

$$P(1) = \frac{(N_1 - N_{-1})}{(N_1 + N_0 + N_{-1})} = \frac{4\tanh(\frac{g_i\mu_i B}{2k_B T})}{3 + \tanh^2(\frac{g_i\mu_i B}{2k_B T})}. \tag{3.14}$$

As shown in Eq. 3.12, the degree of polarization is strongly dependent both on temperature and on the particle magnetic moment. At 1 K temperature and 2.5 T magnetic field, the electron's polarization degree is very high, above 90%, while for the proton it would be only 0.25%, and for the deuteron around 0.05% [63, 65]. This large difference is shown in Fig. 3.10. Such a low degree of polarization is not useful for an experiment. To overcome this problem the Dynamic Nuclear Polarization effect is used.

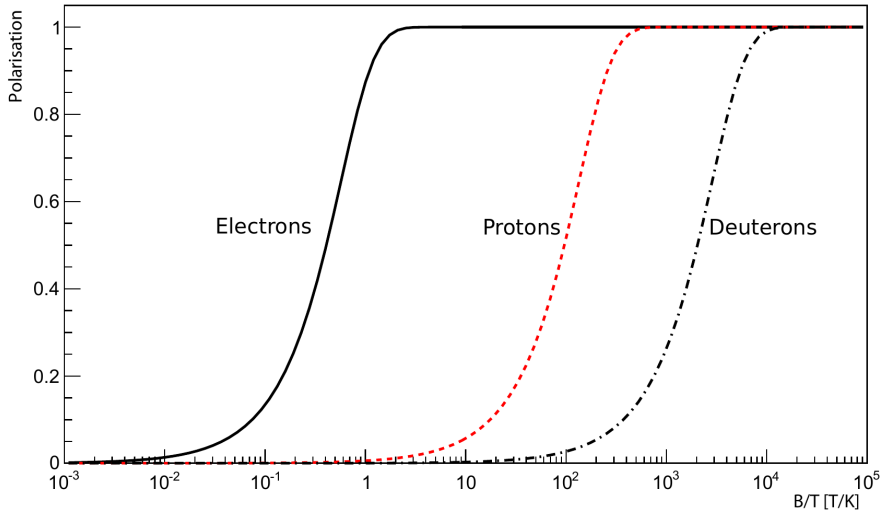

Figure 3.10: Polarization degree for electrons, protons and deuterons, as a function of magnetic field/temperature.

The DNP technique was developed in the '50s [66, 67] and it is a method to transfer the high electron polarization degree to the nuclei (proton or deuteron). This is achieved using microwaves of a specific frequency ν that induces a

simultaneous spin flip of both the electron and the nucleus. The frequency ν is defined as the sum (for positive polarization) of the Larmor frequencies of electron ν_e and nucleus ν_n, or as the difference (for negative polarization) [68]. It can be expressed as:

$$\nu^{\pm} = \nu_e \pm \nu_n = \frac{\mu_e B}{\pi\hbar} \pm \frac{\mu_n B}{\pi\hbar} = \frac{(\mu_e \pm \mu_n)B}{\pi\hbar}. \tag{3.15}$$

To change the orientation of the target polarization it is not necessary to change the magnetic field, it is sufficient to properly select the microwave frequency.

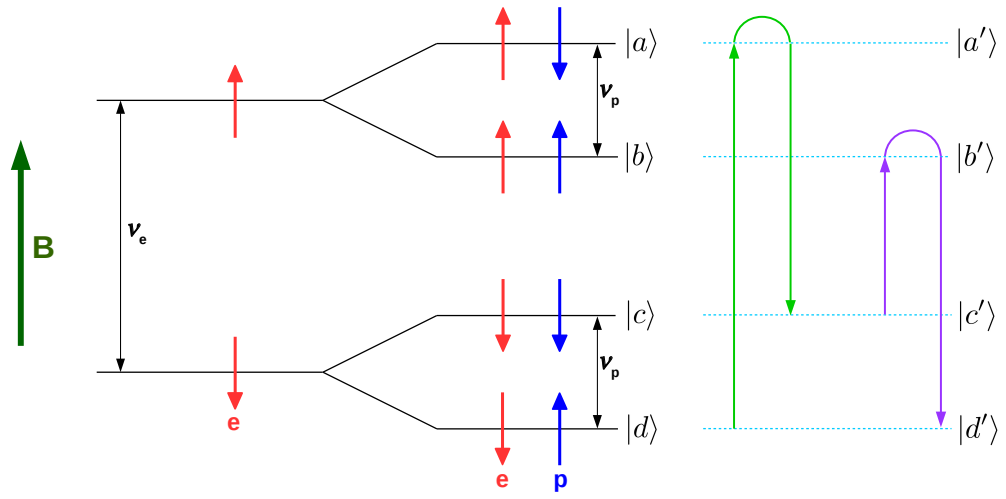

Figure 3.11: Schematic representation of Dynamic Nuclear Polarization for the proton. For positive polarization, DNP brings the electron-proton from state $|a\rangle$ to state $|d\rangle$.

In Fig. 3.11 this process is schematically represented, for the positive proton polarization from state $|c\rangle$ to state $|b\rangle$, and for negative polarization from state $|a\rangle$ to state $|d\rangle$. In the state $|a\rangle$, the electron is polarized by the magnetic field B, while the proton is not polarized (as previously mentioned, the proton polarization would be very low). The microwaves flip the electron-proton couple leading to the state $|d\rangle$, where the proton is negative polarized and the electron flips its polarization. The electron is very sensitive to the external magnetic field, and it flips its orientation again within milliseconds (state $|c'\rangle$), while the proton maintains the negative orientation for a much longer timespan. The electron and the polarized proton decouple and the electron can couple another

non-polarized proton (making another $|a\rangle \longrightarrow |d\rangle$).

To produce a high polarization degree of the target, the magnetic field and the microwaves should provide their effect continuously. This is not possible because the large magnet needed to get a high value of B does not permit the target to be placed inside the Crystal Ball detector. To overcome this problem, the Frozen Spin method is used. Once a high polarization target degree is reached with the DNP technique, the microwaves are switched off and the target is further cooled below 30 mK. At this temperature the spin of the nuclei are almost 'frozen' and a small internal coil is used to create a holding magnetic field of 0.63 T. With the combination of these two effects, the relaxation time becomes long enough to allow normal data taking. Finally, it is possible to switch off the polarizing magnetic field and to remove the large magnet.

For DNP to be effective, it is necessary for paramagnetic centers to be present near the nuclei to be polarized [69].

3.3.2 Target materials

As previously discussed in Sec. 2.6, the deuterium nucleus has been chosen to access the free neutron information. To select a good target material for a nuclear experiment, the following requirements should be taken into account:

- absence of polarizable nuclei apart from the deuteron,
- strength against radiation damage,
- high degree of polarization,
- high dilution factor[1],
- easy to prepare and to reproduce,
- long relaxation time.

The most common options are deuterated-ammonia (ND_3) and deuterated-butanol (C_4D_9OD). Deuterated-butanol was chosen for this experiment; the main advantage of this material is that the carbon and the oxygen nuclei are

[1]It is defined as the ratio between the number of polarizable nucleons and the total number of nucleons.

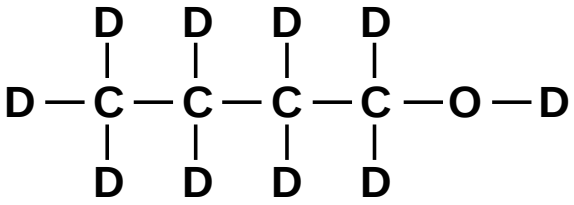

Figure 3.12: Deuterated butanol molecule.

spin-less and hence not sensitive to the polarization. Therefore, the only polarizable part is composed of deuterons. Deuterated butanol is less radiation resistant than ammonia, but this defect does not give a sizeable loss of polarization in a real photon beam. The composition of the deuterated butanol molecule is shown in Fig. 3.12.

In order to have paramagnetic centers near the nuclei, a tiny amount (a few ‰) of doping radicals were added to the deuterated butanol target. Two different types of deuterated butanol with different doping radicals were used for the experiment: trityl (abb. for triphenylmethyl) and TEMPO. The first option was used during the 2014 data taking; it permits a high polarization degree (above 60%), but the frequency range for an effective polarization is very narrow and very sensitive to local inhomogeneity of the magnetic field [69, 70] and therefore it is very difficult to get a reliable measurement of the absolute target polarization value. On the other hand, TEMPO doped butanol was used during the 2015 beamtime; this radical allows a lower polarization degree (max 30%), but the polarization procedure is easier and more reliable [71].

The butanol target material is composed of several little spheres, with a diameter of 2 mm, and they are located inside a target cell with cylindric shape 2 cm long and 2 cm of diameter, as shown in Fig. 3.13. The density of the butanol material is 0.94 g/cm^3, corresponding to a surface density of deuterons inside the target of $9.465 \cdot 10^{22}$ cm^{-2} [72].

For the evaluation of the numerator of the E observable defined in Eq. 2.41, the contribution of these unpolarized nuclei is canceled out. On the other hand, for the evaluation of the denominator, it is crucial to subtract the unpolarized contributions from the oxygen and carbon nuclei and from the target container.

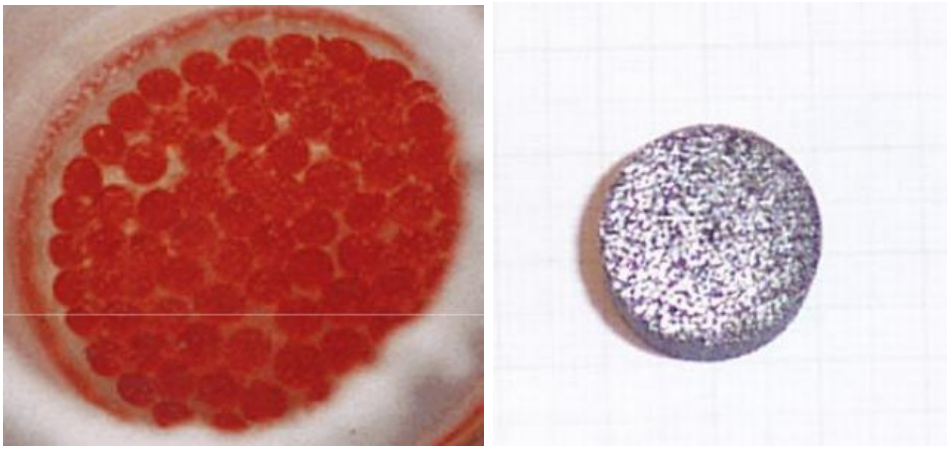

Figure 3.13: Pictures of the target material used for the present experiment. On the left: deuterated butanol; on the right: carbon foam [54].

For this purpose separate data taking has been performed using a carbon foam, shown in Fig. 3.13, in order to evaluate the unpolarized background. This target was produced in order to have the same density of non deuterium nucleons of the butanol target, $6.798 \cdot 10^{23}$ cm^{-2} [72].

3.3.3 Cryostat

A temperature below 50 mK is necessary in order to have a long enough relaxation time for the run of the experiment without re-polarization breaks. Temperatures below 1 K are not feasible with a standard liquid helium refrigerator. The Mainz-Dubna frozen spin target exploits the dilution technique with a mixture of ^{3}He and ^{4}He (6% ^{3}He and 94% ^{4}He) to reach a temperature below 30 mK [73, 74, 75].

At temperatures below 0.88 K the ^{3}He and ^{4}He liquid spontaneously separates into two phases, one predominantly of ^{3}He (^{3}He concentrated phase) and the other predominantly of ^{4}He (^{3}He diluted phase), as shown in Fig. 3.14. The system is in thermal equilibrium and the two phases are separated because of their large mass difference. If the ^{3}He is removed from the dilution phase, the ^{3}He in the concentrated phase will start flowing to the diluted one in order to restore the thermal equilibrium. The osmotic pressure of the different ^{3}He concentration in the two phases can be equated with the pressure acting on a one-component system. The flowing of ^{3}He through the phase boundary requires energy that is absorbed from the mixture, cooling the system [76].

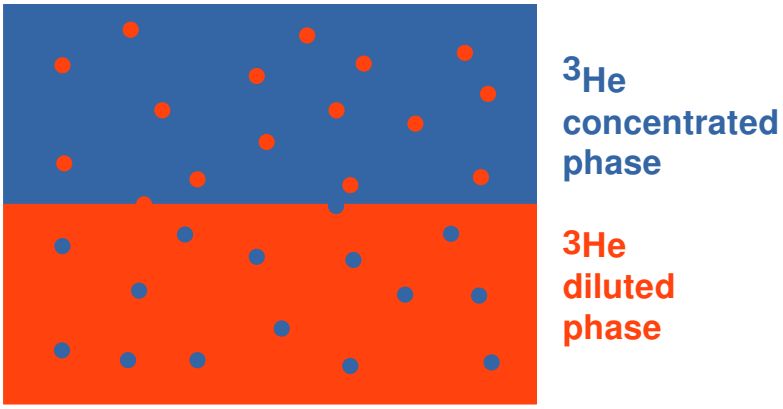

Figure 3.14: Scheme of the ^{3}He and ^{4}He phases separation. At temperatures below 0.88 K the ^{3}He and ^{4}He mixture separates spontaneously into two phases: the concentrated phase, ^{3}He rich, and the diluted one, poor of ^{3}He.

The normal operational temperature of the target cell in the Mainz-Dubna frozen spin target is ∼20/25 mK. The combination of such a low temperature with an internal magnetic field of 0.5 T gives a relaxation time of around ∼1000 h. During data taking, the target is usually re-polarized once a week.

3.4 Detectors

The A2 detector setup is composed of the Crystal Ball (CB) and TAPS apparatuses. The first of them includes: CB itself, two Multiwire Proportional Chambers (MWPCs) and a Particle Identification Detector (PID). The TAPS apparatus includes TAPS itself and Veto.

An overview of the CB-TAPS system is shown in Fig. 3.15.

An additional Čerenkov detector was located between CB and TAPS for vetoing the trigger from spurious events generated by the photon beam.

3.4.1 Crystal Ball

The Crystal Ball (CB) was designed and built in the '70s at the Stanford Linear Accelerator Center, and it was used for the first measurements of the J/Ψ and its excited states. Afterwards, it was transferred to DESY in Hamburg and then to Brookhaven National Laboratory in the USA. Since 2002 the CB has been deployed in the A2 tagger hall at MAMI. Fig. 3.16 shows the CB during

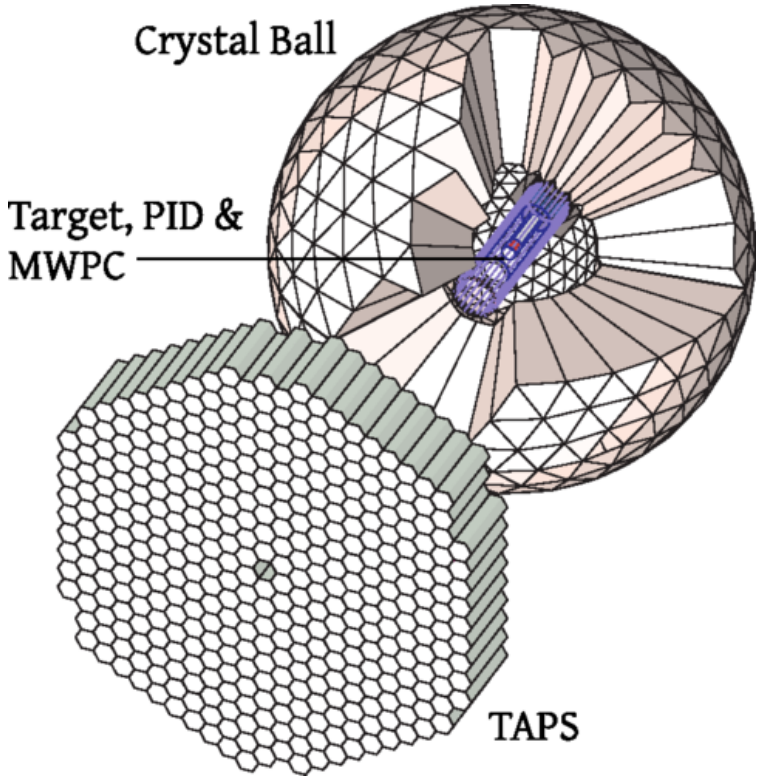

Figure 3.15: Overview of the detectors in A2, the Čerenkov detector is not present in this picture.

the installation in Mainz.

The CB is a calorimeter made of NaI(Tl) (thallium doped sodium iodide) crystals arranged in a regular icosahedron, a regular polyhedron with 20 regular triangle faces. There are two holes facing each other to allow the passage of the photon beam. The planar projection of the icosahedron with the two holes is illustrated in Fig. 3.17.

Each main face is composed of 36 crystals, further grouped in 4 equilateral triangles of 9 crystals each, as shown in Fig. 3.18. Each hole for the beam-line corresponds to 24 crystals, yielding the number of crystals of 672. The frame of the crystals is divided in two hemispheres to allow easier access to the inner detectors and to the target.

The crystals are 40.6 cm long, equivalent to more than 15 radiation lengths, with a truncated triangular pyramid shape. Each of them is optically independent from each other and optically coupled to one photo-multiplier tube at the base of the pyramid.

Figure 3.16: The Crystal Ball with photomultiplier tubes but without cables, during the installation at MAMI in 2002. Picture from [77].

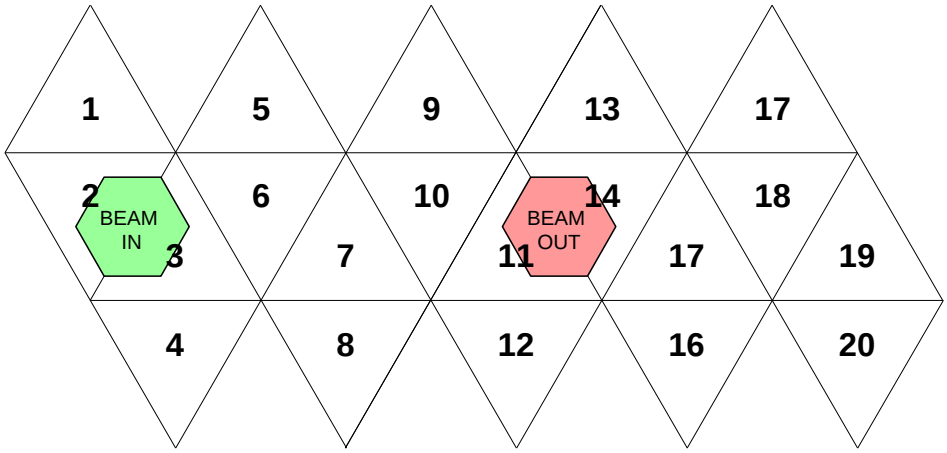

Figure 3.17: Projection of the CB icosahedron, with the two removed sections for the passage of the photon beam.

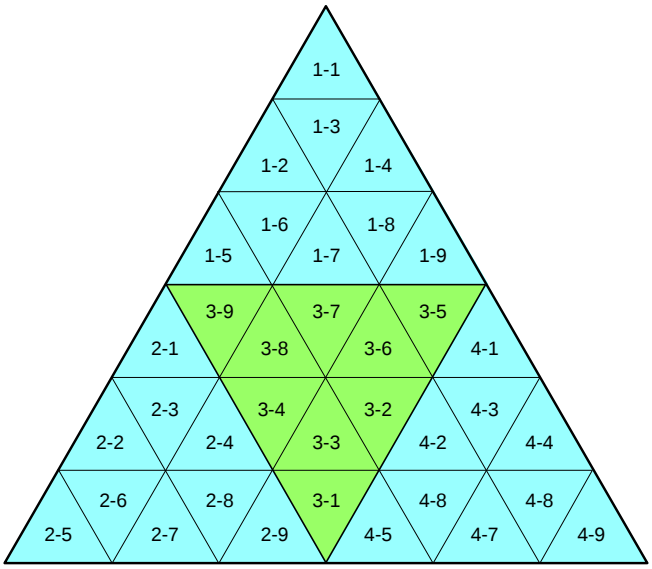

Figure 3.18: Segmentation of one main triangular face of the CB icosahedron.

The CB covers almost the full azimuthal angular range in ϕ and the polar angular range θ from 21° to 159°. The time resolution is $\sim 4-5$ ns while the energy resolution is described by the following formula $(0.0255 \pm 0.0013)E^{3/4}$ giving around 3% in the energy range used for this experiment [78].

The angular resolution depends on the number of crystals involved in the energy deposition; the more they are, the more accurate the calculations of the center of gravity of the interaction and the angular resolutions are. A photon usually deposits its energy by making an electromagnetic shower involving several crystals. In such a case, the CB has a polar angular resolution of $\sim 2-3°$, as well as an azimuthal angular resolution of $\sim 2°/\sin\theta$. The angular resolutions for charged particles are lower due to the lower number of hit crystals.

The CB does not provide information about the charge of the particles detected and, due to the small distance between the target and the NaI crystals, it is not possible to perform a particle identification using the time of flight. On the other hand, it is possible to separate neutral particles into photons or neutrons by performing a cluster size analysis, further described in Sec. 5.2.

The CB is the main detector of the setup and the trigger is generally given only by CB, although sometimes also TAPS contributes, as in the case of the

experiment discussed in this work.

3.4.1.1 PID

The Particle Identification Detector (PID) is a device located inside the CB and devoted to charged particle identification. Developed by the group at the University of Edinburgh, it is a 11 cm radius barrel composed of 24 EJ-204 plastic scintillator strips. The target is located inside the PID barrel.

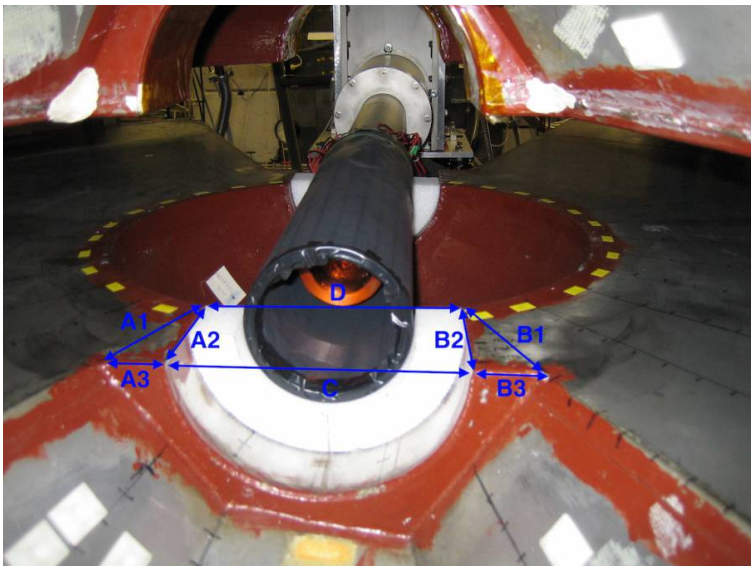

Figure 3.19: Picture of the PID [54].

Each scintillator is 50 cm long, 4 mm thick and covers 15° in the azimuthal angle. Its cross section has an irregular trapezoidal shape in order to better match with the neighboring elements and to maximize the solid angle coverage.

The scintillators are wrapped with aluminium foil and a layer of thin black film, in order to be optically independent from each other, and coupled to photo-multiplier tubes. The whole detector is wrapped with black foil to guarantee that it is lightproof.

The purpose of the PID is to provide information about the charged particles detected by the CB. It can be used as a discriminator to separate the charged tracks from the neutral ones, and can also provide information for particle identification using the $dE - E$ method. The energy deposited into a specific material with thickness dx is given by the Bethe-Bloch formula. In the case of PID the dx corresponds to the thickness of the scintillator strip divided by

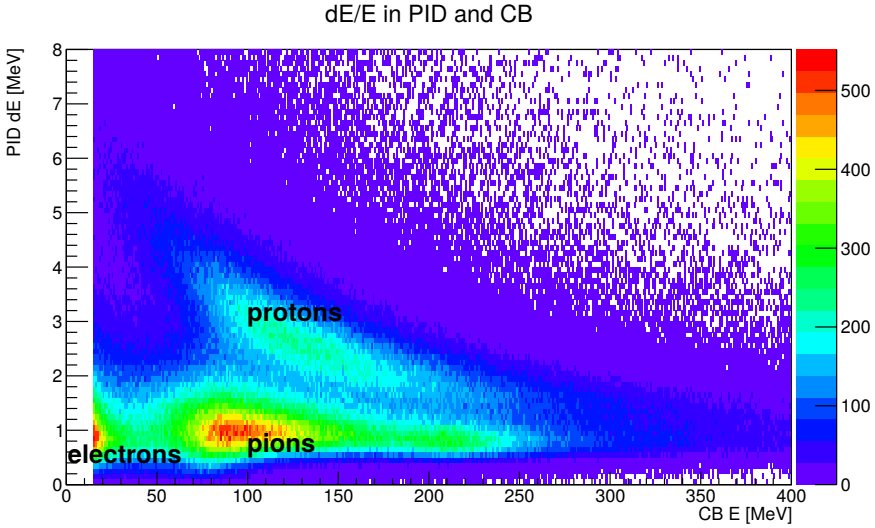

Figure 3.20: Particle identification combining the energy information from PID and CB. Protons, charged pions and electrons show up in different zones of the plot.

sinθ. In Fig. 3.20 a $dE - E$ plot for the PID-CB apparatus is presented.

3.4.1.2 MWPCs

The Multiwire Proportional Chambers (MWPCs) were developed to improve both the angular resolution of the charged particle trajectories detected in the CB and the $dE - E$ analysis. They were built by the photo-nuclear group of the INFN section of Pavia, using as a model the old wire chambers of the DAPHNE experiment [79].

The MWPCs consist of two different coaxial detectors 56 cm long, whose construction parameters are shown in Tab. 3.2. They are located inside the CB, around the PID and longitudinally centered on the beam-line.

Each MWPC is composed of two cathodes provided with strips, and a layer of wires between them. The cathodes are cylinders made of 1 mm thick Rohacell covered with a 25 μm Kapton foil. The surfaces facing the wires are laminated with aluminium strips 2 mm wide, 0.1 μm thick, and with a space of 0.5 mm between each other. These strips are arranged helicoidally in order to form a 45° angle with the wires, oppositely oriented for the inner and outer cathodes, as shown in Fig. 3.22 on the left.

The wires are coaxially located between the cathodes, with a gap of 2 mm

Figure 3.21: Picture of the MWPCs.

between each of them. The wires are 20 µm thick and made of gold-plated tungsten; they are welded to the inner cathode at a tension of 0.5 N. A high voltage is applied at the wires, 2500 V for the inner detector and 2550 V for the outer one.

During operation, the internal spaces of these detectors are filled with a gas mixture with the aim to reach a high gain, good proportionality, and high rate capability. The mixture for the MWPCs in A2 is made of Argon (69.5%), Ethane (30%) and Freon (0.5%). A small amount of methyl alcohol is added to this mixture, to prevent the formation of polymer chains from bursting Ethane.

A charged particle passing through these detectors ionizes the gas, creating a free electron and a positive ion. The potential difference between the anode wires and the cathode strips accelerates the original electron in direction of the wires. The newly created electrons are accelerated by the internal electric

Table 3.2: Construction and operation parameters of the two MWPCs.

MWPC	Ch 1	Ch 2
Length (mm)	560	560
Inner radius (mm)	70	90
External radius (mm)	78	98
Number of wires	232	296
Number of internal strips	69	89
Number of external strips	77	97
Wires voltage (V)	2500	2550

field and they can ionize more molecules of the gas. More electron-ion pairs are generated in this way, resulting in an ionization avalanche. The size of this avalanche is proportional to the number of primary ionization events generated by the charged particle. The electrons from the ionization events are collected on one or more wires, while the ions aggregate on the internal and external cathode strips [82].

The charge distribution of the electrons on the wires gives the information about the azimuthal angle ϕ.

Due to their helicoidal arrangement, the internal and the external strips have two intersection points. From the information of the charge distribution of the positive ions on the strips, there are two ϕ and z solutions, as shown in Fig. 3.22. With the information of the ϕ from the wires, it is possible to select the correct ϕ and z coordinates obtained by the information from the strips, and to calculate the θ angle.

Once the coordinates of the interaction points in both chambers are determined, a straight line is evaluated, which gives the trajectory of the charged particle. If the event includes only one charged track, the 'pseudo' vertex[2] po-

[2]Defined as the 'origin' of the event, where the interaction between a photon and the target occurred.

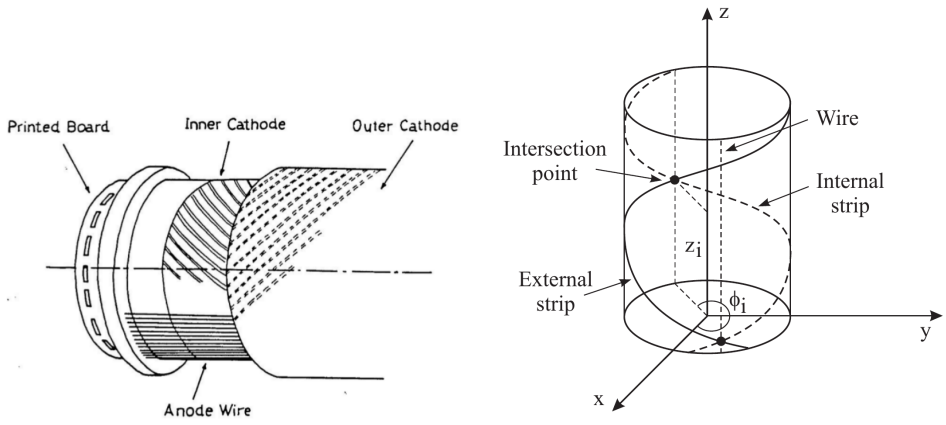

Figure 3.22: On the left, schematic draw of the components of one wire chamber, with the anode wires and the two cathodes with strips, picture from [80]. On the right the principle for the interaction reconstruction coordinates is shown, picture from [81].

sition is reconstructed to be on the closest point to the z-axis. If the events includes two charged trajectories the intersection between them results in the 'true' vertex position. The reconstruction of the vertex position is particularly important because it allows to monitor the target position and its alignment with the detectors.

The MWPCs cover the total angular range in ϕ, and in θ they cover the same range of the CB, from 21° to 159°, with an angular resolution around 2° both in ϕ and θ.

3.4.2 TAPS

The Two Arms Photon Spectrometer (TAPS) is a detector that has been used in the tagger hall of MAMI with different configurations. Its crystals and photomultipliers are today arranged in order to cover the downstream beam opening of the CB as a forward wall. The crystals are positioned within an hexagonal shape, as shown in Fig. 3.24. This detector provides information for tracking, particle identification and calorimetry.

TAPS is located 1.8 m from the target, and it covers the full azimuthal angle and the polar in the range between 5° and 25°.

The total number of crystals is 438, 366 made of BaF_2 and 72 of $PbWO_4$, the latter are located in the two inner rings covering the lower θ region. Each

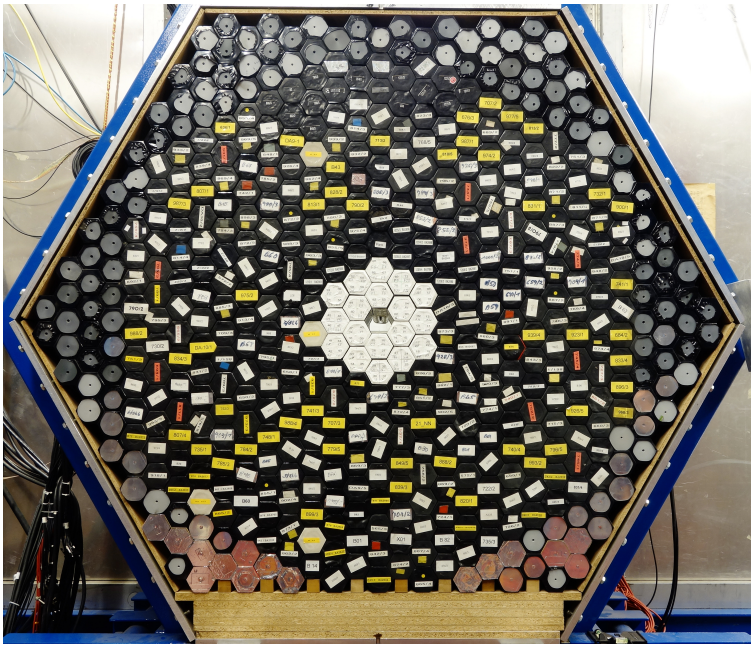

Figure 3.23: Picture of TAPS opened for maintenance, without the Veto. The external elements without labels are plastic parts to keep the crystals in the proper position. The white inner elements are the $PbWO_4$ crystals. Picture from [83].

BaF_2 crystal is a hexagonal polyhedron 22.5 cm long, corresponding at ∼12 radiation lengths, and 5.9 cm thick. The $PbWO_4$ crystals are smaller, four of them correspond to one BaF_2 crystal, as shown in Fig. 3.24. The optical isolation of the TAPS crystals is achieved with 8 layers of 38 µm thick PTFE and one layer of 15 µm thick aluminium foil. Each BaF_2 crystal is optically coupled with a Hamamatsu R2059-01 photomultiplier tube [84], while each $PbWO_4$ is optically coupled with a XP 1911/12 [85].

BaF_2 has a scintillation light with two components: one fast ($\tau \simeq 0.9$ ns) and one slow ($\tau \simeq 650$ ns). Different particles passing through BaF_2 crystals give different contributions to these two components. The analysis of the combination of these two components is a good tool for particle identification, a technique known as Pulse Shape Analysis (for more details see Sec. 5.2.3). The contribution of the fast component is higher for light particles, such as photons, than for protons or neutrons. This feature is particularly useful to separate photons from neutrons, as described in Sec. 5.2. The fast component of the signal provides a very good time resolution and, combined with the large distance between TAPS and the target, it can be used for time of flight parti-

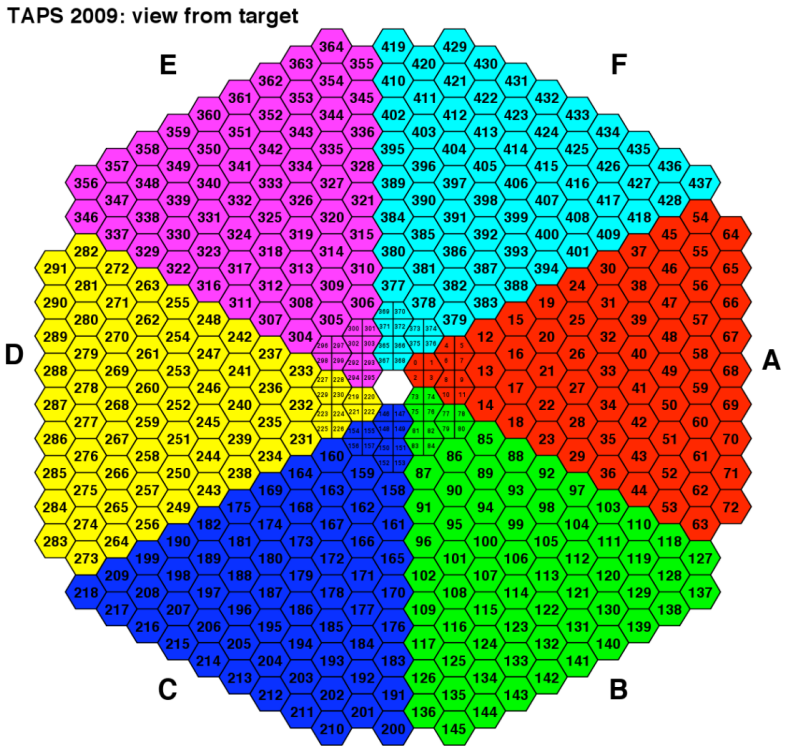

Figure 3.24: Crystal arrangement in TAPS. The two inner rings are the $PbWO_4$ crystals, the different colors show the trigger sections. Picture from [86].

cle identification. More details about the proton and neutron identification in TAPS can be found in Sec. 5.2.

The spacial resolution is $\sim$ 3 cm, giving an angular resolution between 0.7° and 1°, depending on θ. The energy resolution is given by $\Delta E/E = 0.018 + 0.008/E[\text{GeV}]^{0.5}$ [84].

The data used for this work were collected with TAPS triggering in order to have the maximal solid angle coverage. Since in the forward polar region covered by TAPS the background coming from atomic event becomes very relevant, a Čerenkov detector, described in the next section, was used to provide an online veto to the TAPS trigger.

Veto

The Veto is a thin wall of plastic scintillator developed for charged particle identification in the TAPS detector.

An EJ-204 plastic scintillator is mounted in front of each TAPS element.

These scintillators are 5 mm thick and have the same hexagonal shape as the TAPS elements, as shown in Fig. 3.25. Their signals are transferred through wavelength shifting fibers to the photomultiplier tubes. For an easier handling of several signals, the Hamamatsu H6568 16-channel multi-anode PMT was chosen [87].

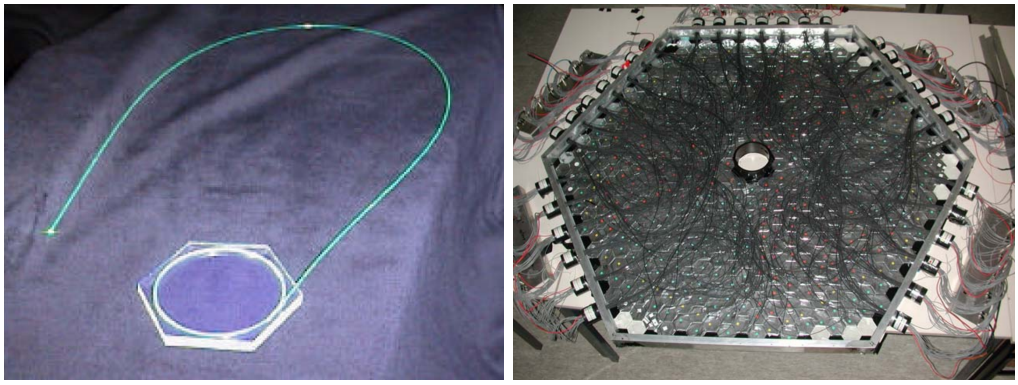

Figure 3.25: Pictures of the Veto. On the left: one single scintillator of the Veto, coupled with its wavelength shifting fiber. On the right: the entire Veto wall. Pictures from [81].

This additional plastic scintillator plane gives information for vetoing charged particles and for ΔE/E particle identification. The energy resolution of the Veto is lower than the PID-CB system due to more complicated coupling between the scintillators and the PMTs, but it is sufficient for the requirements of this work.

3.4.3 Čerenkov detector

The photon beam, interacting with the target atoms, produces a considerable amount of electromagnetic background, mostly in the forward region at small values of θ. The prevalent contributions of the background come from atomic Compton scattering $\gamma + e \rightarrow \gamma' + e'$ and from $e^+ - e^-$ pair production. Since the particle angular distributions of both reactions are very forward peaked, most of these background events are detected by TAPS. During the off-line analysis it is possible to select and remove this background. However, since the cross section of these atomic processes are much higher than the ones of interest, the recorded events would include a huge amount of undesired events and, since the acquisition rate is limited by the electronics, the effective time

for the experiment is not fully exploited.

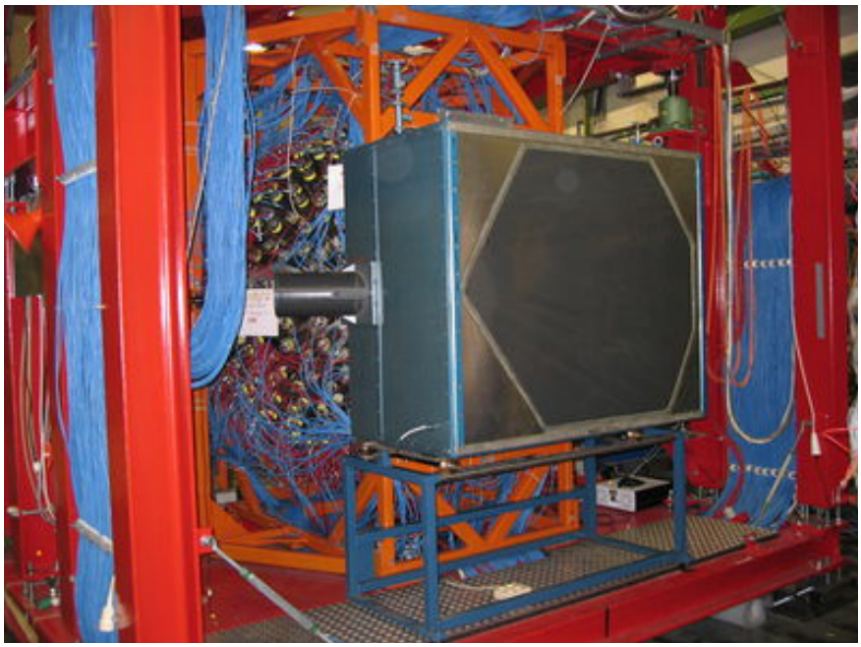

Figure 3.26: Picture of the Čerenkov detector covering the downstream opening of CB. On the left it is possible to see the photomultiplier tube. TAPS is absent in the picture because it was moved downstream for maintenance.

To overcome this problem, a Čerenkov detector can be positioned in the beam-line between CB and TAPS in order to have an online veto of the TAPS trigger. When the Čerenkov detects a fast charged particle, as in the case of an electron, a signal is produced and used to inhibit TAPS from triggering.

The detector operating principle is based on the Čerenkov effect. When a charged particle in a medium moves faster than light inside the medium, the particle emits electromagnetic radiation by a process known as Čerenkov emission [82]. This radiation is emitted with a conical shape with an angle θ described by the following formula:

$$\cos\theta = \frac{1}{\beta n}, \tag{3.16}$$

where n is the refractive index of the medium, and β is the ratio between the speed of the particle and that of light in the vacuum. The value of n determines the speed of light through the medium $v_{light} = c/n$, which is also the velocity threshold for the particle to emit the Čerenkov radiation. The threshold for

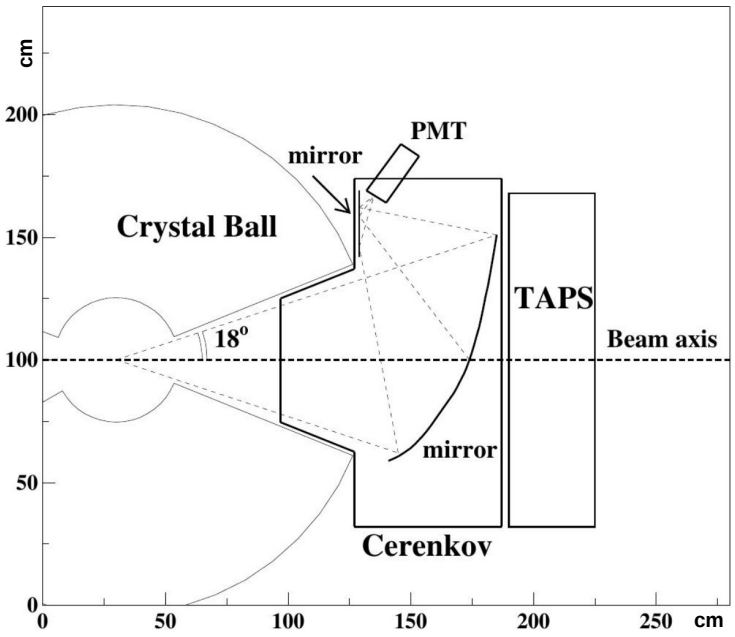

Figure 3.27: Outline of the Čerenkov detector between CB and TAPS.

the Lorentz factor γ_t can be expressed as:

$$\gamma_t = \sqrt{\frac{1}{1-\beta_t}} = \sqrt{\frac{n}{n^2-1}}. \tag{3.17}$$

The energy threshold for Čerenkov radiation of a particle with rest mass m_0 is given by:

$$E > \sqrt{\frac{1n}{n^2-1}} m_0 c^2 \tag{3.18}$$

The Čerenkov detector consists of three parts: a large box filled with a gas, a mirror system to focus the Čerenkov radiation, and a Hamamatsu R1584-03 SEL photomultiplier tube to collect the signal.

A parallelepiped box with a truncated hexagonal pyramidal nose is the main part. It has such a shape to fit inside the CB, as shown in Fig. 3.27. Its main frame is made of aluminium, while the two faces crossed by the beam-line are made of a 100 μm thick mylar foil. The total volume is 1.3 m^3 and the gas inside this volume is C_4F_8, which has a refractive index $n = 1.0013$. Such a refractive index guarantees that the Čerenkov detects electrons, since their energy threshold calculated using Eq. 3.18 is ~ 10 MeV, while it does not

detect charged pions and protons, which have energy thresholds of ~ 2.6 GeV and ~ 20 GeV, respectively.

When the Čerenkov detector is in position, TAPS is located 10 cm farther downstream than usual, so that a small polar gap ($\sim 2°$) between TAPS and CB is created. As a consequence, a small loss of angular coverage has to be taken into account both in the off-line analysis and simulation.

The efficiency of the Čerenkov detector when filled with C_4F_8 is $> 99.9\%$, even if the volume is not completely filled with the gas.

3.5 Data taking electronics

The signal from a particle detected in the A2 experimental setup is collected by a PMT or, in the case of MWPCs, by a preamplifier. The output signal from these devices is an analog signal that must be digitalized and recorded.

All the analog signals are split into two parts: one of these is analyzed for energy information, while the other is used for trigger and timing information. The first signal is digitalized by an Analog-to-Digital Converter (ADC), that produces a digital signal which contains the amplitude or the integral information of the analog input signal. The second signal usually enters into an analog discriminator in order to remove noise and background. The output is further split into two branches, one entering into the trigger logic and being used for enabling the readout, while the other enters into a Time-to-Digital Converter (TDC). This electronic module analyzes the signal time and compares it to a reference time given by the trigger (or by another clock). A digital signal proportional to this time difference is produced at the output.

Among all the detectors in A2, the ADC of the tagger are used only for tuning the detector but not during the normal data taking runs. In this case, the energy information of electrons is extracted from the position of the hit channel. It is particularly crucial to know exactly the number of electrons incident on the tagger to evaluate the correct photon flux, even when high count rates (up to ~ 1 MHz) are present. So, after the discriminator, the signal enters into a CATCH (COMPASS Accumulate, Transfer and Control Hardware) multi-hit TDC. This module can record multiple hits present in one physical event (i.e. in a given time window). To count their number, the second branch of the tagger signals enter into VUPROM scaler units.

The final step of the data taking process is the storage of the full event information on disk. The data acquisition (DAQ) software is called AcquRoot [88] and it was developed for the A2 Collaboration setup. More details are presented in Sec. 4.1.

3.6 Experimental trigger

Because of the very high event rates inside the detector, it is not feasible to record all events one by one. It is then necessary to set conditions in order to only select the events of interests and to minimize as far as possible other unwanted events, without losing any event of interest. Different logics can be used for triggering the data readout of the detector.

The analog output signal from a CB PMT enters into a split/delay module that splits the signal into an additional branch, different from the branches going into the TDCs and ADCs described before. This module adds together the analog signals from 16 PMTs. The summed signals from all the 45 modules covering all PMTs are then added together, in order to have a single analog signal including the information of the total energy deposition in the CB. This value is called the CB Energy Sum (E_{sum}) and a threshold on this value is the standard trigger of the CB. In Fig. 3.28 a diagram of the CB trigger electronics is shown.

An additional contribution for the trigger can be set for TAPS. TAPS is divided into 6 sections, as shown in Fig. 3.24. If any crystal in the section records an energy deposition above a set threshold, a multiplicity event is recorded. As discussed in Sec 3.4.3, when TAPS is included in the trigger logic the Čerenkov detector is used for vetoing the electromagnetic background.

For this experiment the trigger was set using both a threshold for the CB E_{sum} and TAPS multiplicity.

Dead Time

When an event satisfies the trigger conditions, the data acquisition is busy to processing and recording the information from the ADCs, as well as from the TDCs, for that particular event. During this operation the trigger logic is inhibited to avoid interferences that could alter this information. The system is then

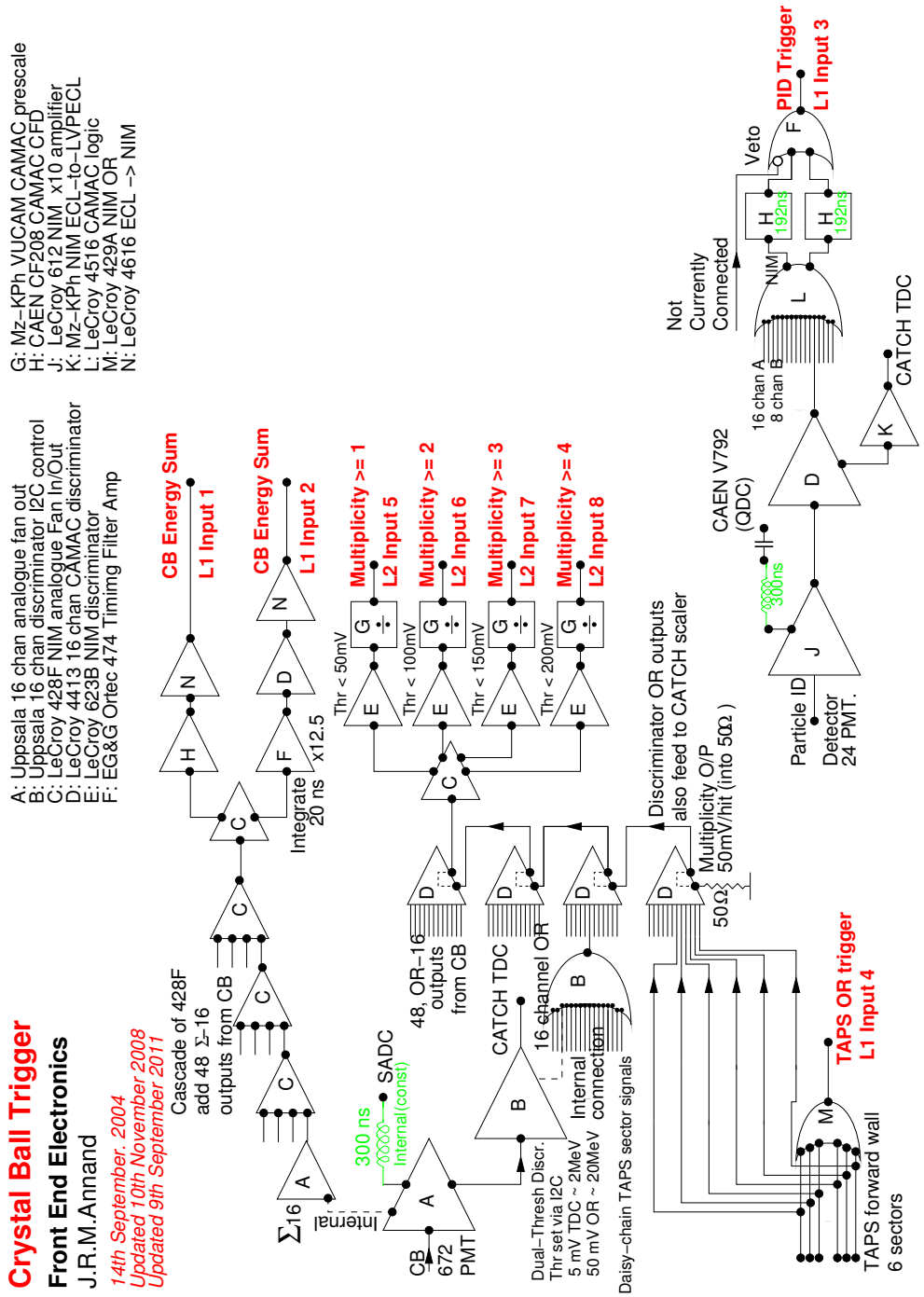

Figure 3.28: CB trigger electronics. Picture from [89].

blind to any additional event; this time window is called 'dead time'. However, the tagger VUPROM scalers are not inhibited and they continuously count the number of the electrons impinging on the focal plane detector. The correct evaluation of the 'dead time' is then crucial for cross section measurements.

3.7 Beamtimes

For the experiment of this work, data from four different beamtimes have been analyzed, two with a polarized deuterated butanol target (with two different doping in the target material) while the other two with a carbon target.

Due to improvements and maintenance, the setup of the experiment was not exactly the same for all the beamtimes. In particular between January 2014 and November 2015 several upgrades were performed on the experimental equipment, resulting in a change of CB configuration, in particularly regarding the number and position of out-of-order channels. The different configuration affects the Carbon subtraction, as later explained in Sec. 5.7. The main parameters and differences of the different data taking periods are listed in Tab. 3.3.

Table 3.3: Experimental setup of the beamtimes analyzed in this work. The effect of the different CB/PID configuration affects both the simulation (see 5.6) and the carbon background subtraction (see 5.7).

	Dec. 2013	Jan. 2014	Oct. 2015	Nov. 2015
Target	Carbon	D-butanol	Carbon	D-butanol
Electron beam energy	1557 MeV	1557 MeV	1557 MeV	1557 MeV
Time of data on disk	85 h	380 h	95 h	194 h
Electron beam current	2.5-3.3 nA	1-2 nA	2.5-3.3 nA	2 nA
Electron beam pol	–	73%−80%	–	71%−75%
CB E_{sum}	$>$ 40MeV	$>$ 40MeV	$>$ 60MeV	$>$ 60MeV
Radiator	Møller & diamond	Møller & diamond	Møller & diamond	Møller
Max target polarization	-	±60%	-	+25%
Helium around the target	No	Yes	Yes	Yes
Collimator diameter	2 mm	2 mm	2 mm	2 mm
CB/PID configuration	A	A	B	B

Chapter 4

Data Analysis I

This chapter describes the software used in this work. It presents the first steps of the analysis, including the use of a cluster algorithm to identify the particle tracks in the detectors, as well as their calibration, and the background subtraction of random events. These steps are standard for any measurement in the A2 experimental hall.

4.1 Software

All of the code used for this analysis is written in C++, and based on the ROOT analysis framework from CERN [90].

The main software of A2 is AcquRoot. Besides being the software of the online data acquisition, it also analyzes the hits in the detectors and extracts the physical parameters of the detected particles from the digital signals recorded by the DAQ [88]. The software for calibration (CaLib) and for Monte Carlo simulation of events (A2Geant) are also written in C++. Furthermore, AcquRoot can also be used for event selection and physics analysis, but for this task the more flexible framework GoAT (Generation of Analysis Trees) was preferred [91].

4.1.1 AcquRoot

AcquRoot is a set of tools for the acquisition and analysis of the data collected in physics experiments. Developed by John Annand at the University of Glasgow [88], it is an object oriented framework, written in C++ and based on the

libraries of the CERN analysis framework ROOT [90]. It consists of three main components: AcquDAQ for data acquisition, AcquRoot for data analysis, and AcquMC for Monte Carlo event generation.

With AcquRoot, it is possible to process the raw data coming from the front-end electronic modules and saved by AcquDAQ in order to extract physical information. Every detector of the A2 experimental setup is modeled, with its own specific properties and features, into a specific class. AcquRoot allows access to physical quantities such as energy from the ADCs, time from the TDCs, as well as the coordinates from the position of the detector elements involved in the detection.

Because a detected particle can hit multiple detectors, and because it usually fires multiple elements in each detector, it is crucial to assign to each particle all of its own detectors hits. AcquRoot includes an algorithm to regroup the information from several nearby elements of each detector, and a class to create a particle track combining the information from different detectors. More details are given in Sec. 4.2 and 4.3, respectively.

An ADC (or a TDC) provides the information about the energy E (or time T) which can be described using the following equations:

$$\begin{aligned} E &= a_E(A - P) \\ T &= a_T(A - O) \end{aligned} \tag{4.1}$$

where A is the amplitude recorded by the ADC (or the time interval given by the TDC) signal, P is the pedestal of the ADC (O is offset of the TDC), and a_E (or a_T) is the linear gain factor converting the digital values into energy (or time). The calibration procedure for the detectors, described in Sec. 4.4, determines the values for the gain factors, the pedestals and the time offsets of the detectors.

AcquRoot was used for the purpose of this work only to generate the trees for GoAT, the software used for the physics analysis. The output trees from AcquRoot contain all the event-by-event information about particle tracks (energy, time and coordinates), trigger, tagger and beam polarization.

AcquMC was used for Monte Carlo event generation to simulate π^0 photoproduction from the nucleon and its decay. The interaction between the particles and the experimental setup was performed using A2Geant, described in the following section.

4.1.2 A2Geant

The A2Geant software was developed by the photo-nuclear group of the University of Edinburgh and it uses the Geant4 CERN simulation libraries [92]. It includes the modeling of the targets and detectors, with their geometrical and physical properties. It simulates the interaction between the detectors and the particles generated by AcquMC. The output of A2Geant is then analyzed with the AcquRoot and GoAT codes, using the same procedure as for normal data.

Simulations were performed to determine the reconstruction efficiency, described in Sec. 5.6, to check the carbon background subtraction, Sec. 5.7, and to evaluate the double pion contamination in the cross section, Sec. 5.8.2.

4.1.3 CaLib

The values of the gains, ADC pedestals, TDC offsets and the relative position of some detectors can change over time. This is because they depend on environmental conditions, such as temperature and humidity, or on setup condition, such as thresholds and supply voltages. Hence, for every dataset these values must be determined using a dedicated procedure. The software to calibrate the detectors and to extract the correct parameters is CaLib, a program developed by the photo-nuclear group of the University of Basel. The raw particle track information is analyzed by the AcquRoot physics class TA2MyCaLib with rough calibration parameters. The output of the TA2MyCaLib class is a set of histograms that are used as input for CaLib, which produces a new set of calibration parameters.

For some parameters one single run of CaLib is enough to determine the correct values, for others it is necessary to perform several iterations to obtain the final calibration set.

Because some parameters and detectors are related to each other, the calibration algorithm must follow a specific order. Sec. 4.4 describes the calibration performed for this work.

4.1.4 GoAT

GoAT (Generation of Analysis Trees) is an extension of AcquRoot. It is a recent development that aimed at overcoming the lack of flexibility of AcquRoot

physics classes. It consists of two parts: the first one, its main core, processes the events and offers several options for particle identification, meson reconstruction and sorting of events. The second one includes the physics classes needed to finalize the analysis.

In this work, this first part was used to select the events with the number of particle tracks for each event and, among them, the ones where it was possible to reconstruct only one π^0. The physics classes included in the second part of GoAT were written so that they included additional cuts (i.e. missing mass and co-planarity cuts), and identify protons and neutrons. The details of the second part are described in Chapter 5.

Finally, GoAT also includes a class to extract the tagging efficiency from the dedicated tagging efficiency data runs.

4.2 Cluster algorithm

A particle interacting inside a calorimeter produces a shower (i.e. secondary particles) that is detected by several elements of the detector. The number of hit crystals depends on the type of particle and on the features of the crystal. The group of individual crystals involved in the energy deposition is called a cluster.

AcquRoot includes an algorithm that provides the identification of the clusters in the CB and TAPS. It starts when a PMT detects an energy deposition above 2 MeV in the CB or above 3 MeV in TAPS. The first step of the algorithm is the selection of the element with the highest energy deposition. It is set as the center of the cluster and its time information is defined as the cluster time. After the completion of the analysis of the neighbor elements around the central one having a deposited energy above 2 MeV, the total energy and the central position of the cluster are assigned.

For the CB, 12 neighbor crystals are taken into account, as shown in the top left of Fig. 4.1.

For TAPS, the analysis of the neighbor elements takes into account the same 'area', but the number of elements can change due to the different size of the $PbWO_4$ crystals. The simplest case is when the highest energy deposition occurs in a BaF_2 crystal, far from the $PbWO_4$ rings. In this case, the algorithm takes into account the 6 elements around the central one, as shown on the top

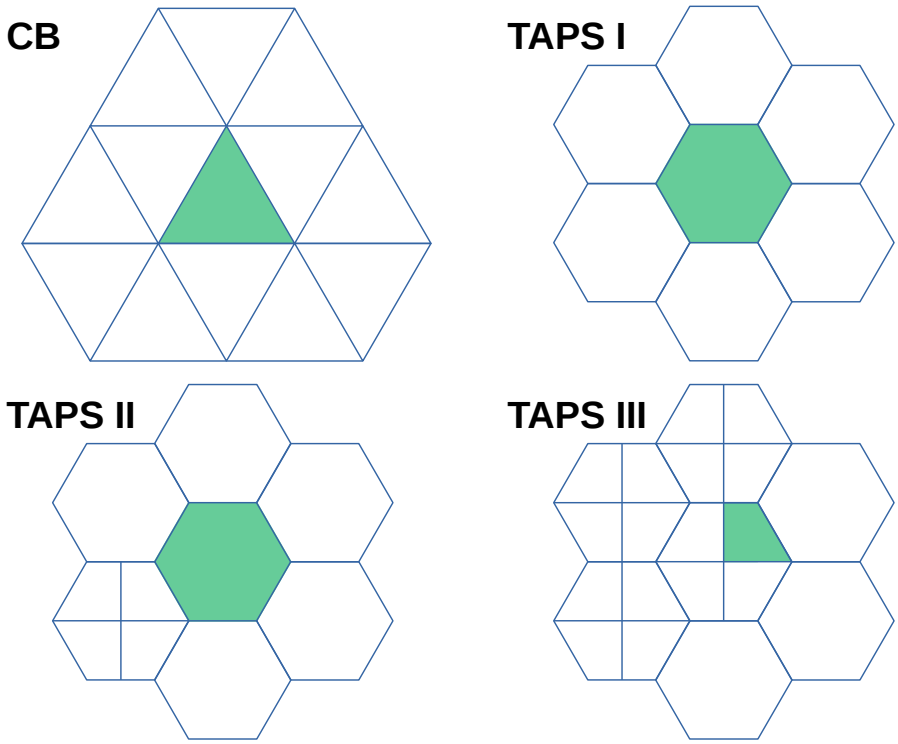

Figure 4.1: Representation of the neighbor elements in the CB and TAPS. On the top: 12 neighbor elements in the CB (left) and the 6 neighbor elements in TAPS (right). On the bottom, neighbor algorithm for $PbWO_4$ elements: in these cases the number of neighbor elements changes due to the different configuration and size of the internal elements.

right of Fig. 4.1. If the energy deposition occurs near, or in one $PbWO_4$ crystal, the number of neighbor elements to consider is larger. Two cases, with 9 or 15 neighbor elements respectively, are illustrated at the bottom of Fig. 4.1.

The elements that form the cluster are removed from the hit list, in order to avoid counting their contribution in more than one cluster. The number of elements that form a cluster is called the cluster size. Once the selection of the cluster elements is completed, the total cluster energy E_{cl} is calculated using the following formula:

$$E_{cl} = \sum_{i=1}^{n} E_i \tag{4.2}$$

where E_i is the energy of the single elements of the cluster. The cluster is saved and taken into account only if the total energy of the cluster is above a

threshold of 20 MeV.

The final step is the calculation of the coordinates of the cluster $\overrightarrow{r_{cl}}$. These are evaluated using the position of the single crystal r_i weighted with a factor $\sqrt{E_i}$:

$$\overrightarrow{r_{cl}} = \frac{\sum_{i=1}^{n} \sqrt{E_i} \cdot \overrightarrow{r_i}}{\sum_{i=1}^{n} \sqrt{E_i}}.$$

AcquRoot runs this procedure over all the possible clusters for each event.

Also in the MWPCs a particle can fire more than one wire or strip, but the events with more than three strips or wires fired are very rare. A simple average of the wires position and a weighted average of the ADCs strips number is evaluated in order to extract the interaction point of the particles.

4.3 Track reconstruction

Once the hits in the elements are grouped in clusters, AcquRoot assigns the clusters from different detectors to the same physical particle track.

For each cluster in the CB, AcquRoot considers all the hits in the PID and calculates the difference in azimuthal angle between ϕ_{PID} and ϕ_{CB}. The PID hit with the minimal difference in azimuthal angle is selected and, if $\phi_{PID} - \phi_{CB}$ is smaller than 15°, the PID hit is assigned to the CB cluster. In this case, the particle track is tagged as a charged track. This track reconstruction is schematically shown in Fig. 4.2.

The same procedure is also iteratively used for the CB and the MWPCs. In this case a condition of ±20° is set for both azimuthal and polar angles.

Even if the events are infrequent, a track can be reconstructed using only the PID and the MWPCs, usually with a ϕ correlation of ±50°. These tracks correspond to very low-energy particles stopped inside the inactive materials surrounding the CB crystals.

For TAPS-Veto the procedure is easier because the elements have the same size and shape, and each Veto element sits just in front of a single BaF_2 TAPS element.

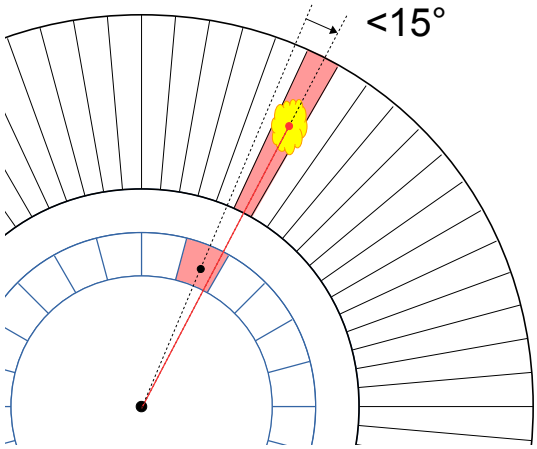

Figure 4.2: Track reconstruction for charged particles grouping the CB and the PID hits.

4.4 Calibration

This section presents an overview of the detector calibration.

The specific order and procedure for the calibration can be found in the CaLib manual [93].

The author performed the calibrations of the two data taking periods with the deuterated butanol target, while the calibrations of data with the carbon target were performed by colleagues at the University of Bonn. The PID energy calibration was performed by colleagues at the University of Edinburgh.

4.4.1 CB

Time calibration

The two parameters needed to convert a TDC signal are the gain and the offset, as described by Eq. 4.1. The gain of the CB TDCs (as well as the PID and tagger TDCs) are set to 117 ns/channel as given by the specifications of the manufacturers, so the offset is the only parameter to be determined in the time calibration procedure.

This step of CaLib calculates the time difference between two neutral hits for any neutral cluster in the CB:

$$\Delta t_1 = t_{\gamma_1} - t_{\gamma_2} = -\Delta t_2. \tag{4.3}$$

This value is plotted for the central element of the cluster, as shown on the left of Fig. 4.3, where the top plot shows the overview over all the CB elements, and the bottom one represents the projection for a single element.

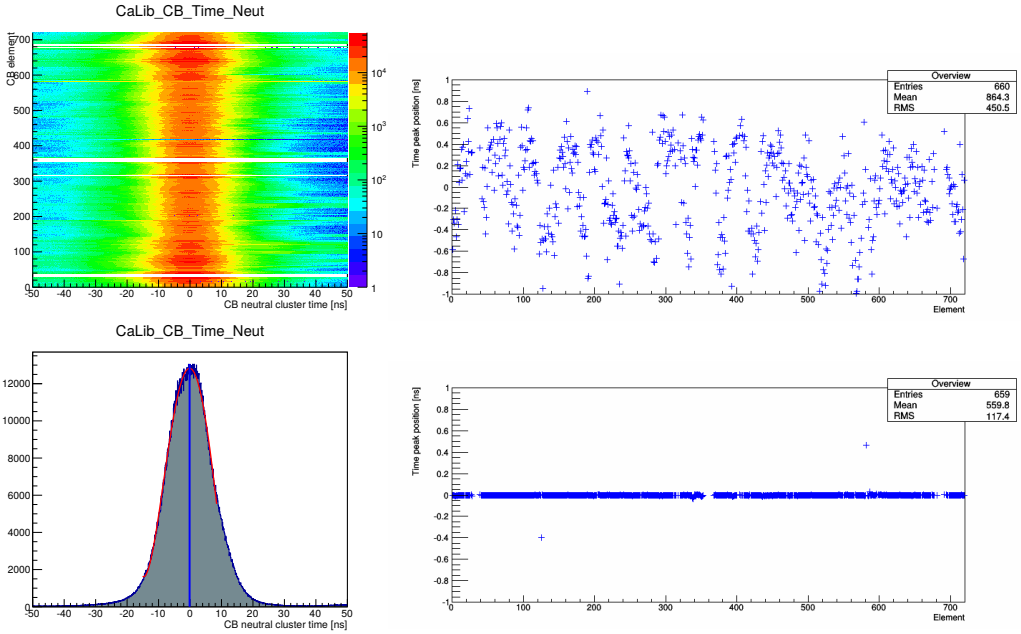

Figure 4.3: CB time calibration. On the left: the distribution of the time difference of two hits in the CB, for all elements (top) and the projection of a single element. On the right: the plots represent the time peak position before (top) and after (bottom) this step.

For each element, the distribution of this value is fitted with a Gaussian, and the resulting mean is the current offset. The old offset is used to calculate the new offset by:

$$O_{new} = O_{old} \frac{mean}{gain}. \tag{4.4}$$

The offset of one element depends on the offsets of the others, for this reason this step must be repeated several times.

The plots on the right of Fig. 4.3 show the time peak position before (top) and after (bottom) the calibration. After this calibration step the time offset is aligned at zero for all the CB elements.

Energy calibration

A preliminary energy calibration is performed placing a $^{241}Am^{9}Be$ source in the center of the CB. This source emits 4.438 MeV photons, and it is used to tune the HV for each PMTs in order to have a calibrated enough output for the Energy Sum going to the trigger. This source calibration is usually performed once a year, or when old or broken PMTs are replaced. Low energy deposition does not allow the evaluation of the gain for events with an energy deposition of several hundred MeV. To overcome this problem, a software calibration is performed after each beamtime, in order to center the 2γ invariant mass peak at the mass of the π^0.

The invariant mass for each pair of neutral hits is plotted against the central crystal of each cluster. The two plots on the left of Fig. 4.4 show the overview plot over all the CB elements (top) and the projection for a single element (bottom).

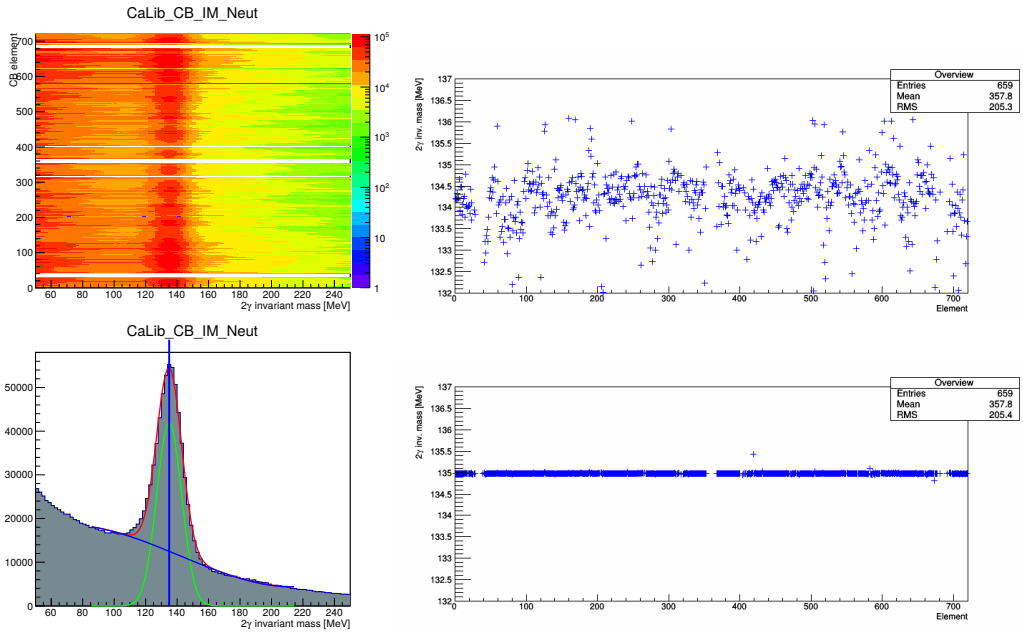

Figure 4.4: CB energy calibration. On the left: invariant mass of two neutral hits in the CB for all the elements (top) and the projection of one element (bottom). The plots on the right represent the 2γ invariant mass position before (top) and after (bottom) the CB energy calibration. After this calibration step the invariant mass peak is centered at the π^0 mass.

The plot for each element is fitted with a Gaussian (for the signal) plus

a negative exponential (for the background), and the new *gain* is calculated using the following formula:

$$a_E^{new} = a_E^{old} \frac{m_{\pi^0}^2}{m_{\gamma\gamma}^2}. \tag{4.5}$$

Because the gain of one element depends on the gains of the others, this step must be repeated several times.

In Fig. 4.4 on the right, the mean of the Gaussian for every channel, before (top) and after (bottom) the calibration, are shown. At the end the invariant mass peak of the 2γ events is aligned at the π^0 mass for all the CB elements.

Time walk calibration

As previously mentioned in Sec. 3.4.1, the NaI crystals of the CB have a slow response time. For this reason the time peak position depends on the amount of energy deposited in that specific element. A two dimensional plot giving the correlation between the time and the energy deposition for a crystal is shown on the left of Fig. 4.5.

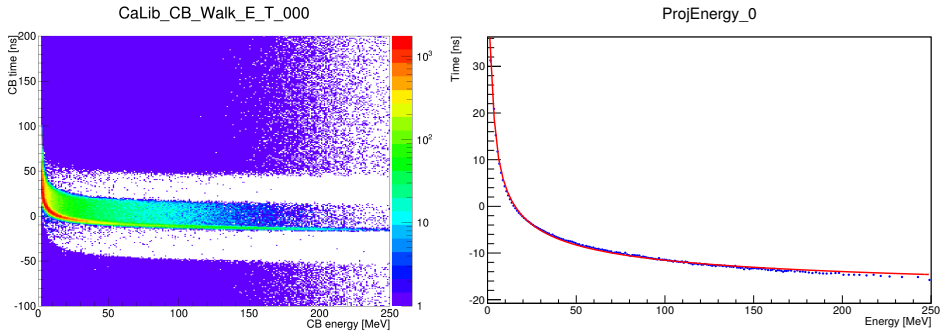

Figure 4.5: CB time walk calibration. The plot on the left represents the time energy distribution of the hits in one crystal. The plot on the right shows final fitting for the time walk calibration of a single element.

The plot is then divided into vertical slices, and each one dimensional slice is fitted with a Gaussian to extract the energy-time dependence plot, as shown on the right of Fig. 4.5. This histogram is fitted using the following function:

$$t(E) = a + \frac{b}{(E+c)^d}, \tag{4.6}$$

where E is the energy deposition and a, b, c, d, are parameters.

After this calibration step, the time information of the CB crystals is no longer related to the energy deposition.

4.4.2 PID

Azimuthal calibration

Because there is not a fixed mechanical connection between the CB and the PID, the evaluation of the ϕ alignment of the PID with respect to the CB is crucial for track reconstruction of charged and neutral particles in the CB.

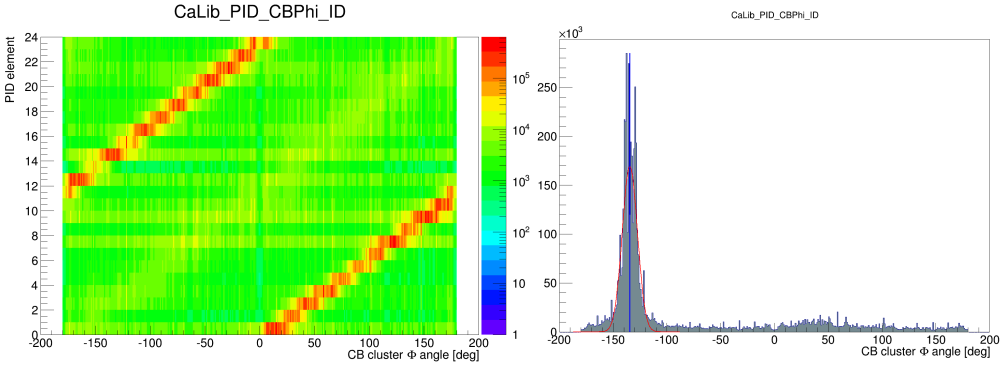

Figure 4.6: PID ϕ calibration. On the left: the events with one cluster in the CB are linked with a hit in a PID element. On the right: fit of the angular distribution in the CB for a single PID element. The small bump shifted 180° from the main peak is originated by the events with two particles, one charged and one neutral emitted back to back.

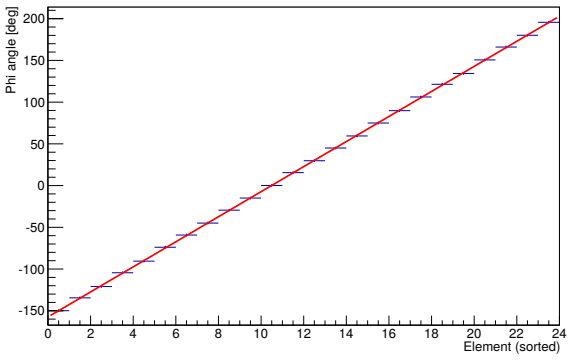

Figure 4.7: Final result of PID ϕ calibration. The ϕ coverage of all 24 PID elements is plotted and than linearly fitted.

The procedure considers only the events with just one cluster in the CB and one PID element in coincidence. For each PID element the distribution of the CB azimuthal angle ϕ_{CB} is plotted and fitted with a Gaussian, as shown on the right plot in Fig. 4.6.

The final correlation between the CB and the PID elements is evaluated using a linear fit of the previously evaluated central azimuthal positions of all 24 PID elements, as shown in Fig. 4.7.

Time calibration

As mentioned before, the TDC gains of the PID are set at 0.117 ns/channel, while the correct offset value has to be determined through calibration. The PID time difference is evaluated using two hits in the PID, and the same procedure is used as for the CB time evaluation described in Sec. 4.4.1. This time difference and the position of the peaks for all the elements of the PID are shown in Fig. 4.8, before (on the top) and after (on the bottom) the calibration.

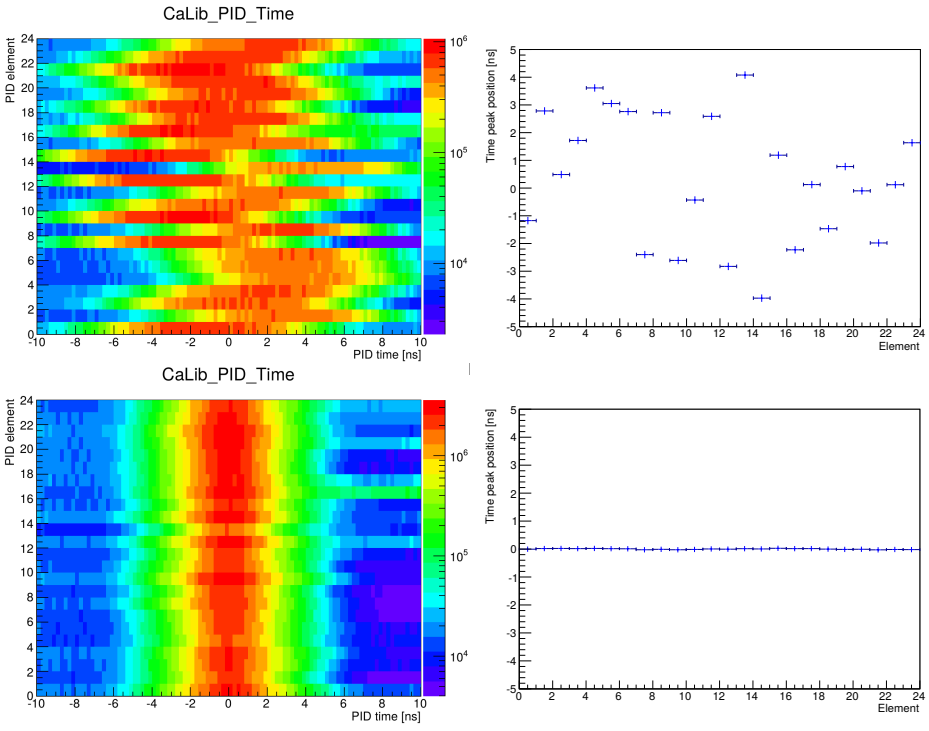

Figure 4.8: Time calibration for the PID. On the top: status before the calibration; on the bottom: results after the calibration.

After this calibration step the time difference for all PID elements is centered

at 0 ns.

Energy calibration

The goal of the PID energy calibration is to have the proton band at the same position as in the simulation. CaLib makes a rough event selection, taking the $\pi^0 p$ events and plotting the $dE - E$ of the charged track with the PID ADC raw information against the CB energy deposition. The projections of these histograms and the ones of simulation are plotted and fitted with a Gaussian. The proton position from simulation and from data are linearly fitted in order to match the positions of the two proton ridges.

Due to an ADC readout error during the January 2014 beamtime, the energy response of the PID for that data taking was very poor. Therefore, the PID was used only for charged/neutral track separation and no selection conditions were based on it [94]. After a repair, the PID functioned correctly during the November 2015 beamtime and could therefore be used as a reference and cross check for setting the selection and the condition on the CB cluster size analysis. A more detailed description will be given in Sec. 5.2.

4.4.3 TAPS

Time calibration

As previously mentioned, thanks to the high time resolution of the BaF_2 crystals, a time of flight analysis can be applied to the TAPS signals. For this reason the time calibration of TAPS is particularly important. The gain of the TDCs is determined by the colleagues at the University of Basel before the data taking, by comparing the readout using different delay cables during a data taking performed using cosmic rays.

The calibration of the offset is performed with the same procedure described for the CB time calibration, and the corresponding plots are shown in Fig. 4.9.

Thanks to the fast response of the BaF_2 crystals, the time walk calibration is not necessary for TAPS.

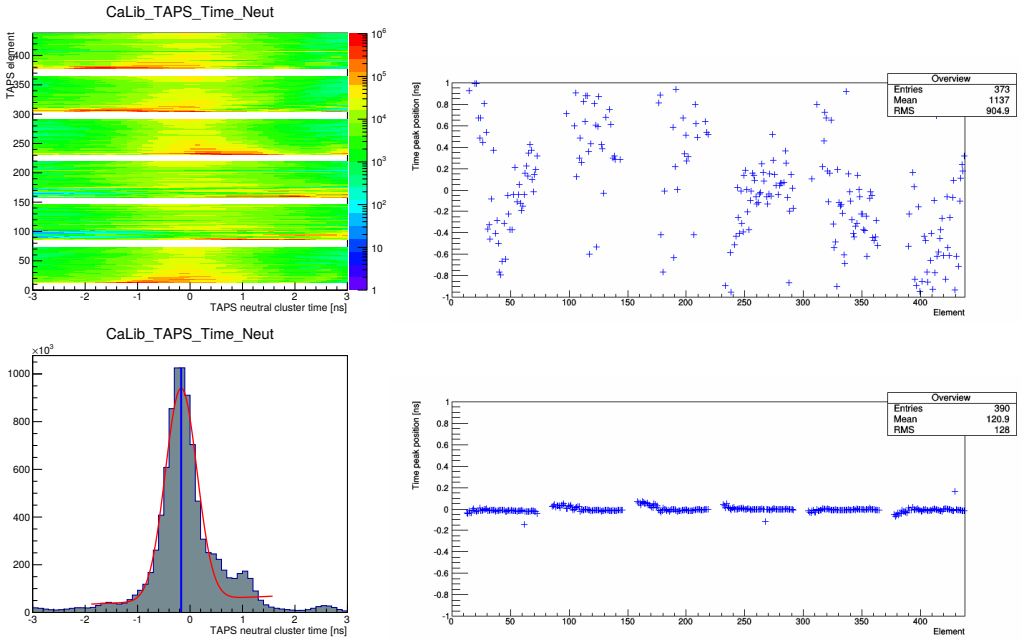

Figure 4.9: TAPS time calibration for the TDC offset. On the left: the distribution of the time difference of two hits in TAPS for all the elements (top) and the projection of one of them (bottom). On the right: the peak position before (top) and after (bottom) this step.

LG energy calibration

The Long Gate (LG) energy calibration of TAPS is equivalent to the CB energy calibration, and the relative procedure is the same. The LG component includes the total energy information from the integral of the TAPS ADCs. Because of the low statistics of events with two neutral tracks in TAPS, the 2γ invariant mass is calculated using one neutral hit in the CB and one neutral hit in TAPS. The corresponding histograms are shown in Fig. 4.10.

SG energy calibration

The Short Gate (SG) is the energy information from the integral of the TAPS ADCs over a shorter time range than the LG signal, including only the fast signal component from the BaF_2. The LG and the SG signals can be combined in order to define the angle and the radius for the Pulse Shape Analysis (PSA) for hadron identification:

$$\phi_{PSA} = \arctan \frac{E_{SG}}{E_{LG}}, \tag{4.7}$$

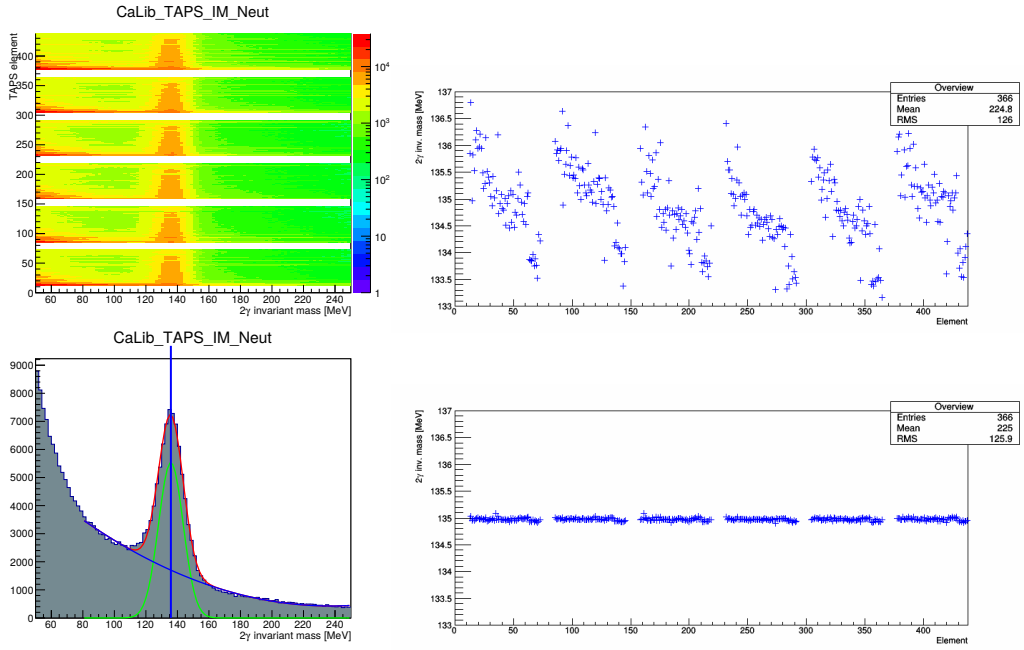

Figure 4.10: TAPS LG energy calibration. On the left: the invariant mass of two neutral hits (one in the CB and one in TAPS) for all the TAPS elements (top) and the projection of one of them (bottom). On the right: the 2γ invariant mass before (top) and after (bottom)of the LG energy calibration. After several iterations, the invariant mass peak is centered at the π^0 mass.

$$r_{PSA} = \sqrt{E_{SG}^2 + E_{LG}^2}. \tag{4.8}$$

Because the photon energy deposition inside the BaF_2 is very fast, their SG and LG contributions are the same. The goal of the SG energy calibration is to have the photon contribution for the ϕ_{PSA} sitting at 45°. For each element, CaLib produces a 2-D plot with PSA angle and radius, and it creates two projections for different PSA radius values, as shown in Fig. 4.11. More details about the PSA are given in Sec. 5.2.

These two plots are fitted each with a Gaussian and, from the average of the two means, the new gain values are calculated.

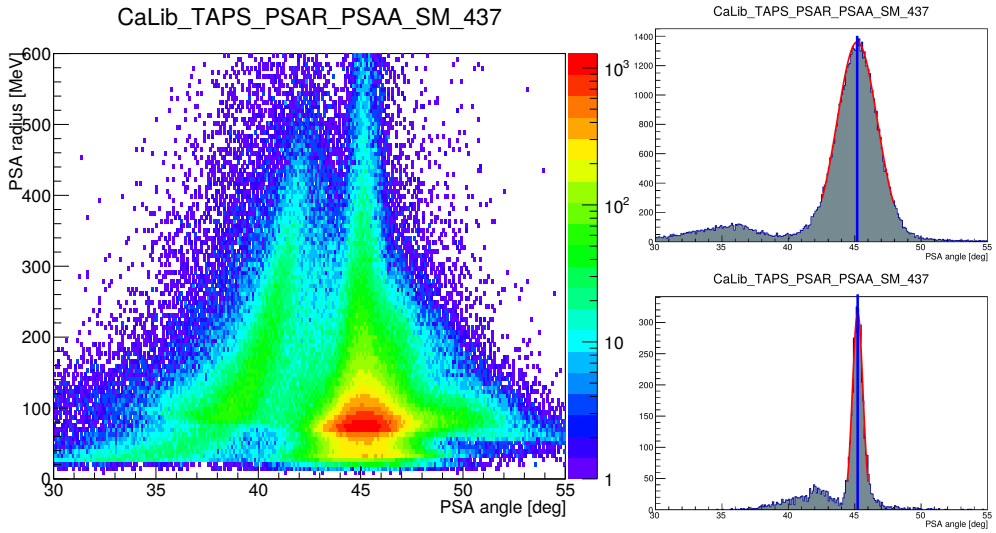

Figure 4.11: SG energy calibration for one element. On the left: plot with the PSA radius and angle. On the right: projections at low {0-50} (top) and high {500-600} (bottom) value of PSA radius.

4.4.4 Veto

Time calibration

For the Veto time calibration the only parameter to be determined is the offset, because the hardware gains are set at 0.05 ns/channel. The procedure is the same as used for the CB time calibration, i.e. CaLib creates a 2-D plot with the time difference between two hits against the Veto element. The projections for each element are fitted with a Gaussian function, as shown in Fig. 4.12.

Energy calibration

The Veto energy calibration is very similar to the PID energy calibration, with an aim to have the proton band in the same position as given by the simulation. CaLib plots the $dE - E$ histogram for TAPS-Veto, and it calculates the new gain by comparing the proton band position from data and from simulation. Due to its low energy resolution, the Veto energy information was only used to cut the electron background and not for a proton selection, as discussed in Sec. 5.2.

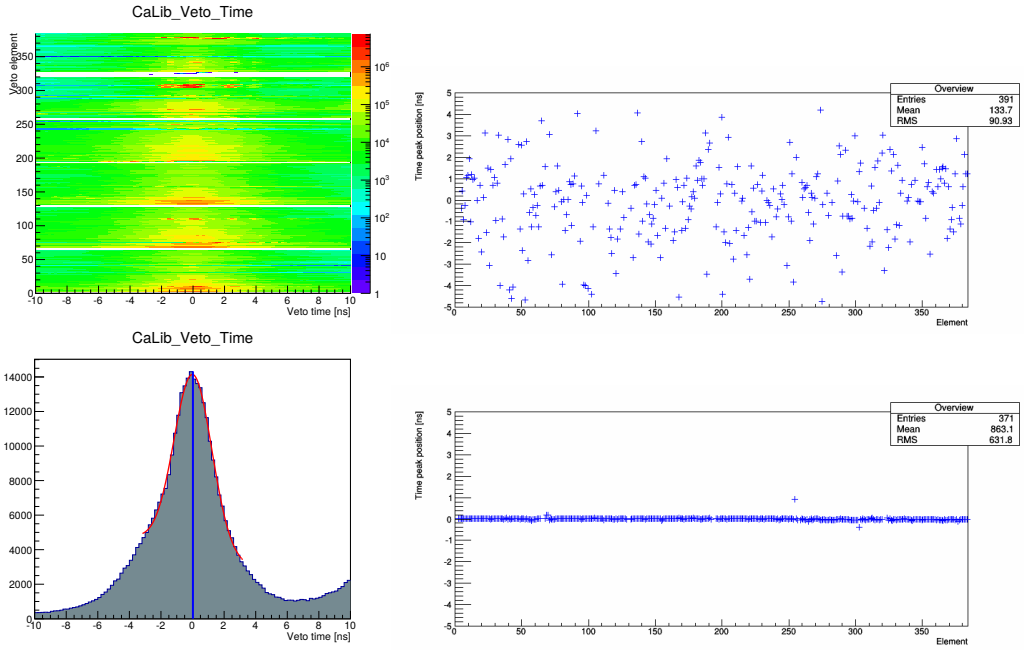

Figure 4.12: Veto time calibration. On the left: the time difference distribution of two hits in the Veto, for all the elements (top) and the projection of one element (bottom). On the right: the peak position before (top) and after (bottom) the calibration.

4.4.5 Tagger

Time calibration

As mentioned before, the gain of the tagger TDCs are hardware set at 0.117 ns/channel, hence the offset is the only parameter to be evaluated with the software calibration.

The time difference between the tagger hits and a reference time from the detector hits is plotted for each tagger channel. For a time reference only the neutral hits in TAPS are used, due to the better time resolution in TAPS, and to avoid slow particles as such protons.

The resulting plot for all the tagger elements and for the projection of one element are shown on the top and bottom plots on the left of Fig. 4.13, respectively. The projections are fitted with a Gaussian function and the resulting peak positions are plotted on the right of Fig. 4.13 before (top) and after (bottom) the calibration procedure. Since the time difference depends only on TAPS time, it needs to be done after the TAPS time calibration and only one

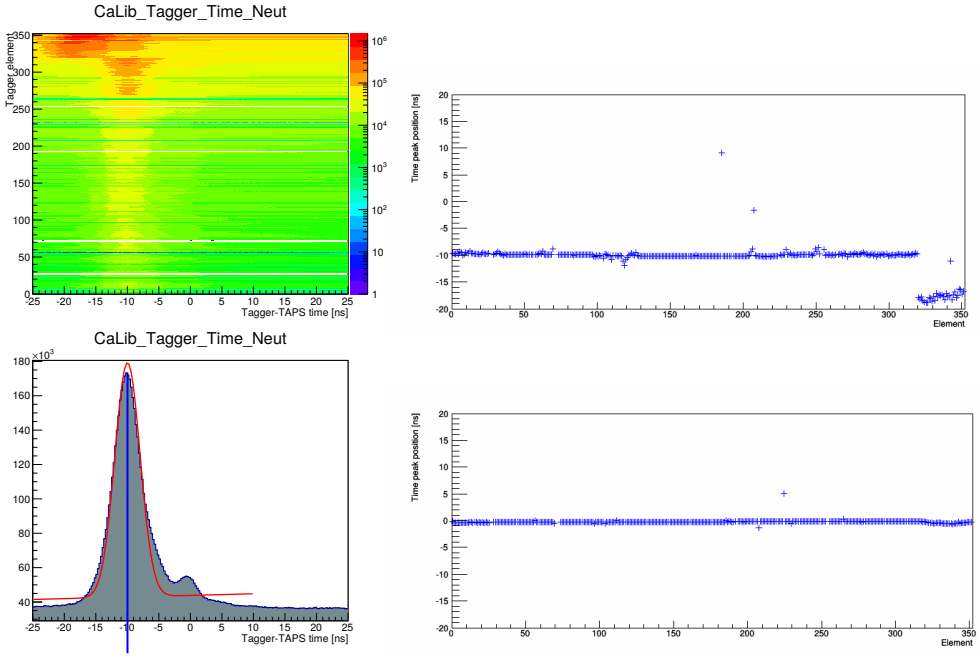

Figure 4.13: Tagger time calibration.

iteration is necessary and the result gives the offsets for the tagger TDCs.

4.4.6 Target position

The calibration of the target position is performed with two different methods: one with the MWPCs and one with CaLib.

The first method considers the measurement of the vertex coordinates using two charged tracks in the MWPCs. It is mainly used to verify the target position on the Z axis, as shown in Fig. 4.14, but it also provides information about the X and Y axes. If the shift from 0 is sizable (> 0.5 cm), the CB is moved in order to set the target vertex on the origin. This is one of the standard checks performed at the beginning of every data taking period.

The second method to determine the target position is a class inside CaLib. This procedure consists of evaluating the 2γ invariant mass for different assumed positions of the target, as shown in Fig. 4.15.

The projections for different target positions are fitted with a Gaussian, and the variances are plotted on the right of Fig. 4.15. This plot is fitted with a polynomial function, and the minimum gives the position of the target center.

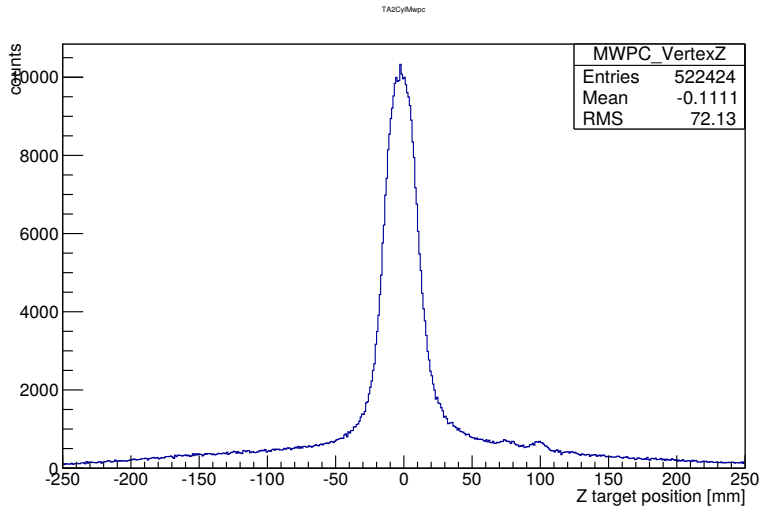

Figure 4.14: Z vertex position evaluated from events having two charged tracks as measured with the MWPCs.

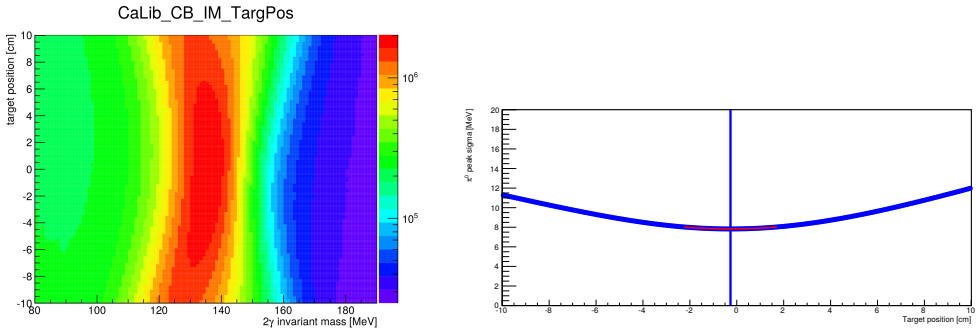

Figure 4.15: Target position calibration performed with CaLib.

4.5 Random background subtraction

When the trigger enables the data acquisition, the tagger detects many electrons in the allowed time window of each event, due to the high rate of the electron beam. Among these electrons, it is necessary to identify the one linked to the photon that induced the triggered reaction, in order to know the event energy.

With the setup for this work, an average of 40-50 electrons are recorded for each event, as shown in Fig. 4.16.

For each electron, the time difference between the trigger time and the tagger time is evaluated:

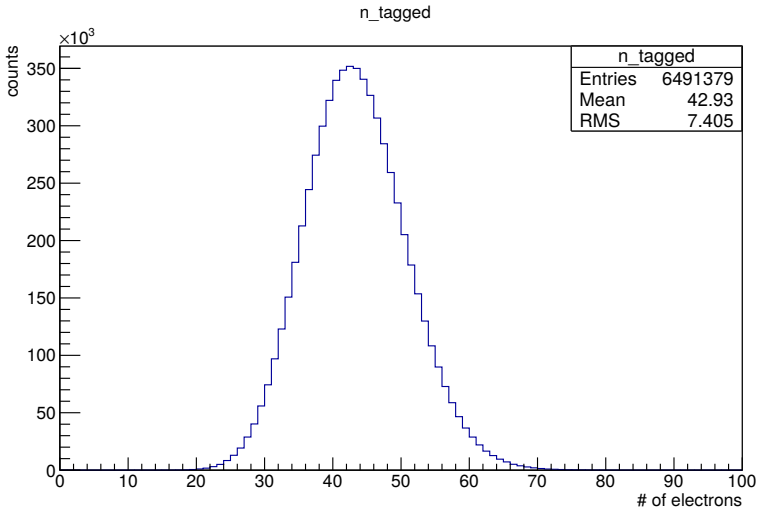

Figure 4.16: Number of electrons detected for each event.

$$\Delta T = T_{trigger} - T_{tagger}. \tag{4.9}$$

The distribution of this variable is shown in Fig. 4.17. The events with a real time coincidence between CB/TAPS and the tagger signals are located around $\Delta T = 0$, where a peak is clearly present. These events are referred to as 'prompt' events, while the events outside the peak region are 'random' events.

Not every event in the peak is a 'good' event because in this time region a random contribution is also present. Before proceeding with the background subtraction, three time windows are selected: two in the random region Δt_{rnd1} and Δt_{rnd2} (the red areas in the figure) and one prompt region Δt_{promt} (the green area).

Because the random coincidence distribution is flat, the number of good events N_{result} can be evaluated using the following relation:

$$N_{result} = N_{prompt} - N_{rnd1+rnd2} \cdot \frac{\Delta t_{promt}}{\Delta t_{rnd1} + \Delta t_{rnd2}}, \tag{4.10}$$

where N_{promt} is the number of events in the prompt region Δt_{promt}, and $N_{rnd1+rndm2}$ is the number of events in the two random region $\Delta t_{rndm1} + \Delta t_{rnd2}$.

The prompt and random time windows are not the same for all beamtimes, but their ranges are tuned for each data set.

The background subtraction is by default implemented inside GoAT; a rou-

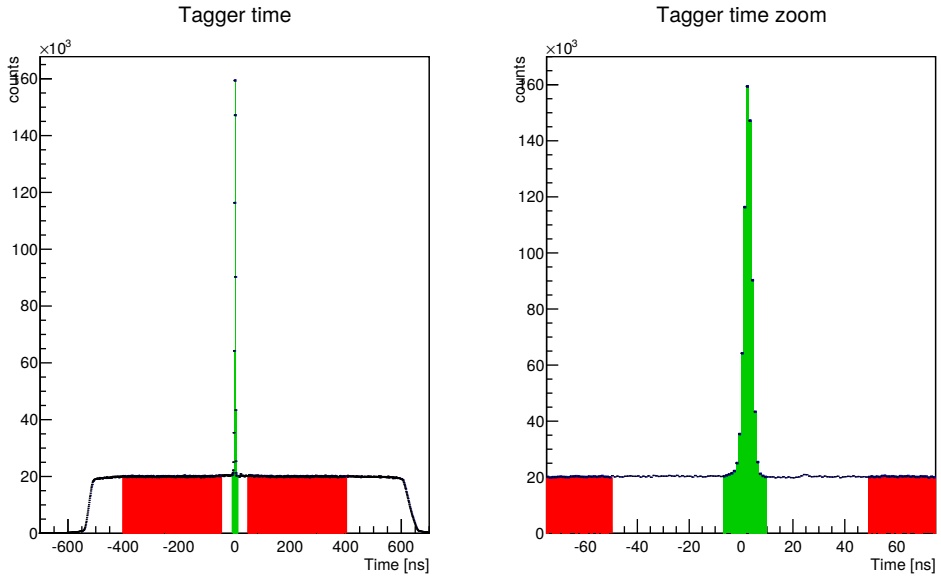

Figure 4.17: Time distribution of the electrons in the tagger. The events with a real coincidence between tagger and CB/TAPS signals are located in the peak region around $\Delta T = 0$, while the flat base is due to background events. The green and the red areas define the 'prompt' and 'random' windows, respectively.

tine separates particles having signals in the 'prompt' and 'random' windows for each event.

Chapter 5

Data Analysis II

This chapter focuses on the event selection and physics analyses that were performed to derive the inclusive helicity dependence of single π^0 photoproduction cross section on the deuteron and the two exclusive channels of the single π^0 polarization observable E from quasi-free protons and quasi-free neutrons.

The selection of the events having only one photoproduced π^0 in the final state is described in Sec. 5.1. The proton and neutron identification is described in Sec. 5.2. The tagging efficiency calculation and the evaluation of the simulated efficiency of the experimental setup are described in Sec. 5.1 and in Sec. 5.2, respectively. These two parameters are crucial for the cross section evaluation. The determination of the contribution due to the carbon and oxygen nuclei inside the butanol molecule, essential for the calculation of the E observable, is described in Sec. 5.7. Finally, the last section of this chapter discusses the statistical and systematical errors.

5.1 Single π^0 events selection

The π^0 meson has a very short lifetime, $8.52 \pm 0.18 \cdot 10^{-17}$ s, and it decays dominantly into a pair of photons with a branching ratio of $98.823 \pm 0.034\%$ [9]. The high detection efficiency of the CB-TAPS apparatus allows a precise measurement of their emission parameters.

In the first step of the analysis, only the events fulfilling the following conditions were processed:

- from two to four hits in both calorimeters,

- an invariant mass (IM) of the reconstructed π^0 included in a window of ± 40 MeV around the nominal value of the π^0 mass 134.9766(6) MeV/c^2 [9],
- missing mass (MM) of the reaction included between 850 and 1050 MeV.

The parameters of these cuts were tuned in order to maximize the selection of π^0 events and minimize the background contributions. They were checked iteratively using both real data and simulated events.

5.1.1 Number of the selected tracks

In the ideal case, single π^0 photoproduction on the deuteron produces three tracks in the calorimeters: two clusters from the photons of the π^0 decay, and one cluster from the participating nucleon.

At low energies, the participating nucleon does not have enough energy to reach the detectors, and only the two photons produce clusters in the detectors. Even if this case is not useful for the E observable measurement, it gives a large statistical contribution to the single π^0 cross section on the deuteron.

On the other hand, a photon can split into an electron-positron pair before entering inside the calorimeters, thus originating two different clusters and hence increasing the number of hits in the detectors. In addition, an electromagnetic shower can occasionally release energy in non-neighbouring crystals, due to far-traveling photons giving rise to two different clusters.

Several different conditions for the number of raw clusters and for the number of reconstructed particles have been tested and checked, both with simulated and real data. The best method found for this work was to analyze events with 2, 3 or 4 clusters.

For the measurement of the E observable, the requirement of the nucleon identification (see Sec. 5.2) obviously excludes the events with only two clusters.

5.1.2 π^0 reconstruction

GoAT includes the GMesonReconstruction class for evaluating the π^0 emission parameters from the clusters of the selected events. The first step of this procedure is the π^0 invariant mass (IM) evaluation by adding the four momenta vectors from all the neutral clusters of the event:

$$m_{\pi^0} = \sqrt{(\sum \overrightarrow{p}_i)^2}, \;\; i = 2, 3, 4. \tag{5.1}$$

If the resulting invariant mass value is included within the predefined limits, the reconstruction is considered successful and the next event is analyzed. The invariant mass window ω selected for this work was ± 40 MeV around the PDG π^0 nominal mass m_{π^0} [9], as shown in Fig. 5.1. This interval was selected after different tests both with simulated and real data. The selected range is quite large in order to minimize the probability of rejecting good events. A non-negligible fraction of the background events are still accepted after this cut, and they are removed in the following step of the analysis. The main sources of background events are: reactions on unpolarized C and O nuclei in the deuterated butanol molecule (only for the E asymmetry measurements, see Sec. 5.7), atom interactions (as Compton scattering, electron-positron pair production) or, double π and η events for $E_\gamma > 400$ MeV.

In particular, the E observable calculation is very sensitive to the background, but the strict conditions applied for the proton/neutron identification guarantee a very good suppression.

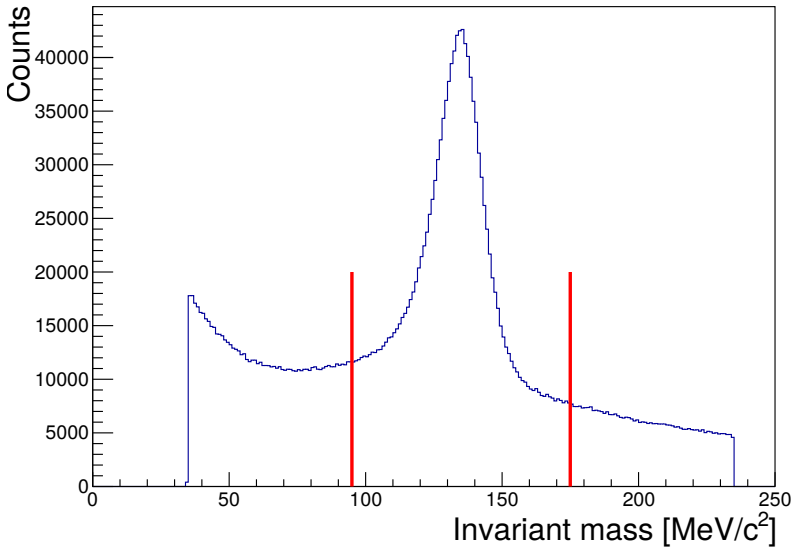

Figure 5.1: Invariant mass distribution for the π^0 reconstruction procedure. The red lines define the ± 40 MeV cut around the nominal m_{π^0} value.

When the previous attempt fails, GoAT calculates the invariant mass of all the possible 2-clusters combinations of the event:

$$m_{\gamma,\gamma} = \sqrt{(\overrightarrow{p}_i + \overrightarrow{p}_j)^2}, \;\; i \neq j. \tag{5.2}$$

Among all the pairs having an invariant mass within the ±40 MeV window, GoAT selects the pair with the best χ defined as:

$$\chi = \frac{|m_{\pi^0} - m_{\gamma,\gamma}|}{\omega}. \tag{5.3}$$

For the case of the few events with four clusters, an additional routine was added in order to check the invariant mass with three clusters.

If the reconstructed π^0 fulfills the invariant mass condition, it is then stored and it proceeds to the next analysis steps.

5.1.3 Missing mass condition

In the following analysis step a cut on the missing mass value (MM) is applied to further reduce the background contribution. At this stage, the possible presence of the nucleon N involved in the reaction has not been checked yet (even if a cluster can be created by it), but its mass can be reconstructed using the 4 momentum vectors of the photon and nucleon in the initial state and of the reconstructed π^0. The momentum and energy conservation laws for the $\gamma + N \rightarrow \pi^0 + N$ reaction can be written as:

$$(\overrightarrow{p_\gamma}, E_\gamma) + (\overrightarrow{p_N}, E_N) = (\overrightarrow{p_{\pi^0}}, E_{\pi^0}) + (\overrightarrow{p_{N'}}, E_{N'}) \tag{5.4}$$

where $(\overrightarrow{p_\gamma}, E_\gamma)$ and $(\overrightarrow{p_N}, E_N)$ are the 4 momentum vectors for the photon and the rest nucleon in the initial state, respectively. The $(\overrightarrow{p_{\pi^0}}, E_{\pi^0})$ vector describes the reconstructed π^0 while $(\overrightarrow{p_{N'}}, E_{N'})$ describes the momentum of the missing nucleon. The value of the missing mass is then calculated as:

$$m_{MM} = \sqrt{(E_\gamma + m_N - E_{\pi^0})^2 - (\overrightarrow{p_\gamma} - \overrightarrow{p_{\pi^0}})^2}. \tag{5.5}$$

The distribution of calculated missing mass values, shown in Fig. 5.2, is expected to be centered around the nominal nucleon mass. The one-dimensional missing mass distribution is presented on the left, while on the right it is shown as a function of tagger channel number (the relation between tagger channel number and photon energy is given in App. C.).

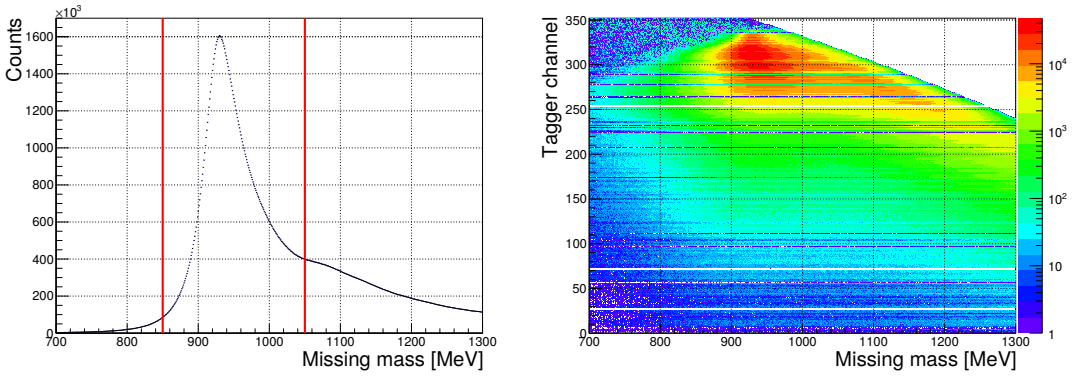

Figure 5.2: Missing mass distribution of the selected π^0 events after the first analysis step. The left plot shows the distribution for all photon energies, while on the right the distribution for each tagger channel number is given. The relation between tagger channel and photon energy is presented in App. C. The red lines define the MM cut applied afterwards.

A cut is applied to the missing mass distribution, in order to reduce the background contribution. Only the events with a missing mass value between 850 and 1050 MeV are taken into account for the next analysis steps.

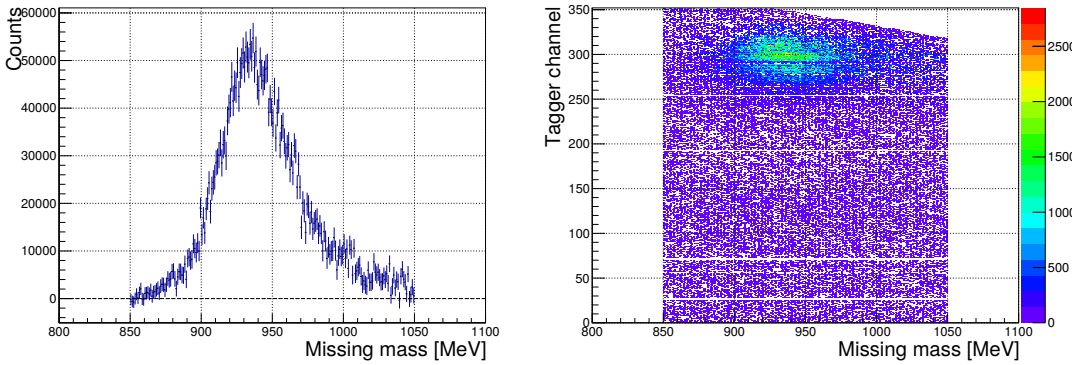

Figure 5.3: Helicity difference of the missing mass distribution after the MM cut. The left plot shows the distribution for all photon energies, while on the right the distribution for each tagger channel number is given.

As it can be clearly seen from Fig. 5.2, a relevant background is still present after the first analysis step, in particular on the right side of the peak. This is mainly due to the presence of the carbon and oxygen nuclei in the butanol molecule. The difference between the missing mass distributions of the parallel and anti-parallel event configurations (that is needed for evaluating the numerator of Eq. 2.52) allows a verification of this hypothesis since all the non-

polarized contribution vanishes. In Fig. 5.3, it is clear that the background on the right tail of the distribution almost completely disappears in the helicity difference.

The event selection for the calculation of the helicity dependent single π^0 cross section on the deuteron is completed and it does not need any additional cut nor condition to be applied, but it requires the tagging efficiency measurement and the efficiency simulation, presented in Sec. 5.3 and 5.6, respectively.

5.2 Proton and neutron identification

In order to extract the E observable for the $p - \pi^0$ and for the $n - \pi^0$ final states, it is necessary to properly detect and identify one proton or one neutron in addition to the π^0.

The analysis steps described in this section focused on the events having one additional track not previously used for the π^0 identification. The first step is to remove the events where this track is not coplanar with the reconstructed π^0. The particles that are coplanar with the π^0 are 'good candidates' to be a proton (if charged), or neutron (if neutral). Additional conditions are also applied to properly select only the tracks generated by a nucleon. Finally, additional checks are performed in order to verify the validity of the previous steps.

The cleanness of the nucleon selection from any background is crucial for a reliable calculation of the E observable. Hence the cuts and the conditions for proton and neutron identification were redundant and strict.

As before, different selection criteria were tested, but only the algorithm that was finally selected is described in this thesis.

5.2.1 Coplanarity cut

Due to momentum conservation, the incident photon, the π^0 and the recoil nucleon lie in the same plane as shown in Fig. 5.4.

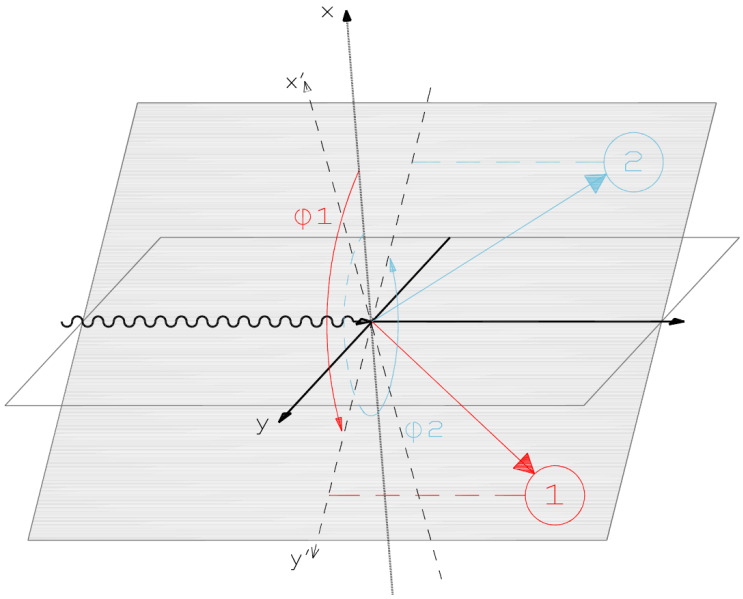

Figure 5.4: Diagram of the π^0 production. The photon, the π^0 and the recoil nucleon lie in the same plane.

The difference between the azimuthal angles ϕ of the π^0 and of the recoil nucleon is calculated as follows:

$$\Delta\phi_{\pi^0 N} = \begin{cases} \phi_{\pi^0} - \phi_N & \text{if } \phi_{\pi^0} - \phi_N \geq 0^\circ \\ 360^\circ - |\phi_{\pi^0} - \phi_N| & \text{if } \phi_{\pi^0} - \phi_N < 0^\circ \end{cases} . \tag{5.6}$$

The resulting $\Delta\phi_{\pi^0 N}$ distribution is shown in Fig. 5.5. There is an evident peak centered at 180°.

The further analysis only takes into account the events having $140^\circ \leq \Delta\phi \leq 220^\circ$ (called in the next sections 'candidate nucleon' track).

The target nucleon has an initial momentum described by a Fermi distribution since it is not free, but bound inside the deuterium nucleus. This effect gives a non-zero value to the transverse nucleon momentum component, which affects the coplanarity distribution and gives a broader peak than the free proton case.

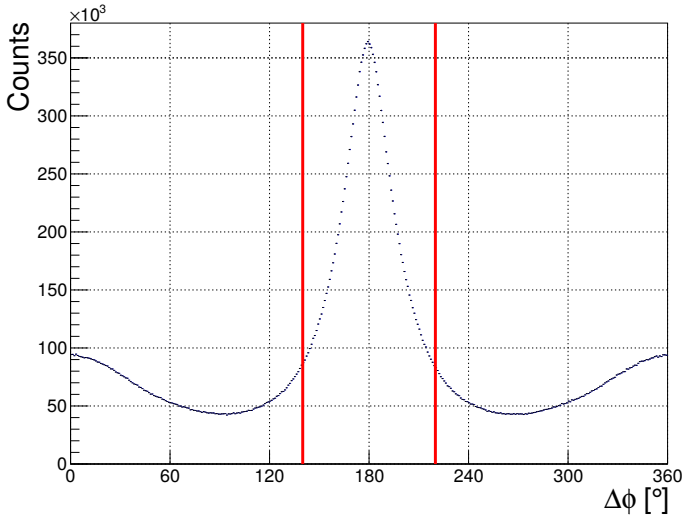

Figure 5.5: $\Delta\phi_{\pi^0 N}$ distribution, the red lines show the cut applied.

5.2.2 CB cluster size

If the candidate nucleon track is detected by the CB, the most powerful tool for nucleon selection is the analysis of the number of crystals (cluster size). This selection is particularly important for the neutral tracks because it allows a separation of photons from neutrons. Due to the reaction kinematics, the nucleons detected in the CB fire only few crystals. This is due to their large θ trajectory angle ($\theta > 20°$), which implies a low kinetic energy (< 100 MeV). On the other hand, the cluster size of photons is much larger due to the larger spread of the electromagnetic shower.

The 2-D plot of the cluster size versus the cluster energy allows identification of two different regions where these two particles are concentrated, as shown in Fig. 5.6.

This 2-D distribution is significantly changed when only the tracks not used for π^0 reconstruction are taken into account. As shown in Fig. 5.7, basically no event now remains in the 'photon' region. This cut was particularly useful to tune the coplanarity cut range.

Therefore the cluster size cut is almost redundant and it just rejects the few events remaining above the red line.

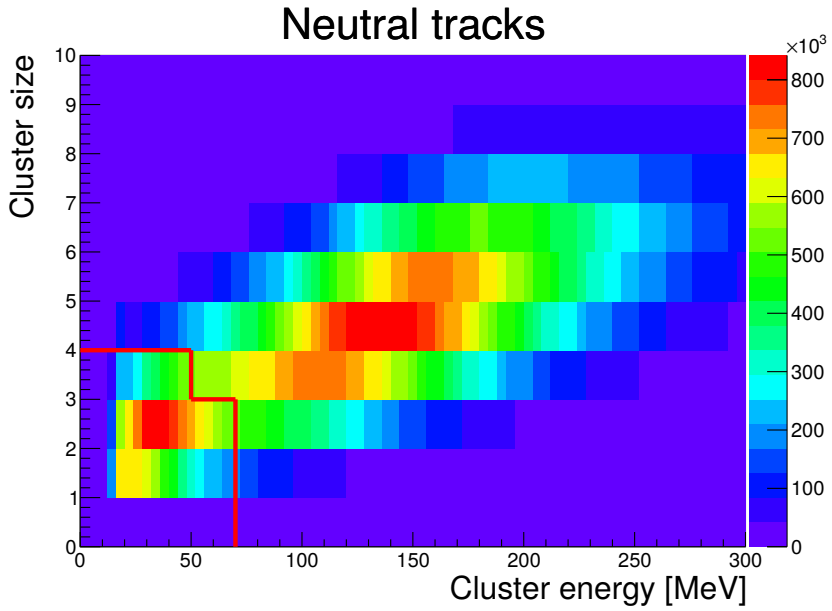

Figure 5.6: Cluster size distribution for all the neutral tracks in the CB at the start of the analysis (before π^0 reconstruction). Neutrons aggregate in the red spot on the bottom left, while photons aggregate around the red spot in the middle of the plot. The tracks below the red line were tagged as neutrons.

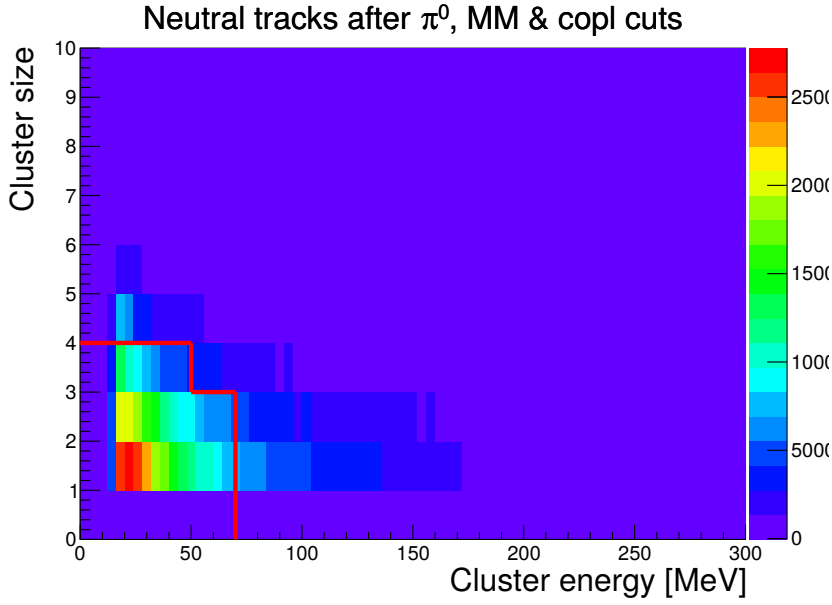

Figure 5.7: Cluster size distribution for neutral tracks in the CB after π^0 reconstruction and coplanarity cut.

5.2.3 PSA in TAPS

As previously mentioned, the signal of the TAPS crystals consists of a 'fast' (short gate, SG) and a 'slow' (fast gate, FG) component. Two variables can be evaluated from their combination: the PSA radius and the PSA angle, described by Eq. 4.8 and 4.7, respectively. The SG and the FG components for light and fast particles such as photons are quite similar, resulting in a PSA angle of about 45°.

The PSA plots for any neutral and charged tracks of the selected events are shown in Fig. 5.8. The particles lying on the left of the red line are neutrons or protons in case of neutral or charged tracks, respectively.

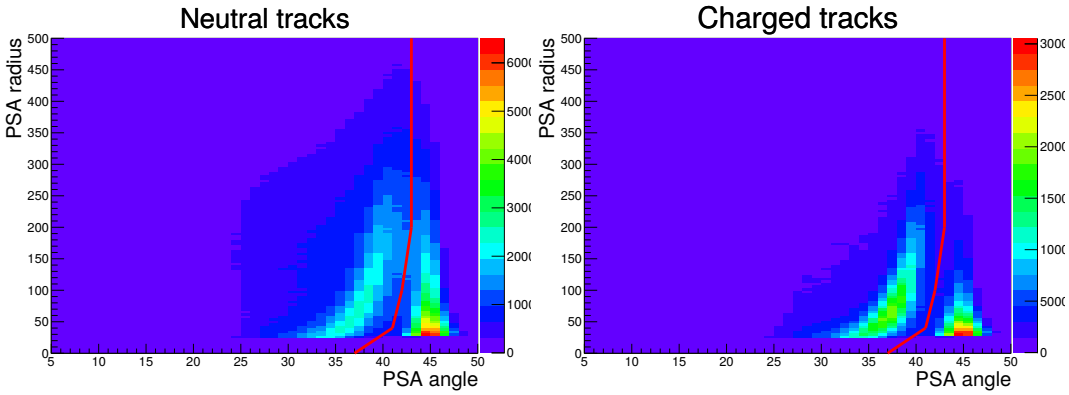

Figure 5.8: PSA plots for neutral (left) and charged (right) tracks before the π^0 reconstruction.

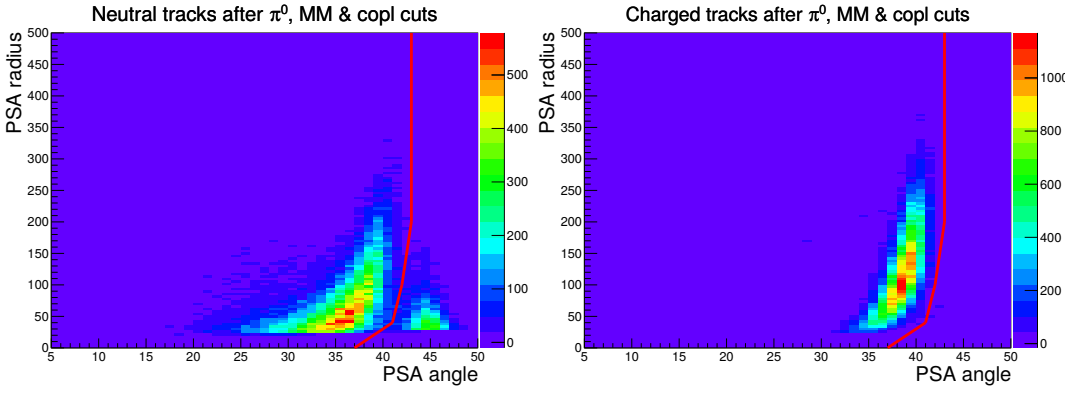

Figure 5.9: PSA plots for neutral (left) and charged (right) tracks after π^0 reconstruction, MM and coplanarity cuts.

If the same plots are filled with only the 'good proton and neutron candidate'

tracks, the light particle background is massively reduced in the neutral case and completely removed for the charged one, as shown in Fig. 5.9. This effect is an additional proof of the efficacy of the previous analysis steps.

All the events having the 'good candidate' track lying on the right of the red line are rejected. This selection is particularly effective to remove the remaining background in the neutral track case.

5.2.4 Time of flight

Due to the combination of a fast response and a large distance from the target center (∼1.8m), the signal from TAPS can be used to perform a time of flight (TOF) analysis. Fig. 5.10 and Fig. 5.11 show the correlation between time of flight and energy deposition for neutral tracks and charged tracks, respectively.

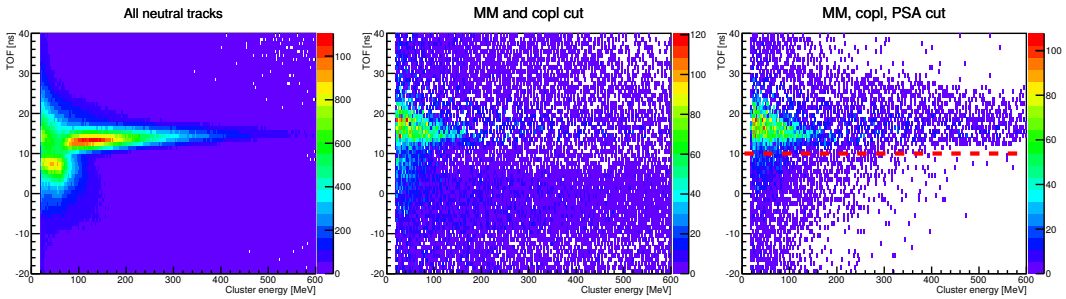

Figure 5.10: TOF for neutral tracks. The plot on the left includes all the neutral tracks before π^0 reconstruction. The central plot shows the tracks after MM and coplanarity cuts. The plot on the right shows the result after the PSA cut.

In both these figures, the left plots are filled with all the neutral (or charged) tracks before π^0 reconstruction. Particles with a TOF higher than 10 ns are hadrons. Photons and electrons have a shorter time of flight. The effect of MM and coplanarity cuts is shown in the central plots. In the right plots the PSA cut is also applied and the tracks below the dotted red line are rejected.

5.2.5 $dE - E$ plot in TAPS

The low energy efficiency of the Veto does not permit an accurate $dE - E$ analysis of the charged particles in TAPS. However, after the PSA cut, the $dE - E$ plot from the Veto and TAPS shows a clean proton band without any

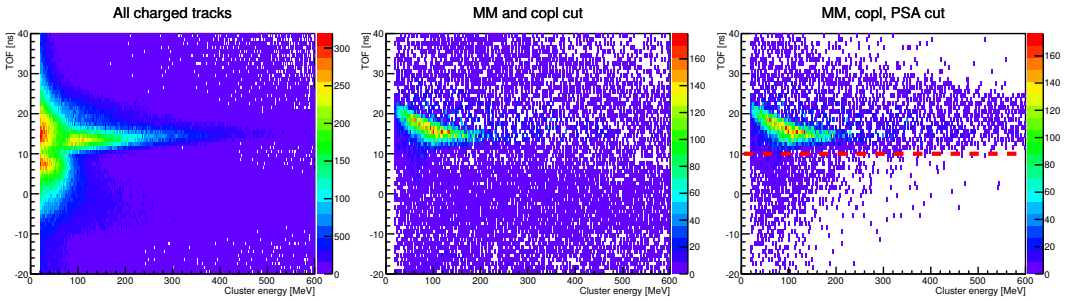

Figure 5.11: TOF analysis for charged tracks. The plot on the left includes all the neutral tracks, before π^0 reconstruction. The central plot shows the tracks after MM and coplanarity cuts. The plot on the right shows the result after the PSA cut.

nearby background. Nevertheless, some 'good candidate' tracks are located in the area usually occupied by electrons.

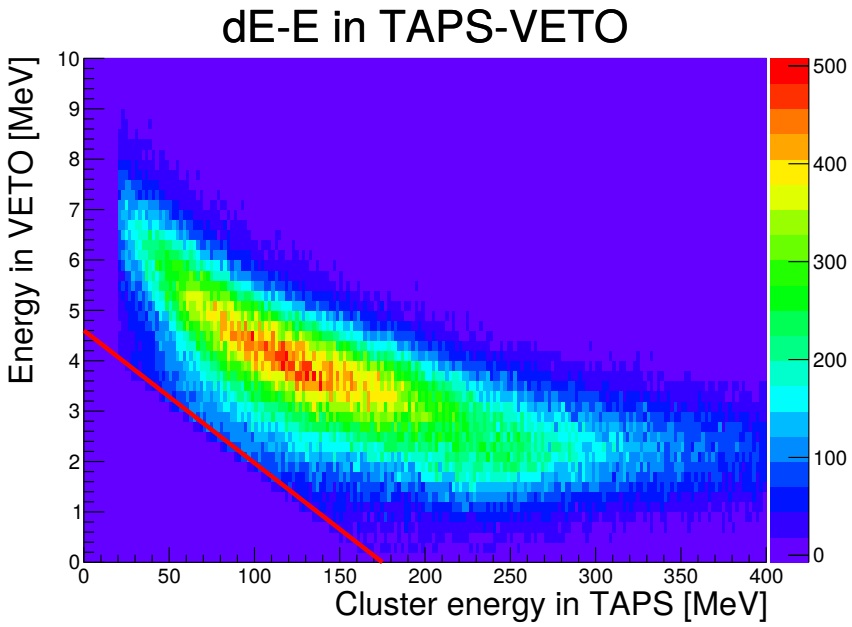

Figure 5.12: $dE - E$ analysis in TAPS. All the events with the 'good candidates' for a proton below the red line were rejected.

An addition cut is applied in order to reject the events in the bottom-left corner, as shown by the red diagonal line in Fig. 5.12.

5.2.6 Additional checks

In addition to the cuts previously described, the A2 apparatus provides additional information that can be used for the nucleon identification. These checks described below have not been used for event selection, but for tuning the previous steps and to verify the quality of the overall analysis.

$dE - E$ plot in CB

This plot was not used for the proton identification analysis, since during the 2014 D-butanol beamtime, the PID was not properly working due to an ADC readout error. The $dE - E$ plot from 2015 D-butanol data was used as a reference to set the previous cuts. In particular, in order to tune the coplanarity cut to have only protons inside the $dE - E$ plot, different intervals were tested.

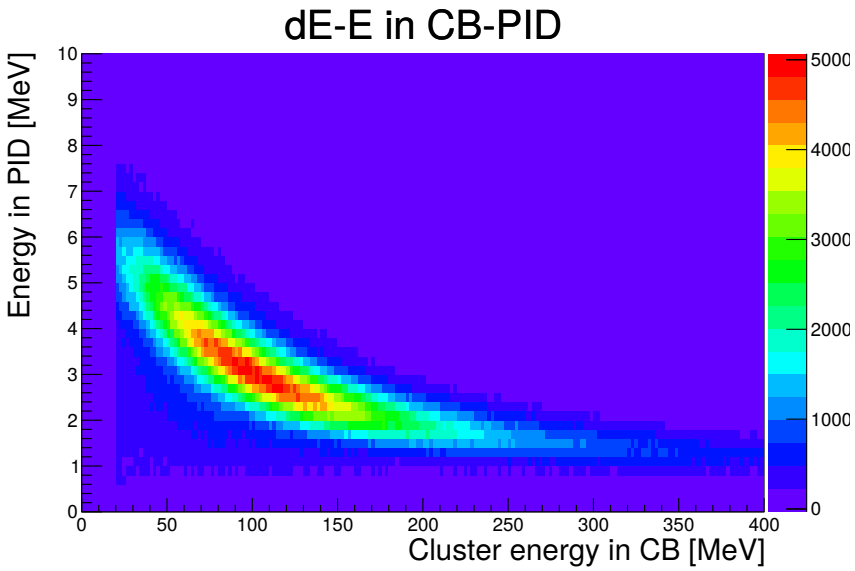

Figure 5.13: $dE-E$ plot with the energy information from the PID and the CB after MM, coplanarity and cluster size cuts. Data from 2015 D-butanol beamtime.

The final plot obtained is shown in Fig. 5.13. Only protons are present in the plot; this supports the validity of all previous analysis steps for the identification of the protons detected in the CB.

Difference between calculated and measured θ

An additional cross check was the comparison between the measured polar angle θ_{det} of the participant nucleon with the angle θ_{calc} calculated in the free nucleon kinematical conditions (App. B). This is the simple case (with $\overrightarrow{p}_p = 0$ and $E_p = 0$) of the equations given in App. B.

The resulting $\theta_{det} - \theta_{calc}$ difference is shown in Fig. 5.14, both for the proton and the neutron cases. The distribution is correctly centered around zero, with a small dispersion around the peak value. The free-nucleon approximation used for calculating θ_{calc}, instead of the quasi-free situation of the real target nucleons θ_{det}, contributes to the distribution broadening.

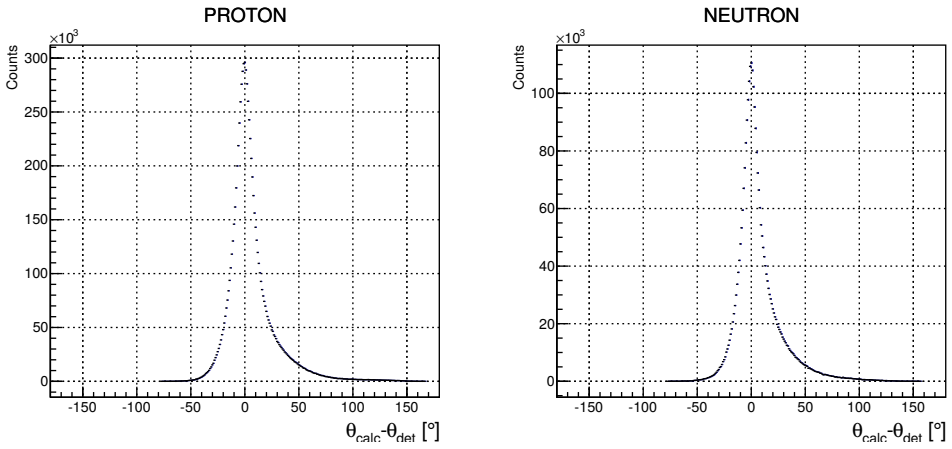

Figure 5.14: Results of the $\theta_{det} - \theta_{calc}$ for proton (left) and neutron (right).

Fermi motion calculations

When the nucleon involved in the reaction is also detected, enough variables are known to calculate the angle and the momentum of the recoil nucleon.

The energy resolution of the detected nucleon is not sufficient to be used as input for the calculation. However, the angle information is enough to perform the calculation described in App. B.

The overall calculations of the momentum and angle of the recoil neutron (when a proton is detected) and proton (when a neutron is detected) are shown in the top and in the bottom of Fig. 5.15, respectively. These distributions do not represent the situation of the proton and neutron bound inside the deuterium nucleus. This is due to the presence of the oxygen and the carbon nuclei inside the butanol molecule.

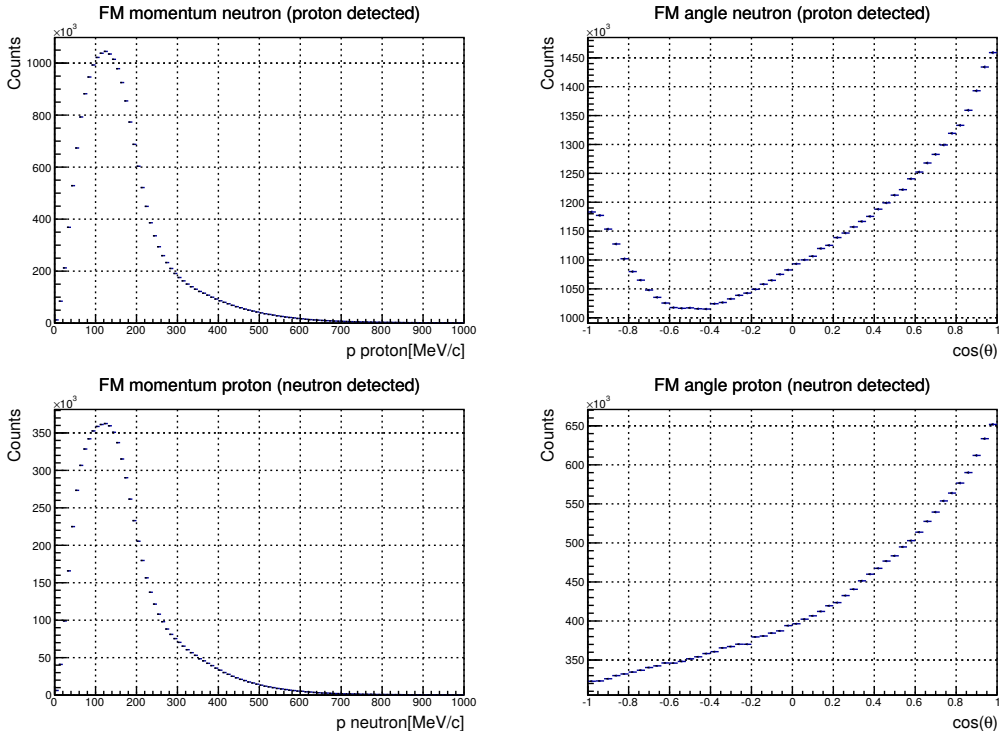

Figure 5.15: Calculation of the recoil nucleon momentum and angle.

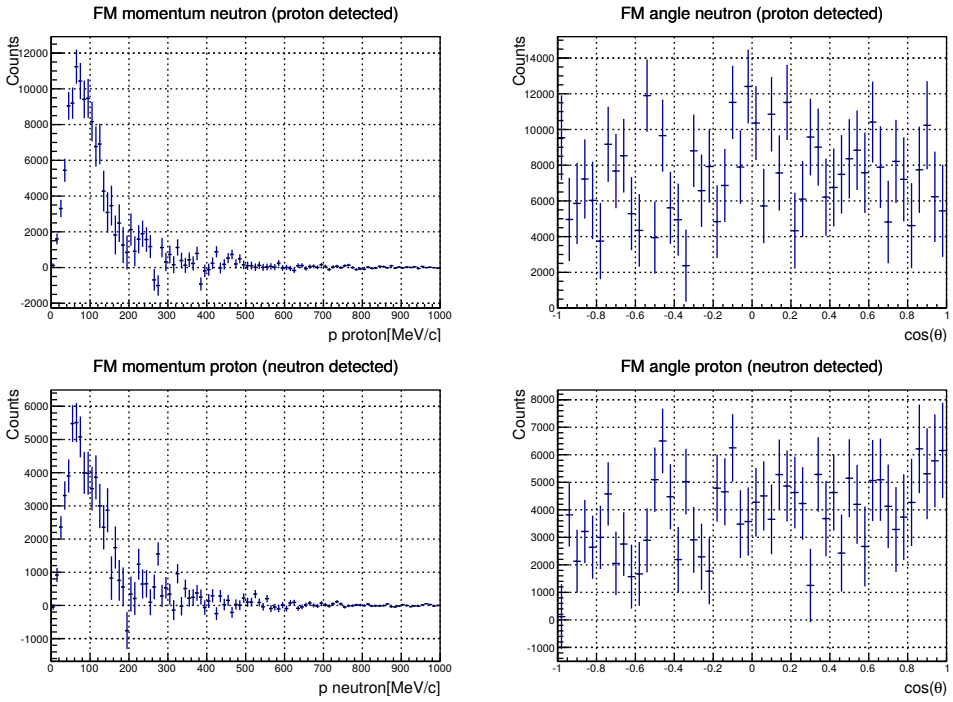

Figure 5.16: Helicity difference of the recoil nucleon momentum and angle.

The helicity difference of these quantities (see Fig. 5.16) gives a better representation of the Fermi motion distribution for the quasi-free nucleons, with the momentum distribution peaked around 50 MeV/c, and a flat angular distribution.

5.3 Tagging efficiency analysis

As previously mentioned in Sec. 3.2.3, the absolute measurement of the tagging efficiency ϵ_{TAGG} is performed with the lead glass detector during dedicated runs taken once per day. A complementary relative measurement was performed using the pair spectrometer during the normal data taking phase. The tagging efficiency is strongly dependent on the radiator used for the bremsstrahlung production. The 2014 data were collected using both the Møller and the diamond radiators, while in 2015 only the Møller radiator was used.

A set of lead glass tagging efficiency runs is composed of the following measurements:

- one initial background measurement without beam,
- data taking with beam (both the Møller radiator and two different polarization configurations of the diamond radiator were used during the 2014 beamtime. Only the Møller radiator was used during the 2015 data taking),
- a final background measurement without beam.

The value of the background (mainly from cosmic radiation and from the decay of activated material) used for the tagging efficiency is calculated using the average of the two background runs.

The evaluated tagging efficiency values for the 2014 beamtime with Møller and with diamond radiators are shown in Fig. 5.17 and 5.18, respectively, as a function of the tagger channel number. The 2015 results are shown in Fig. 5.19.

A precise evaluation of the photon flux, and hence of the tagging efficiency, is obviously essential for the cross section extraction, as can be easily seen from Eq. 2.52. The pair spectrometer output allows a precise control of the

tagging efficiency run by run. For the Møller runs, only the absolute scale factor and not the shape of the tagging efficiency can significantly change over time. In this case the output of the pair spectrometer was used to evaluate an overall average tagging efficiency correction factor for each run. For the data taken with the diamond radiator, due to different and unstable positions of the coherent peak (Fig. 5.18), the pair spectrometer was used to extract the absolute tagging efficiency for each tagger channel.

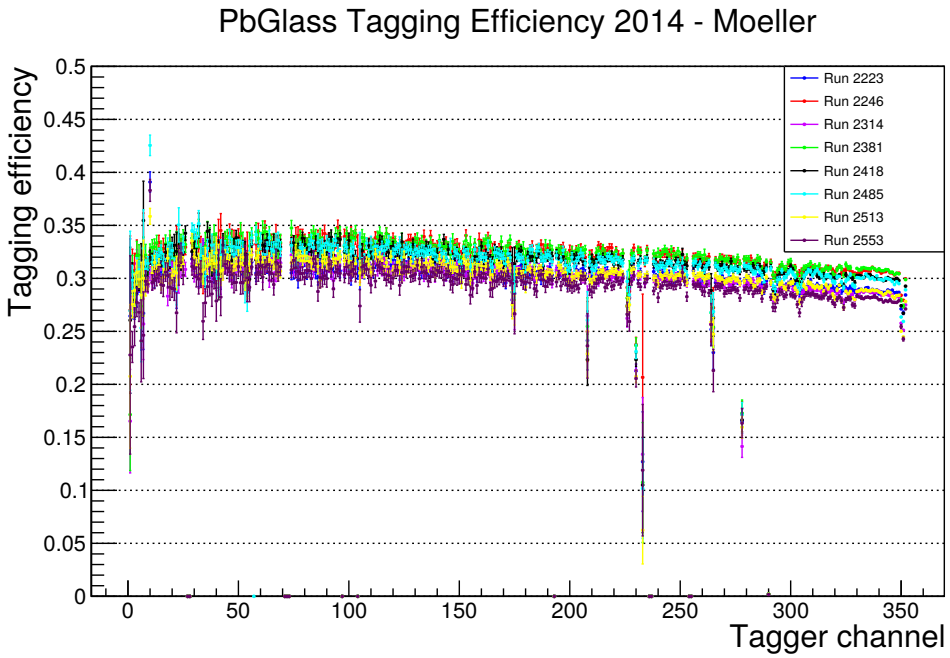

Figure 5.17: Selection of tagging efficiency runs for the D-butanol 2014 beamtime with the Møller radiator.

The 'dead time' (see Sec. 3.5) is included in the analysis software. The number of detected electrons of each scaler read is scaled by the 'dead time' value.

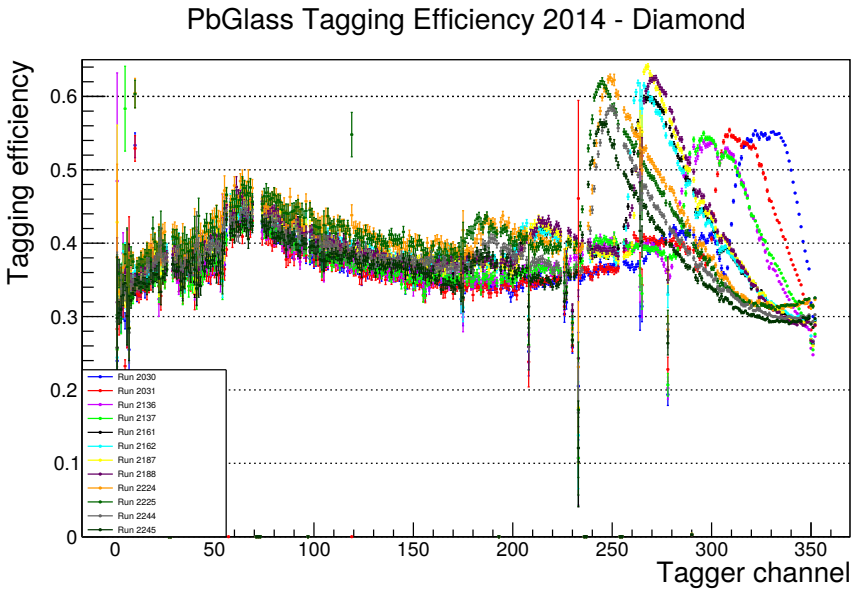

Figure 5.18: Selection of tagging efficiency runs for the D-butanol 2014 beamtime with the diamond radiator. The effect of coherent Bremsstrahlung can be clearly seen in the upper part of the spectrum (low photon energy).

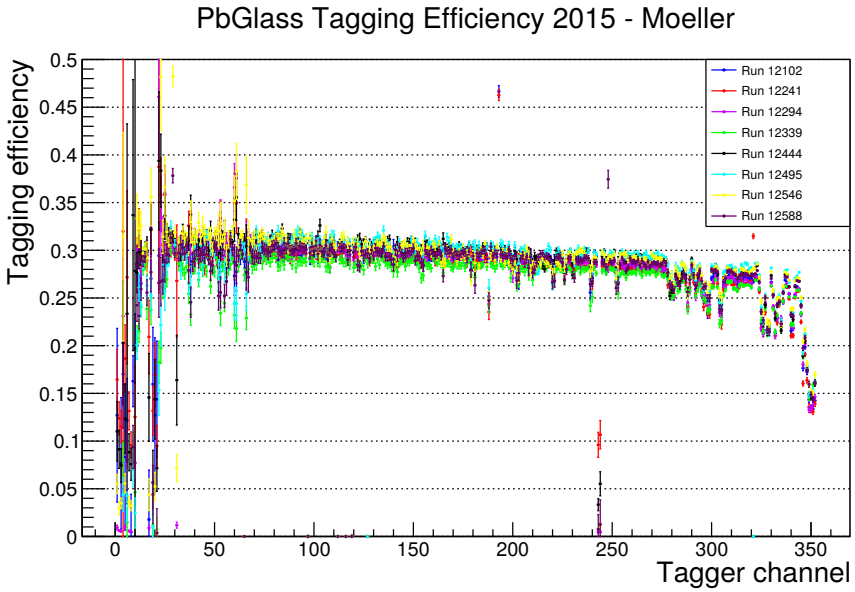

Figure 5.19: Selection of tagging efficiency runs for the D-butanol 2015 beamtime with the Møller radiator.

5.4 Target polarization

The target polarization degree P_t was measured at the start of the each data taking period (right after the target polarization procedure is complete), as well as at its end. Additional measurements were performed in the middle of the data taking if the target was re-polarized or its polarization orientation was changed. The initial and final target polarization degrees for each polarization period are defined as P_0 and P_1, respectively. From these values the relaxation time τ is calculated using the following relation:

$$P_1 = P_0 \cdot \exp^{-\frac{-\Delta T}{\tau}}, \tag{5.7}$$

where ΔT is the time difference between the two measurements. This formula is valid if the target temperature stays the same during ΔT. A dedicated control system ensures the temperature stability within $\pm$0.01 K [71].

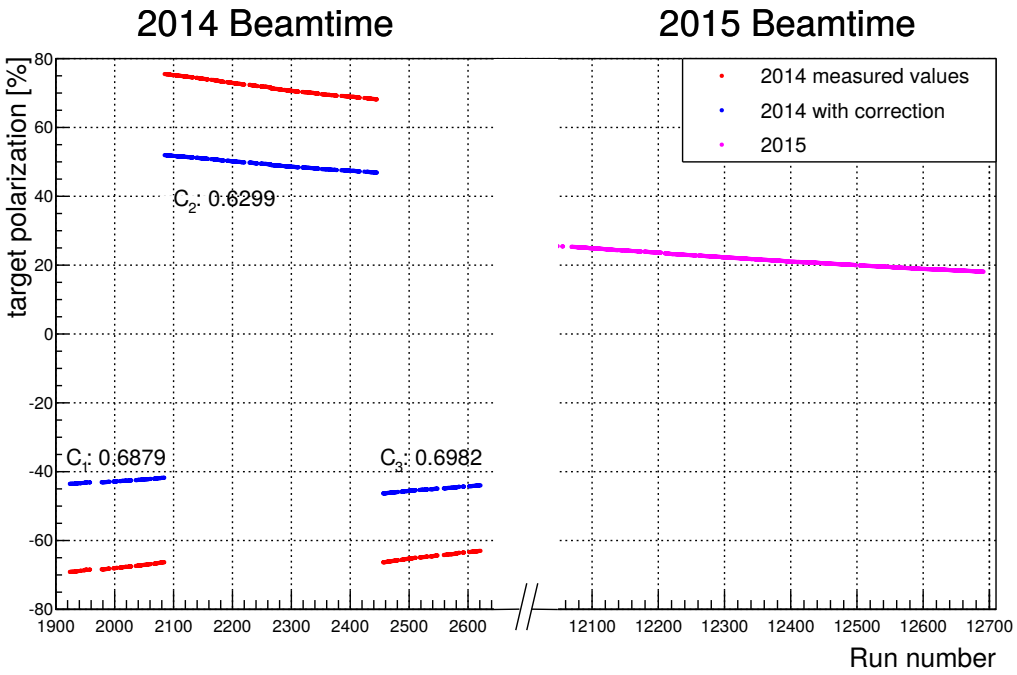

Figure 5.20: Target polarization for the 2014 and the 2015 D-butanol beamtimes. The measurement of the target polarization during the 2014 data taking was not reliable. The result of the single π^0 cross section on the deuteron from the 2015 was used as a reference in order to extract a correction factor for each target polarization period.

Afterwards, using the same relation, the target polarization degree for each run P_i (instead of P_1) can be evaluated, where ΔT is the time difference between the P_0 measurement and the time of each run.

As mentioned in Sec. 3.3, two different materials were used for the target. The preliminary analysis of the 2014 beamtime data collected with the trityl doped D-butanol, showed a number of polarized events lower than expected based on the existing measurements. The target group investigated in detail the local dependence and inhomogeneities of the target polarization measurement procedure. The 2015 beamtime was then planned to collect data with a more familiar and more reliable target material (TEMPO doped D-butanol), but with a lower polarization degree.

With all the other variables under control, correction factors for recovering the 2014 data were extracted from the new data. The average value of the single π^0 polarized cross section integrated over the Δ-resonance region was set as a reference value. The results from the three different 2014 polarization periods were scaled in order to match the 2015 result. The target polarization and the correction factors C_i for the three 2014 polarization periods are shown in Fig. 5.20.

5.5 Beam polarization and asymmetry

The MAMI group performs the measurement of the electron beam polarization degree once a day after the tagging efficiency runs, using the Mott polarimeter described in Sec. 3.1.

This measurement is cross checked analyzing the Møller polarimeter data collected with this radiator. The results of the Møller polarimeter include a systematic scaling factor extracted during a specific beamtime dedicated to the comparison between the Møller and the Mott measurements [95].

The time evolution of the beam polarization measured during the Møller runs is fitted in order to extract the beam polarization degree for the runs with the diamond radiator.

The photon beam polarization degree P_γ for each tagger channel energy is evaluated by inserting the value of the electron beam polarization into Eq. 3.7.

Fig. 5.21 and 5.22 show the Mott and the Møller measurements of the electron beam polarization.

The Mott measurement of run 12580 in the 2015 beamtime is clearly discrepant from the other points, presumably due to an error in the measurement procedure, and was therefore discarded.

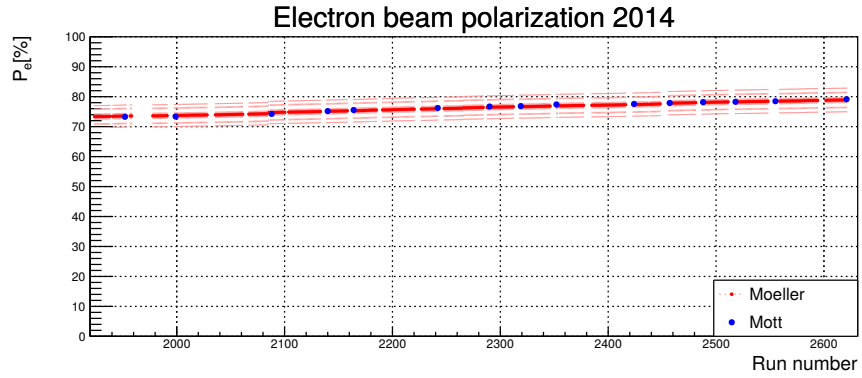

Figure 5.21: Electron beam polarization with Møller and Mott measurements for the 2014 D-butanol beamtime.

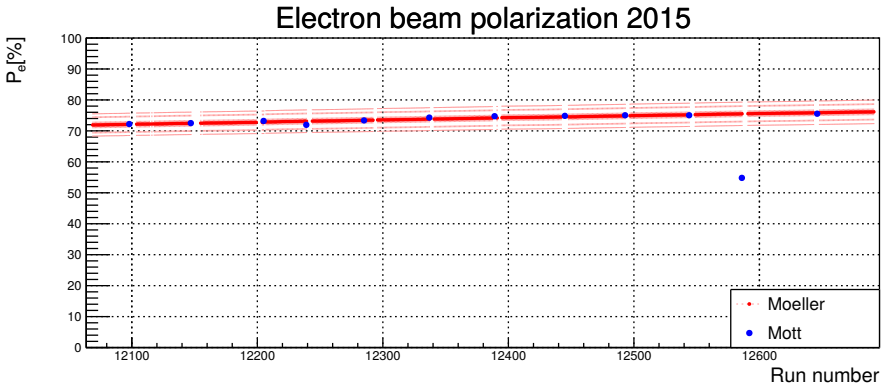

Figure 5.22: Electron beam polarization with Møller and Mott measurements for the 2015 D-butanol beamtime.

Another beam parameter to be taken into account during the analysis is the electron beam helicity asymmetry. The MAMI source flips the spin with a frequency of ~ 1 Hz, and it is registered in the data acquisition. However, there is a small asymmetry between the total number of electrons with positive and negative helicity. This difference can be extracted using the Møller radiator, and it is defined as $Asy_{beam} = \frac{hel^+ - hel^-}{hel^+ + hel^-}$, where hel^+ and hel^- are the number of electrons with positive and negative helicity configurations, respectively.

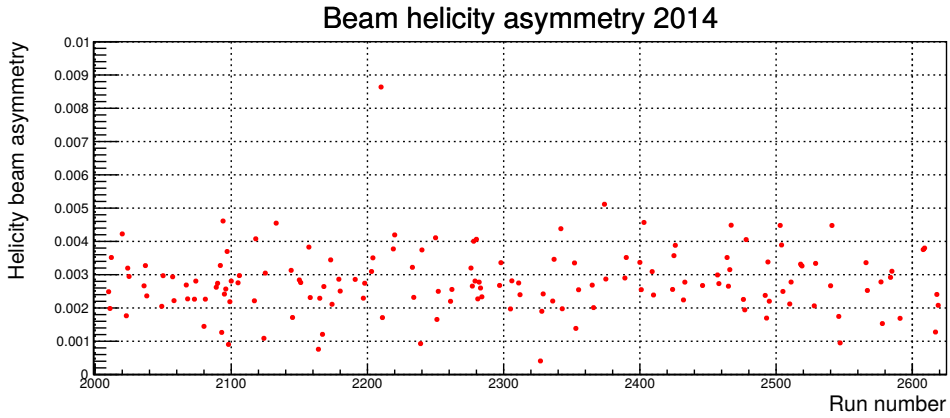

Figure 5.23: Beam helicity asymmetry for the 2014 for the D-butanol beamtime. The red dots are the values measured during the Møller runs.

Regarding the 2014 beamtime, the results obtained from the Møller runs are used to evaluate the correction parameter for the diamond runs, as shown in Fig. 5.23.

5.6 π^0 reconstruction efficiency

An evaluation of the π^0 reconstruction efficiency ϵ_{rec} is necessary to evaluate the fraction of the events that are lost during the data taking and the offline analysis.

Two different files were generated using AcquMC to take into account the π^0 production possibilities from deuterium:

$$\begin{aligned} \gamma + d \rightarrow \pi^0 + p + (n) \\ \gamma + d \rightarrow \pi^0 + n + (p) \end{aligned}, \tag{5.8}$$

where (n) and (p) are the spectator nucleons.

The geometry and the physical properties of the target and detectors are included by the A2geant simulation program. In particular, the reconstruction of the detector geometry allows the evaluation of the non-sensitive zones such as: the gap between the CB and TAPS due to the presence of the Cerenkov detector, the spacing between the two CB hemispheres, and the backward CB hole for the beam. The interaction of the generated events with the CB-TAPS setup takes into account particle interactions with the detector materials, and determines how many tracks are detected.

The A2Geant output files are finally analyzed with the π^0 reconstruction physics classes described in Sec. 5.1.

The reconstruction efficiency ϵ_{rec} is evaluated for each π^0 channel using the following relation:

$$\epsilon_{rec}(E_\gamma, \theta_{\pi^0}) = \frac{N_{rec}(E_\gamma, \theta_{\pi^0})}{N_{gen}(E_\gamma, \theta_{\pi^0})}, \tag{5.9}$$

where $N_{rec}(E_\gamma, \theta_{\pi^0})$ and $N_{gen}(E_\gamma, \theta_{\pi^0})$ are the number of reconstructed and generated π^0 events, respectively. The results of the reconstruction efficiency for π^0 production from the proton and from the neutron are very similar, and their average was used for the extraction of the inclusive π^0 cross section from the deuteron.

The $\epsilon_{rec}(E_\gamma, \theta_{\pi^0})$ for inclusive π^0 production from the deuteron is shown in Fig. 5.24.

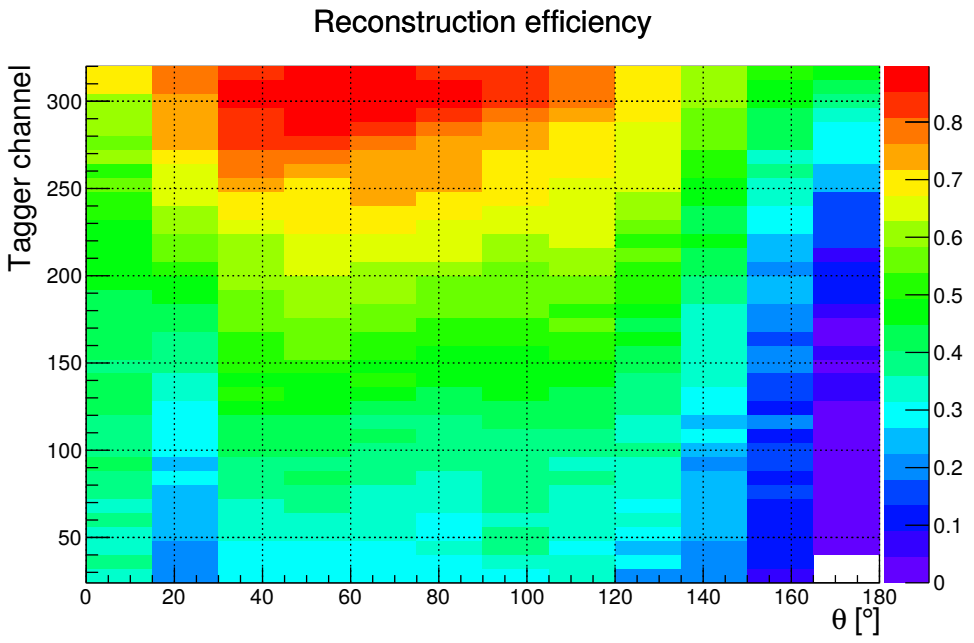

Figure 5.24: π^0 reconstruction efficiency as a function of tagger channel and θ_{Lab}.

5.7 Unpolarized nuclei background subtraction

Due to the presence of carbon and oxygen nuclei in the D-butanol molecule, the data collected do not permit the direct extraction of the E observable. The contribution of the non-polarizable carbon and oxygen nuclei can be evaluated by introducing the dilution factor D_f in Eq. 2.42, as follows:

$$E(W,\theta) = \frac{N_{1/2}^{BUT}(W,\theta) - N_{3/2}^{BUT}(W,\theta)}{N_{1/2}^{BUT}(W,\theta) + N_{3/2}^{BUT}(W,\theta)} \cdot \frac{1}{P_z^T} \cdot \frac{1}{P_\odot^\gamma} \cdot \frac{1}{D_f}. \tag{5.10}$$

The static dilution factor for a molecule is defined as the ratio between the number of polarizable nucleons N_{POL} and the total number of nucleons N_{TOT}:

$$D_f = \frac{N_{POL}}{N_{TOT}} = \frac{N_{POL}}{N_{POL} + N_{UNPOL}}. \tag{5.11}$$

For the D-butanol, D_f is the ratio between the number of the deuterium nucleons N_D and the sum of the nucleons of deuterium, carbon and oxygen nuclei:

$$D_f = \frac{N_D}{N_{BUT}} = \frac{N_D}{N_D + N_C + N_O} = \frac{2 \cdot 10}{2 \cdot 10 + 4 \cdot 12 + 16} = \frac{20}{84} \approx 0.24. \tag{5.12}$$

However, the static dilution factor does not include the effects of the different cuts included in the event reconstruction procedure, as well as the small background due to the He and target cell materials. An effective determination of the energy and angular dependence of these effects was performed by collecting data with the carbon foam target described in Sec. 3.3.

The subtraction of the carbon foam background can be included in Eq. 2.42 as follows:

$$E = \frac{N_{1/2}^{BUT} - N_{3/2}^{BUT}}{(N_{1/2}^{BUT} + N_{3/2}^{BUT}) - S_f \cdot N_C} \cdot \frac{1}{P_z^T} \cdot \frac{1}{P_\odot^\gamma}, \tag{5.13}$$

where N_C represents the events from the carbon target and S_f is the scaling factor necessary to normalize the different amounts of statistics collected with the two different targets.

The extraction of S_f, including its energy dependence, is performed by using two different methods, described in the next subsections. The first method,

based on the missing mass plots, shows a better stability over the full energy range of the experiment, and was used to extract the final results.

5.7.1 Scaling factor from the missing mass plots

The first method to extract the scaling factor S_f is based on the missing mass plots. The procedure was initially tuned and tested using the data collected in 2015 with the D-butanol and carbon targets.

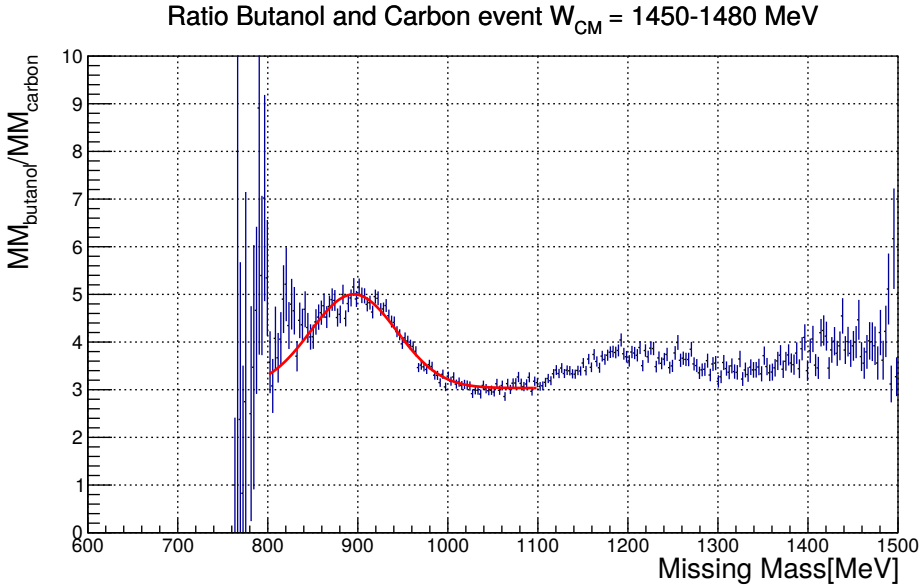

Figure 5.25: Ratio of the D-butanol and carbon missing mass distributions for the proton events (the blue and the magenta points of Fig. 5.26, respectively). The red line represents the fitting function, which is the sum of a Gaussian distribution and a constant value.

The extraction of the scaling factor is performed separately for proton and neutron events. The proton events having W_{CM} between 1450 and 1480 MeV are used as an example to describe this method. The summary of the results for all the energy bins for both proton and neutron cases are collected in App. D.

The first step is to extract the ratio between the D-butanol and the carbon missing mass distributions of the unpolarized proton events, shown in Fig. 5.25.

The resulting distribution is fitted around the single π^0 peak using a function (represented by the red curve in the figure) defined as the sum of a Gaussian and a constant value.

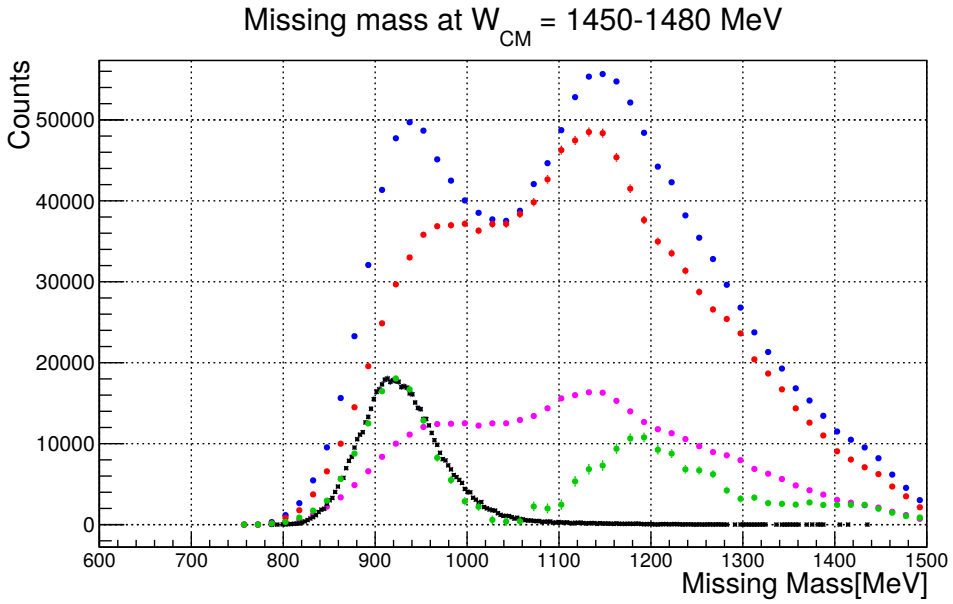

Figure 5.26: Carbon subtraction using the missing mass plot for the 2015 D-butanol and 2015 carbon data for proton events. The points represent the missing mass distribution for: the D-butanol target (blue dots), the carbon target (magenta dots), the scaled carbon (red dots) and the proton events (green dots). The proton events are obtained by subtracting the scaled carbon events from the D-butanol events. The black dots show the simulated distribution of proton events from the deuterium target.

The constant value extracted from the fit procedure is used to scale the original carbon distribution (the magenta and the red dots in Fig. 5.26 are the carbon before and after the scaling, respectively). As a result of the selected fit range, the scaled carbon distribution matches the D-butanol distribution for missing mass values between the single and the double pion peak, where no effect from the deuteron is expected.

The results of each energy bin are checked in order to verify that the D-butanol distribution is always above the scaled carbon within the statistical errors.

The amount of unpolarized events from the quasi-free protons bound inside the deuteron (green dots in Fig. 5.26) is extracted by subtracting the scaled carbon distribution from the D-butanol one.

The resulting unpolarized proton distribution is compared with the simulated data for the $\gamma + d \to \pi^0 + p + (n)$ channel (the black dots in Fig. 5.26).

The selection of the fit range, which leads the scaled carbon to match the

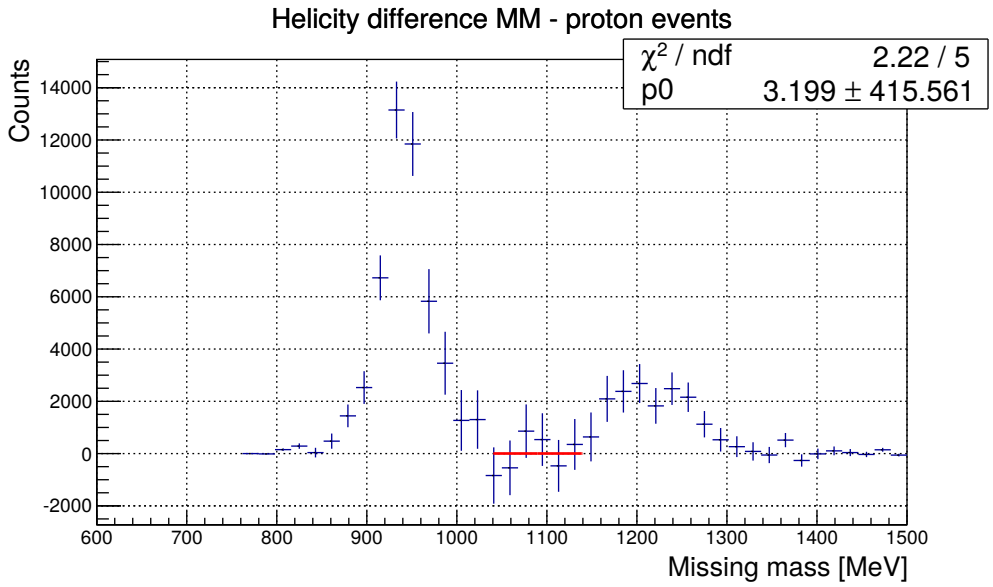

Figure 5.27: Helicity difference of the missing mass distribution for polarized proton events on D-butanol data. Due to low statistics, the picture includes the events from several energy bins in order to verify the position of the minimum between the single and the double pion peaks.

D-butanol distribution in the region between the single and the double pion peaks, can be validated by analyzing the helicity difference of the missing mass distribution. This distribution is shown in Fig. 5.27 where, due to low statistics, multiple energy bins are summed together.

The position of the minimum of the distribution between the single and the double pion peaks and the agreement of the resulting distribution with the simulation validate this scaling procedure.

A different S_f is extracted for each energy bin. The angular dependence of S_f was tested as well. For each energy bin, four $\cos(\theta_{\pi^0})$ bins were taken into account. Fig. 5.28 shows an example for the same energy bin used for the previous figures and with the constant S_f value. It was not observed that S_f is angular dependent.

Once the procedure was tuned using the 2015 D-butanol and the 2015 carbon data, it was also applied to the 2014 D-butanol data.

The 2015 carbon data were collected with the target cell surrounded with the He mixture, while the previous carbon measurements was collected without it. Although the quantity of the He mixture is low [72], these data are expected to better describe the unpolarized background.

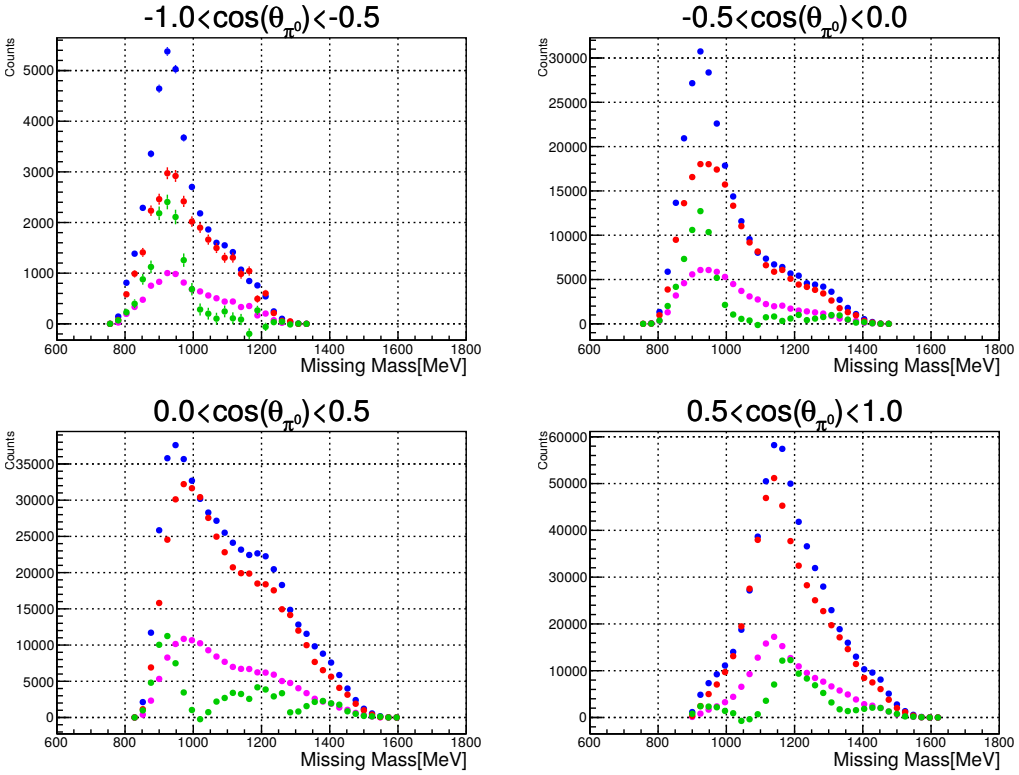

Figure 5.28: Angular dependence of S_f. The missing mass plot of Fig. 5.26 is split in four different $\cos(\theta_{\pi^0})$ bins. For the colors legend see Fig. 5.26.

The carbon subtraction distribution for the 2014 D-butanol data using the 2015 carbon data is shown in Fig. 5.29.

The resulting proton distribution is different from the one obtained with the 2015 D-butanol data. It does not match the simulation, the position of the minimum between the two peaks is shifted and, in the region of the double pion peak, the distribution is negative. These features appear in almost every energy bin from both proton and neutron events.

In order to overcome this problem, the carbon data collected in 2013 (just a couple of months before the D-butanol beamtime) without the He mixture were analyzed.

The result of the carbon subtraction with the 2014 D-butanol and the 2013 carbon data is shown in Fig. 5.30. With this configuration, the resulting proton distribution matches the simulation. Therefore, the 2013 carbon data were used for subtracting the unpolarized background from the 2014 D-butanol data.

This discrepancy observed between the 2015 carbon and the 2014 butanol

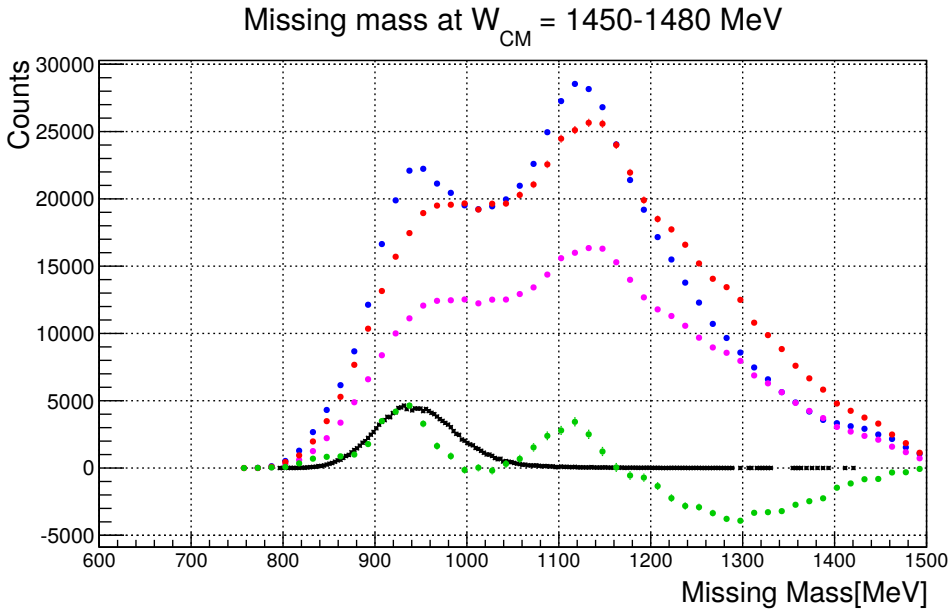

Figure 5.29: Carbon subtraction using the missing mass plots for the 2014 D-butanol and 2015 carbon data for proton events. For the colors legend see Fig. 5.26.

data are due to:

- upgrades of the data acquisition system implemented between the January 2014 and the October 2015 data taking periods resulting in a different structure of the trigger setup,

- different configuration of the missing CB elements. some of the PMTs broken in 2013/2014 were replaced, but some other channels were not working in 2015,

- and the intrinsic energy thresholds for the CB elements were slightly different between 2014 and 2015.

It is difficult to exactly evaluate in a quantitative way the effect of these setup differences. Since the 2013 carbon data can better describe the D-butanol 2014 unpolarized background, the effect of the He mixture is surely smaller than the differences in the experimental setup.

The absence of the He mixture around the target during the 2013 carbon data taking is included in the systematic uncertainties discussed in Sec. 5.8.2.

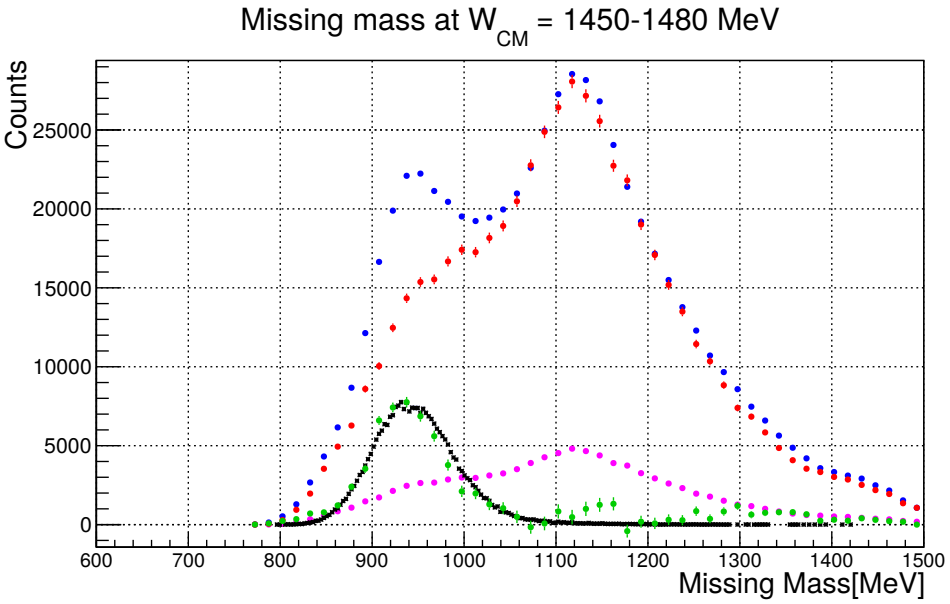

Figure 5.30: Carbon subtraction using the missing mass plots for the 2014 D-butanol and 2013 carbon data for proton events. For the colors legend see Fig. 5.26.

5.7.2 Scaling factor from coplanarity plots

A different method was developed comparing the butanol and carbon coplanarity distributions. This allows a cross check of S_f from the missing mass distributions, previously described.

The scaling factor was evaluated by matching the scaled carbon coplanarity spectra in the region around the peak, as shown in Fig. 5.31. This procedure was tested on the missing mass plot, and a distribution equivalent to the one shown in Fig. 5.26 was obtained.

With the scaling factor based on the coplanarity plot the problems for 2014 D-butanol and 2015 carbon were also observed and it was preferred to use the 2013 carbon data for evaluating the background of the 2015 butanol data.

The missing mass method was ultimately preferred because it was easier to tune over the entire measured energy range.

The difference between the scaling factors extracted with the two methods is included in the evaluation of the systematic uncertainties.

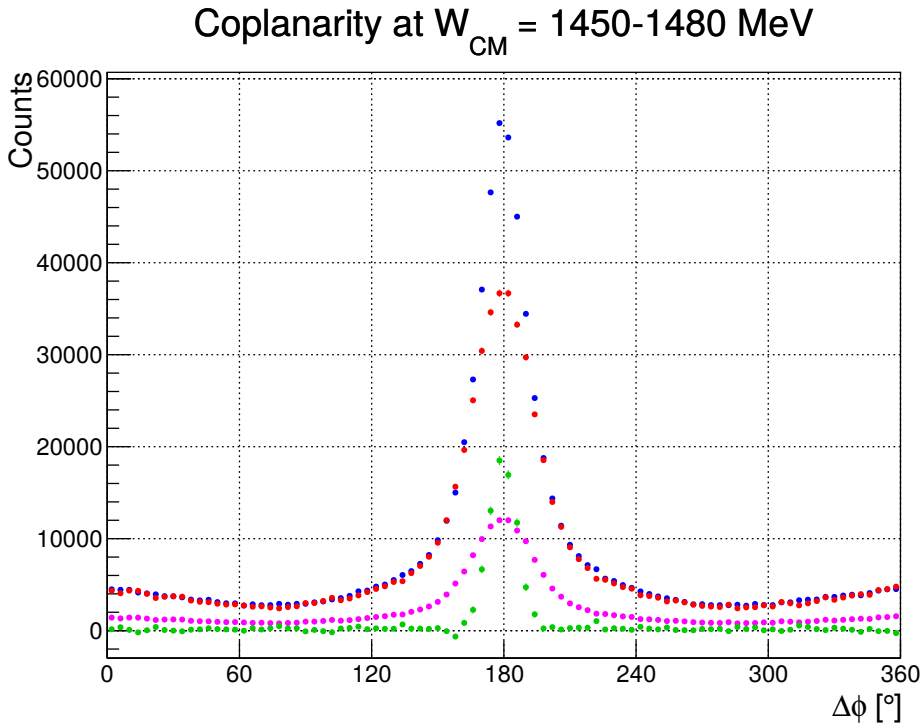

Figure 5.31: Carbon subtraction based on the coplanarity plots for the 2015 butanol and 2015 carbon data for proton events. For the colors legend see of Fig. 5.26.

5.8 Error analysis

In this section the evaluation of the errors, both statistical and systematic, is discussed.

5.8.1 Statistical uncertainties

The largest contribution to the statistical uncertainties (the symbol Δ^{stat} is used instead of σ to avoid confusion with the cross section symbol) comes from the propagation of the error of the number of selected π^0 events. The errors of the prompt and random regions described in Sec. 4.5 are evaluated as the $\sqrt{N}$ of the events of each region. The statistical error is calculated using the error propagation formula:

$$(\Delta^{stat})^2 = \sum_{i=1}^{i_{max}} (\frac{\mathrm{d}f_i}{\mathrm{d}x_i})^2 (\Delta_i^{stat})^2, \tag{5.14}$$

where $i_{max} = 3$ indicates the three regions in the prompt-random subtraction procedure. Eq. 5.14 is also used to combine the two configurations of the events selection ($N^{\uparrow\downarrow}$ and $N^{\uparrow\uparrow}$) and, in the case of the E observable results, the selected events with carbon target.

The results from the two different beamtimes, both for the polarized cross section and for the E asymmetry, have been obtained using the weighted average to combine the two independent results. The final result is given by the following formula:

$$\bar{x}_{final} = \frac{\sum_{i=2014,2015} \bar{x}_i/(\Delta_i^{stat})^2}{\sum_{i=2014,2015} 1/(\Delta_i^{stat})^2}, \tag{5.15}$$

with the final statistical error:

$$\Delta_{final}^{stat} = \sqrt{\frac{1}{\sum_{i=2014,2015} 1/(\Delta_i^{stat})^2}}. \tag{5.16}$$

The photon flux (in the case of the cross section results), target polarization and beam polarization degree uncertainties contribute only to the systematic errors.

5.8.2 Systematic uncertainties

In this section the different contributions to the systematic uncertainties are discussed.

Target polarization and filling factor

The systematic error of the target polarization measurement was evaluated by the target group and is 2%. An additional 3% is included for the correction factors extracted for the 2014 beamtime. The total systematic error for the target polarization results becomes:

$$\frac{\Delta P_z^T}{P_z^T} = \sqrt{0.02^2 + 0.03^2} = 3.6\% \tag{5.17}$$

An additional 1.5 % is included for the filling factor ($F_{filling}$) of the target material inside its cell.

Beam polarization

The uncertainty of the polarization of the electron beam, measured by the MAMI group using the Mott polarimeter, is $\sim 2.8\%$ [50, 96]. This value is directly propagated into the photon polarization degree by Eq. 3.7.

Photon flux

Due to the high number of electrons detected by the tagger, the statistical error of the photon flux is negligible. However, a systematic error for the tagging efficiency, which accounts for r the instability of the coherent peak during the diamond runs, has been taken into account.

Because the efficiency of the lead glass detector is 100 %, the systematic error for the Møller runs is mainly due to the small movement of the beam during the data taking. The run by run tagging efficiency of each tagger channel is measured with the pair spectrometer. Thanks to this overall correction of the tagging efficiency run by run, the systematic error for the Møller is evaluated to be below 2 %.

For the data collected using the diamond radiator also the shift of the coherent peak gives a contribution to the systematic uncertainties. From the comparison between the tagging efficiencies obtained with the lead glass detector and the pair spectrometer run the systematic of the photon flux for the diamond run is evaluated to be $\sim 5\%$.

Since the contributions of the Møller and diamond data to the overall statistics are approximately the same, the final systematic error for the photon flux is estimated to be the average of the two values:

$$\frac{\Delta N_\gamma}{N_\gamma} = 3.5\%. \tag{5.18}$$

Background in the event selection

During the selection of single π^0 events other kinds of events can also be selected. In particular, for high missing mass values (just at the upper cut at 1050 MeV) double pion events can be included. Events from double pion channels have been simulated, and then multiplied with the correspondent value of the cross section. The total contribution of these events (δ_{bkg}) to the cross section results is evaluated to be below 1 μb, as shown in Fig. 5.32.

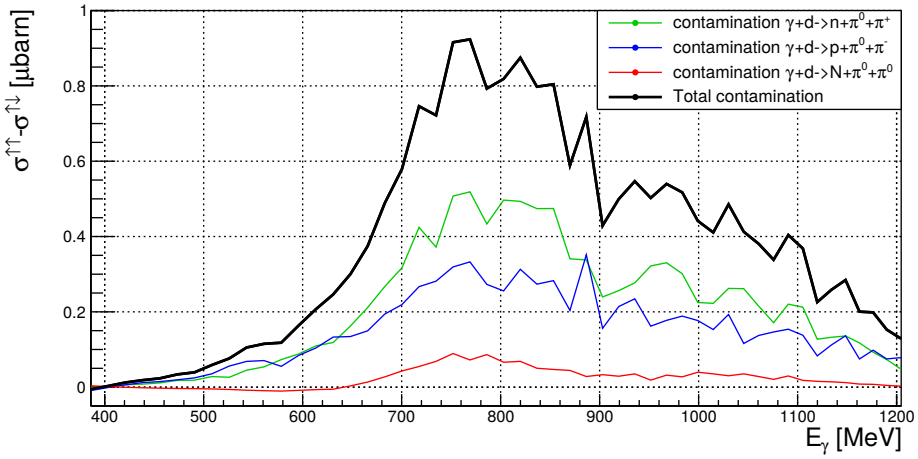

Figure 5.32: Total contamination from double pion channels of the single π^0 polarized cross section.

If a proton or a neutron is also required in the analysis (the events selection used for the E asymmetry), the contribution from the double pion channels is negligible.

Carbon background subtraction

The accuracy of the carbon background subtraction is affected by the available statistics collected with D-butanol and carbon targets. However, the systematic error of the procedure is higher than the statistical errors. The difference between the scaling factors obtained using either the coplanarity or the missing mass plots was determined to be smaller than 4.0 %.

Total systematic uncertainty the for polarized cross section

The components of the total systematic uncertainty for the polarized cross section ($\overrightarrow{\sigma}$) are uncorrelated, so they add as follows:

$$\Delta\overrightarrow{\sigma}^{sys} = \sqrt{\left[\left(\frac{\Delta P_z^T}{P_z^T}\right)^2 + \left(\frac{\Delta F_{filling}}{F_{filling}}\right)^2 + \left(\frac{\Delta P_\odot^\gamma}{P_\odot^\gamma}\right)^2 + \left(\frac{\Delta N_\gamma}{N_\gamma}\right)^2\right] \cdot \overrightarrow{\sigma}^2 + \delta_{bkg}^2}, \tag{5.19}$$

resulting in a maximum systematic error of 5.8 %.

Total systematic uncertainty for E observable

The components of the total systematic uncertainty for the E asymmetry add as follows:

$$\Delta E^{sys} = \sqrt{\left[\left(\frac{\Delta P_z^T}{P_z^T}\right)^2 + \left(\frac{\Delta F_{filling}}{F_{filling}}\right)^2 + \left(\frac{\Delta P_\odot^\gamma}{P_\odot^\gamma}\right)^2 + \left(\frac{\Delta S_f}{S_f}\right)^2\right]} \cdot E, \quad (5.20)$$

resulting in a maximum systematic error of 6.2 %, as shown in Tab. 5.1.

Table 5.1: Total systematic uncertainty for the E observable.

Filling factor	Target polarization	Beam polarization	Carbon subtraction	Total
1.5%	3.6%	2.8%	4.0%	6.2%

Chapter 6

Results

This chapter presents the final results of this work. Sec. 6.1 presents the results of the helicity dependent single π^0 photoproduction cross section on the deuteron. The results of the E observable for single π^0 photoproduction on quasi-free protons and quasi-free neutrons are shown in Sec. 6.2 and 6.3, respectively. Finally, in Sec. 6.4 the fitting procedure of the E asymmetry measurements with Legendre polynomials is described.

6.1 Inclusive polarized π^0 photoproduction cross section on the deuteron

The helicity dependent cross section of inclusive single π^0 photoproduction on the deuteron was introduced in Eq. 2.52 and was evaluated using the following formula:

$$\frac{\mathrm{d}\overrightarrow{\sigma}}{\mathrm{d}\Omega}(E_\gamma) = \frac{\mathrm{d}\sigma^{\uparrow\uparrow}}{\mathrm{d}\Omega}(E_\gamma) - \frac{\mathrm{d}\sigma^{\uparrow\downarrow}}{\mathrm{d}\Omega}(E_\gamma) = 2 \cdot \frac{N^{\uparrow\uparrow}(E_\gamma,\theta) - N^{\uparrow\downarrow}(E_\gamma,\theta)}{N_\gamma(E_\gamma) \cdot \epsilon_{REC}(E_\gamma,\theta) \cdot \Delta\Omega \cdot d} \cdot \frac{1}{P_\odot^\gamma} \cdot \frac{1}{P_z^T}, \tag{6.1}$$

where:

- $N^{\uparrow\uparrow}(E_\gamma,\theta)$ and $N^{\uparrow\downarrow}(E_\gamma,\theta)$, are the numbers of neutral pion events on deuteron with anti-parallel and parallel spin configuration, respectively. The different spin configurations correspond to a flipping of the electron beam orientation,

- N_γ is the total photon flux. It includes the photons from both spin configurations and it is compensated by scaling the equation by a factor 2. The correction factor for the beam helicity asymmetry described in Sec. 5.5 is included in $N^{\uparrow\uparrow}(E_\gamma, \theta)$ and $N^{\uparrow\downarrow}(E_\gamma, \theta)$.
- $\epsilon_{REC}(E_\gamma, \theta)$is the reconstruction efficiency of the π^0 events (see Sec. 5.6),
- d is the surface density of the target,
- $P_\odot^\gamma$ is the photon beam polarization degree,
- P_z^T is the target polarization degree.

The obtained total cross section is shown in Fig. 6.1 and the region with $E_\gamma >$ 550 MeV is shown in Fig. 6.2.

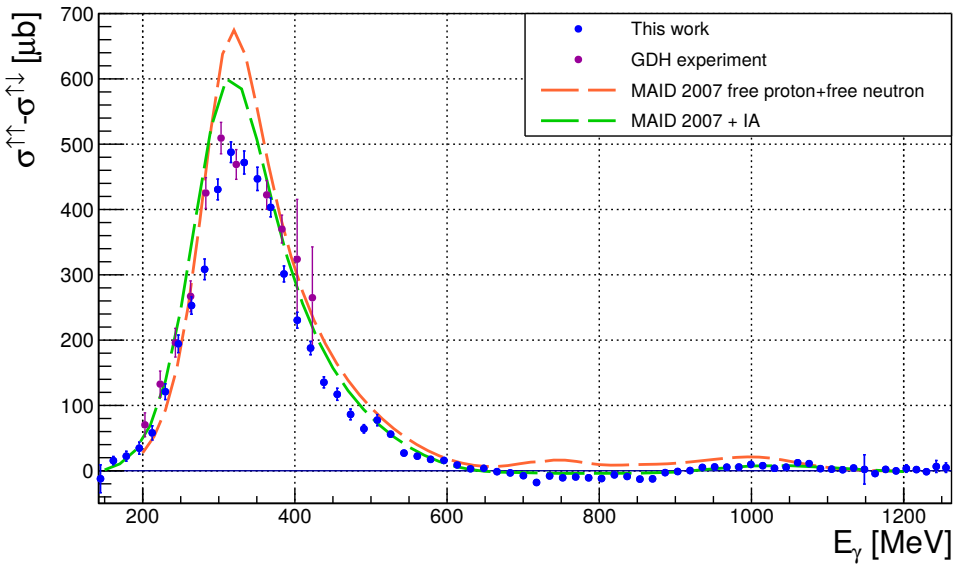

Figure 6.1: Helicity dependent total cross section for single π^0 photoproduction on the deuteron.

For comparison, the results of this work (blue dots) are shown along with the measurement from the GDH experiment (red dots) [44], as well as with the sum of MAID models for free protons and free neutrons [31], without and with impulse approximation (green and gray line, respectively) [97].

A selection of the differential cross section values obtained at various energy bins are shown in Fig. 6.3 and Fig. 6.4. The maximally backward data points for energies above 650 MeV is not shown due to the low efficiency.

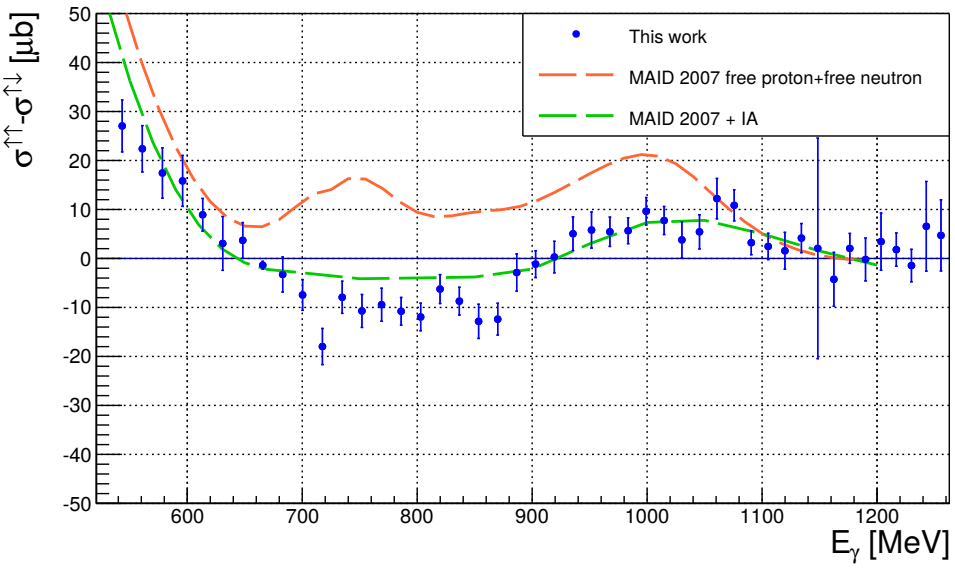

Figure 6.2: Helicity dependent total cross section for single π^0 photoproduction on the deuteron with $E_\gamma > 550$ MeV.

All the numerical values can be found in App. E.

Discussion

The result of the polarized cross section of single π^0 photoproduction on the deuteron shows a strong effect from final state interactions, especially in the $\Delta-$resonance region, where the determined cross section is not well described by the model which includes impulse approximation corrections only (green line). This is because final state interactions affect both spin configurations, and in regions where the difference between them is high (as in Δ-region), the contribution of the final state interactions is higher. This is particularly evident for $E_\gamma < 400\,\text{MeV}$. At higher photon energy, the energy of the π^0 is higher, and the probability of a hadronic scattering with the spectator nucleon is reduced. For these reasons, for energies above the $\Delta-$region the model with the impulse approximation corrections and the experimental results are in good agreement. It is useful to note that for $E_\gamma > 650\,\text{MeV}$ the free model predicts positive values for the helicity dependent total cross section. However the theoretical model including the impulse approximation gives negative value in this energy range. For the energies shown in Fig. 6.4, the theoretical calculations with impulse

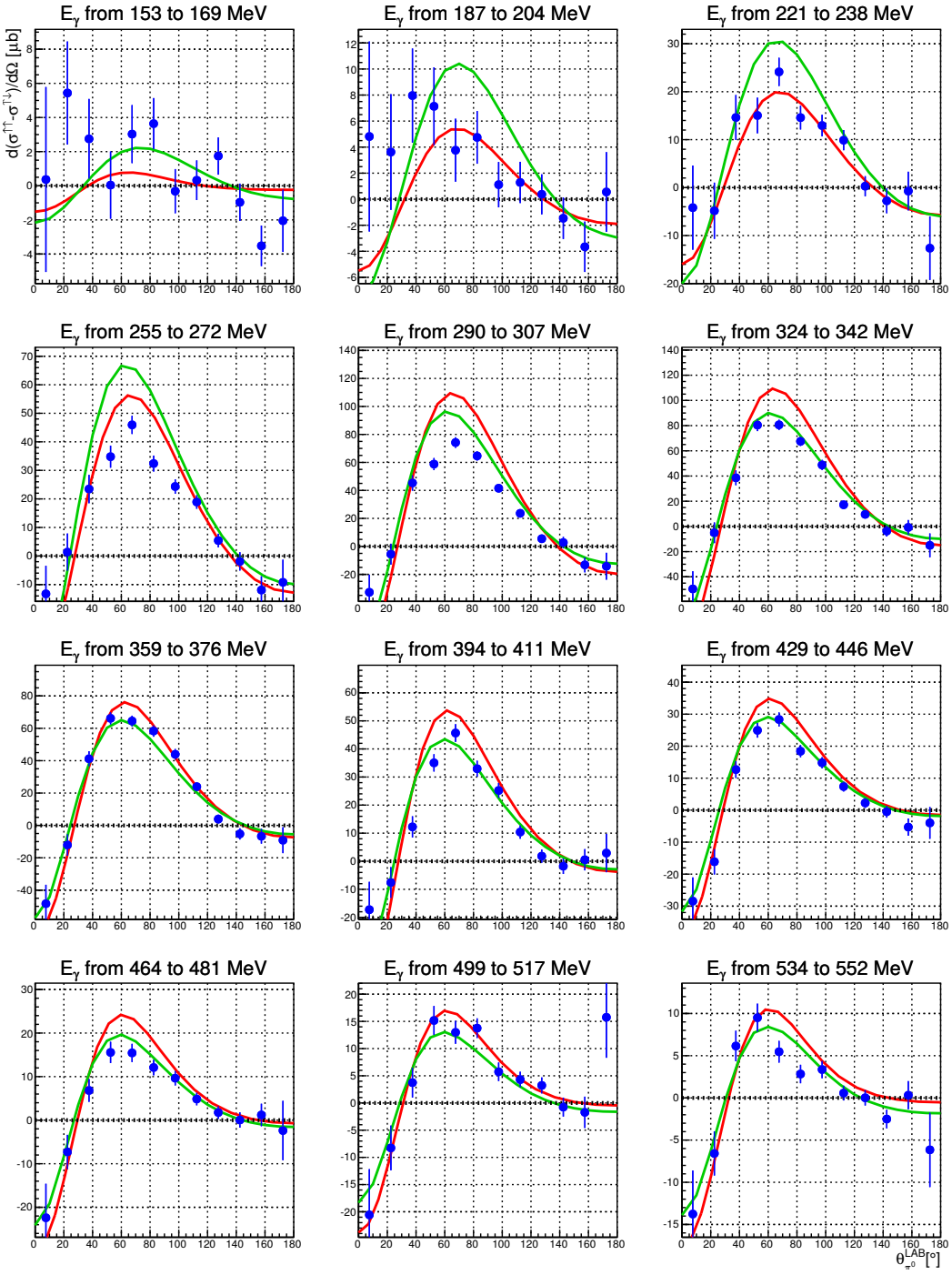

Figure 6.3: Helicity dependent differential cross section for single π^0 photoproduction on the deuteron as function of $\theta_{\pi^0}^{\mathrm{LAB}}$, shown for $E_\gamma < 560$ MeV. The legend is shown in Fig. 6.4.

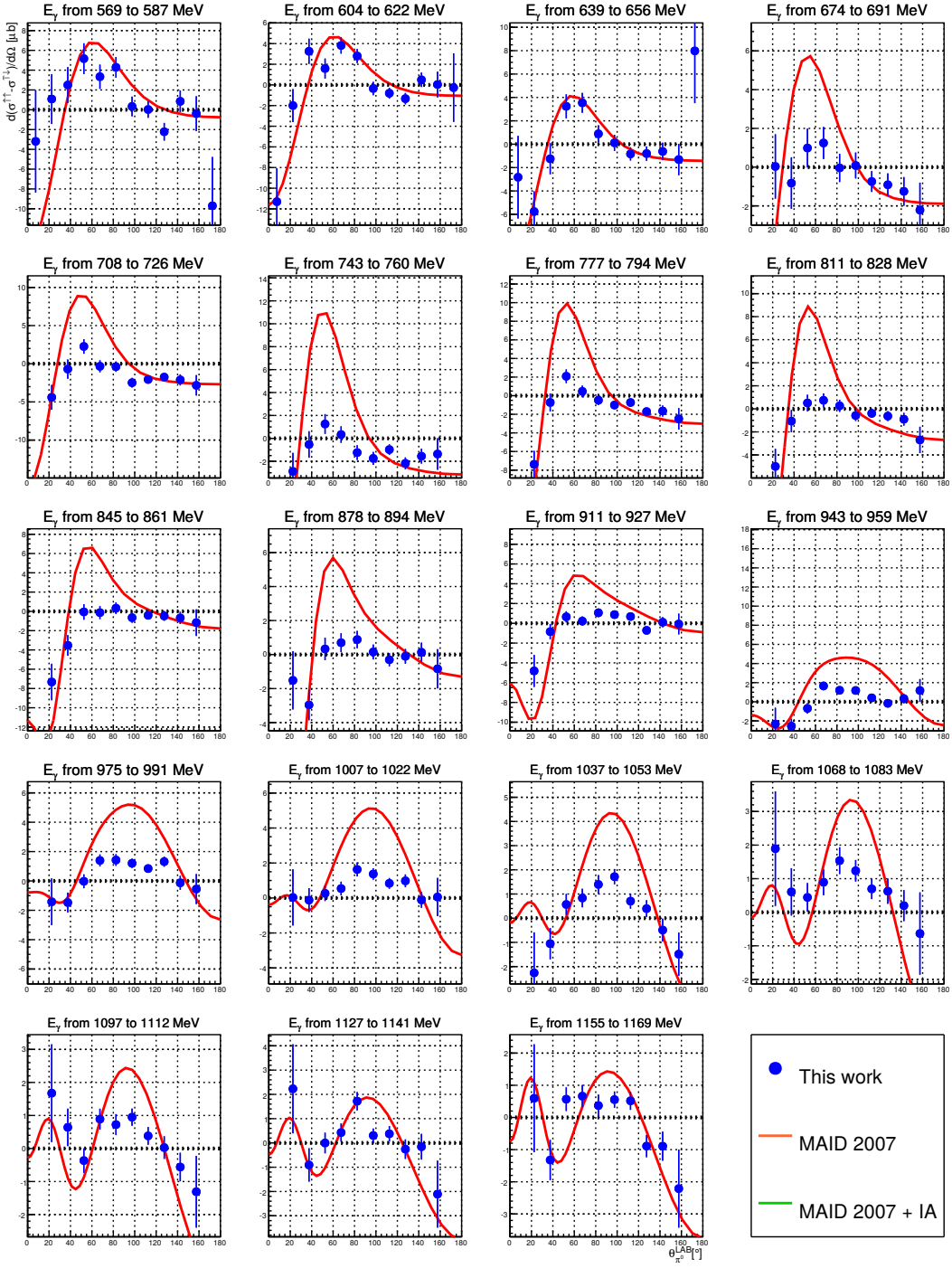

Figure 6.4: Helicity dependent differential cross section for single π^0 photoproduction on the deuteron as function of $\theta_{\pi^0}^{\mathrm{LAB}}$, shown for $E_\gamma > 560$ MeV. The legend is valid also for Fig. 6.3.

approximation were not available, but it is, however, possible to observe that the the results of this work are below or around zero value, while the free model line is mainly positive.

These data can provide a strong constraint on all nucleon models that describe the $N - N$ and $\pi - N$ interactions.

6.2 E observable for single π^0 photoproduction on the proton

The E observable for single π^0 photoproduction on quasi-free protons is evaluated with the following formula:

$$E_p(W,\theta) = \frac{N_p^{\uparrow\downarrow}(W,\theta) - N_p^{\uparrow\uparrow}(W,\theta)}{[N_p^{\uparrow\downarrow}(W,\theta) + N_p^{\uparrow\uparrow}(W,\theta)]} \cdot \frac{1}{P_\odot^\gamma} \cdot \frac{1}{P_z^T} \tag{6.2}$$

where:

- $N_p^{\uparrow\downarrow}(W,\theta)$ and $N_p^{\uparrow\uparrow}(W,\theta)$ respectively, are the single π^0 events from the polarized proton[1],
- $P_\odot^\gamma$ is the photon beam polarization degree,
- P_z^T is the target polarization degree.

The results for the E observable on the proton are shown in Fig. 6.5, 6.6 and 6.7. In the first figure the resulting observable E of this work (blue dots) is shown along with the results from a free proton target (green triangles) [98] and, for $W_{CM} > 1350\,\text{MeV}$, with the results from an independent analysis on a different data set collected by A2 collaboration (red dots) [99]. In the other figures, the results are shown along with the following theoretical models:

- BG 2014 02, the free proton model from Bonn-Gatchina [36],
- SAID 12, the free proton model from SAID [35],
- MAID 2007, the free proton model from MAID [31],
- MAID 2007 + IA, the MAID model with Fermi motion (IA) based on the Arenhövel-Fix model [97],
- MAID 2007 + IA + FSI, the MAID model with Fermi motion plus final state interaction (FSI) contribution based on the Arenhövel-Fix model [97].

All the numerical values can be found in App. E.

[1]By convention, the E observable has opposite sign than the polarized cross section.

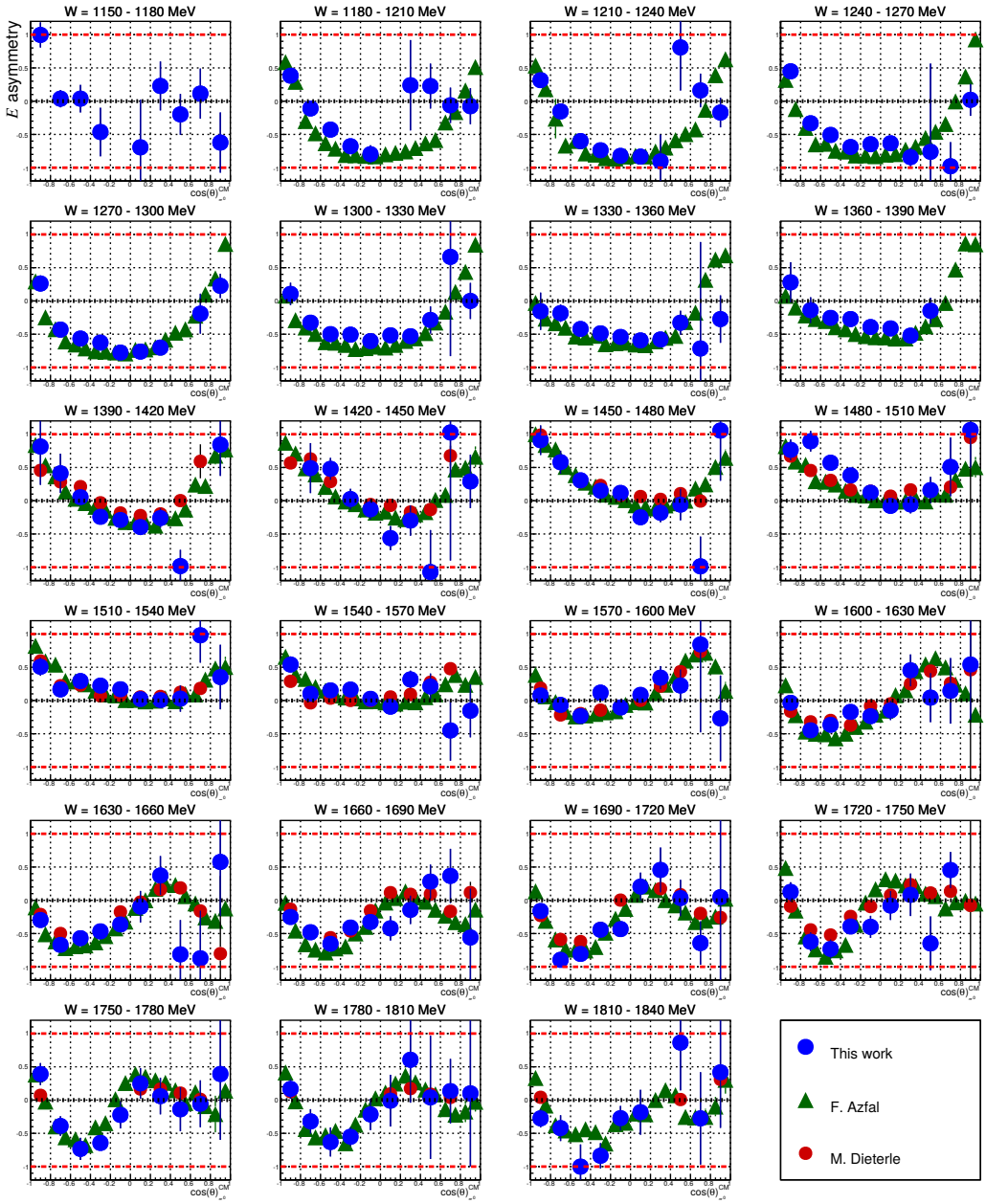

Figure 6.5: Results for the E observable from quasi-free protons as a function of $\cos(\theta)^{\mathrm{CM}}_{\pi^0}$. For comparison, the results of this work (blue dots) are plotted along with the results from free protons [98] and, for $W_{CM} > 1330$ MeV, with the results from [99]. The red dotted lines show the limits for the asymmetry.

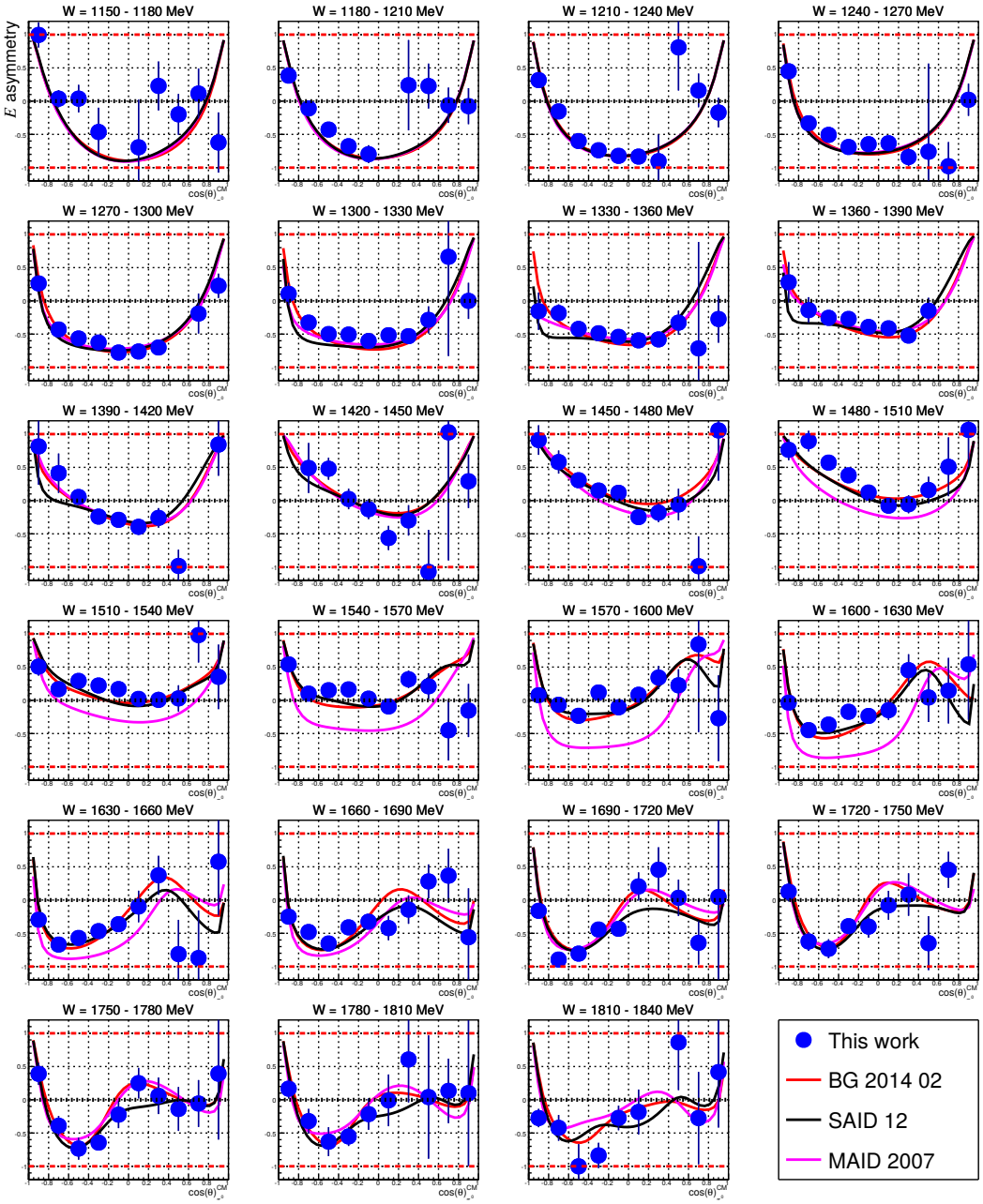

Figure 6.6: Results for the E observable from quasi-free protons as a function of $\cos(\theta)^{\mathrm{CM}}_{\pi^0}$. For comparison, the results of this work (blue dots) are plotted along with different free models, described in the text. The red dotted lines show the limits for the asymmetry.

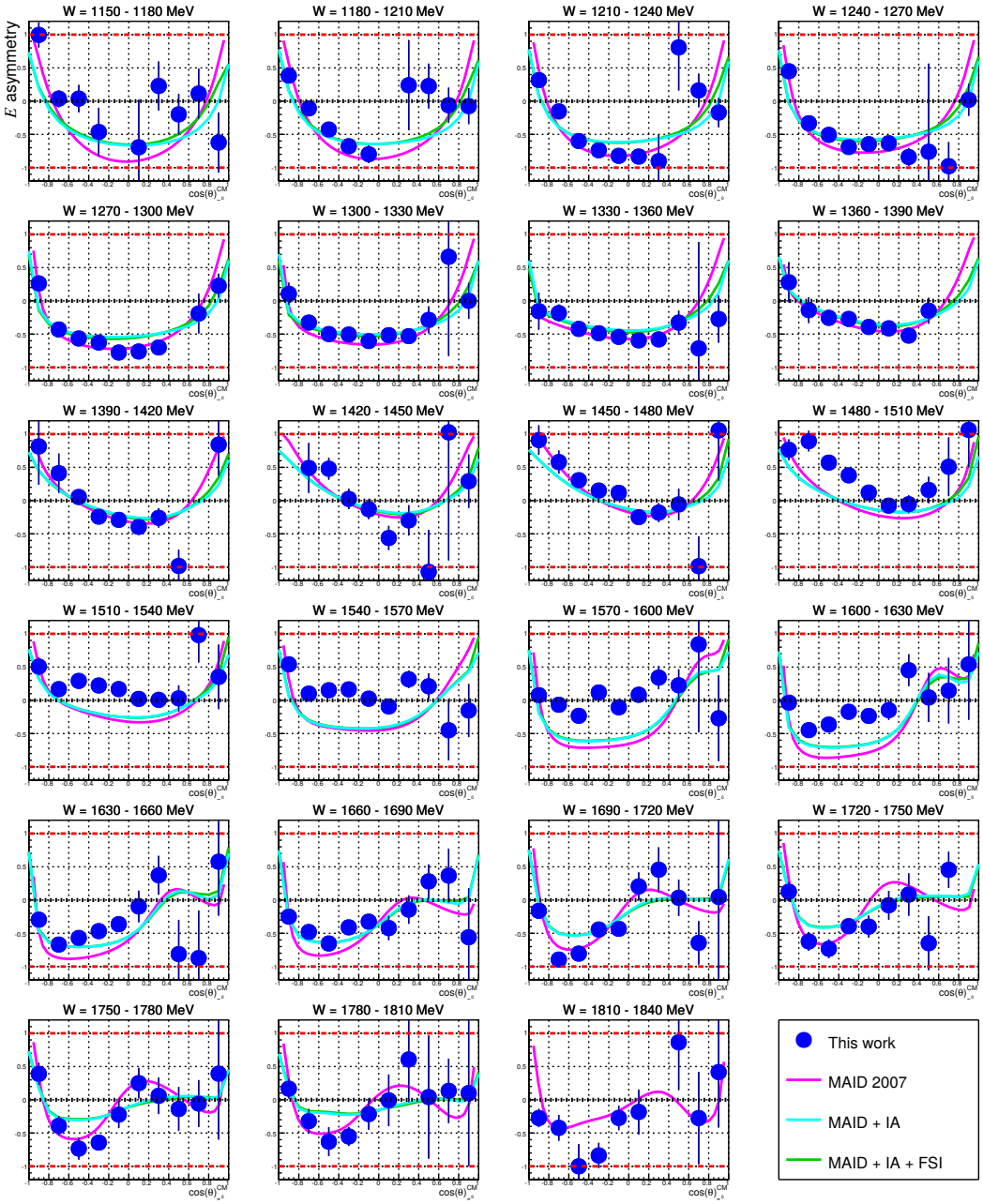

Figure 6.7: Results for the E observable from quasi-free protons as a function of $\cos(\theta)^{\mathrm{CM}}_{\pi^0}$. For comparison, the results of this work (blue dots) are plotted along with MAID model, MAID + IA and MAID + IA + FSI, as described in the text. The red dotted lines show the limits for the asymmetry.

Discussion

The results of the E asymmetry for the quasi-free proton channel are in agreement with the experimental results from free proton target [98]. This is due to the fact that the final state interaction affects both the numerator and the denominator of Eq. 2.41, and its global contribution to the E observable is smaller than in the absolute cross section case. This experimental observation is particularly important because it shows that the polarization asymmetry can be used to directly access the internal structure of the nucleon without the need for complicated model-dependent corrections. Another observation is that the MAID model, (compared to the experimental data,the SAID and Bonn-Gatchina model predictions) overestimates the cross section $\sigma_{\uparrow\uparrow}$ and underestimates $\sigma_{\uparrow\downarrow}$ in the energy region between $W = 1480$ MeV and $W = 1660$ MeV.

For $W > 1330\,\mathrm{MeV}$ the two independent results extracted by the A2 collaboration are in agreement with each other within the systematic errors.

6.3 E observable for single π^0 photoproduction on the neutron

The E observable for single π^0 photoproduction on quasi-free neutrons is given by the following formula:

$$E_n(W,\theta) = \frac{N_n^{\uparrow\downarrow}(W,\theta) - N_n^{\uparrow\uparrow}(W,\theta)}{[N_n^{\uparrow\downarrow}(W,\theta) + N_n^{\uparrow\uparrow}(W,\theta)]} \cdot \frac{1}{P_\odot^\gamma} \cdot \frac{1}{P_z^T} \tag{6.3}$$

where:

- $N_n^{\uparrow\uparrow}(W,\theta)$ and $N_n^{\uparrow\downarrow}(W,\theta)$ are the single π^0 events from the polarized neutron,
- $P_\odot^\gamma$ is the photon beam polarization degree,
- P_z^T is the target polarization degree.

The results for the E asymmetry for the neutron channel are shown in Fig. 6.8, 6.9 and 6.10. In the first figure, the resulting observable E of this work (blue dots) are shown, for $W_{CM} > 1350\,\text{MeV}$, along with the results from an independent analysis on a different data set collected in the same collaboration (red dots) [99]. In the other figures, the results are shown along with the following theoretical models:

- BG 2014 02, the free neutron model from Bonn-Gatchina [36],
- BG 2014 02 + IA, the free neutron model from Bonn-Gatchina with Fermi motion contribution [36],
- SAID 12, the free neutron model from SAID [35],
- MAID 2007, the free neutron model from MAID [31],
- MAID 2007 + IA, the MAID model with Fermi motion (IA) based on the Arenhövel-Fix model [97],
- MAID 2007 + IA + FSI, the MAID model with Fermi motion (IA) plus final state interaction (FSI) contributions based on the Arenhövel-Fix model [97].

All the numerical values can be found in App. E.

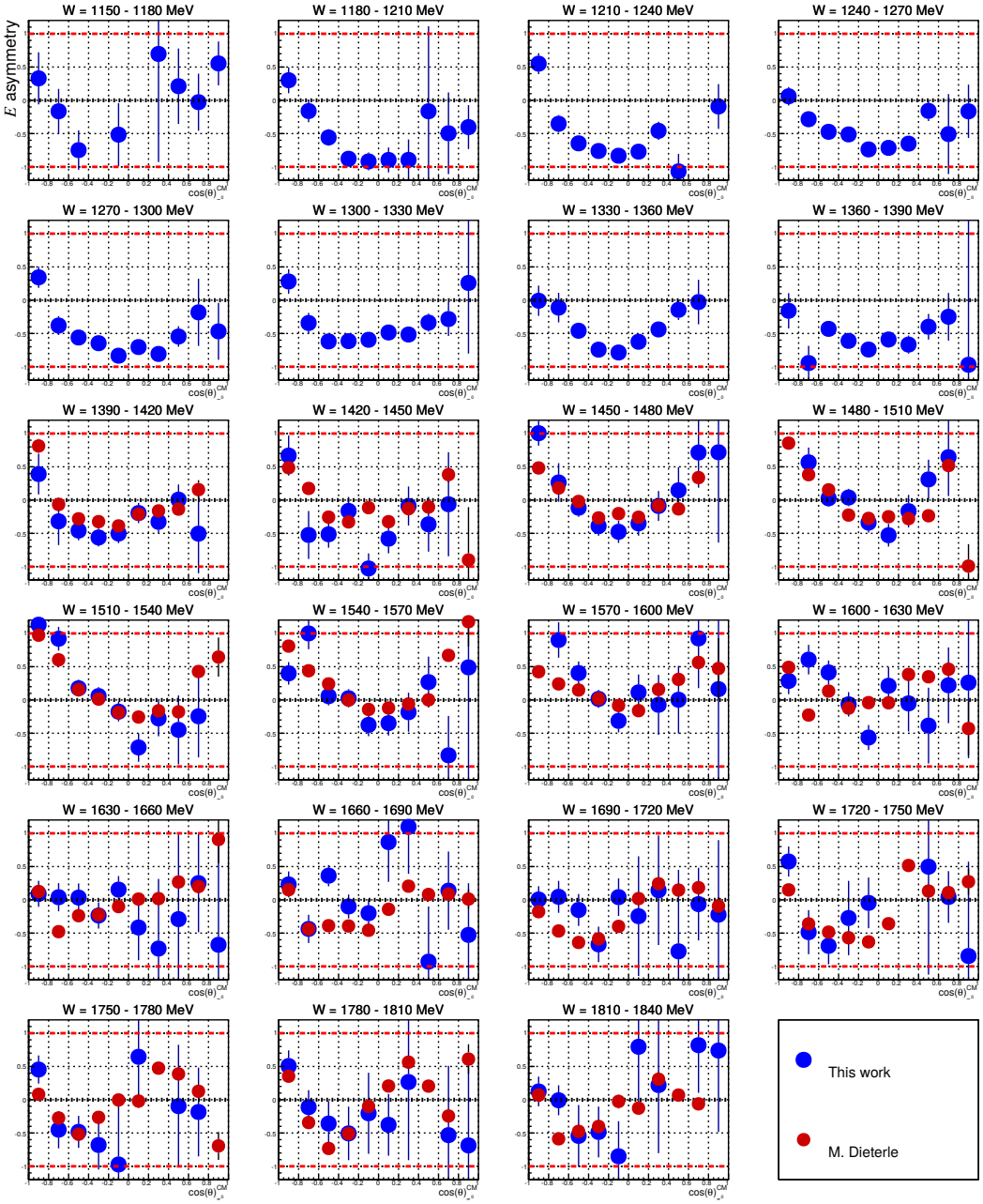

Figure 6.8: Results for the E observable from quasi-free neutrons as a function of $\cos(\theta)^{\mathrm{CM}}_{\pi^0}$. For $W_{CM} > 1330$ MeV the results from [99] are also plotted. The red dotted lines show the limits for the asymmetry.

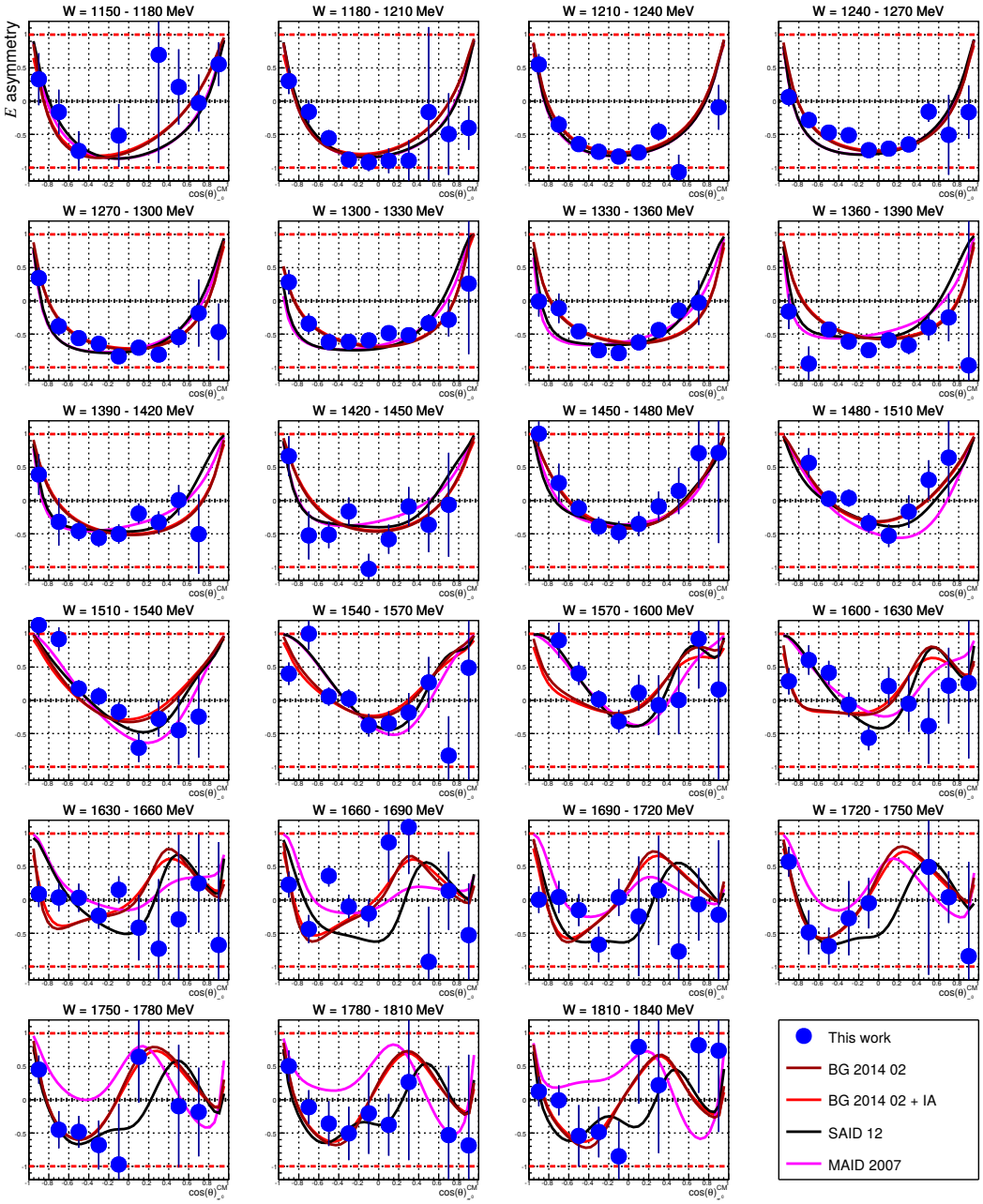

Figure 6.9: Results for the E observable from quasi-free neutrons as a function of $\cos(\theta)_{\pi^0}^{\mathrm{CM}}$. The results of this work (blue dots) are shown along with those of different models, as described in the text. The red dotted lines show the limits for the asymmetry.

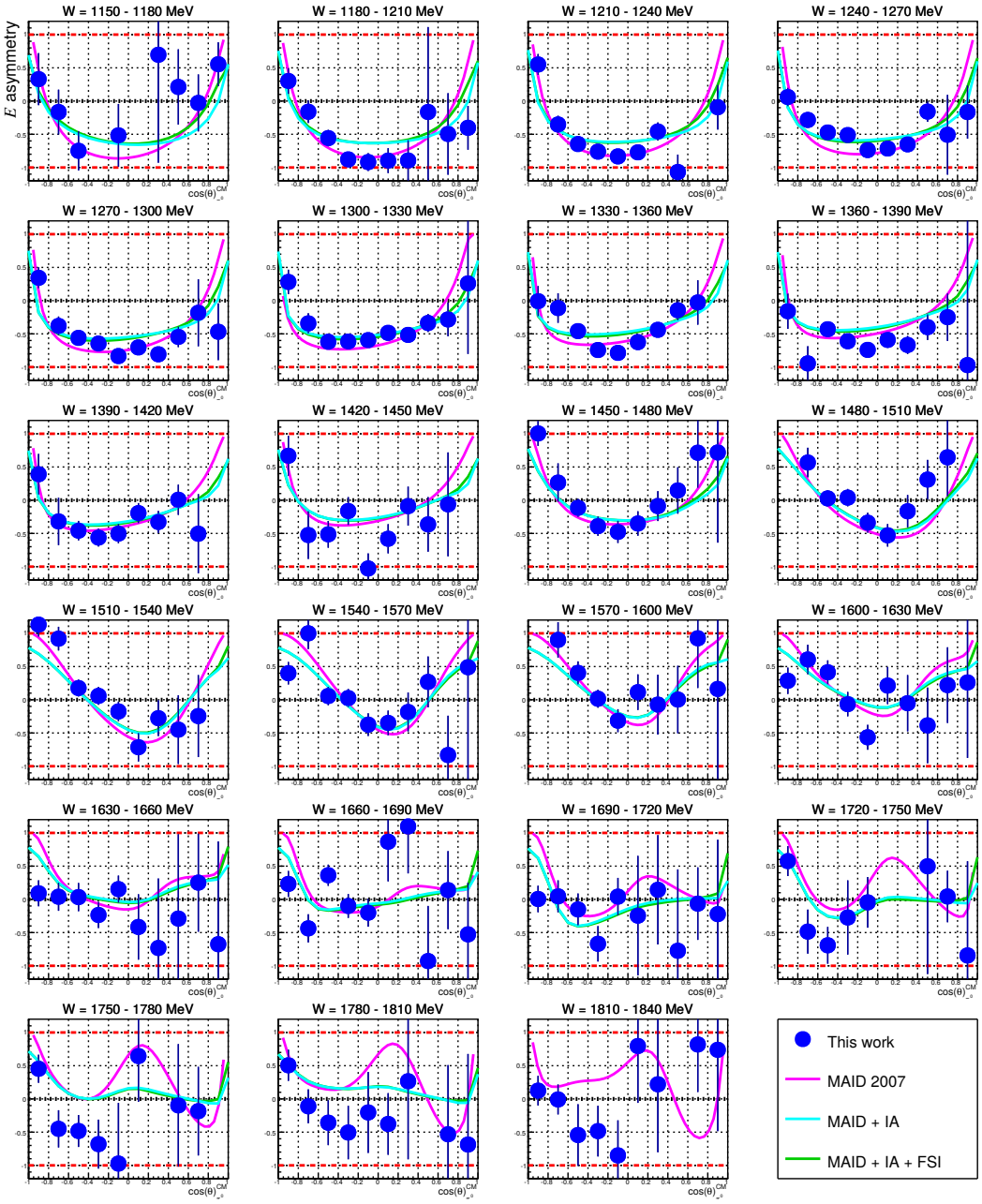

Figure 6.10: Results for the E observable from quasi-free neutrons as a function of $\cos(\theta)^{\mathrm{CM}}_{\pi^0}$. The results of this work (blue dots) are shown along with MAID, MAID + IA and MAID + IA + FSI models, as described in the text. The red dotted lines show the limits for the asymmetry.

Discussion

Despite the low statistics, the two independent results extracted by the A2 collaboration are in agreement with each other within the systematic errors. The data for W_{CM} <1350 MeV were acquired for the first time and offer the first description of the $\pi^0 - E$ observable of the neutron in the $\Delta-$resonance region. As shown for the case of the proton target, the effect of the final state interaction on the E observable is marginal. Therefore the study of observables which lead to a better understanding of the nucleon is feasible even without the availability of a free neutron target.

6.4 Partial wave fits

In order to perform the partial wave analysis formulated in Eq. 2.46, the results for the E observable have been multiplied by the unpolarized differential cross section from the SAID model [35], which fairly well reproduces the available unpolarized data both on the proton and on the neutron.

6.4.1 Legendre coefficients for the quasi-free proton

In Fig. 6.11 a sample of the results of Legendre polynomials fitted to the $\pi^0 p$ channel with $l_{max} = 1, 2, 3$, are shown.

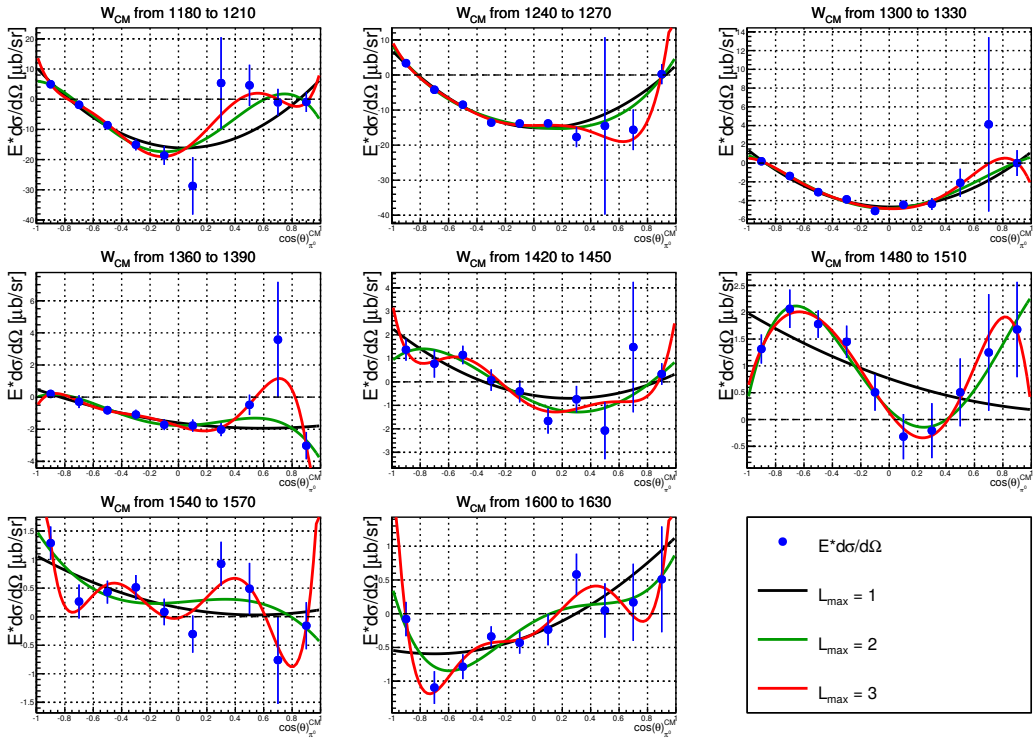

Figure 6.11: Sample of results on the parameter $\check{E}$ as a function of $\cos(\theta)^{\mathrm{CM}}_{\pi^0}$ for the $\pi^0 p$ channel, fitted with associated Legendre polynomials truncated at $l_{max} = 1$ (black), 2 (green) or 3 (red).

In Fig. 6.12 the resulting χ^2 and reduced χ^2 (χ^2/ndf) values are shown. Due to the low statistics in the collected data, it is not possible to identify a proper trend in the χ^2/ndf behavior, that could give a good indication for the optimal l_{max} selection. Nevertheless, with only ten data points, $l_{max} = 2$ has

been chosen as the best trade-off between fit efficacy and wave contribution analysis. The resulting parameters for $l_{max} = 2$ are shown in Fig. 6.13.

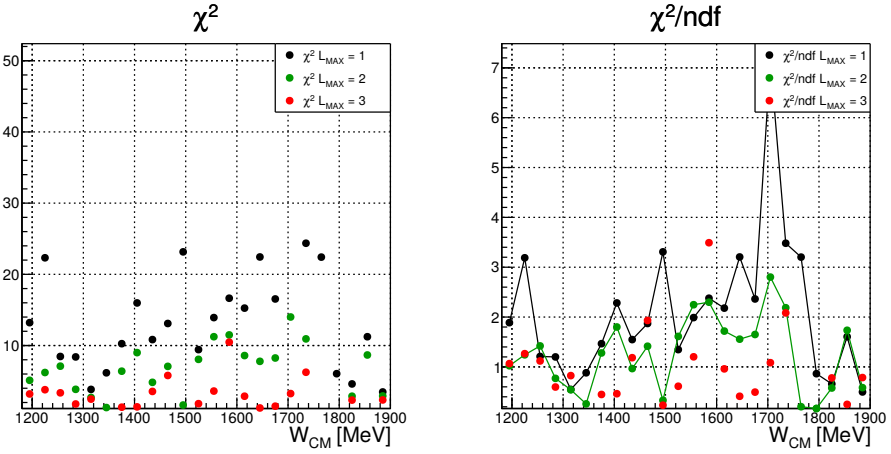

Figure 6.12: Resulting χ^2 and χ^2/ndf value for different l_{max} for the $\pi^0 p$ channel.Resulting χ^2 and χ^2/ndf values for the $\pi^0 p$ channel, shown for different l_{max} values.

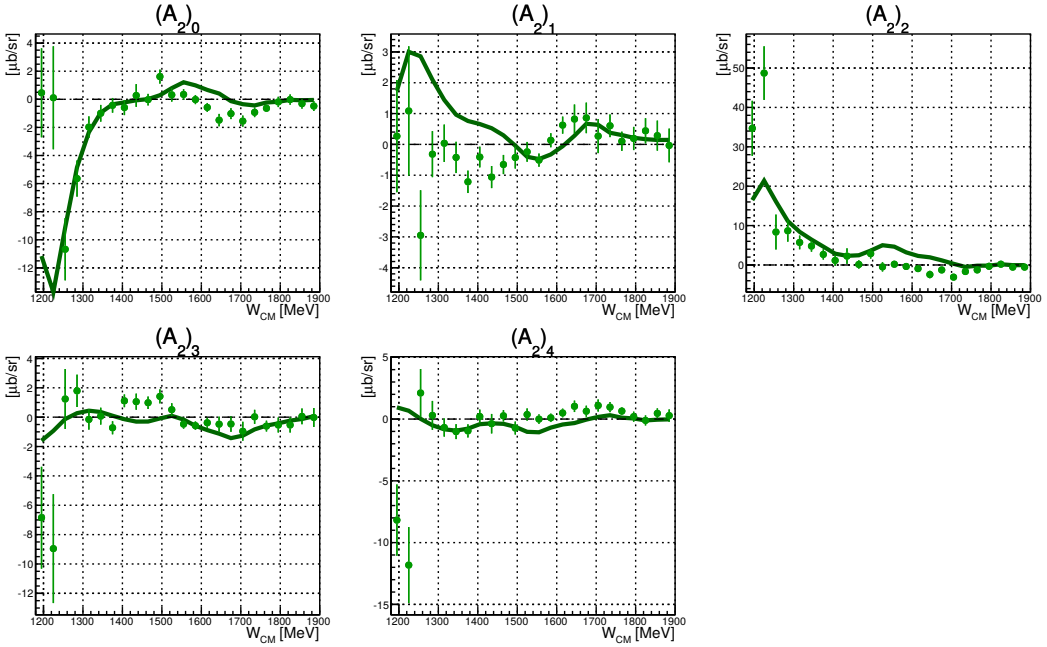

Figure 6.13: Resulting Legendre coefficients from the analysis of $\check{E}$ for $\pi^0 p$ channel with $l_{max} = 2$. The line shows the Legendre coefficients derived from the SAID model.

6.4.2 Legendre coefficients for the quasi-free neutron

The results of Legendre polynomials fitting to the $\pi^0 n$ channel with $l_{max} = 1, 2, 3$, are shown in Fig. 6.14.

As in the case of the proton channel, the statistics for the neutron channel as well is not enough to observe a trend in the χ^2/ndf behavior. Iig. 6.15 show the resulting χ^2 and χ^2/ndf values.

The resulting parameters with $l_{max} = 2$ are shown in Fig. 6.16.

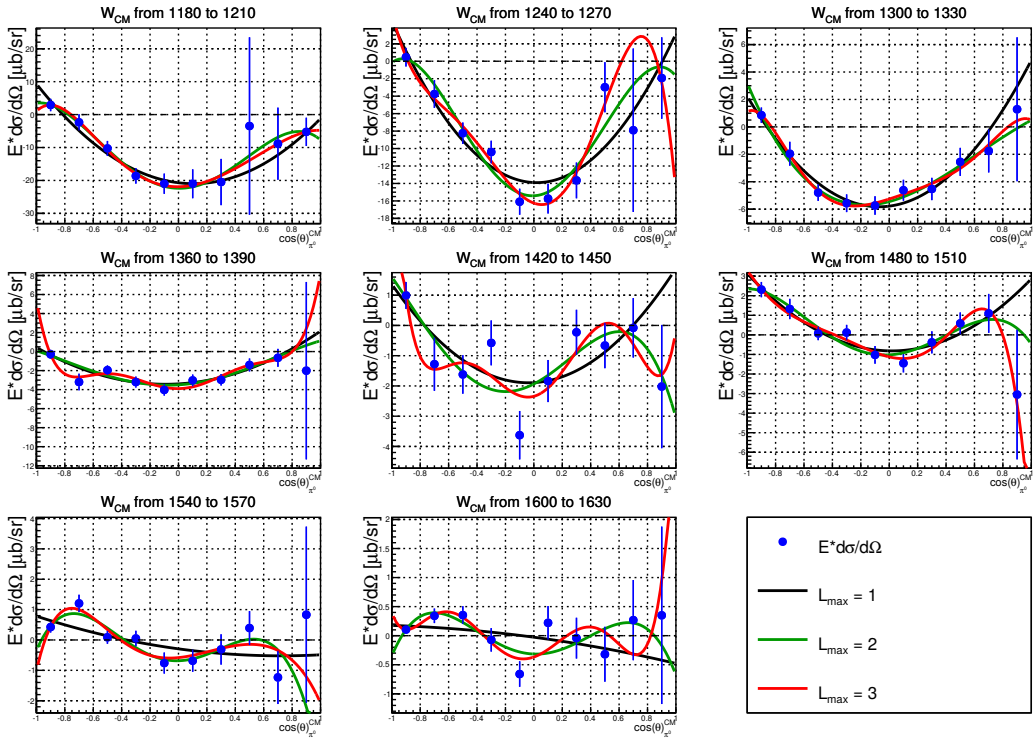

Figure 6.14: Sample of $\check{E}$ as a function of $\cos(\theta)^{\mathrm{CM}}_{\pi^0}$ for the $\pi^0 n$ channel, fitted with associated Legendre polynomials truncated at $l_{max} = 1$ (black), 2 (green) or 3 (red).

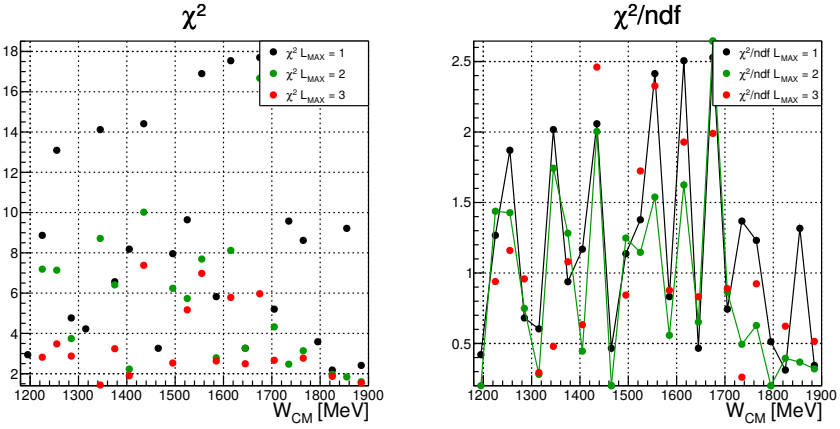

Figure 6.15: Resulting χ^2 and χ^2/ndf values for the $\pi^0 n$ channel, shown for different l_{max} values.

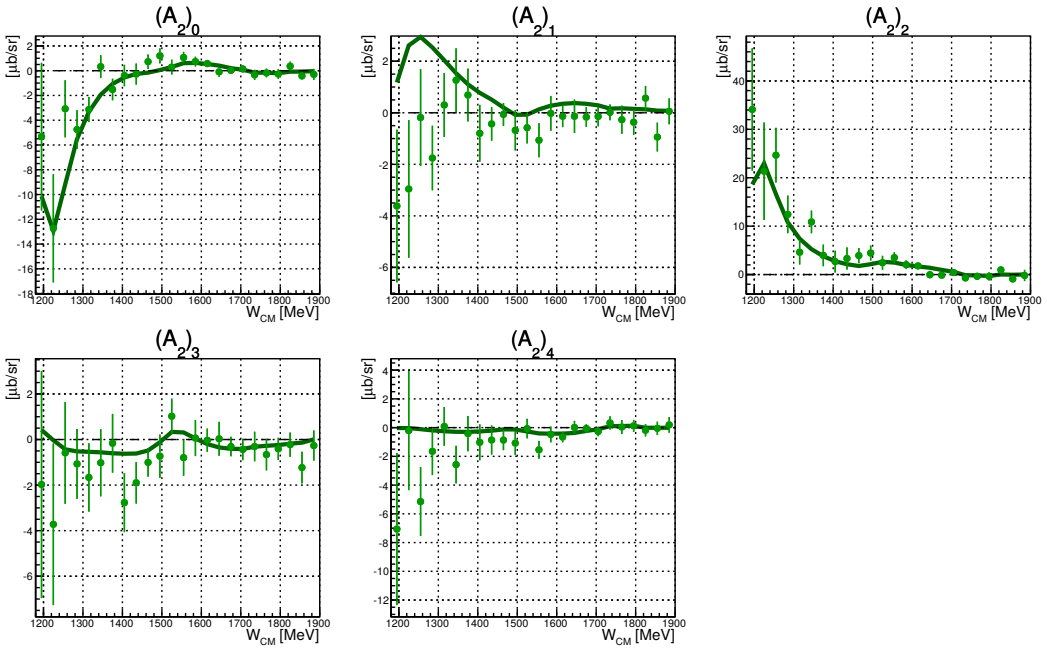

Figure 6.16: Legendre coefficients of $\check{E}$ for the $\pi^0 n$ channel with $l_{max} = 2$. The line shows the Legendre coefficients for the SAID model.

Discussion

The interferences of the partial waves up to $l_{max} = 3$, that are necessary to understand the Legendre polynomials fits, are shown in Tab. 6.1.

For the proton, it is possible to observe that, for energies in the range 1250-1400 MeV and $l_{max} = 1$, the χ^2/ndf is below 1.5. This is due to the fact that

in this energy region the dominant resonance is $\Delta(1232)$, which is described mainly by the $P-$wave. Above 1400 MeV the dominant resonance is $N(1520)$, described by the $D-$wave. At energies above 1700 MeV the contribution from the $F-$wave is also necessary to describe the third resonance region. Therefore $l_{max} = 2$ is not sufficient and the χ^2/ndf associated with this value increases above 1700 MeV, as shown in Fig. 6.12.

Above 1700 MeV the χ^2/ndf drops below 1 for any l_{max}. This is a result of the low statistics in this energy range. Due to the large error bars, any fit produces seemingly good results.

Table 6.1: Contributions of the partial wave interferences up to $l_{max} = 4$.

n	$l_{max} = 1$	$l_{max} = 2$	$l_{max} = 3$
0	$\langle S,S\rangle + \langle P,P\rangle$	$\langle D,D\rangle$	$\langle F,F\rangle$
1	$\langle S,P\rangle$	$\langle P,D\rangle$	$\langle D,F\rangle$
2	$\langle P,P\rangle$	$\langle S,D\rangle + \langle D,D\rangle$	$\langle P,F\rangle + \langle F,F\rangle$
3		$\langle P,D\rangle$	$\langle S,F\rangle + \langle D,F\rangle$
4		$\langle D,D\rangle$	$\langle P,F\rangle + \langle F,F\rangle$
5			$\langle D,F\rangle$
6			$\langle F,F\rangle$

From observation of the coefficients in Fig. 6.13, it is possible to underline a better defined structure in the coefficients $(A_2)_0$ and $(A_2)_2$ with smaller statistical error bars than in $(A_2)_1$ and $(A_2)_3$. This is because $(A_2)_0$ is only sensitive to pure interferences of terms with the same l (especially from $\langle S,S\rangle$ and $\langle P,P\rangle$), and $(A_2)_2$, although it includes additional interferences between different l, it depends mainly on $\langle P,P\rangle$. In this case, the $\Delta-$resonance contribution dominates in the measured energy range. On the other hand, $(A_2)_1$ and $(A_2)_3$ (valid also for any other odd coefficients with larger l) are only sensitive to interferences of terms with different values of l. Since the role of higher resonances in the measured energy range is small, the effect of those interference

terms is also quite small and consistent with zero over most of the measured interval.

Similar observations can also be made with regard to the quasi-free neutron target. The low statistics achieved because of the low-detection efficiency for the neutron, makes interpretation of the results for χ^2/ndf of Fig. 6.15 rather difficult. Therefore, it is difficult to observe an increasing trend for a value of $l_{max} = 1$ up to 1500 MeV, which was indeed observed for the proton channel. On the other hand, the drop of the χ^2/ndf values at energy above 1700 MeV due to the low statistics, is also evident in the neutron channel results.

Chapter 7

Conclusions

This work is part of the meson photoproduction experiments on nucleons performed in the A2 tagger hall of the Institut für Kernphysik at the University of Mainz.

This thesis focused on the study of the helicity dependence of single π^0 photoproduction using a deuteron target. The measurement was performed using either circularly or elliptically polarized photon beam of energy up to $E_\gamma = 1400$ MeV and a longitudinally polarized deuterated butanol target. For the first data taking, a new target material was used (deuterated butanol with trityl doping radicals). This new composition was very promising, with a target polarization degree, which was measured during the test, higher than 60%. During the data taking, the measurement of the target polarization degree was not precise, because the new material was very sensitive to local inhomogeneity of the magnetic field and the frequency range for an effective polarization was very narrow. An additional data taking with a better known target material (deuterated butanol with TEMPO doping), which had a lower target polarization degree, was performed in order to extract a correction factor and recover the old data.

The inclusive polarized cross section for single π^0 photoproduction on the deuteron was measured in the range $E_\gamma = 153 - 1300$ MeV, with a precise and effective control of the photon flux. This measurement was also used as reference and cross check for better understanding of the target polarization. The results obtained from the data collected with the trityl target were normalized in order to match the results obtained with the TEMPO target. Moreover the cross section results show agreement with the existing measurements, are

provided within an enlarged energy range, have a reduced statistical errors and cover the full solid angle.

The double polarized observable E for single π^0 photoproduction on the proton and on the neutron have been measured in the energy range $W = 1150 - 1870$ MeV with a full coverage of the angular range. For the extraction of this asymmetry it is crucial to evaluate the background contribution of the unpolarized target nuclei inside the butanol molecule. A dedicated data taking was done with use of a carbon foam target in order to measure the unpolarized nuclei contributions. A detailed analysis was performed to perform the subtraction of the carbon foam data from the deuterated butanol data.

The comparison of the results on a quasi-free proton target from this work with the results on a free proton target, provides new information which can be used to better study the Fermi motion and the final state interactions inside the deuteron. In particular, the small impact of the final state interactions gives the opportunity to study the neutron, despite the impossibility of a free neutron target.

The results for the neutron in the energy range $W = 1150 - 1350$ MeV are the first world data available, and they are the principal outcome of this work. Thanks to the large acceptance Crystal-Ball/TAPS apparatus, it was possible to cover the full angular range, and to achieve a precise identification of the recoil neutron.

These new experimental results enlarge the global set of experimental data available both for the inclusive polarized single π^0 photoproduction cross section on the deuteron, and for the single π^0 E observable for the proton and neutron. This additional information provides precious input towards a better understanding of the nucleon resonances and new constrains for the theoretical models describing those resonances.

Appendix A

Polarization observables

The general form of the cross section with all the contributions from target, beam and recoil polarization can be written [26]:

$$
\begin{aligned}
d\sigma^{B,T,R}(\vec{P^{\gamma}},\vec{P^{T}},\vec{P^{R}}) =& \frac{1}{2}\{d\sigma_0[1 - P_L^{\gamma}P_y^T P_{y'}^R cos(2\phi_\gamma)] \\
&+ \hat{\Sigma}[-P_L^{\gamma}\cos(2\phi_\gamma) + P_y^T P_{y'}^R] \\
&+ \hat{T}[P_y^T - P_L^{\gamma}P_{y'}^R\cos(2\phi_\gamma)] \\
&+ \hat{P}[P_{y'}^R - P_L^{\gamma}P_y^T\cos(2\phi_\gamma)] \\
&+ \hat{E}[-P_{\odot}^{\gamma}P_z^T - P_L^{\gamma}P_x^T P_{y'}^R\sin(2\phi_\gamma)] \\
&+ \hat{G}[P_L^{\gamma}P_z^T\sin(2\phi_\gamma) - P_{\odot}^{\gamma}P_x^T P_{y'}^R] \\
&+ \hat{F}[P_{\odot}^{\gamma}P_x^T - P_L^{\gamma}P_z^T P_{y'}^R\sin(2\phi_\gamma)] \\
&+ \hat{H}[P_L^{\gamma}P_x^T\sin(2\phi_\gamma) - P_{\odot}^{\gamma}P_z^T P_{y'}^R] \\
&+ \hat{C_{x'}}[P_{\odot}^{\gamma}P_{x'}^R - P_L^{\gamma}P_y^T P_{z'}^R\sin(2\phi_\gamma)] \\
&+ \hat{C_{z'}}[P_{\odot}^{\gamma}P_{\prime}^R - P_L^{\gamma}P_y^T P_{x'}^R\sin(2\phi_\gamma)] \\
&+ \hat{O_{x'}}[P_L^{\gamma}P_{x'}^R\sin(2\phi_\gamma) + P_{\odot}^{\gamma}P_y^T P_{x'}^R] \\
&+ \hat{O_{z'}}[P_L^{\gamma}P_{z'}^R\sin(2\phi_\gamma) - P_{\odot}^{\gamma}P_y^T P_{z'}^R] \\
&+ \hat{L_{x'}}[P_z^T P_{x'}^R - P_L^{\gamma}P_x^T P_{z'}^R\cos(2\phi_\gamma)] \\
&+ \hat{L_{z'}}[P_z^T P_{z'}^R - P_L^{\gamma}P_x^T P_{x'}^R\cos(2\phi_\gamma)] \\
&+ \hat{T_{x'}}[P_x^T P_{x'}^R - P_L^{\gamma}P_x^T P_{z'}^R\cos(2\phi_\gamma)] \\
&+ \hat{T_{z'}}[P_x^T P_{x'}^R - P_L^{\gamma}P_x^T P_{z'}^R\cos(2\phi_\gamma)]
\end{aligned}
\tag{A.1}
$$

Table A.1: Helicity and transversity representation of the spin observables.

Spin observable	Helicity representation	Transversity representation
σ_0	$\frac{1}{2}(\lvert H_1\rvert^2 + \lvert H_2\rvert^2 + \lvert H_3\rvert^2 + \lvert H_4\rvert^2)$	$\frac{1}{2}(\lvert b_1\rvert^2 + \lvert b_2\rvert^2 + \lvert b_3\rvert^2 + \lvert b_4\rvert^2)$
Σ	$\mathrm{Re}(-H_1H_4^* + H_2H_3^*)$	$\frac{1}{2}(\lvert b_1\rvert^2 + \lvert b_2\rvert^2 - \lvert b_3\rvert^2 - \lvert b_4\rvert^2)$
T	$-\mathrm{Im}(H_1H_2^* + H_3H_4^*)$	$\frac{1}{2}(\lvert b_1\rvert^2 - \lvert b_2\rvert^2 - \lvert b_3\rvert^2 + \lvert b_4\rvert^2)$
P	$\mathrm{Im}(H_1H_3^* + H_2H_4^*)$	$\frac{1}{2}(-\lvert b_1\rvert^2 + \lvert b_2\rvert^2 - \lvert b_3\rvert^2 + \lvert b_4\rvert^2)$
G	$\mathrm{Im}(H_1H_4^* + H_2H_3^*)$	$\mathrm{Im}(-b_1b_3^* - b_2b_4^*)$
H	$\mathrm{Im}(-H_2H_4^* + H_1H_3^*)$	$\mathrm{Re}(b_1b_3^* - b_2b_4^*)$
E	$\frac{1}{2}(\lvert H_1\rvert^2 - \lvert H_2\rvert^2 + \lvert H_3\rvert^2 - \lvert H_4\rvert^2)$	$\mathrm{Re}(b_1b_3^* + b_2b_4^*)$
F	$\mathrm{Re}(-H_2H_1^* + H_4H_3^*)$	$\mathrm{Im}(b_1b_3^* - b_2b_4^*)$
O_x	$\mathrm{Im}(-H_2H_1^* + H_4H_3^*)$	$\mathrm{Re}(-b_1b_4^* + b_2b_3^*)$
O_z	$-\mathrm{Im}(H_1H_4^* + H_2H_3^*)$	$-\mathrm{Im}(-b_1b_4^* - b_2b_3^*)$
C_x	$-\mathrm{Re}(H_2H_4^* + H_1H_3^*)$	$-\mathrm{Im}(b_1b_4^* - b_2b_3^*)$
C_z	$\frac{1}{2}(\lvert H_1\rvert^2 + \lvert H_2\rvert^2 - \lvert H_3\rvert^2 - \lvert H_4\rvert^2)$	$-\mathrm{Re}(b_1b_4^* + b_2b_3^*)$
T_x	$-\mathrm{Re}(-H_1H_4^* - H_2H_3^*)$	$-\mathrm{Re}(-b_1b_2^* + b_3b_4^*)$
T_z	$-\mathrm{Re}(-H_1H_2^* + H_4H_3^*)$	$-\mathrm{Im}(b_1b_2^* - b_3b_4^*)$
L_x	$\mathrm{Re}(H_2H_4^* - H_1H_3^*)$	$\mathrm{Im}(-b_1b_2^* - b_3b_4^*)$
L_z	$\frac{1}{2}(-\lvert H_1\rvert^2 + \lvert H_2\rvert^2 + \lvert H_3\rvert^2 - \lvert H_4\rvert^2)$	$\mathrm{Re}(-b_1b_2^* - b_3b_4^*)$

Appendix B

Reaction kinematics

This section presents the kinematic equations to describe the single π^0 photoproduction from the deuteron, in the case where the proton is involved in the reaction, and the neutron is spectator:

$$\gamma + d \rightarrow \pi^0 + p + (n) \tag{B.1}$$

The energy and the momentum conservation for the reaction can be written as follows:

$$E_\gamma + E_d = E_{\pi^0} + E_p + E_n, \tag{B.2}$$

$$\overrightarrow{p}_\gamma + \overrightarrow{p}_d = \overrightarrow{p}_{\pi^0} + \overrightarrow{p}_p + \overrightarrow{p}_n. \tag{B.3}$$

As it is the standard in relativistic kinematics, the speed of light c is considered unitary. The momentum of the photon $\overrightarrow{p}_\gamma$ in Eq. B.3 can be replaced with E_γ.

For the reaction of interest for this work, the initial state is fully known because E_γ is provided by the tagger, and the deuteron is at rest; thus $p_d = 0$, and $E_d = m_d$ can be plugged in Eq. B.2 and in Eq. B.3, respectively. It is important to note that the neutron and the proton inside the deuteron are not at rest, but they have a momentum (equal and opposite) given by the Fermi motion, so following this relation:

$$|p_d| = |p_{n_0}| - |p_{p_0}| = 0 \tag{B.4}$$

Because the neutron is not involved in the reaction, its momentum is constant $p_{n_0} = p_n$, from Eq. B.4 it follows:

$$|p_{p_0}| = |p_{n_0}| = |p_n| \,. \tag{B.5}$$

After the interaction, the A2 detectors provide the full kinetic information (energy and trajectory) about the π^0 and the trajectory of the proton. The energy of the proton E_p, the energy of the neutron E_n and the coordinates of the neutron spectator are unknown. The total energy of the proton E_p can be written as:

$$E_p = T_p + m_p,$$

where T_p is the kinetic energy of the proton. This quantity can be determined using the known quantities from the detectors. For simplicity, the following three parameters are defined:

$$\begin{aligned} a &= p_{\pi^0,x} \cdot \sin\theta_p \cdot \sin\phi_p + p_{\pi^0,y} \cdot \sin\theta_p \cdot \sin\phi_p + (p_{\pi^0,z} - E_\gamma) cos\theta_p, \\ b &= E_{\pi^0} - E_\gamma - m_d, \\ c &= (E_{\pi^0} + m_p - E_\gamma - m_d)^2 - (m_n^2 + p_{\pi^0}^2 + E_\gamma^2 - 2E_\gamma p_{\pi^0,z}). \end{aligned} \tag{B.6}$$

The kinetic energy of the proton T_p can be written as:

$$T_p = \frac{-(4bc - 8a^2 m_p) + \sqrt{(4bc - 8a^2 m_p)^2 - 4(4b^2 - 4a^2) \cdot c^2}}{2(4b^2 - 4a^2)}. \tag{B.7}$$

The momentum of the proton can be expressed as:

$$|p_p| = \sqrt{E_p^2 - m_p^2} = \sqrt{(T_p + m_p)^2 - m_p^2} = \sqrt{T_p(T_p + 2m_P)}.$$

From Eq. B.2, the energy of the neutron E_n can be calculated:

$$E_n = E_\gamma + m_d - E_{\pi^0} - E_p,$$

The momentum of the neutron $|p_n|$ can be written as:

$$|p_n| = \sqrt{E_n^2 - m_n^2},$$

and, from Eq. B.5, it also corresponds to $|p_{p_0}|$ and to $|p_{n_0}|$.

Because the z-axis of the frame is aligned along the photon beamline, it is possible to select only this component from Eq. B.3, as it follows:

$$p_\gamma = E_\gamma = p_{\pi^0,z} + p_{p,z} + p_{n,z},$$

where the z component of $\overrightarrow{p}_n$ is unknown, but it can be extracted using the following relations:

$$\cos\theta_n = \frac{E_\gamma - p_{\pi^0} \cdot \cos\theta_{\pi^o} - p_p \cos\theta_p}{p_n},$$
$$p_{n,z} = \overrightarrow{p}_n \cos\theta_n.$$

Once that all the information about energy and momentum in Eq. B.1 are known, it is possible to switch from the laboratory to the CM frame. W_{CM} can be expressed as:

$$W = \sqrt{s} = \sqrt{(E_\gamma + E_{p_0})^2 - E_\gamma^2 - p_{p_0}^2 - 2E_\gamma p_{p_0}},$$

from where, the photon energy and the pion energy in CM E^*_γ and $E^*_{\pi^0}$ can be expressed as:

$$E^*_\gamma = \frac{E_\gamma(E_{p_0} - p_{p_0,z})}{W}, \tag{B.8}$$

$$E^*_{\pi^0} = \frac{(s + m^2_{\pi^0} - m^2_p)}{2W}. \tag{B.9}$$

Finally, the pion angle in the CM is derived:

$$\cos\theta^*_{\pi^0} = \frac{E^*_{\pi^0}}{p^*_{\pi^0}}[1 - \frac{E_\gamma E_{\pi^0}}{E^*_\gamma E^*_{\pi^0}} \cdot (1 - \frac{p_{\pi^0}}{E_{\pi^0}} \cos\theta_{\pi^0})]. \tag{B.10}$$

For the case where the π^0 is produced on the neutron and the proton is spectator, it is sufficient to switch proton and neutron in all the previous equations.

Appendix C

Tagger channels energy

The photon and electron energy for each tagger channel are showed in the table below.

Table C.1: Photon energy, electron energy and energy width for the tagger channels.

Channel number	Electron Energy [MeV]	Photon Energy [MeV]	Width [MeV]	Channel number	Electron Energy [MeV]	Photon Energy [MeV]	Width [MeV]
1	110.294	1446.706	1.982	177	714.038	842.962	4.662
2	112.291	1444.709	2.065	178	718.271	838.729	4.593
3	114.373	1442.627	2.149	179	722.412	834.588	4.518
4	116.537	1440.463	2.231	180	726.607	830.393	4.546
5	118.785	1438.215	2.318	181	730.807	826.193	4.573
6	121.118	1435.882	2.408	182	735.013	821.987	4.6
7	123.544	1433.456	2.5	183	739.223	817.777	4.627
8	126.061	1430.939	2.591	184	743.439	813.561	4.655
9	128.665	1428.335	2.68	185	747.659	809.341	4.681
10	131.354	1425.646	2.765	186	751.884	805.116	4.707
11	134.125	1422.875	2.847	187	756.114	800.886	4.735
12	136.976	1420.024	2.923	188	760.349	796.651	4.762
13	139.9	1417.1	2.996	189	764.648	792.352	4.67
14	142.892	1414.108	3.063	190	768.831	788.169	4.576
15	145.947	1411.053	3.124	191	773.08	783.92	4.602

16	149.056	1407.944	3.176	192	777.333	779.667	4.63
17	152.213	1404.787	3.223	193	781.59	775.41	4.655
18	155.407	1401.593	3.257	194	785.851	771.149	4.682
19	158.634	1398.366	3.283	195	790.116	766.884	4.708
20	161.878	1395.122	3.301	196	794.385	762.615	4.735
21	165.134	1391.866	3.301	197	798.659	758.341	4.761
22	168.387	1388.613	3.293	198	802.936	754.064	4.786
23	171.63	1385.37	3.273	199	807.218	749.782	4.814
24	174.849	1382.151	3.243	200	811.502	745.498	4.84
25	178.034	1378.966	3.206	201	815.844	741.156	4.759
26	181.179	1375.821	3.162	202	820.083	736.917	4.679
27	184.276	1372.724	3.11	203	824.379	732.621	4.704
28	187.321	1369.679	3.06	204	828.678	728.322	4.729
29	190.312	1366.688	3.006	205	832.981	724.019	4.755
30	193.249	1363.751	2.956	206	837.286	719.714	4.782
31	196.138	1360.862	2.911	207	841.596	715.404	4.807
32	198.987	1358.013	2.871	208	845.908	711.092	4.833
33	201.778	1355.222	2.88	209	850.224	706.776	4.858
34	204.58	1352.42	2.932	210	854.543	702.457	4.884
35	207.368	1349.632	2.971	211	858.864	698.136	4.91
36	210.164	1346.836	2.995	212	863.189	693.811	4.937
37	212.978	1344.022	3.008	213	867.581	689.419	4.833
38	215.814	1341.186	3.027	214	871.846	685.154	4.727
39	218.702	1338.298	2.977	215	876.178	680.822	4.753
40	221.525	1335.475	2.928	216	880.514	676.486	4.777
41	224.394	1332.606	2.954	217	884.852	672.148	4.803
42	227.276	1329.724	2.984	218	889.192	667.808	4.828
43	230.169	1326.831	3.01	219	893.534	663.466	4.852
44	233.071	1323.929	3.041	220	897.88	659.12	4.877
45	235.986	1321.014	3.068	221	902.227	654.773	4.902
46	238.911	1318.089	3.098	222	906.576	650.424	4.927
47	241.847	1315.153	3.126	223	910.928	646.072	4.953
48	244.792	1312.208	3.154	224	915.282	641.718	4.978

49	247.789	1309.211	3.106	225	919.704	637.296	4.869
50	250.72	1306.28	3.055	226	923.994	633.006	4.758
51	253.701	1303.299	3.086	227	928.354	628.646	4.782
52	256.692	1300.308	3.112	228	932.715	624.285	4.807
53	259.694	1297.306	3.142	229	937.078	619.922	4.83
54	262.709	1294.291	3.17	230	941.442	615.558	4.855
55	265.736	1291.264	3.197	231	945.808	611.192	4.879
56	268.774	1288.226	3.226	232	950.176	606.824	4.903
57	271.855	1285.145	3.191	233	954.545	602.455	4.927
58	274.882	1282.118	3.151	234	958.916	598.084	4.952
59	277.955	1279.045	3.18	235	963.287	593.713	4.976
60	281.039	1275.961	3.208	236	967.66	589.34	4.999
61	284.134	1272.866	3.237	237	972.094	584.906	4.906
62	287.241	1269.759	3.264	238	976.41	580.59	4.809
63	290.361	1266.639	3.293	239	980.786	576.214	4.833
64	293.492	1263.508	3.325	240	985.164	571.836	4.857
65	296.634	1260.366	3.353	241	989.542	567.458	4.88
66	299.788	1257.212	3.382	242	993.92	563.08	4.904
67	302.953	1254.047	3.41	243	998.301	558.699	4.926
68	306.171	1250.829	3.358	244	1002.682	554.318	4.951
69	309.319	1247.681	3.304	245	1007.063	549.937	4.973
70	312.519	1244.481	3.333	246	1011.445	545.555	4.997
71	315.732	1241.268	3.361	247	1015.827	541.173	5.02
72	318.956	1238.044	3.39	248	1020.211	536.789	5.044
73	322.192	1234.808	3.42	249	1024.655	532.345	4.943
74	325.439	1231.561	3.448	250	1028.978	528.022	4.844
75	328.698	1228.302	3.477	251	1033.362	523.638	4.867
76	331.968	1225.032	3.508	252	1037.747	519.253	4.888
77	335.286	1221.714	3.467	253	1042.132	514.868	4.912
78	338.545	1218.455	3.423	254	1046.517	510.483	4.933
79	341.849	1215.151	3.453	255	1050.902	506.098	4.958
80	345.167	1211.833	3.48	256	1055.287	501.713	4.979
81	348.495	1208.505	3.512	257	1059.672	497.328	5.001

82	351.833	1205.167	3.538	258	1064.057	492.943	5.025
83	355.185	1201.815	3.568	259	1068.442	488.558	5.047
84	358.548	1198.452	3.597	260	1072.826	484.174	5.069
85	361.922	1195.078	3.627	261	1077.274	479.726	4.965
86	365.344	1191.656	3.582	262	1081.595	475.405	4.86
87	368.704	1188.296	3.537	263	1085.978	471.022	4.883
88	372.112	1184.888	3.564	264	1090.361	466.639	4.904
89	375.532	1181.468	3.595	265	1094.745	462.255	4.925
90	378.962	1178.038	3.624	266	1099.128	457.872	4.949
91	382.403	1174.597	3.652	267	1103.509	453.491	4.969
92	385.856	1171.144	3.682	268	1107.89	449.11	4.991
93	389.32	1167.68	3.711	269	1112.271	444.729	5.013
94	392.795	1164.205	3.74	270	1116.651	440.349	5.034
95	396.315	1160.685	3.704	271	1121.029	435.971	5.056
96	399.778	1157.222	3.664	272	1125.407	431.593	5.077
97	403.285	1153.715	3.693	273	1129.839	427.161	4.99
98	406.804	1150.196	3.722	274	1134.162	422.838	4.905
99	410.333	1146.667	3.751	275	1138.537	418.463	4.925
100	413.874	1143.126	3.78	276	1142.911	414.089	4.945
101	417.425	1139.575	3.81	277	1147.284	409.716	4.966
102	420.986	1136.014	3.841	278	1151.656	405.344	4.989
103	424.559	1132.441	3.869	279	1156.026	400.974	5.009
104	428.183	1128.817	3.816	280	1160.396	396.604	5.029
105	431.735	1125.265	3.762	281	1164.765	392.235	5.05
106	435.34	1121.66	3.791	282	1169.132	387.868	5.072
107	438.953	1118.047	3.821	283	1173.497	383.503	5.092
108	442.579	1114.421	3.849	284	1177.862	379.138	5.113
109	446.213	1110.787	3.878	285	1182.292	374.708	5.001
110	449.859	1107.141	3.908	286	1186.587	370.413	4.887
111	453.514	1103.486	3.936	287	1190.947	366.053	4.907
112	457.18	1099.82	3.966	288	1195.305	361.695	4.928
113	460.855	1096.145	3.995	289	1199.661	357.339	4.948
114	464.579	1092.421	3.95	290	1204.016	352.984	4.969

115	468.237	1088.763	3.905	291	1208.369	348.631	4.987
116	471.943	1085.057	3.933	292	1212.721	344.279	5.008
117	475.658	1081.342	3.963	293	1217.07	339.93	5.028
118	479.384	1077.616	3.991	294	1221.419	335.581	5.047
119	483.119	1073.881	4.021	295	1225.765	331.235	5.068
120	486.864	1070.136	4.051	296	1230.108	326.892	5.087
121	490.618	1066.382	4.08	297	1234.506	322.494	4.994
122	494.382	1062.618	4.109	298	1238.79	318.21	4.899
123	498.155	1058.845	4.139	299	1243.128	313.872	4.919
124	501.983	1055.017	4.077	300	1247.464	309.536	4.938
125	505.73	1051.27	4.013	301	1251.798	305.202	4.957
126	509.531	1047.469	4.041	302	1256.129	300.871	4.977
127	513.341	1043.659	4.071	303	1260.458	296.542	4.995
128	517.161	1039.839	4.1	304	1264.785	292.215	5.016
129	520.99	1036.01	4.13	305	1269.11	287.89	5.033
130	524.827	1032.173	4.158	306	1273.433	283.567	5.054
131	528.674	1028.326	4.189	307	1277.753	279.247	5.071
132	532.53	1024.47	4.217	308	1282.071	274.929	5.092
133	536.395	1020.605	4.246	309	1286.444	270.556	4.992
134	540.315	1016.685	4.18	310	1290.699	266.301	4.896
135	544.149	1012.851	4.113	311	1295.009	261.991	4.915
136	548.039	1008.961	4.141	312	1299.317	257.683	4.933
137	551.938	1005.062	4.171	313	1303.621	253.379	4.952
138	555.845	1001.155	4.198	314	1307.924	249.076	4.97
139	559.761	997.239	4.227	315	1312.224	244.776	4.988
140	563.685	993.315	4.255	316	1316.522	240.478	5.008
141	567.617	989.383	4.284	317	1320.816	236.184	5.026
142	571.558	985.442	4.313	318	1325.108	231.892	5.042
143	575.506	981.494	4.342	319	1329.397	227.603	5.062
144	579.463	977.537	4.371	320	1333.684	223.316	5.078
145	583.477	973.523	4.299	321	1337.966	219.034	5.098
146	587.4	969.6	4.227	322	1342.306	214.694	4.998
147	591.38	965.62	4.255	323	1346.523	210.477	4.897

148	595.368	961.632	4.283	324	1350.798	206.202	4.915
149	599.363	957.637	4.313	325	1355.069	201.931	4.933
150	603.366	953.634	4.339	326	1359.338	197.662	4.948
151	607.377	949.623	4.368	327	1363.604	193.396	4.967
152	611.395	945.605	4.396	328	1367.866	189.134	4.985
153	615.42	941.58	4.425	329	1372.125	184.875	5.003
154	619.453	937.547	4.454	330	1376.382	180.618	5.019
155	623.493	933.507	4.482	331	1380.635	176.365	5.036
156	627.593	929.407	4.406	332	1384.885	172.115	5.055
157	631.594	925.406	4.327	333	1389.131	167.869	5.071
158	635.655	921.345	4.357	334	1393.375	163.625	5.089
159	639.723	917.277	4.382	335	1397.675	159.325	4.984
160	643.798	913.202	4.412	336	1401.852	155.148	4.88
161	647.879	909.121	4.439	337	1406.085	150.915	4.897
162	651.967	905.033	4.468	338	1410.315	146.685	4.914
163	656.062	900.938	4.495	339	1414.542	142.458	4.931
164	660.163	896.837	4.524	340	1418.766	138.234	4.948
165	664.271	892.729	4.551	341	1422.985	134.015	4.965
166	668.385	888.615	4.578	342	1427.202	129.798	4.981
167	672.56	884.44	4.499	343	1431.415	125.585	4.997
168	676.632	880.368	4.415	344	1435.625	121.375	5.014
169	680.765	876.235	4.441	345	1439.831	117.169	5.03
170	684.904	872.096	4.47	346	1444.033	112.967	5.046
171	689.049	867.951	4.497	347	1448.232	108.768	5.063
172	693.199	863.801	4.524	348	1452.488	104.512	4.955
173	697.356	859.644	4.552	349	1456.62	100.38	4.848
174	701.518	855.482	4.578	350	1460.808	96.192	4.863
175	705.686	851.314	4.608	351	1464.993	92.007	4.881
176	709.859	847.141	4.634	352	1469.173	87.827	4.895

Appendix D

Carbon scaling results

In this chapter the resulting plots for the unpolarized background subtraction are presented. Fig. D.1 and D.2 show the results of 2015 D-butanol and 2015 carbon data for the proton and for the neutron channel, respectively. Fig. D.3 and D.4 show the result for 2014 D-butanol and 2013 carbon data.

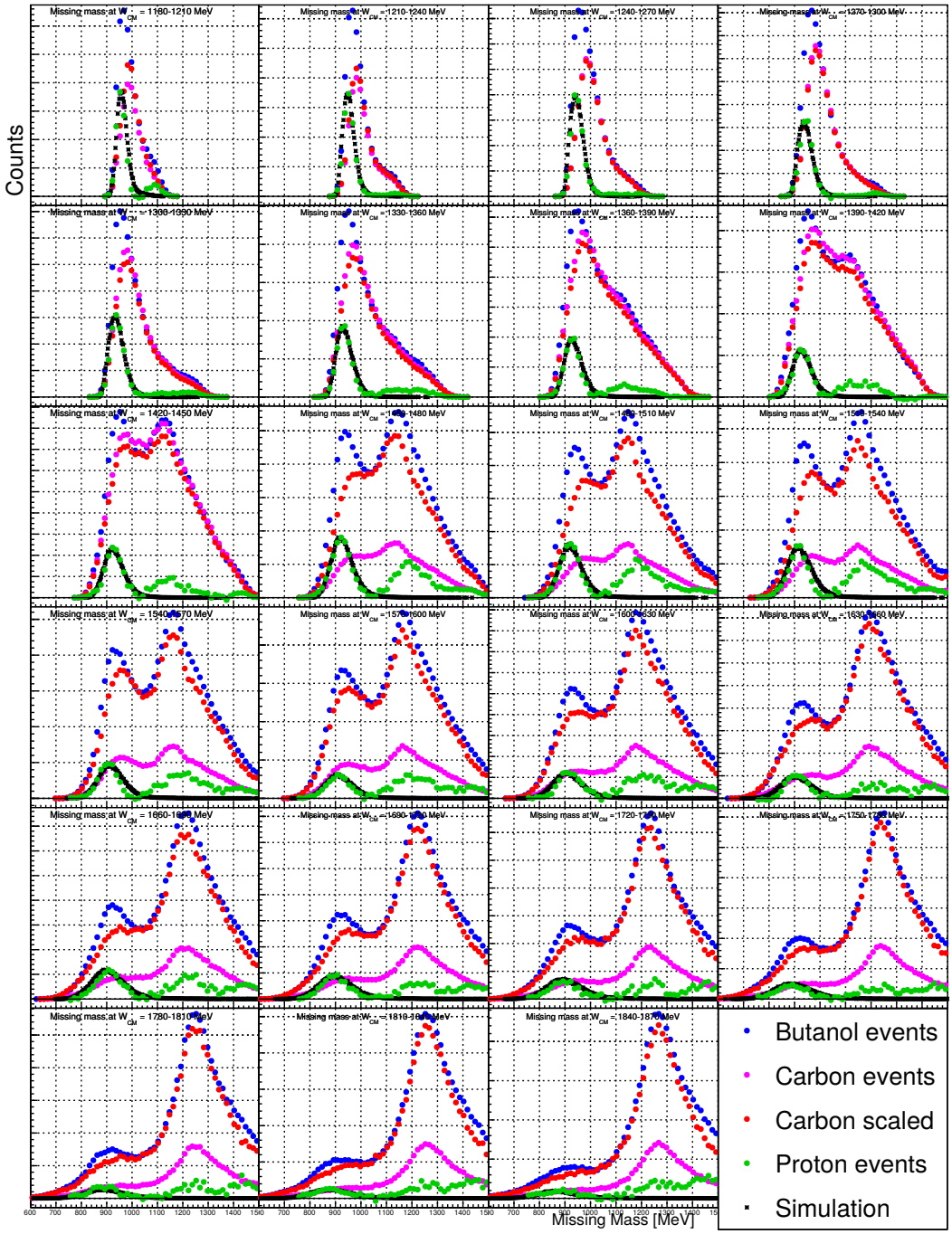

Figure D.1: Carbon scaling for proton channel for 2015 D-butanol and 2015 carbon data.

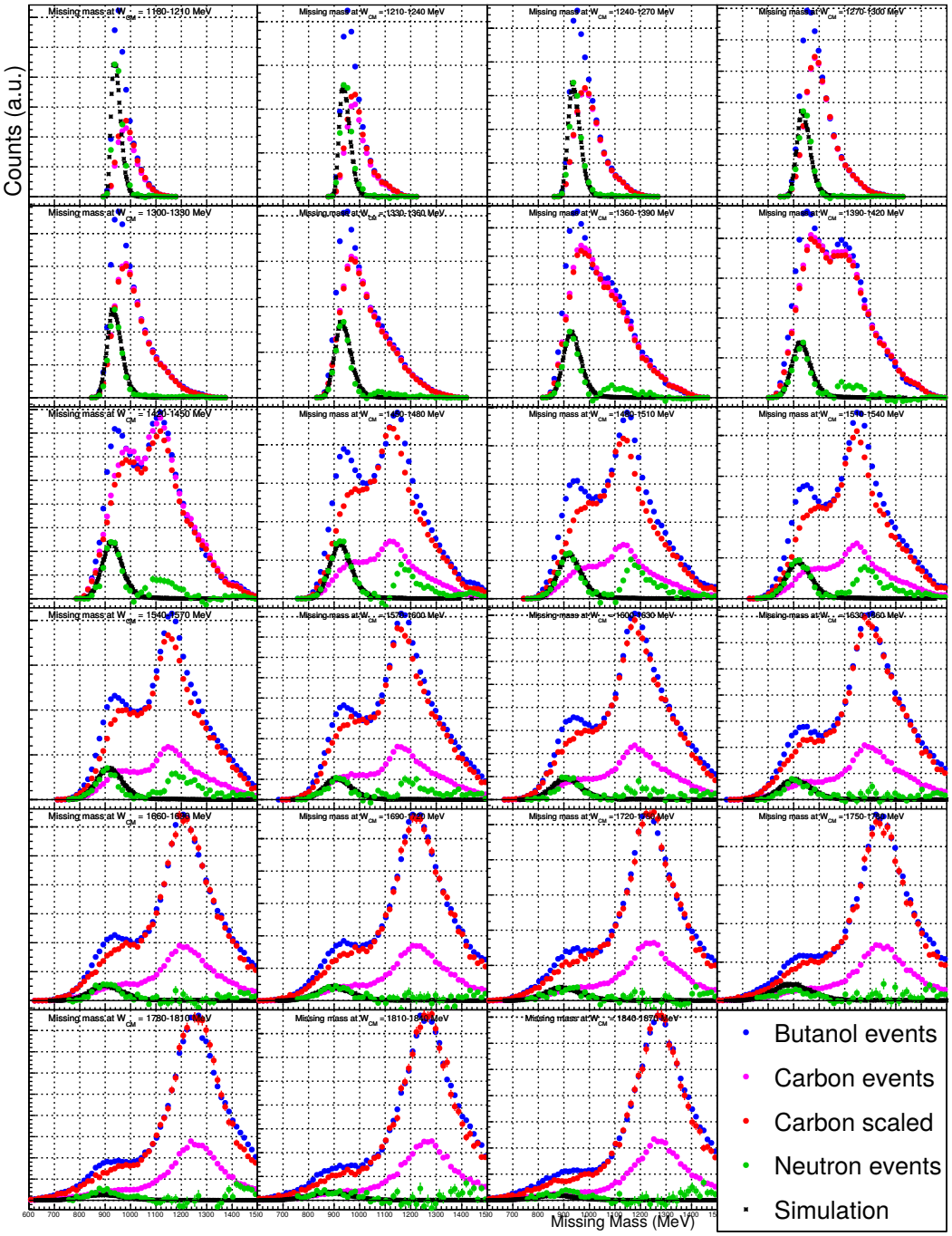

Figure D.2: Carbon scaling for neutron channel for 2015 D-butanol and 2015 carbon data.

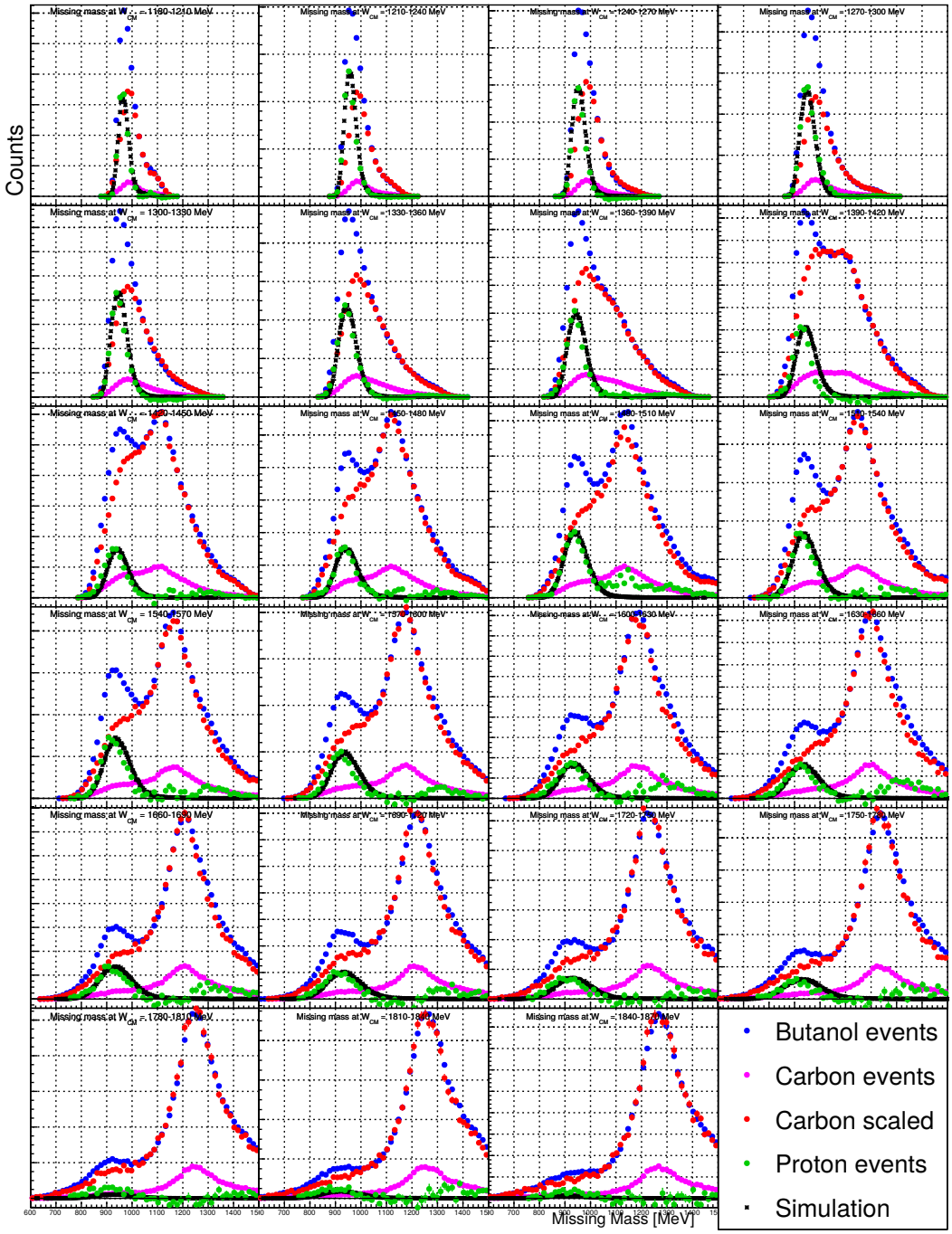

Figure D.3: Carbon scaling for proton channel for 2014 D-butanol and 2013 carbon data.

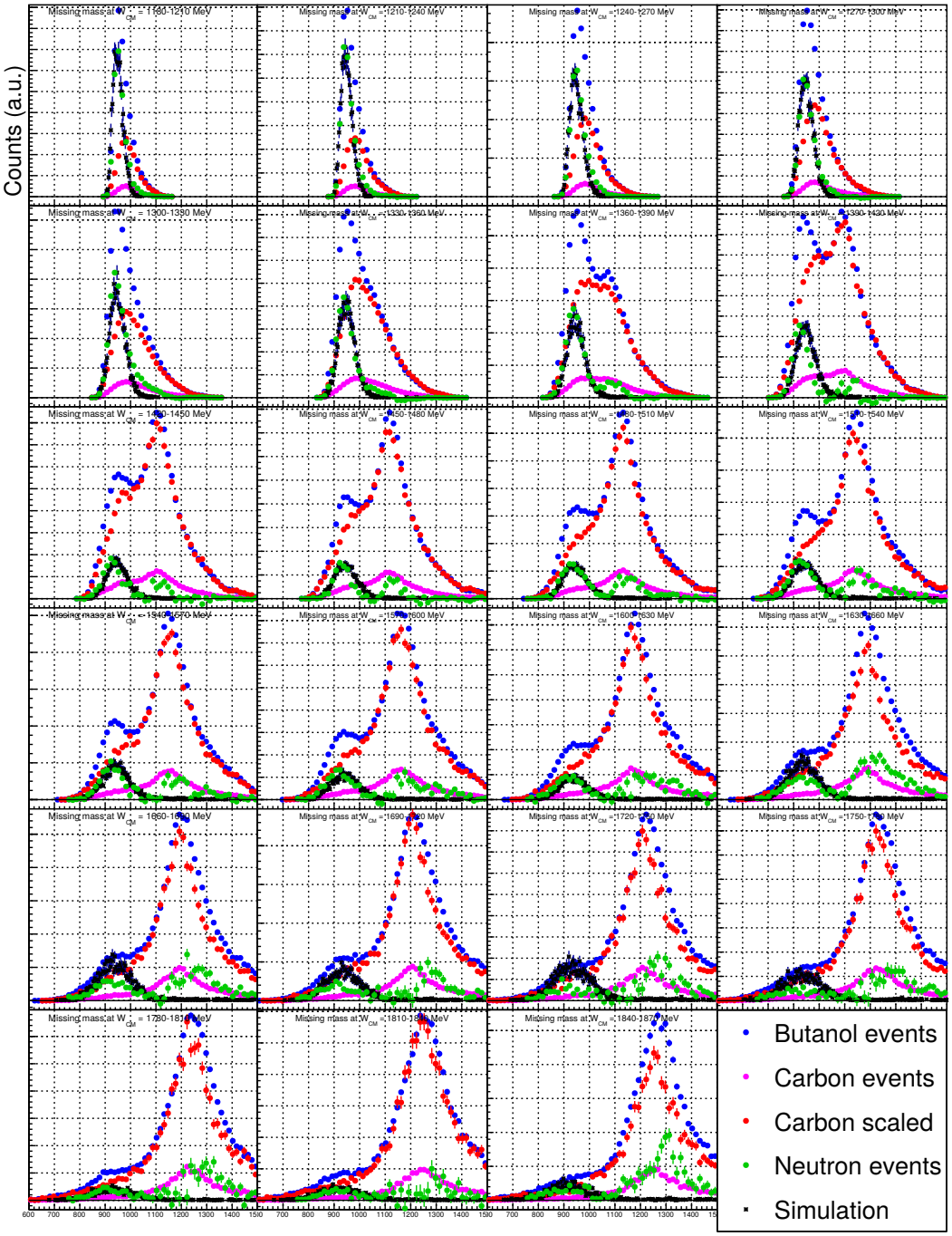

Figure D.4: Carbon scaling for neutron channel for 2014 D-butanol and 2013 carbon data.

Appendix E

Results tables

Inclusive polarized π^0 total cross section on deuteron

Table E.1: Results of the helicity dependent π^0 photoproduction total cross section on deuteron.

E_γ range [MeV]	$\sigma^{\uparrow\uparrow} - \sigma^{\uparrow\downarrow}$ [μb]	Statistical error	E_γ range [MeV]	$\sigma^{\uparrow\uparrow} - \sigma^{\uparrow\downarrow}$ [μb]	Statistical error
153.0 - 170.0	15.42	6.40	777.5 - 794.5	-10.79	2.83
170.0 - 187.0	22.26	7.52	794.5 - 811.4	-11.94	2.81
187.0 - 204.1	34.58	9.22	811.4 - 828.3	-6.25	2.95
204.1 - 221.2	57.93	10.88	828.3 - 845.0	-8.72	2.84
221.2 - 238.3	121.06	12.03	845.0 - 861.7	-12.84	3.49
238.3 - 255.5	194.33	13.50	861.7 - 878.3	-12.39	3.25
255.5 - 272.8	252.96	13.31	878.3 - 894.8	-2.87	3.80
272.8 - 290.1	308.42	15.78	894.8 - 911.1	-1.16	2.74
290.1 - 307.4	430.70	15.81	911.1 - 927.4	0.29	3.22
307.4 - 324.7	487.72	15.75	927.4 - 943.6	5.05	3.44
324.7 - 342.1	471.95	17.61	943.6 - 959.6	5.80	3.69
342.1 - 359.5	433.87	17.79	959.6 - 975.5	5.45	2.99
359.5 - 377.0	403.32	14.56	975.5 - 991.3	5.66	2.64
377.0 - 394.4	301.32	12.17	991.3 - 1007.0	9.64	2.80
394.4 - 411.9	230.50	12.16	1007.0 - 1022.5	7.75	2.87
411.9 - 429.4	187.88	10.20	1022.5 - 1037.9	3.79	3.68

429.4 - 446.9	135.39	8.38	1037.9 - 1053.1	5.43	3.49
446.9 - 464.4	117.04	9.22	1053.1 - 1068.2	12.21	4.12
464.4 - 482.0	86.32	8.24	1068.2 - 1083.2	10.84	3.17
482.0 - 499.5	64.24	6.36	1083.2 - 1098.0	3.22	2.45
499.5 - 517.1	77.54	8.55	1098.0 - 1112.6	2.45	2.69
517.1 - 534.6	56.01	5.77	1112.6 - 1127.0	1.57	3.76
534.6 - 552.1	27.05	5.30	1127.0 - 1141.3	4.16	2.97
552.1 - 569.6	22.39	4.73	1141.3 - 1155.4	2.06	22.51
569.6 - 587.1	17.44	5.15	1155.4 - 1169.4	-4.25	5.49
587.1 - 604.6	15.83	5.20	1169.4 - 1183.1	2.05	3.06
604.6 - 622.1	8.92	3.32	1183.1 - 1196.7	-0.20	4.38
622.1 - 639.5	3.06	5.49	1196.7 - 1210.1	3.43	5.85
639.5 - 656.9	3.70	3.63	1210.1 - 1223.4	1.80	3.40
656.9 - 674.3	-1.39	0.80	1223.4 - 1236.4	-1.45	3.31
674.3 - 691.6	-3.27	3.59	1236.4 - 1249.2	6.56	9.15
691.6 - 708.9	-7.46	3.13	1249.2 - 1261.9	4.71	7.27
708.9 - 726.2	-17.98	3.69	1261.9 - 1274.4	1.50	2.15
726.2 - 743.3	-7.93	3.29	1274.4 - 1286.7	-1.54	2.48
743.3 - 760.5	-10.72	3.36	1286.7 - 1298.8	-11.59	3.87
760.5 - 777.5	-9.45	3.37	-	-	-

Inclusive helicity dependent π^0 differential cross section on deuteron

Table E.2: Results of the helicity dependent π^0 photoproduction differential cross section on deuteron.

$\theta_{\pi^0}^{LAB}$ [°]	$\frac{d(\sigma^{\uparrow\uparrow}-\sigma^{\uparrow\downarrow})}{d\Omega}$ [μb]	Statistical Error	$\theta_{\pi^0}^{LAB}$ [°]	$\frac{d(\sigma^{\uparrow\uparrow}-\sigma^{\uparrow\downarrow})}{d\Omega}$ [μb]	Statistical Error
E_γ range 153.0 - 170.0 [MeV]			E_γ range 777.5 - 794.5 [MeV]		
0 - 15	0.37	5.42	0 - 15	-2.98	2.62
15 - 30	5.44	3.02	15 - 30	-7.37	1.43
30 - 45	2.75	2.34	30 - 45	-0.73	0.97
45 - 60	0.04	1.97	45 - 60	2.09	0.73
60 - 75	3.03	1.70	60 - 75	0.46	0.62
75 - 90	3.64	1.50	75 - 90	-0.48	0.53
90 - 105	-0.32	1.29	90 - 105	-1.01	0.47
105 - 120	0.32	1.16	105 - 120	-0.73	0.40
120 - 135	1.74	1.09	120 - 135	-1.71	0.43
135 - 150	-0.97	1.09	135 - 150	-1.65	0.59
150 - 165	-3.52	1.19	150 - 165	-2.49	1.15
165 - 180	-2.05	1.83	165 - 180	3.57	5.20
E_γ range 170.0 - 187.0 [MeV]			E_γ range 794.5 - 811.5 [MeV]		
0 - 15	3.90	6.25	0 - 15	-4.45	2.56
15 - 30	5.00	3.57	15 - 30	-5.67	1.42
30 - 45	1.89	2.90	30 - 45	-0.65	1.02
45 - 60	3.80	2.39	45 - 60	0.47	0.75
60 - 75	2.18	2.01	60 - 75	-0.03	0.64
75 - 90	0.47	1.70	75 - 90	-1.20	0.55
90 - 105	2.75	1.47	90 - 105	-0.61	0.49
105 - 120	0.99	1.31	105 - 120	-1.18	0.41
120 - 135	2.09	1.22	120 - 135	-1.10	0.45
135 - 150	0.63	1.25	135 - 150	-1.46	0.56
150 - 165	-2.55	1.41	150 - 165	-1.53	1.28
165 - 180	-1.43	2.20	165 - 180	5.82	4.00

E_γ range 187.0 - 204.1 [MeV]			E_γ range 811.5 - 828.3 [MeV]		
0 - 15	4.82	7.30	0 - 15	-2.97	2.75
15 - 30	3.62	4.45	15 - 30	-5.00	1.53
30 - 45	7.96	3.61	30 - 45	-1.07	0.96
45 - 60	7.13	3.00	45 - 60	0.51	0.72
60 - 75	3.76	2.42	60 - 75	0.74	0.60
75 - 90	4.75	2.02	75 - 90	0.26	0.52
90 - 105	1.12	1.74	90 - 105	-0.58	0.47
105 - 120	1.29	1.58	105 - 120	-0.39	0.39
120 - 135	0.37	1.54	120 - 135	-0.63	0.43
135 - 150	-1.46	1.59	135 - 150	-0.90	0.55
150 - 165	-3.66	1.93	150 - 165	-2.70	1.14
165 - 180	0.56	3.06	165 - 180	6.22	6.69
E_γ range 204.1 - 221.2 [MeV]			E_γ range 828.3 - 845.0 [MeV]		
0 - 15	0.48	7.79	0 - 15	-2.13	2.58
15 - 30	-2.35	4.99	15 - 30	-7.01	1.55
30 - 45	3.96	4.23	30 - 45	-0.55	0.95
45 - 60	13.75	3.48	45 - 60	0.70	0.71
60 - 75	7.20	2.79	60 - 75	0.75	0.61
75 - 90	6.09	2.32	75 - 90	-0.70	0.53
90 - 105	7.47	2.05	90 - 105	-0.97	0.46
105 - 120	3.87	1.93	105 - 120	-0.18	0.39
120 - 135	1.87	1.89	120 - 135	-0.31	0.43
135 - 150	2.11	2.19	135 - 150	-1.42	0.58
150 - 165	-8.08	3.05	150 - 165	-3.87	1.29
165 - 180	-3.90	5.05	165 - 180	8.78	5.14
E_γ range 221.2 - 238.3 [MeV]			E_γ range 845.0 - 861.7 [MeV]		
0 - 15	-4.18	8.78	0 - 15	4.42	3.21
15 - 30	-4.83	5.87	15 - 30	-7.33	1.89
30 - 45	14.63	4.69	30 - 45	-3.53	1.07
45 - 60	15.04	3.72	45 - 60	-0.06	0.81
60 - 75	24.13	2.95	60 - 75	-0.13	0.67
75 - 90	14.60	2.49	75 - 90	0.33	0.59

90 - 105	12.94	2.25	90 - 105	-0.65	0.53
105 - 120	9.89	2.10	105 - 120	-0.41	0.45
120 - 135	0.29	2.09	120 - 135	-0.47	0.50
135 - 150	-2.76	2.59	135 - 150	-0.68	0.63
150 - 165	-0.72	4.04	150 - 165	-1.17	1.38
165 - 180	-12.63	6.64	165 - 180	-10.33	8.55
E_γ range 238.3 - 255.5 [MeV]			E_γ range 861.7 - 878.3 [MeV]		
0 - 15	-18.42	9.87	0 - 15	-6.36	2.76
15 - 30	-4.54	6.57	15 - 30	-7.14	1.69
30 - 45	22.52	5.20	30 - 45	-2.55	0.94
45 - 60	30.77	4.05	45 - 60	-0.85	0.71
60 - 75	30.78	3.25	60 - 75	-0.67	0.59
75 - 90	30.54	2.83	75 - 90	-0.41	0.52
90 - 105	20.56	2.54	90 - 105	0.23	0.46
105 - 120	8.43	2.36	105 - 120	-0.70	0.39
120 - 135	3.94	2.38	120 - 135	-0.91	0.45
135 - 150	-3.99	3.04	135 - 150	-0.49	0.60
150 - 165	-6.38	4.89	150 - 165	0.18	1.25
165 - 180	-5.00	7.53	165 - 180	4.73	8.91
E_γ range 255.5 - 272.7 [MeV]			E_γ range 878.3 - 894.8 [MeV]		
0 - 15	-13.27	9.83	0 - 15	-3.74	2.73
15 - 30	1.35	6.53	15 - 30	-1.51	1.71
30 - 45	23.46	4.98	30 - 45	-2.96	0.90
45 - 60	34.80	3.86	45 - 60	0.33	0.66
60 - 75	45.94	3.19	60 - 75	0.70	0.56
75 - 90	32.38	2.81	75 - 90	0.88	0.51
90 - 105	24.34	2.54	90 - 105	0.15	0.44
105 - 120	18.92	2.37	105 - 120	-0.30	0.39
120 - 135	5.42	2.37	120 - 135	-0.10	0.43
135 - 150	-1.89	3.22	135 - 150	0.14	0.57
150 - 165	-11.93	4.83	150 - 165	-0.84	1.15
165 - 180	-9.22	7.94	165 - 180	-1.63	13.22
E_γ range 272.7 - 290.1 [MeV]			E_γ range 894.8 - 911.2 [MeV]		

0 - 15	-25.94	12.52	0 - 15	-4.25	2.38
15 - 30	-10.25	7.65	15 - 30	-5.56	1.52
30 - 45	31.91	5.73	30 - 45	-0.09	0.77
45 - 60	49.32	4.48	45 - 60	0.63	0.57
60 - 75	55.77	3.75	60 - 75	0.47	0.48
75 - 90	42.09	3.35	75 - 90	0.25	0.44
90 - 105	34.73	3.09	90 - 105	0.96	0.38
105 - 120	15.15	2.85	105 - 120	0.13	0.34
120 - 135	8.80	2.90	120 - 135	-0.56	0.37
135 - 150	-7.08	3.84	135 - 150	-0.68	0.49
150 - 165	-14.95	5.49	150 - 165	-0.28	1.00
165 - 180	-14.23	10.55	165 - 180	5.66	7.62
E_γ range 290.1 - 307.4 [MeV]			E_γ range 911.2 - 927.4 [MeV]		
0 - 15	-32.77	12.59	0 - 15	-9.07	2.57
15 - 30	-5.56	7.46	15 - 30	-4.82	1.62
30 - 45	45.34	5.53	30 - 45	-0.84	0.76
45 - 60	58.79	4.34	45 - 60	0.65	0.56
60 - 75	74.19	3.80	60 - 75	0.22	0.48
75 - 90	64.65	3.39	75 - 90	1.06	0.45
90 - 105	41.54	3.14	90 - 105	0.88	0.39
105 - 120	23.62	2.96	105 - 120	0.69	0.34
120 - 135	5.47	3.13	120 - 135	-0.71	0.40
135 - 150	2.72	4.08	135 - 150	0.11	0.52
150 - 165	-13.19	5.37	150 - 165	-0.07	1.05
165 - 180	-14.19	9.63	165 - 180	7.35	10.66
E_γ range 307.4 - 324.7 [MeV]			E_γ range 927.4 - 943.6 [MeV]		
0 - 15	-57.70	12.31	0 - 15	0.26	3.08
15 - 30	10.26	7.30	15 - 30	0.39	2.08
30 - 45	43.11	5.30	30 - 45	-3.23	0.95
45 - 60	74.91	4.32	45 - 60	-0.38	0.70
60 - 75	79.76	3.74	60 - 75	0.81	0.59
75 - 90	66.07	3.33	75 - 90	1.93	0.55
90 - 105	51.19	3.31	90 - 105	1.68	0.48

105 - 120	25.61	3.02	105 - 120	-0.03	0.42
120 - 135	13.31	3.17	120 - 135	0.25	0.47
135 - 150	-7.53	4.06	135 - 150	1.48	0.66
150 - 165	-4.78	5.13	150 - 165	-0.70	1.44
165 - 180	-18.96	10.52	165 - 180	0.16	9.03
E_γ range 324.7 - 342.1 [MeV]			E_γ range 943.6 - 959.6 [MeV]		
0 - 15	-49.59	14.04	0 - 15	-0.75	2.58
15 - 30	-5.04	8.20	15 - 30	-2.33	1.71
30 - 45	38.58	5.87	30 - 45	-2.54	0.77
45 - 60	80.44	4.82	45 - 60	-0.69	0.55
60 - 75	80.62	4.06	60 - 75	1.66	0.46
75 - 90	67.55	3.72	75 - 90	1.20	0.45
90 - 105	48.79	4.03	90 - 105	1.18	0.38
105 - 120	17.18	3.38	105 - 120	0.41	0.35
120 - 135	9.60	3.47	120 - 135	-0.16	0.39
135 - 150	-3.65	4.39	135 - 150	0.33	0.51
150 - 165	-0.78	5.86	150 - 165	1.18	1.19
165 - 180	-15.03	9.46	165 - 180	13.91	13.46
E_γ range 342.1 - 359.5 [MeV]			E_γ range 959.6 - 975.5 [MeV]		
0 - 15	-26.28	13.64	0 - 15	-0.13	2.52
15 - 30	-4.37	8.17	15 - 30	-0.10	1.73
30 - 45	38.21	5.81	30 - 45	-1.03	0.78
45 - 60	60.30	4.73	45 - 60	-0.09	0.54
60 - 75	68.86	3.97	60 - 75	1.21	0.48
75 - 90	62.05	4.10	75 - 90	1.30	0.44
90 - 105	45.23	4.13	90 - 105	2.03	0.39
105 - 120	24.29	3.45	105 - 120	0.72	0.35
120 - 135	8.31	3.54	120 - 135	0.72	0.41
135 - 150	5.96	4.34	135 - 150	-0.93	0.52
150 - 165	-13.51	5.62	150 - 165	-0.35	1.30
165 - 180	8.02	9.81	165 - 180	-6.79	8.68
E_γ range 359.5 - 376.9 [MeV]			E_γ range 975.5 - 991.4 [MeV]		
0 - 15	-48.37	11.69	0 - 15	1.85	2.07

15 - 30	-12.08	6.67	15 - 30	-1.42	1.59
30 - 45	41.19	4.65	30 - 45	-1.47	0.68
45 - 60	66.18	3.75	45 - 60	-0.02	0.47
60 - 75	64.48	3.34	60 - 75	1.40	0.41
75 - 90	58.36	3.55	75 - 90	1.43	0.40
90 - 105	43.94	3.30	90 - 105	1.20	0.33
105 - 120	23.92	2.85	105 - 120	0.84	0.29
120 - 135	3.90	2.82	120 - 135	1.32	0.35
135 - 150	-5.24	3.48	135 - 150	-0.13	0.48
150 - 165	-6.69	4.55	150 - 165	-0.55	1.02
165 - 180	-9.14	8.00	165 - 180	-5.84	7.81
E_γ range 376.9 - 394.4 [MeV]			E_γ range 991.4 - 1007.0 [MeV]		
0 - 15	-45.87	9.77	0 - 15	3.13	2.21
15 - 30	-17.88	5.55	15 - 30	0.47	1.72
30 - 45	30.02	3.84	30 - 45	-1.08	0.73
45 - 60	50.20	3.09	45 - 60	0.62	0.48
60 - 75	51.92	2.97	60 - 75	0.88	0.44
75 - 90	45.64	2.91	75 - 90	2.19	0.42
90 - 105	28.53	2.70	90 - 105	0.87	0.35
105 - 120	13.43	2.43	105 - 120	0.81	0.34
120 - 135	4.29	2.37	120 - 135	0.59	0.36
135 - 150	-0.06	2.78	135 - 150	0.21	0.49
150 - 165	0.39	3.78	150 - 165	1.03	0.94
165 - 180	7.72	7.12	165 - 180	-0.97	8.39
E_γ range 394.4 - 411.9 [MeV]			E_γ range 1007.0 - 1022.5 [MeV]		
0 - 15	-17.25	9.92	0 - 15	0.98	2.06
15 - 30	-7.58	5.49	15 - 30	0.03	1.61
30 - 45	12.24	3.78	30 - 45	-0.12	0.68
45 - 60	35.04	3.09	45 - 60	0.26	0.44
60 - 75	45.68	3.16	60 - 75	0.54	0.39
75 - 90	32.96	2.84	75 - 90	1.63	0.40
90 - 105	25.21	2.69	90 - 105	1.37	0.33
105 - 120	10.39	2.37	105 - 120	0.84	0.30

120 - 135	1.82	2.34	120 - 135	0.98	0.37
135 - 150	-1.76	2.76	135 - 150	-0.11	0.45
150 - 165	0.53	3.79	150 - 165	0.05	1.10
165 - 180	2.91	6.84	165 - 180	-4.09	9.40
E_γ range 411.9 - 429.4 [MeV]			E_γ range 1022.5 - 1037.9 [MeV]		
0 - 15	-32.49	8.00	0 - 15	-3.32	1.99
15 - 30	0.97	4.77	15 - 30	2.52	1.58
30 - 45	18.56	3.18	30 - 45	-0.59	0.66
45 - 60	30.23	2.63	45 - 60	0.25	0.43
60 - 75	38.59	2.74	60 - 75	0.97	0.38
75 - 90	26.81	2.35	75 - 90	1.21	0.37
90 - 105	17.86	2.18	90 - 105	0.82	0.32
105 - 120	8.78	1.93	105 - 120	0.68	0.29
120 - 135	-0.27	1.90	120 - 135	0.16	0.34
135 - 150	-2.63	2.29	135 - 150	0.11	0.44
150 - 165	-4.75	3.17	150 - 165	-1.79	1.09
165 - 180	-9.90	6.70	165 - 180	-8.54	14.44
E_γ range 429.4 - 446.9 [MeV]			E_γ range 1037.9 - 1053.1 [MeV]		
0 - 15	-28.44	7.42	0 - 15	-0.13	2.16
15 - 30	-16.13	3.97	15 - 30	-2.26	1.68
30 - 45	12.70	2.63	30 - 45	-1.05	0.65
45 - 60	24.96	2.29	45 - 60	0.57	0.43
60 - 75	28.34	2.21	60 - 75	0.83	0.38
75 - 90	18.43	1.88	75 - 90	1.39	0.39
90 - 105	14.81	1.75	90 - 105	1.72	0.31
105 - 120	7.38	1.55	105 - 120	0.71	0.31
120 - 135	2.26	1.55	120 - 135	0.39	0.35
135 - 150	-0.49	1.85	135 - 150	-0.49	0.47
150 - 165	-5.30	2.69	150 - 165	-1.49	0.89
165 - 180	-3.98	4.96	165 - 180	3.32	13.33
E_γ range 446.9 - 464.4 [MeV]			E_γ range 1053.1 - 1068.3 [MeV]		
0 - 15	-17.52	8.32	0 - 15	2.38	2.15
15 - 30	-0.96	4.38	15 - 30	-0.96	1.78

30 - 45	9.43	2.90	30 - 45	0.22	0.69
45 - 60	19.62	2.65	45 - 60	-0.70	0.45
60 - 75	21.29	2.41	60 - 75	1.22	0.40
75 - 90	16.99	2.03	75 - 90	2.14	0.40
90 - 105	11.63	1.91	90 - 105	1.35	0.32
105 - 120	5.54	1.67	105 - 120	0.43	0.32
120 - 135	0.65	1.67	120 - 135	0.54	0.37
135 - 150	2.48	2.07	135 - 150	-0.28	0.53
150 - 165	-4.85	2.87	150 - 165	-1.18	1.10
165 - 180	-4.84	5.49	165 - 180	23.97	16.46
E_γ range 464.4 - 481.9 [MeV]			E_γ range 1068.3 - 1083.2 [MeV]		
0 - 15	-22.40	7.80	0 - 15	-1.22	1.99
15 - 30	-7.30	3.93	15 - 30	1.89	1.71
30 - 45	6.83	2.62	30 - 45	0.61	0.71
45 - 60	15.56	2.44	45 - 60	0.44	0.43
60 - 75	15.43	2.09	60 - 75	0.89	0.38
75 - 90	12.08	1.78	75 - 90	1.54	0.40
90 - 105	9.63	1.66	90 - 105	1.24	0.32
105 - 120	4.85	1.44	105 - 120	0.70	0.30
120 - 135	1.77	1.48	120 - 135	0.63	0.38
135 - 150	0.04	1.76	135 - 150	0.20	0.46
150 - 165	1.19	2.58	150 - 165	-0.63	1.23
165 - 180	-2.38	6.82	165 - 180	5.64	11.08
E_γ range 481.9 - 499.5 [MeV]			E_γ range 1083.2 - 1098.0 [MeV]		
0 - 15	-13.05	6.37	0 - 15	-1.69	1.83
15 - 30	-10.52	3.03	15 - 30	0.00	1.54
30 - 45	4.72	2.03	30 - 45	-0.40	0.62
45 - 60	14.83	1.97	45 - 60	-0.19	0.38
60 - 75	12.59	1.59	60 - 75	0.26	0.34
75 - 90	11.02	1.34	75 - 90	1.38	0.36
90 - 105	8.53	1.27	90 - 105	1.14	0.27
105 - 120	2.94	1.11	105 - 120	0.38	0.27
120 - 135	-0.15	1.13	120 - 135	-0.07	0.34

135 - 150	-3.49	1.35	135 - 150	-0.57	0.41
150 - 165	-2.91	1.98	150 - 165	-1.69	1.08
165 - 180	-0.95	4.84	165 - 180	4.17	7.38
E_γ range 499.5 - 517.1 [MeV]			E_γ range 109.08 - 1112.6 [MeV]		
0 - 15	-20.57	8.41	0 - 15	-4.11	1.66
15 - 30	-8.26	4.11	15 - 30	1.67	1.48
30 - 45	3.74	2.74	30 - 45	0.64	0.57
45 - 60	15.18	2.66	45 - 60	-0.36	0.37
60 - 75	12.99	2.10	60 - 75	0.89	0.32
75 - 90	13.76	1.80	75 - 90	0.72	0.32
90 - 105	5.74	1.71	90 - 105	0.95	0.26
105 - 120	4.30	1.45	105 - 120	0.38	0.27
120 - 135	3.23	1.47	120 - 135	0.03	0.34
135 - 150	-0.76	1.74	135 - 150	-0.56	0.43
150 - 165	-1.72	2.88	150 - 165	-1.31	1.09
165 - 180	15.75	7.44	165 - 180	-5.52	9.32
E_γ range 517.1 - 534.6 [MeV]			E_γ range 1112.6 - 1127.0 [MeV]		
0 - 15	-9.75	5.49	0 - 15	2.98	2.55
15 - 30	-0.72	2.77	15 - 30	1.11	2.02
30 - 45	3.07	1.90	30 - 45	-1.87	0.77
45 - 60	9.77	1.85	45 - 60	-0.15	0.47
60 - 75	10.36	1.41	60 - 75	0.94	0.42
75 - 90	8.81	1.21	75 - 90	1.70	0.43
90 - 105	4.54	1.15	90 - 105	0.90	0.33
105 - 120	2.19	0.98	105 - 120	0.78	0.34
120 - 135	1.06	0.99	120 - 135	-0.04	0.43
135 - 150	1.11	1.22	135 - 150	-1.08	0.58
150 - 165	0.19	1.86	150 - 165	1.28	1.37
165 - 180	-2.60	4.46	165 - 180	-19.69	13.56
E_γ range 534.6 - 552.1 [MeV]			E_γ range 1127 - 1141.3 [MeV]		
0 - 15	-13.76	5.16	0 - 15	0.17	2.26
15 - 30	-6.58	2.62	15 - 30	2.23	1.83
30 - 45	6.15	1.81	30 - 45	-0.91	0.69

45 - 60	9.50	1.67	45 - 60	0.00	0.42
60 - 75	5.47	1.29	60 - 75	0.43	0.38
75 - 90	2.83	1.09	75 - 90	1.72	0.38
90 - 105	3.36	1.03	90 - 105	0.31	0.29
105 - 120	0.57	0.87	105 - 120	0.38	0.32
120 - 135	0.01	0.91	120 - 135	-0.26	0.40
135 - 150	-2.51	1.10	135 - 150	-0.16	0.53
150 - 165	0.32	1.67	150 - 165	-2.11	1.38
165 - 180	-6.15	4.41	165 - 180	4.35	9.37
E_γ range 552.1 - 569.6 [MeV]			E_γ range 1141.3 - 1155.5 [MeV]		
0 - 15	-10.61	4.77	0 - 15	-4.21	2.07
15 - 30	-6.67	2.30	15 - 30	-2.19	1.98
30 - 45	1.28	1.63	30 - 45	-0.71	0.71
45 - 60	9.52	1.44	45 - 60	-0.07	0.45
60 - 75	5.09	1.13	60 - 75	0.46	0.40
75 - 90	2.48	0.97	75 - 90	0.52	0.41
90 - 105	1.36	0.93	90 - 105	0.90	0.31
105 - 120	1.04	0.77	105 - 120	0.49	0.33
120 - 135	0.31	0.80	120 - 135	0.06	0.41
135 - 150	-0.73	1.00	135 - 150	-0.07	0.59
150 - 165	-1.46	1.64	150 - 165	0.89	1.21
165 - 180	4.13	4.37	165 - 180	3.84	104.61
E_γ range 569.6 - 587.1 [MeV]			E_γ range 1155.5 - 1169.4 [MeV]		
0 - 15	-3.19	5.18	0 - 15	-1.72	1.73
15 - 30	1.08	2.52	15 - 30	0.60	1.68
30 - 45	2.50	1.82	30 - 45	-1.32	0.62
45 - 60	5.16	1.55	45 - 60	0.57	0.37
60 - 75	3.34	1.22	60 - 75	0.66	0.35
75 - 90	4.29	1.05	75 - 90	0.37	0.34
90 - 105	0.33	0.99	90 - 105	0.55	0.25
105 - 120	0.03	0.84	105 - 120	0.52	0.28
120 - 135	-2.22	0.90	120 - 135	-0.89	0.35
135 - 150	0.85	1.10	135 - 150	-0.89	0.45

150 - 165	-0.40	1.76	150 - 165	-2.21	1.21
165 - 180	-9.70	4.94	165 - 180	-16.49	23.97
E_γ range 587.1 - 604.6 [MeV]			E_γ range 1169.4 - 1183.2 [MeV]		
0 - 15	-0.45	5.24	0 - 15	-2.30	1.88
15 - 30	-4.16	2.46	15 - 30	-0.46	1.68
30 - 45	0.19	1.88	30 - 45	-0.31	0.63
45 - 60	4.58	1.55	45 - 60	0.10	0.35
60 - 75	6.50	1.24	60 - 75	0.16	0.34
75 - 90	0.73	1.06	75 - 90	0.46	0.34
90 - 105	1.98	0.99	90 - 105	0.53	0.26
105 - 120	-0.30	0.85	105 - 120	0.19	0.29
120 - 135	0.98	0.86	120 - 135	0.00	0.37
135 - 150	-1.95	1.11	135 - 150	-1.25	0.52
150 - 165	-1.16	1.89	150 - 165	-2.19	1.12
165 - 180	0.03	4.95	165 - 180	16.32	10.97
E_γ range 604.6 - 622.1 [MeV]			E_γ range 1183.2 - 1196.8 [MeV]		
0 - 15	-11.30	3.24	0 - 15	0.31	1.88
15 - 30	-2.00	1.60	15 - 30	-0.06	1.74
30 - 45	3.25	1.22	30 - 45	0.31	0.66
45 - 60	1.59	0.97	45 - 60	0.13	0.40
60 - 75	3.82	0.79	60 - 75	0.16	0.35
75 - 90	2.80	0.68	75 - 90	0.59	0.36
90 - 105	-0.35	0.65	90 - 105	0.26	0.26
105 - 120	-0.81	0.52	105 - 120	0.55	0.30
120 - 135	-1.33	0.55	120 - 135	-0.01	0.35
135 - 150	0.50	0.70	135 - 150	-0.54	0.57
150 - 165	0.04	1.25	150 - 165	0.26	1.30
165 - 180	-0.26	3.32	165 - 180	-13.03	18.03
E_γ range 622.1 - 639.5 [MeV]			E_γ range 1196.8 - 1210.2 [MeV]		
0 - 15	-2.72	5.60	0 - 15	0.00	1.77
15 - 30	-2.99	2.59	15 - 30	-0.94	1.57
30 - 45	0.65	2.06	30 - 45	-0.69	0.57
45 - 60	0.93	1.60	45 - 60	-0.10	0.33

60 - 75	3.62	1.32	60 - 75	0.09	0.31
75 - 90	1.08	1.11	75 - 90	0.42	0.30
90 - 105	0.14	1.05	90 - 105	0.24	0.24
105 - 120	-0.63	0.87	105 - 120	-0.07	0.26
120 - 135	-2.17	0.92	120 - 135	0.18	0.34
135 - 150	-0.28	1.14	135 - 150	-0.77	0.47
150 - 165	0.25	2.01	150 - 165	0.73	1.04
165 - 180	0.51	5.31	165 - 180	17.78	26.00
E_γ range 639.5 - 657.0 [MeV]			E_γ range 1210.2 - 1223.4 [MeV]		
0 - 15	-2.83	3.53	0 - 15	-3.63	1.63
15 - 30	-5.76	1.73	15 - 30	-0.93	1.60
30 - 45	-1.25	1.33	30 - 45	-0.52	0.56
45 - 60	3.24	1.02	45 - 60	0.27	0.33
60 - 75	3.54	0.85	60 - 75	0.74	0.32
75 - 90	0.89	0.73	75 - 90	0.31	0.31
90 - 105	0.12	0.69	90 - 105	0.61	0.22
105 - 120	-0.83	0.56	105 - 120	-0.06	0.27
120 - 135	-0.80	0.61	120 - 135	0.04	0.35
135 - 150	-0.62	0.75	135 - 150	0.03	0.45
150 - 165	-1.31	1.34	150 - 165	-0.64	1.23
165 - 180	7.98	4.47	165 - 180	5.28	13.36
E_γ range 657.0 - 674.3 [MeV]			E_γ range 1223.4 - 1236.4 [MeV]		
0 - 15	-0.11	0.74	0 - 15	-4.27	2.23
15 - 30	-3.03	0.37	15 - 30	1.17	1.90
30 - 45	0.40	0.30	30 - 45	-0.91	0.71
45 - 60	0.50	0.23	45 - 60	-0.50	0.42
60 - 75	1.31	0.19	60 - 75	0.26	0.40
75 - 90	0.27	0.16	75 - 90	0.49	0.40
90 - 105	-0.38	0.15	90 - 105	0.46	0.30
105 - 120	-0.03	0.12	105 - 120	0.20	0.33
120 - 135	-0.34	0.13	120 - 135	0.20	0.42
135 - 150	-0.79	0.17	135 - 150	0.07	0.59
150 - 165	-1.92	0.32	150 - 165	-0.46	1.41

165 - 180	0.83	1.03	165 - 180	-9.34	11.27
E_γ range 674.3 - 691.6 [MeV]			E_γ range 1236.4 - 1249.3 [MeV]		
0 - 15	-1.05	3.42	0 - 15	-2.37	4.18
15 - 30	0.04	1.66	15 - 30	-1.85	3.19
30 - 45	-0.83	1.33	30 - 45	-2.40	1.08
45 - 60	0.99	1.00	45 - 60	0.85	0.65
60 - 75	1.25	0.83	60 - 75	0.94	0.62
75 - 90	-0.04	0.73	75 - 90	0.21	0.61
90 - 105	0.08	0.67	90 - 105	0.76	0.43
105 - 120	-0.74	0.54	105 - 120	1.11	0.52
120 - 135	-0.91	0.59	120 - 135	-0.69	0.66
135 - 150	-1.25	0.74	135 - 150	-1.30	0.87
150 - 165	-2.22	1.42	150 - 165	-0.73	2.10
165 - 180	-2.49	4.74	165 - 180	34.86	39.31
E_γ range 691.6 - 708.9 [MeV]			E_γ range 1249.3 - 1261.9 [MeV]		
0 - 15	-3.22	2.76	0 - 15	0.48	2.00
15 - 30	-2.27	1.43	15 - 30	-0.52	1.90
30 - 45	-0.39	1.14	30 - 45	0.25	0.63
45 - 60	-0.12	0.85	45 - 60	0.19	0.37
60 - 75	0.16	0.71	60 - 75	-0.05	0.37
75 - 90	0.80	0.61	75 - 90	1.24	0.37
90 - 105	-1.16	0.56	90 - 105	0.63	0.27
105 - 120	-0.64	0.45	105 - 120	0.41	0.33
120 - 135	-0.69	0.49	120 - 135	0.28	0.41
135 - 150	-0.56	0.64	135 - 150	-1.12	0.52
150 - 165	-0.41	1.26	150 - 165	0.05	1.34
165 - 180	-8.27	5.22	165 - 180	7.39	32.41
E_γ range 708.9 - 726.2 [MeV]			E_γ range 1261.9 - 1274.4 [MeV]		
0 - 15	-1.58	3.34	0 - 15	-1.26	2.42
15 - 30	-4.39	1.62	15 - 30	1.63	1.81
30 - 45	-0.70	1.26	30 - 45	-1.53	0.59
45 - 60	2.27	0.95	45 - 60	0.14	0.36
60 - 75	-0.34	0.79	60 - 75	0.78	0.34

75 - 90	-0.38	0.67	75 - 90	0.90	0.33
90 - 105	-2.48	0.64	90 - 105	0.92	0.25
105 - 120	-2.06	0.50	105 - 120	0.45	0.31
120 - 135	-1.75	0.54	120 - 135	-0.30	0.40
135 - 150	-2.12	0.73	135 - 150	-0.81	0.55
150 - 165	-2.83	1.34	150 - 165	-2.42	1.57
165 - 180	-12.47	7.95	165 - 180	0.00	0.00
E_γ range 726.2 - 743.3 [MeV]			E_γ range 1274.4 - 1286.7 [MeV]		
0 - 15	-3.86	2.96	0 - 15	-1.16	2.05
15 - 30	-0.50	1.60	15 - 30	-3.54	2.10
30 - 45	1.67	1.19	30 - 45	-0.66	0.71
45 - 60	0.53	0.88	45 - 60	-0.10	0.43
60 - 75	1.34	0.74	60 - 75	0.89	0.42
75 - 90	0.53	0.64	75 - 90	0.35	0.41
90 - 105	-2.58	0.59	90 - 105	0.78	0.30
105 - 120	-1.76	0.47	105 - 120	0.15	0.36
120 - 135	-2.09	0.52	120 - 135	-0.38	0.48
135 - 150	-0.62	0.67	135 - 150	-1.23	0.66
150 - 165	-2.16	1.27	150 - 165	0.03	1.74
165 - 180	-2.19	5.43	165 - 180	0.00	0.00
E_γ range 743.3 - 760.5 [MeV]			E_γ range 1286.7 - 1298.8 [MeV]		
0 - 15	2.07	2.98	0 - 15	-1.93	2.43
15 - 30	-2.88	1.62	15 - 30	-7.53	2.35
30 - 45	-0.53	1.16	30 - 45	-1.61	0.71
45 - 60	1.26	0.86	45 - 60	0.25	0.43
60 - 75	0.33	0.72	60 - 75	1.20	0.41
75 - 90	-1.24	0.64	75 - 90	0.11	0.40
90 - 105	-1.75	0.56	90 - 105	0.73	0.31
105 - 120	-0.98	0.46	105 - 120	-0.79	0.38
120 - 135	-2.18	0.51	120 - 135	-0.23	0.49
135 - 150	-1.55	0.65	135 - 150	-1.40	0.65
150 - 165	-1.36	1.38	150 - 165	-1.56	2.55
165 - 180	2.90	6.72	165 - 180	-20.91	12.33

E_γ range 760.5 - 777.5 [MeV]			-		
0 - 15	-4.59	3.03	-	-	-
15 - 30	-4.19	1.69	-	-	-
30 - 45	1.69	1.18	-	-	-
45 - 60	1.63	0.88	-	-	-
60 - 75	1.96	0.75	-	-	-
75 - 90	-0.40	0.65	-	-	-
90 - 105	-1.25	0.58	-	-	-
105 - 120	-1.82	0.47	-	-	-
120 - 135	-1.40	0.51	-	-	-
135 - 150	-1.51	0.68	-	-	-
150 - 165	-3.21	1.37	-	-	-
165 - 180	-8.65	6.10	-	-	-

E observable for single π^0 on quasi-free proton

Table E.3: Results of the E observable for single π^0 photoproduction on quasi-free proton.

$\theta^{CM}_{\pi^0}$ [cosθ]	E observable	Statistical Error	$\theta^{CM}_{\pi^0}$ [cosθ]	E observable	Statistical Error
W range 1150 - 1180 [MeV]			W range 1510 - 1540 [MeV]		
-0.9	0.996	0.189	-0.9	0.508	0.136
-0.7	0.037	0.130	-0.7	0.168	0.116
-0.5	0.038	0.207	-0.5	0.292	0.074
-0.3	-0.464	0.365	-0.3	0.223	0.070
-0.1	-1.330	2.341	-0.1	0.169	0.074
0.1	-0.694	0.716	0.1	0.021	0.098
0.3	0.229	0.368	0.3	0.007	0.122
0.5	-0.199	0.307	0.5	0.029	0.197
0.7	0.114	0.376	0.7	0.981	0.412
0.9	-0.622	0.453	0.9	0.353	0.485
W range 1180 - 1210 [MeV]			W range 1540 - 1570 [MeV]		
-0.9	0.384	0.094	-0.9	0.541	0.122
-0.7	-0.109	0.058	-0.7	0.101	0.114
-0.5	-0.428	0.064	-0.5	0.152	0.071
-0.3	-0.678	0.085	-0.3	0.164	0.069
-0.1	-0.798	0.135	-0.1	0.025	0.069
0.1	-1.228	0.407	0.1	-0.092	0.098
0.3	0.240	0.679	0.3	0.317	0.132
0.5	0.227	0.337	0.5	0.211	0.195
0.7	-0.062	0.265	0.7	-0.450	0.455
0.9	-0.075	0.271	0.9	-0.153	0.400
W range 1210 - 1240 [MeV]			W range 1570 - 1600 [MeV]		
-0.9	0.316	0.083	-0.9	0.077	0.114
-0.7	-0.154	0.046	-0.7	-0.067	0.105
-0.5	-0.600	0.044	-0.5	-0.233	0.082
-0.3	-0.739	0.049	-0.3	0.118	0.074

-0.1	-0.823	0.062	-0.1	-0.105	0.083
0.1	-0.834	0.114	0.1	0.084	0.118
0.3	-0.903	0.400	0.3	0.342	0.173
0.5	0.808	0.647	0.5	0.226	0.241
0.7	0.161	0.253	0.7	0.842	1.320
0.9	-0.171	0.222	0.9	-0.269	0.645
W range 1240 - 1270 [MeV]			W range 1600 - 1630 [MeV]		
-0.9	0.449	0.095	-0.9	-0.035	0.112
-0.7	-0.332	0.052	-0.7	-0.448	0.099
-0.5	-0.508	0.042	-0.5	-0.365	0.085
-0.3	-0.690	0.040	-0.3	-0.172	0.077
-0.1	-0.648	0.044	-0.1	-0.235	0.089
0.1	-0.633	0.059	0.1	-0.148	0.145
0.3	-0.841	0.137	0.3	0.453	0.240
0.5	-0.761	1.326	0.5	0.043	0.369
0.7	-0.978	0.363	0.7	0.145	0.493
0.9	0.021	0.242	0.9	0.541	0.832
W range 1270 - 1300 [MeV]			W range 1630 - 1660 [MeV]		
-0.9	0.262	0.122	-0.9	-0.295	0.105
-0.7	-0.430	0.071	-0.7	-0.670	0.097
-0.5	-0.566	0.050	-0.5	-0.570	0.087
-0.3	-0.627	0.045	-0.3	-0.468	0.081
-0.1	-0.777	0.048	-0.1	-0.363	0.104
0.1	-0.761	0.058	0.1	-0.097	0.237
0.3	-0.701	0.100	0.3	0.373	0.292
0.5	-1.574	1.152	0.5	-0.813	0.515
0.7	-0.191	0.300	0.7	-0.872	0.716
0.9	0.227	0.182	0.9	0.577	0.810
W range 1300 - 1330 [MeV]			W range 1660 - 1690 [MeV]		
-0.9	0.106	0.168	-0.9	-0.250	0.101
-0.7	-0.327	0.091	-0.7	-0.481	0.087
-0.5	-0.499	0.054	-0.5	-0.654	0.091
-0.3	-0.507	0.047	-0.3	-0.410	0.082

-0.1	-0.604	0.047	-0.1	-0.325	0.100
0.1	-0.516	0.053	0.1	-0.421	0.183
0.3	-0.531	0.077	0.3	-0.143	0.214
0.5	-0.286	0.204	0.5	0.280	0.256
0.7	0.663	1.492	0.7	0.367	0.407
0.9	0.000	0.271	0.9	-0.559	0.735
W range 1330 - 1360 [MeV]			W range 1690 - 1720 [MeV]		
-0.9	-0.155	0.280	-0.9	-0.162	0.116
-0.7	-0.184	0.130	-0.7	-0.895	0.110
-0.5	-0.422	0.069	-0.5	-0.806	0.107
-0.3	-0.487	0.062	-0.3	-0.443	0.086
-0.1	-0.542	0.060	-0.1	-0.433	0.115
0.1	-0.594	0.068	0.1	0.205	0.211
0.3	-0.580	0.091	0.3	0.457	0.337
0.5	-0.327	0.180	0.5	0.034	0.273
0.7	-0.715	1.601	0.7	-0.643	0.326
0.9	-0.273	0.356	0.9	0.046	1.338
W range 1360 - 1390 [MeV]			W range 1720 - 1750 [MeV]		
-0.9	0.280	0.303	-0.9	0.126	0.145
-0.7	-0.139	0.194	-0.7	-0.623	0.141
-0.5	-0.255	0.086	-0.5	-0.732	0.143
-0.3	-0.272	0.077	-0.3	-0.393	0.094
-0.1	-0.393	0.078	-0.1	-0.399	0.166
0.1	-0.413	0.088	0.1	-0.079	0.218
0.3	-0.522	0.106	0.3	0.083	0.319
0.5	-0.148	0.195	0.5	-0.648	0.406
0.7	1.353	1.362	0.7	0.455	0.271
0.9	-1.321	0.372	0.9	-1.318	1.239
W range 1390 - 1420 [MeV]			W range 1750 - 1780 [MeV]		
-0.9	0.815	0.576	-0.9	0.390	0.166
-0.7	0.412	0.296	-0.7	-0.390	0.147
-0.5	0.054	0.108	-0.5	-0.734	0.166
-0.3	-0.241	0.104	-0.3	-0.644	0.114

-0.1	-0.289	0.102	-0.1	-0.223	0.203
0.1	-0.395	0.122	0.1	0.250	0.229
0.3	-0.260	0.147	0.3	0.060	0.274
0.5	-0.983	0.244	0.5	-0.138	0.330
0.7	-1.535	1.120	0.7	-0.056	0.352
0.9	0.842	0.469	0.9	0.392	0.990
W range 1420 - 1450 [MeV]			W range 1780 - 1810 [MeV]		
-0.9	1.720	0.587	-0.9	0.167	0.148
-0.7	0.491	0.376	-0.7	-0.321	0.184
-0.5	0.479	0.165	-0.5	-0.630	0.218
-0.3	0.025	0.155	-0.3	-0.551	0.143
-0.1	-0.129	0.149	-0.1	-0.215	0.236
0.1	-0.562	0.182	0.1	-0.009	0.389
0.3	-0.297	0.228	0.3	0.606	0.645
0.5	-1.072	0.631	0.5	0.041	0.927
0.7	1.026	1.925	0.7	0.134	0.485
0.9	0.291	0.402	0.9	0.101	1.095
W range 1450 - 1480 [MeV]			W range 1810 - 1840 [MeV]		
-0.9	0.910	0.222	-0.9	-0.274	0.138
-0.7	0.579	0.173	-0.7	-0.422	0.194
-0.5	0.306	0.101	-0.5	-1.001	0.334
-0.3	0.151	0.097	-0.3	-0.837	0.190
-0.1	0.117	0.103	-0.1	-0.273	0.185
0.1	-0.248	0.119	0.1	-0.183	0.337
0.3	-0.180	0.142	0.3	2.291	3.277
0.5	-0.058	0.236	0.5	0.864	0.719
0.7	-0.986	0.447	0.7	-0.275	0.694
0.9	1.055	0.754	0.9	0.417	0.834
W range 1480 - 1510 [MeV]			W range 1840 - 1870 [MeV]		
-0.9	0.764	0.157	-0.9	0.341	0.152
-0.7	0.716	0.155	-0.7	-0.411	0.178
-0.5	0.457	0.082	-0.5	-0.301	0.200
-0.3	0.304	0.079	-0.3	-0.121	0.167

-0.1	0.121	0.081	-0.1	-0.403	0.286
0.1	-0.076	0.101	0.1	-0.430	0.344
0.3	-0.055	0.135	0.3	1.418	1.866
0.5	0.159	0.199	0.5	0.974	0.876
0.7	0.508	0.442	0.7	0.262	1.316
0.9	1.063	0.563	0.9	-0.131	0.716

E observable for single π^0 on quasi-free neutron

Table E.4: Results of the E observable for single π^0 photoproduction on quasi-free neutron.

$\theta_{\pi^0}^{CM}$ [cosθ]	E observable	Statistical Error	$\theta_{\pi^0}^{CM}$ [cosθ]	E observable	Statistical Error
W range 1150 - 1180 [MeV]			W range 1510 - 1540 [MeV]		
-0.9	0.330	0.392	-0.9	1.131	0.181
-0.7	-0.165	0.336	-0.7	0.920	0.178
-0.5	-0.748	0.296	-0.5	0.176	0.127
-0.3	-1.413	0.317	-0.3	0.059	0.134
-0.1	-0.516	0.473	-0.1	-0.175	0.147
0.1	-1.453	1.164	0.1	-0.714	0.215
0.3	0.697	1.625	0.3	-0.277	0.269
0.5	0.212	0.567	0.5	-0.449	0.517
0.7	-0.028	0.429	0.7	-0.245	0.617
0.9	0.555	0.330	0.9	1.232	0.926
W range 1180 - 1210 [MeV]			W range 1540 - 1570 [MeV]		
-0.9	0.302	0.195	-0.9	0.400	0.169
-0.7	-0.161	0.168	-0.7	1.000	0.237
-0.5	-0.558	0.124	-0.5	0.057	0.138
-0.3	-0.878	0.111	-0.3	0.026	0.137
-0.1	-0.918	0.134	-0.1	-0.374	0.170
0.1	-0.896	0.187	0.1	-0.349	0.185
0.3	-0.895	0.307	0.3	-0.184	0.293
0.5	-0.165	1.279	0.5	0.269	0.383
0.7	-0.495	0.614	0.7	-0.832	0.592
0.9	-0.402	0.330	0.9	0.490	1.711
W range 1210 - 1240 [MeV]			W range 1570 - 1600 [MeV]		
-0.9	0.551	0.157	-0.9	1.302	0.222
-0.7	-0.352	0.131	-0.7	0.902	0.266
-0.5	-0.647	0.080	-0.5	0.405	0.173
-0.3	-0.761	0.074	-0.3	0.016	0.135

-0.1	-0.833	0.080	-0.1	-0.315	0.173
0.1	-0.772	0.098	0.1	0.114	0.268
0.3	-0.458	0.137	0.3	-0.073	0.450
0.5	-1.068	0.262	0.5	0.004	0.508
0.7	-2.479	2.876	0.7	0.925	0.748
0.9	-0.093	0.336	0.9	0.163	2.304
W range 1240 - 1270 [MeV]			W range 1600 - 1630 [MeV]		
-0.9	0.061	0.139	-0.9	0.286	0.198
-0.7	-0.284	0.120	-0.7	0.606	0.222
-0.5	-0.473	0.070	-0.5	0.414	0.179
-0.3	-0.512	0.064	-0.3	-0.065	0.183
-0.1	-0.737	0.068	-0.1	-0.564	0.188
0.1	-0.715	0.077	0.1	0.214	0.280
0.3	-0.651	0.098	0.3	-0.051	0.423
0.5	-0.159	0.153	0.5	-0.385	0.569
0.7	-0.507	0.601	0.7	0.221	0.569
0.9	-0.165	0.401	0.9	0.261	1.136
W range 1270 - 1300 [MeV]			W range 1630 - 1660 [MeV]		
-0.9	0.344	0.158	-0.9	0.091	0.195
-0.7	-0.381	0.141	-0.7	0.039	0.212
-0.5	-0.561	0.079	-0.5	0.034	0.212
-0.3	-0.646	0.070	-0.3	-0.235	0.196
-0.1	-0.834	0.074	-0.1	0.154	0.204
0.1	-0.704	0.083	0.1	-0.415	0.492
0.3	-0.807	0.109	0.3	-0.732	1.046
0.5	-0.546	0.154	0.5	-0.290	1.270
0.7	-0.183	0.504	0.7	0.252	0.739
0.9	-0.468	0.427	0.9	-0.675	1.547
W range 1300 - 1330 [MeV]			W range 1660 - 1690 [MeV]		
-0.9	0.281	0.184	-0.9	0.232	0.195
-0.7	-0.343	0.153	-0.7	-0.437	0.212
-0.5	-0.619	0.078	-0.5	0.363	0.159
-0.3	-0.615	0.071	-0.3	-0.099	0.179

-0.1	-0.595	0.070	-0.1	-0.200	0.211
0.1	-0.485	0.080	0.1	0.868	0.597
0.3	-0.516	0.093	0.3	1.097	0.707
0.5	-0.337	0.135	0.5	-0.929	0.829
0.7	-0.283	0.254	0.7	0.139	0.588
0.9	0.259	1.061	0.9	-0.527	0.777
W range 1330 - 1360 [MeV]			W range 1690 - 1720 [MeV]		
-0.9	-0.008	0.227	-0.9	0.005	0.200
-0.7	-0.111	0.222	-0.7	0.045	0.240
-0.5	-0.459	0.093	-0.5	-0.152	0.240
-0.3	-0.743	0.095	-0.3	-0.669	0.266
-0.1	-0.786	0.086	-0.1	0.041	0.282
0.1	-0.625	0.098	0.1	-0.245	0.900
0.3	-0.439	0.116	0.3	0.144	0.823
0.5	-0.145	0.151	0.5	-0.774	1.225
0.7	-0.028	0.334	0.7	-0.064	0.546
0.9	5.597	2.112	0.9	-0.222	1.120
W range 1360 - 1390 [MeV]			W range 1720 - 1750 [MeV]		
-0.9	-0.159	0.265	-0.9	0.576	0.225
-0.7	-0.945	0.259	-0.7	-0.485	0.331
-0.5	-0.431	0.112	-0.5	-0.691	0.277
-0.3	-0.611	0.110	-0.3	-0.273	0.558
-0.1	-0.741	0.110	-0.1	-0.046	0.381
0.1	-0.591	0.120	0.1	-1.460	1.382
0.3	-0.667	0.136	0.3	-2.864	5.303
0.5	-0.399	0.193	0.5	0.498	1.622
0.7	-0.249	0.358	0.7	0.043	0.388
0.9	-0.970	4.506	0.9	-0.844	1.417
W range 1390 - 1420 [MeV]			W range 1750 - 1780 [MeV]		
-0.9	0.391	0.306	-0.9	0.454	0.211
-0.7	-0.319	0.357	-0.7	-0.450	0.280
-0.5	-0.458	0.147	-0.5	-0.482	0.240
-0.3	-0.562	0.135	-0.3	-0.680	0.368

-0.1	-0.502	0.145	-0.1	-0.973	0.913
0.1	-0.194	0.151	0.1	0.646	0.689
0.3	-0.327	0.166	0.3	-2.373	2.793
0.5	0.007	0.227	0.5	-0.096	0.922
0.7	-0.504	0.596	0.7	-0.184	0.667
0.9	-5.141	7.104	0.9	-6.704	7.697
W range 1420 - 1450 [MeV]			W range 1780 - 1810 [MeV]		
-0.9	0.669	0.300	-0.9	0.507	0.235
-0.7	-0.524	0.360	-0.7	-0.111	0.255
-0.5	-0.514	0.202	-0.5	-0.358	0.337
-0.3	-0.163	0.210	-0.3	-0.505	0.402
-0.1	-1.027	0.226	-0.1	-0.204	0.609
0.1	-0.580	0.220	0.1	-0.377	0.464
0.3	-0.089	0.293	0.3	0.266	1.174
0.5	-0.364	0.411	0.5	5.771	13.350
0.7	-0.062	0.782	0.7	-0.532	1.041
0.9	-2.013	2.030	0.9	-0.687	1.363
W range 1450 - 1480 [MeV]			W range 1810 - 1840 [MeV]		
-0.9	1.005	0.187	-0.9	0.124	0.223
-0.7	0.265	0.290	-0.7	-0.008	0.225
-0.5	-0.115	0.137	-0.5	-0.543	0.464
-0.3	-0.390	0.146	-0.3	-0.484	0.382
-0.1	-0.476	0.167	-0.1	-0.850	0.527
0.1	-0.351	0.184	0.1	0.796	0.855
0.3	-0.089	0.225	0.3	0.220	1.023
0.5	0.147	0.349	0.5	1.556	1.979
0.7	0.715	0.528	0.7	0.820	0.715
0.9	0.718	1.357	0.9	0.739	1.224
W range 1480 - 1510 [MeV]			W range 1840 - 1870 [MeV]		
-0.9	1.235	0.208	-0.9	0.198	0.229
-0.7	0.567	0.223	-0.7	-0.287	0.218
-0.5	0.027	0.125	-0.5	-0.786	0.316
-0.3	0.039	0.130	-0.3	-0.364	0.475

-0.1	-0.339	0.150	-0.1	-0.147	0.334
0.1	-0.528	0.170	0.1	-1.402	4.351
0.3	-0.166	0.245	0.3	-0.422	1.869
0.5	0.310	0.296	0.5	-0.520	0.582
0.7	0.646	0.585	0.7	-0.436	0.662
0.9	-1.740	1.889	0.9	-2.663	1.332

Bibliography

[1] I. Newton. *Philosophiæ Naturalis Principia Mathematica*. 1687.

[2] J. C. Maxwell. *A treatise on electricity and magnetism I-II*. Oxford Press, 1873.

[3] Standard Model of Elementary Particles. `https://commons.wikimedia.org/wiki/File:Standard_Model_of_Elementary_Particles_modified_version.svg`. [Online, visited on 12/04/2018].

[4] E. Rutherford. The scattering of alpha and beta particles by matter and the structure of the atom. *Phil. Mag. Ser.6*, 21:669–688, 1911.

[5] J. Chadwick. Possible Existence of a Neutron. *Nature*, 129:312, 1932.

[6] Murray Gell-Mann. Nonleptonic weak decays and the eightfold way. *Phys. Rev. Lett.*, 12:155–156, 1964.

[7] G. Zweig. An SU(3) model for strong interaction symmetry and its breaking. Version 2. Technical report, 1964.

[8] O. W. Greenberg. Spin and Unitary Spin Independence in a Paraquark Model of Baryons and Mesons. *Phys. Rev. Lett.*, 13:598–602, 1964.

[9] C. Patrignani et al. Review of Particle Physics. *Chin. Phys.*, C40(10):100001, 2016.

[10] K. Peters. Hadron physics. `http://slideplayer.com/slide/3387472/`, 2003. [Online, visited on 17/04/2018].

[11] Kenneth G. Wilson. Confinement of Quarks. *Phys. Rev.*, D10:2445–2459, 1974.

[12] D. Hornidge and A. M. Bernstein. Neutral Pion Production in the Threshold Region. *Eur. Phys. J. ST*, 198:133–140, 2011.

[13] Ulrich Loring, Bernard C. Metsch, and Herbert R. Petry. The Light baryon spectrum in a relativistic quark model with instanton induced quark forces: The Strange baryon spectrum. *Eur. Phys. J.*, A10:447–486, 2001.

[14] Robert G. Edwards, Jozef J. Dudek, David G. Richards, and Stephen J. Wallace. Excited state baryon spectroscopy from lattice QCD. *Phys. Rev.*, D84:074508, 2011.

[15] A. V., Anisovich et al. Pion-and photo-induced transition amplitudes to ΛK, ΣK and Nη. *The European Physical Journal A*, 48(6):88, 2012.

[16] J. Bjorken and S. Drell. *Relativistic Quantum Mechanics.* McGraw Hill, New York, 1964.

[17] A. Nagl, V. Devanathan, and H. Überall. *Nuclear Pion Photoproduction.* (Springer-Verlag, Heidelberg,, 1991.

[18] B. Krusche and S. Schadmand. Study of nonstrange baryon resonances with meson photoproduction. *Prog. Part. Nucl. Phys.*, 51:399–485, 2003.

[19] R. M. Davidson. Photoproduction and electroproduction of mesons. *Czech. J. Phys.*, 44:365–403, 1995.

[20] R. L. Workman. Single-energy amplitudes for pion photoproduction in the first resonance region. *Phys. Rev.*, C83:035201, 2011.

[21] D. Drechsel and L. Tiator. Threshold pion photoproduction on nucleons. *J. Phys.*, G18:449–497, 1992.

[22] Lothar Tiator. Complete Experiments for Pion Photoproduction. *Bled Workshops Phys.*, 13(1):55–61, 2012.

[23] I. S. Barker, A. Donnachie, and J. K. Storrow. Complete Experiments in Pseudoscalar Photoproduction. *Nucl. Phys.*, B95:347–356, 1975.

[24] W. Chiang and F. Tabakin. Completeness rules for spin observables in pseudoscalar meson photoproduction. *Phys. Rev.*, C55:2054–2066, 1997.

[25] Y. Wunderlich, R. Beck, and L. Tiator. The complete-experiment problem of photoproduction of pseudoscalar mesons in a truncated partial-wave analysis. *Phys. Rev.*, C89(5):055203, 2014.

[26] A. M. Sandorfi, S. Hoblit, H. Kamano, and T.-S. H. Lee. Determining pseudoscalar meson photo-production amplitudes from complete experiments. *J. Phys.*, G38:053001, 2011.

[27] Lothar Tiator. Towards a model-independent partial wave analysis for pseudoscalar meson photoproduction. *AIP Conf. Proc.*, 1432(1):162–167, 2012.

[28] Y. Wunderlich, F. Afzal, A. Thiel, and R. Beck. Determining the dominant partial wave contributions from angular distributions of single- and double-polarization observables in pseudoscalar meson photoproduction. *Eur. Phys. J.*, A53(5):86, 2017.

[29] D. Drechsel, O. Hanstein, S. S. Kamalov, and L. Tiator. A Unitary isobar model for pion photoproduction and electroproduction on the proton up to 1-GeV. *Nucl. Phys.*, A645:145–174, 1999.

[30] D. Drechsel, S. S. Kamalov, and L. Tiator. Unitary Isobar Model - MAID2007. *The European Physical Journal A*, 34:69–97, 2007.

[31] MAID online database. `https://maid.kph.uni-mainz.de/`. [Online, visited on 17/02/2019].

[32] R. A. Arndt, R. L. Workman, Z. Li, and L. D. Roper. Pion photoproduction resonance couplings in the second resonance region. *Phys. Rev.*, C42:1864–1866, 1990.

[33] R. A. Arndt, W. J. Briscoe, I. I. Strakovsky, and R. L. Workman. Extended partial-wave analysis of piN scattering data. *Phys. Rev.*, C74:045205, 2006.

[34] R. A. Arndt, W. J. Briscoe, I. I. Strakovsky, and R. L. Workman. Analysis of pion photoproduction data. *Phys. Rev.*, C66:055213, 2002.

[35] SAID online database. `http://gwdac.phys.gwu.edu/`. [Online, visited on 17/02/2019].

[36] Bonn-Gatchina online database. `https://pwa.hiskp.uni-bonn.de/`. [Online, visited on 17/05/2018].

[37] H. Arenhoevel, E. M. Darwish, A. Fix, and M. Schwamb. Present status of electromagnetic reactions on the deuteron above pion threshold. *Mod. Phys. Lett.*, A18:190–199, 2003.

[38] Geoffrey F. Chew and M. L. Goldberger. The Scattering of Elementary Particles by Complex Nuclei-A Generalization of the Impulse Approximation. *Phys. Rev.*, 87:778–782, 1952.

[39] H. Arenhovel and A. Fix. Incoherent pion photoproduction on the deuteron with polarization observables. I. Formal expressions. *Phys. Rev.*, C72:064004, 2005.

[40] A. Fix and H. Arenhoevel. Incoherent pion photoproduction on the deuteron with polarization observables. II. Influence of final state rescattering. *Phys. Rev.*, C72:064005, 2005.

[41] M. I. Levchuk, A. Yu. Loginov, A. A. Sidorov, V. N. Stibunov, and Martin Schumacher. Incoherent pion photoproduction on the deuteron in the first resonance region. *Phys. Rev.*, C74:014004, 2006.

[42] V. E. Tarasov, W. J. Briscoe, H. Gao, A. E. Kudryavtsev, and I. I. Strakovsky. Extracting the photoproduction cross section off the neutron gn–>pi-p from deuteron data with FSI effects. *Phys. Rev.*, C84:035203, 2011.

[43] J. Ahrens et al. Helicity dependence of gamma p –> N pi below 450-MeV and contribution to the Gerasimov-Drell-Hearn sum rule. *Phys. Rev. Lett.*, 84:5950–5954, 2000.

[44] J. Ahrens and al. . Measurement of the gerasimov-drell-hearn integrand for ^{2}H from 200 to 800 mev. *Phys. Rev. Lett.*, 97:202303, Nov 2006.

[45] Parameters of the Mainz Microtron-MAMI. `http://portal.kph.uni-mainz.de/B1/params.php`. [Online, visited on 20/05/2018].

[46] History on the Mainz Microtron-MAMI. `http://portal.kph.uni-mainz.de/B1/history.php`. [Online, visited on 20/05/2018].

[47] M. Dehn, K. Aulenbacher, R. Heine, H. J. Kreidel, U. Ludwig-Mertin, and A. Jankowiak. The MAMI C accelerator: The beauty of normal conducting multi-turn recirculators. *Eur. Phys. J. ST*, 198:19–47, 2011.

[48] D. T. Pierce, F. Meier, and P. Zürcher. Negative electron affinity GaAs: A new source of spin-polarized electrons. *Applied Physics Letters*, 26:670, 1975.

[49] K. Aulenbacher et al. The MAMI source of polarized electrons. *Nucl. Instrum. Meth.*, A391:498–506, 1997.

[50] V. Tioukine, K. Aulenbacher, and E. Riehn. A Mott polarimeter operating at MeV electron beam energies. *Rev. Sci. Instrum.*, 82:033303, 2011.

[51] V. Tioukine. Mott polarimeter at MAMI. `http:www.fe.infn.it/PST2009/body/talks/tioukine.pdf`, 2009. [Online, visited on 29/05/2018].

[52] V. Tioukine and K. Aulenbacher. Operation of the MAMI accelerator with a Wien filter based spin rotation system. *Nucl. Instrum. Meth.*, A568:537–542, 2006.

[53] A. Jankowiak. The Mainz Microtron MAMI: Past and future. *Eur. Phys. J.*, A28S1:149–160, 2006.

[54] A2 internal documentation. `https://wwwa2.kph.uni-mainz.de/intern/daqwiki/start`. [Online, visited on 12/06/2018].

[55] H. W. Koch and J. W. Motz. Bremsstrahlung Cross-Section Formulas and Related Data. *Rev. Mod. Phys.*, 31:920–955, 1959.

[56] D. Lohmann et al. Linearly polarized photons at MAMI (Mainz). *Nucl. Instrum. Meth.*, A343:494–507, 1994.

[57] A. B. Apyan, R. O. Avakian, S. M. Darbinian, K. A. Ispirian, and Peter E. Bosted. Circularly polarized photon beams produced by channeled longitudinally polarized electrons. *Nucl. Instrum. Meth.*, B145:142–145, 1998.

[58] Haakon Olsen and L. C. Maximon. Photon and Electron Polarization in High-Energy Bremsstrahlung and Pair Production with Screening. *Phys. Rev.*, 114:887–904, 1959.

[59] I. Anthony, J. D. Kellie, S. J. Hall, G. J. Miller, and J. Ahrens. Design of a tagged photon spectrometer for use with the Mainz 840-MeV microtron. *Nucl. Instrum. Meth.*, A301:230–240, 1991.

[60] S. J. Hall, G. J. Miller, R. Beck, and P. Jennewein. A focal plane system for the 855-MeV tagged photon spectrometer at MAMI-B. *Nucl. Instrum. Meth.*, A368:698–708, 1996.

[61] J. C. McGeorge et al. Upgrade of the Glasgow photon tagging spectrometer for Mainz MAMI-C. *Eur. Phys. J.*, A37:129–137, 2008.

[62] A. Thomas. Review on the last developments on polarized targets at Mainz. `http://wwwa2.kph.uni-mainz.de/images/target/saclay_2013_thomas.ppt`. [Online, visited on 12/06/2018].

[63] D. G. Crabb and W. Meyer. Solid polarized targets for nuclear and particle physics experiments. *Ann. Rev. Nucl. Part. Sci.*, 47:67–109, 1997.

[64] M. I. Darby. Tables of the Brillouin function and of the related function for the spontaneous magnetization. *Brit. J. Appl. Phys*, 18(10):1415–1417, 1967.

[65] C. Keith. Frozen Spin Nutshell 3. `https://www.jlab.org/~ckeith/Frozen/FrozenSpinNutshell3.pdf`. [Online, visited on 22/05/2018].

[66] Albert W. Overhauser. Polarization of Nuclei in Metals. *Phys. Rev.*, 92:411–415, 1953.

[67] T. R. Carver and C. P. Slichter. Polarization of Nuclear Spins in Metals. *Phys. Rev.*, 92:212–213, 1953.

[68] W.Th. Wenckebach. Dynamic nuclear polarization via thermal mixing: Beyond the high temperature approximation. *Journal of Magnetic Resonance*, 277:68 – 78, 2017.

[69] M. Pluckthun, C. Bradtke, H. Dutz, R. Gehring, S. Goertz, J. Harmsen, W. Meyer, G. Reicherz, and P. Kingsberry. Polarization measurements of TEMPO-doped butanol targets. *Nucl. Instrum. Meth.*, A400:133–136, 1997.

[70] E. Rickert. Untersuchung der Ortsabhängigkeit der polarization des Mainzer Frozen-Spin-Targets. Master's thesis, Johannes Gutenberg-Universit 2015.

[71] A. Thomas. Private Communication, 2018.

[72] A. Thomas. Numbers of Nucleons and Nuclei in Butanol Target. `http://wwwa2.kph.uni-mainz.de/internalpages/detectors-and-setup/target.html`. [Online, visited on 15/06/2018].

[73] T. O. Niinikoski and F. Udo. Frozen Spin Polarized Target. *Nucl. Instrum. Meth.*, 134:219, 1976.

[74] B. S. Neganov, N. S. Borisov and M. Yu. Liburg. A method of producing very low temperatur by dissolving He^3 in He^4. *JETP*, 50:1445–1457, 1966. English translation available on: `http://www.jetp.ac.ru/cgi-bin/e/index/r/50/6/p1445?a=list`.

[75] H. London, G. R. Clarke, and Eric Mendoza. Osmotic Pressure of He-3 in Liquid He-4, with Proposals for a Refrigerator to Work below 1-degrees K. *Phys. Rev.*, 128:1992–2005, 1962.

[76] H. Dutz. Highlights of polarized solid state target instrumentation. *Nucl. Instrum. Meth.*, A526:117–125, 2004.

[77] CB installation in Mainz. `https://wwwa2.kph.uni-mainz.de/intern/daqwiki/pictures/cb`. [Online, visited on 12/06/2018].

[78] Elliott D. Bloom and C. Peck. Physics with the Crystal Ball Detector. *Ann. Rev. Nucl. Part. Sci.*, 33:143–197, 1983.

[79] G. Audit et al. DAPHNE: A Large acceptance tracking detector for the study of photoreactions at intermediate-energies. *Nucl. Instrum. Meth.*, A301:473–481, 1991.

[80] P. Pedroni A. Braghieri, V. Isbert. *MWPCs tracks fitting.* DAPHNE internal note, 1992.

[81] P. A. Bartolome. *First Doubly Polarized Photoproduction on ^{3}He at the Photon Beam of MAMI.* PhD thesis, Johannes Gutenberg-Universität Mainz, 2010.

[82] W. R. Leo. *Techniques for Nuclear and Particle Physics Experiments: A How to Approach.* Berlin, Germany: Springer (1987), 1987.

[83] TAPS manual. `https://wwwa2.kph.uni-mainz.de/intern/daqwiki/experiment/detectors/taps/start`. [Online, visited on 12/06/2018].

[84] R. Novotny. The BaF2 spectrometer taps: A system for high energy photon and neutral meson detection. *Nuclear Tracks and Radiation Measurements*, 21(1):23 – 26, 1993.

[85] S. Bender. Aufbau und Test eines Bleiwolframat-Kalorimeters für das Crystal Ball/TAPS-Experiment an MAMI. Master's thesis, Johannes Gutenberg-Universit 2009.

[86] TAPS elements geometry. `https://wwwa2.kph.uni-mainz.de/intern/daqwiki/_media/experiment/detectors/taps/taps2009_from_target.png`. [Online, visited on 15/07/2018].

[87] M. Thiel. *In-medium Properties of the ω-Meson Studied in Photonuclear Reactions near the Production Threshold.* PhD thesis, Universität Giessen, 2010.

[88] J.R.M. Annand. *Data Analysis within an AcquRoot Framework.* University of Glasgow, 2008. `www.nuclear.gla.ac.uk/~acqusys/doc/AcquRoot.11.08.pdf`, [Online, visited on 19/07/2018].

[89] Trigger electronics. `https://wwwa2.kph.uni-mainz.de/internalpages/detectors-and-setup/experiment-trigger.html`. [Online, visited on 15/07/2018].

[90] R. Brun and F. Rademakers. ROOT: An object oriented data analysis framework. *Nucl. Instrum. Meth.*, A389:81–86, 1997.

[91] GoAT manual and repository. https://github.com/A2-Collaboration-dev/a2GoAT. [Online, visited on 12/02/2018].

[92] Simulation of the Crystal Ball and associated apparatus at MAMI. https://www.ph.ed.ac.uk/nuclear-physics/research-activities/nuclear-and-hadron-physics/the-edinburgh-g4-simulation-of-the-crystal-ball-detector. [Online, visited on 12/06/2018].

[93] D. Werthmüller. Calibration procedure of A2 data using the CaLib software. https://wwwa2.kph.uni-mainz.de/intern/daqwiki/analysis/software/calib. [Online, visited on 22/06/2018].

[94] L. Zana. PID calibration. Private communication.

[95] S. Costanza. Report on the Moeller analysis of the Jan/Feb 2014 beamtime. Technical report, INFN, 2014. [Online, visited on 17/06/2018].

[96] P. B. Otte. *Erste Messung der π^0-Photoproduktion an transversal polarizierten Protonen Nahe der Schwelle.* PhD thesis, Johannes Gutenberg-Universität Mainz, 2010.

[97] A. Fix. Private Communication, 2016. FSI calculations based on [39, 40].

[98] F. N. Afzal. *Measurement of the beam and helicity asymmetries in the reactions $\gamma p \to \pi^0 p$ and $\gamma p \to \eta p$.* PhD thesis, Rheinischen Friedrich-Wilhelms-Universität Bonn, 2019.

[99] M. Dieterle, L. Witthauer, F. Cividini, et al. First measurement of the polarization observable E and helicity-dependent cross sections in single π^0 photoproduction from quasi-free nucleons. *Phys. Lett.*, B770:523–531, 2017.